METHODOLOGIES FOR ANALYZING RETINAL NERVE FIBER LAYER THICKNESS/AREA USING SPECTRAL DOMAIN OPTICAL COHERENCE TOMOGRAPHY.

By

Nimesh Patel, OD

DISSERTATION

In partial satisfaction of the requirements for the degree of

DOCTOR OF PHILOSOPHY

in

PHYSIOLOGICAL OPTICS

Presented to the Graduate Faculty of the

College of Optometry
University of Houston

May 2012

Approved:

_____
Ronald S. Harwerth, OD, PhD (Chair)

_____
Laura J. Frishman, PhD

_____
Michael D. Twa, OD, PhD

_____
Jason Porter, PhD

_____
Louvenia Carter-Dawson, PhD

Committee in Charge

Dedication

To my family and Baba

Acknowledgements

I am very grateful to the University of Houston and the College of Optometry, for giving me the opportunity to continue teaching and seeing patients while pursuing a graduate degree. I am very fortunate to have had the chance to learn from some of the best teachers, scientists and clinicians. Thank you.

Early in my optometric career, I remember reading a paper, authored by Dr. Harwerth, on ganglion cell losses associated with visual field defects in glaucoma. I found it amazing that rhesus monkeys could be trained to perform visual fields, and with such excellent reliability. Having the opportunity to work in Dr. Harwerth's lab has been an invaluable experience, and a dream come true. I thank my mentor for everything he has taught me, from the critical assessment of optic nerve heads to methods of training rhesus monkeys for perimetry experiments. I thank him for his patience and willingness to teach me and guide me.

This work would not be possible without the useful input from my committee members. Dr. Porter not only taught me aspects of imaging devices, but also showed me the importance of accurate transverse retinal scaling. Dr. Twa took his time to teach me methodologies for image segmentation and OCT analysis. Dr. Carter-Dawson helped with all the histology and guided me on histological techniques. I value the conversations I have with Dr. Frishman as they make me think outside the box, and her insights into electrophysiology are invaluable. I thank all the members of my committee for everything they have taught me and for all their guidance.

I am very grateful to the office of graduate studies at the college. Michele has helped me every single step of the way, and always with a smile. I thank her for her time and dedication to the program. Words cannot express my gratitude to Dr. Frishman. She has always encouraged me, given me advice and pointed me in the right direction.

There have been several who have guided me in my education. I am grateful for individuals such as Mr. Acharya, Dr. Donna Wear, and Dr. Gary Wickham who encouraged me, and helped build my confidence as a student, an instructor and a clinician. I thank Dr. Michelle Welch, Dr. Richard Castillo, Dr. Lisa Schifanella, and Dr. Jeff Miller, who taught me as a resident, and always pushed me to learn more. I value their continuing support.

Finally, and most importantly, I would like to acknowledge my family. My wife, Harsha, from the day I brought up the idea of graduate school, has supported me each and every step of the way. Our two boys, Saiyan and Soham who always manage to bring a smile to my face, and are the joy in our life. Bapuji (Dad) and Ba (Mom), have not only supported us this entire time, but have helped raise our two boys. I cannot thank them enough for everything that they have done for us, and their commitment to educating their children. My brother (Dipen bhai) has always been an inspiration to me. I thank him for introducing me to Optometry, and his encouragement throughout my education. My sister-in-law (Ekta bhabhi), nephew (Nilay) and niece (Naya) have always given me words of encouragement, and I thank them for their endless support. Lastly, I would like to thank my in laws, Dad, Mom, Kamal Bhai, Dimple Ben, and Ameya, who have been extremely supportive these last five years.

Support: NIH R01 EY001139, P30 EY007551, K23 EY021761, UHCO Student VRSG, Minnie Flaura Turner Memorial Fund, Fight for Sight, and the Optometric Glaucoma Society Ezell Fellowship.

Methodologies for Analyzing Retinal Nerve Fiber Layer Thickness/Area Using Spectral Domain Optical Coherence Tomography.

By

NIMESH PATEL, OD

AN ABSTRACT OF A DISSERTATION

Presented to the

Faculty of the College of Optometry

University of Houston

Submitted in Partial Fulfillment

Of the Requirements for the Degree

of

DOCTOR OF PHILOSOPHY

May 2012

ABSTRACT

Purpose: Glaucoma is a group of optic neuropathies that can lead to irreversible vision loss, especially when not treated. Having an unknown cause, the diagnosis or progression is dependent on accurate clinical measures of structural and functional signs of the disease. The most common quantifiable retinal structure is the peripapillary retinal nerve fiber layer (RNFL), a surrogate for the total ganglion cell content within the eye. With technologies such as spectral domain optical coherence tomography (SD OCT), the RNFL thickness can be quantified with resolutions approaching 5 μm. Although these measures have been shown to be reliable, the accuracy of thickness measures is related to ocular biometry and the retinal scan path, which have not been investigated systematically. The purpose of this dissertation was to develop methodologies that will improve the precision and accuracy of SD OCT measures of retinal structures. These methods were then applied to investigate morphological changes in the non-human primate ocular hypertensive glaucoma model.

Methods: 1) For the first experiment, 16 infant rhesus monkeys were scanned with an SD OCT system, at regular intervals, starting at around 36 ± 6 days of age until 628 ± 27 days. Changes in ocular magnification were investigated using both image registration and a three surface schematic eye. The total retinal thickness, and pit morphology at each scan session were quantified using a semi-automated segmentation algorithm. Individual layers of the retina were manually identified with the aid of reflectivity profiles through the region of interest. 2) The second experiment investigated the influence of anterior segment power change, induced by soft contact lenses, on ocular magnification and RNFL scan path. 15 healthy human subjects were scanned with soft contact lenses ranging from -12 to +8 D in 2 D steps. Changes in ocular magnification were

investigated using both image registration and the schematic eye. RNFL thickness was quantified using a custom semi-automated segmentation algorithm that also compensated for major retinal vasculature. RNFL area measures were calculated by multiplying thickness measures from each A-scan by its calculated width. 3) The influence of ocular biometry, and segmentation algorithms on RNFL measures were further investigated in 45 human eyes scanned with two clinical SD OCT instruments. 4) The scaling and RNFL segmentation algorithms developed were applied to investigations of scan path distance from the optic nerve head (ONH) rim margin and RNFL thickness measures. For this experiment, RNFL thickness and area, with and without blood vessel subtraction were measured for elliptical scan paths 300-600 μm from the rim margin in 40 normal rhesus monkeys. 5) For the fifth experiment, RNFL thickness measures from an elliptical scan path 550 μm from the rim margin was investigated along with ONH morphology and total macula volume in 6 ocular hypertensive experimental glaucoma animals.

Results: 1) Transverse scaling based on schematic eye calculations correlated with axial length related changes in retinal image size for the 16 infant animals followed longitudinally ($R^2 = 0.88$, slope = 0.98, $p < 0.01$). Most changes in total retinal thickness was attributable to the outer retinal layers, and were complete around 120 days of age. The Nyquist limit calculated from outer nuclear layer thickness was in agreement with previously published histological data. 2) In human subjects, the region of the retina scanned increased with increase in contact lens power ($R^2 = 0.94$, $p < 0.01$), and was accurately modeled with the schematic eye ($R^2 = 0.97$, $p < 0.01$). The relationship between contact lens power and RNFL thickness was attributed to differences in the length of the scan path. When the scan circumference was incorporated, RNFL area

was not related to contact lens power (R^2 = 0.003, p = 0.47). 3) For the 45 eyes included, there were significant differences in instrument derived RNFL thickness between the two clinical instruments used (mean difference = 6.7 ± 4.8 μm, ICC = 0.62). However, when the same scan path and segmentation algorithm were used, these differences were reduced (mean difference = 0.1 ± 3.1 μm, ICC = 0.92). Global RNFL thickness from both the instrument derived and the custom segmentation were linearly related to axial length (slope = -3 μm/mm, R^2 = 0.24, p < 0.01). However, when transverse scaling was incorporated, RNFL area was not related to axial length (R^2 = 0.004, p = 0.69). 4) For the 40 eyes of rhesus monkeys scanned, RNFL thickness decreased with increase in scan distance from the ONH rim when custom elliptical scans were used (R^2 = 0.61, p < 0.01). In contrast, global RNFL area did not change over this same region (R^2 = 0.002, p =0.49). The major retinal vascular contribution accounted for 9.3% of global measures, and was similar for all scan locations. 5) For ocular hypertensive animals, the RNFL area did not change until after the ONH neural rim volume decreased by about 60%. While the percent vascular contribution to the RNFL increased (R^2 = 0.64, p < 0.64), the overall vessel area decreased (R^2 = 0.33, p < 0.01) with disease progression.

Conclusion: Measurements of RNFL thickness by SD OCT are dependent on the optics of the eye, including both anterior segment power and axial length. The results suggest that the RNFL cross sectional area after compensation for major retinal vasculature is an accurate surrogate for retinal ganglion cell axonal content within the eye. As morphological changes in the ONH precede RNFL thinning, it is important to assess both in determining glaucomatous disease and disease stage.

Table of Contents

List of Figures

List of Tables

CHAPTER 1

GENERAL INTRODUCTION

THE STRUCTURE FUNCTIONAL RELATIONSHIP

The relationship between structure and function is of interest in all facets of science. Both are not only interrelated, but each must also provide important insight into the other. A classic example of structure-function interrelation is the force-velocity tradeoffs in Darwin's finches.[1] While the significant differences in beak structure between species occurred as they adapted to their diets[2], the beak structure also influenced vocal sounds[3] and hence recognition of mates.

In the field of neuroscience, structural assessment of neuronal networks and their association with function has been studied since the 19th century. Initial histological work by Joseph von Gerlach and refined by Camillo Golgi with his black reaction[4] staining technique, was known as the diffuse nervous network or reticular theory.[5] In brief, the theory suggested that all neurons were continuous, with interconnected cell membranes and cytoplasm. In contrast, Santiago Ramón y Cajal, using similar methodologies as Golgi, illustrated that neuronal cells were independent entities separated by synapses, and established the neuron doctrine.[6] Although the majority of Cajal's work and drawings were based on the histological structure of the cerebellum, he had a keen interest in the retina. Specifically, the layered structure of the retina helped explain the principle of 'dynamic polarization', the flow of information from one neuron to the next. Although the principles of dynamic polarization fall short in explaining lateral inhibition, feedback, and the role of horizontal and amacrine cells, the basic principles of the neuron doctrine are sound.[7] Based on this doctrine, the number of neurons, their firing rates, and the cells they synapse with would determine sensory perception and/or motor output.[8]

THE VISUAL SYSTEM

The visual system is supposedly the most complex sensory component of the central nervous system. As light energy passes through the optics of the eye, it is captured by either the photopigment[9] within the photoreceptor outer segments or by intrinsically photosensitive retinal ganglion cells (RGC).[10,11] Within the visual pathway, the capture of photons by photoreceptors results in a change in the cell membrane potential and subsequently neurotransmitter release. In the most basic pathway, this sensory signal is passed from photoreceptor to bipolar cell to the RGC whose axon exits the eye and synapses in the lateral geniculate nucleus (LGN). Neurons in the LGN relay the signal to the visual cortex (V1) where the input is integrated and transmitted to higher order visual processing centers. Both psychophysical[12,13] and physiological[14-17] studies have found that capture of relatively few photons under dark adapted conditions is sufficient for a functional response. In addition, changes in the psychophysical threshold,[18] with background illuminations from scotopic to photopic conditions, can be attributed to physiological changes within the retina.[19-21] Hence, there should be good correspondence between visual function and the structural RGC output from the eye.[22]

As the neural tissue of the eye can be assessed non-invasively through a dilated pupil, the visual system is an ideal component of the central nervous system for studying neural networks and structural changes associated with disease processes. The main aim of the series of experiments described in this dissertation was to develop and apply precise and accurate measures of retinal structure using a non-invasive *in vivo* methodology, and investigate its use in an ocular hypertension model of experimental glaucoma.

GLAUCOMA

Glaucoma defines a group of progressive optic neuropathies that can lead to irreversible blindness if left untreated. Common features associated with the disease include a loss of RGCs, thinning of the retinal nerve fiber layer (RNFL), non-physiological optic nerve head (ONH) cupping, and loss of visual sensitivity. Although several risk factors including, but not limited to, intraocular pressure, family history, central corneal thickness, hypertension, diabetes and sleep apnea, have been identified, the exact cause of the disease remains elusive.[23] Hence, the diagnosis or progression of glaucoma requires structural and functional measures of the features that define the disease.

Defects of visual functional are most commonly assessed over the central 48 to 60 degrees of the visual field using white-on-white stimuli to measure visual thresholds, which is referred to as standard automated perimetry (SAP).[24,25] The resulting threshold map for a healthy eye has high sensitivity in the central vision that decreases with increasing eccentricity, i.e. the 'hill of vision'. For disease detection, threshold measures are compared to age matched normative data to determine the depth or severity of the defect. The classical visual field defects associated with glaucoma include; 1) Seidel scotomas, 2) Bjerrum scotomas, 3) nasal steps, and 4) paracentral scotomas, all which commonly respect the horizontal midline.[26-28] These functional defects often correspond to structural loss of RNFL thickness, and ONH neural rim notches, as observed with direct or indirect ophthalmoscopy.[29-31] For example, a thinning of the inferior RNFL or an inferior ONH rim notch would correspond to a superior visual field defect. However, in the clinical setting both visual field testing and clinical examination of the posterior segment are subjective, with significant inter and intra-individual variability.[32-38] Consequently, when initiating or changing therapy, confirmatory visual field tests are

usually recommended.[33,39,40] Hence, an accurate structure-functional relationship would aid significantly in this diagnostic process.

THE RELATIONSHIP BETWEEN STRUCTURE AND FUNCTION IN GLAUCOMA

In principle, there should be a good relationship between visual function and structural measures from retinal ganglion cells in glaucoma. Specifically, the associated losses of retinal ganglion cells should correspond with visual field threshold measures at each location sampled. In initial histological studies of human eyes, there was a good correspondence between RGC density and visual field sensitivity, but a visual field defect was only noted when there was a 25-35% loss of RGCs.[41,42] Since these initial reports, several maps[43-46] and models, linear[47-49] and non-linear, have been proposed to link structure and functional measures in glaucoma. Although there is general agreement between these models,[50] there are significant and notable differences between the models. While the non-linear model is based on a logarithmic relationship between visual sensitivity and RGC density that varies with eccentricity, the linear model suggests a direct relationship between RGC cell loss and the age adjusted total deviation in sensitivity for each test location. In addition, the non-linear model suggests an age and disease state related non-neuronal component, whereas this component is thought to be constant in the linear model.

The accuracy of either model is limited by the accuracy and precision of the measuring tools used. For example, the subjective retinal sensitivity measures from SAP are highly variable within and between individuals. Hence, non-invasive objective techniques such as automated assessment of pupil function,[51,52] multifocal electroretinograms[53-57] and multifocal visual evoked potentials,[58-60] are being investigated to improve functional measures. For structural assessment of the optic nerve and retina,

several non-invasive imaging technologies have been developed. Although these instruments have less variability than an ophthalmoscopic examination, there are significant differences between the instruments themselves.[61-63] One of the aims for the presented work is the investigation of a new methodology of structural assessment using optical coherence tomography.

RETINAL IMAGING

It first was possible to examine the retina and ONH using non-invasive methodology around 1847-1851 when Charles Babbage and Hermann von Helmholtz independently invented the ophthalmoscope.[64,65] Since its invention, a direct or indirect ophthalmoscopic evaluation of the retina and optic nerve has been standard of care for the clinical evaluation of the posterior segment of the eye. In glaucoma, the loss of RGCs and associated RNFL results in thinning of the neural retinal rim tissue and an increase in ONH cupping.[66] Although a valuable tool in glaucoma management, ophthalmoscopy is subjective, and has high inter and intra-individual variability.[36,37] Hence, for comparison across visits, clinicians will often photograph (flat fundus or stereoscopic) the ONH of glaucoma and glaucoma suspect patients at baseline examination and at any point at which a change is noted. Both color and red-free[30,31] fundus photography provide valuable qualitative information on the optic nerve, but with quantifiable features limited to ONH rim, and cup parameters.[67-69] With the advent of scanning laser technology, additional features of the posterior segment, including the optic nerve and macula, such as total retinal thickness and individual retinal layer thicknesses can be measured. The three main scanning laser devices used in clinical care include; 1) the confocal scanning laser ophthalmoscope (CSLO), 2) scanning laser polarimetry (SLP), and 3) optical coherence tomography (OCT).

Scanning Laser Ophthalmoscopy and Scanning Laser Polarimetry

CSLO technology utilizes a small beam of light scanned across a region of interest within the retina to create a reflection image.[70] By using a confocal aperture or pupil, these systems have reduced light scatter and the ability to image tissues at varying depths. Subsequently, captured images can be used to create three dimensional data sets that typically have higher transverse resolution than axial resolution. In general, morphological measures of the optic nerve using these three dimensional data have been shown to be repeatable.[71,72] For the commercially available instrument, HRT (Heidelberg Retinal Tomograph, Heidelberg Engineering, Heidelberg, Germany), these measures are made from an instrument determined reference plane that is nominally 50 μm deep at the temporal rim margin.[73] However, there is significant inter and intra-subject variability in this reference plane that needs to be taken into consideration when diagnosing disease or disease progression.[74,75]

Scanning laser polarimetry is a scanning laser ophthalmoscope (SLO) system with a polarized laser diode light source (780 nm), that takes advantage of the birenfrigence properties of the axons in the RNFL.[76,77] Specifically, the thickness of the RNFL is considered to be linearly related to the retardation of polarized light that passes through the retina.[76] However, ocular structures such as the cornea and crystalline lens also have birenfrigence properties that can result in erroneous RNFL thickness measures when not corrected in the retardation image. Although the initial versions of this instrument used a fixed corneal polarization axis (15 degrees)[78] and did not compensate for variability in corneal birenfringence, there have been significant improvements in the newer iterations of SLP technology (GDx Extended Corneal Compensator, Carl Zeiss Meditec Inc., Dublin, CA). Overall, measures from SLP are repeatable[79] and have good sensitivity and specificity in diagnosing glaucoma.[80,81]

Optical Coherence Tomography

Although three dimensional data acquired using CSLO technology have high transverse resolution, the technology cannot be used to produce high resolution cross sectional images of the retina, which are essential in locating pathology within the retina and for quantification of retinal layers. Such images can be acquired using OCT technology that utilizes low coherence interferometry. Recent advances in this technology, specifically, spectral domain optical coherence tomography (SD OCT) produces axial resolution of approximately 5 μm.

The basic principles of OCT technology can be compared to that of B-scan ultrasonography. In ultrasound technology, acoustic waveforms are reflected off a tissue, whose backscatter is then detected and converted into a signal. In brief, adjacent acoustic signals (A-scans), acquired with an oscillating probe, are aligned to create a two dimensional image (B-scan). Fujimoto and colleagues, in the late 1980s were pioneers in using light energy to image biological tissues with similar concepts as those of ultrasonography. Specifically, they used a 65 femtosecond pulsed laser, to determine time of flight information and subsequently quantified corneal thickness in a rabbit with 15 μm resolution.[82] Soon thereafter, cost efficient optical setups that included low coherent light from a superluminescent diode (SLD) and a Michelson interferometer, were illustrated to produce similar results.[83,84] In 1988, this technology was then applied to *in vivo* measurements for axial lengths (A-scan) in human eyes, with an accuracy of 0.03 mm.[85] However, it wasn't until 1991 that the first B-scan images of human tissue were published in the scientific literature using OCT technology.[86] Subsequently, a commercial instrument was developed,[87] and has been an invaluable tool for vision research and clinical eye care.

The first generation clinical OCT instruments were time domain (TD) systems, whose main features included a moving reference arm, and a single photodetector that captured the interference data from the Michelson interferometer (Fig 1-1A). When scanning, the signal from the photodetector is filtered, processed and displayed as successive A-scans corresponding to the scan location. These A-scans are then aligned by cross correlation, resulting in an OCT B-scan of the posterior segment. A typical TD OCT system captures A-scans at a frequency of 400 Hz, taking over a second to capture a high resolution 30 degree B-scan (17 A-scans/deg) of the posterior segment. The axial resolution of the system is based on the bandwidth of the illumination source, and can be calculated using equation 1-1.[87] In this equation, Δl is theoretical axial resolution of the system, λo is the central wavelength of the SLD and Δλ is the bandwidth of the SLD. For most low coherent sources used in OCT systems, the axial resolution ranges from 3 to 10 μm.

Equation 1-1

$$\Delta l = \frac{2.ln2}{\pi} \times \frac{\lambda_o^2}{\Delta\lambda}$$

The transverse resolution of the system is based on the imaging spot size on the retina, which is dependent on the optics of the instrument, the optical quality of the ocular media, and the biometry of the eye.

The second generation of OCT systems operates in the spectral or Fourier domain (SD or FD). In addition to a stationary reference arm, these systems include a diffraction grating and line scan camera that detects the signal from the tissue being scanned (Fig 1-1B). In contrast to TD systems, SD OCT systems can capture A-scans at 40 kHz, are less susceptible to eye motion artifact, and can efficiently acquire volumetric data through a region of interest. While there is only one TD OCT system

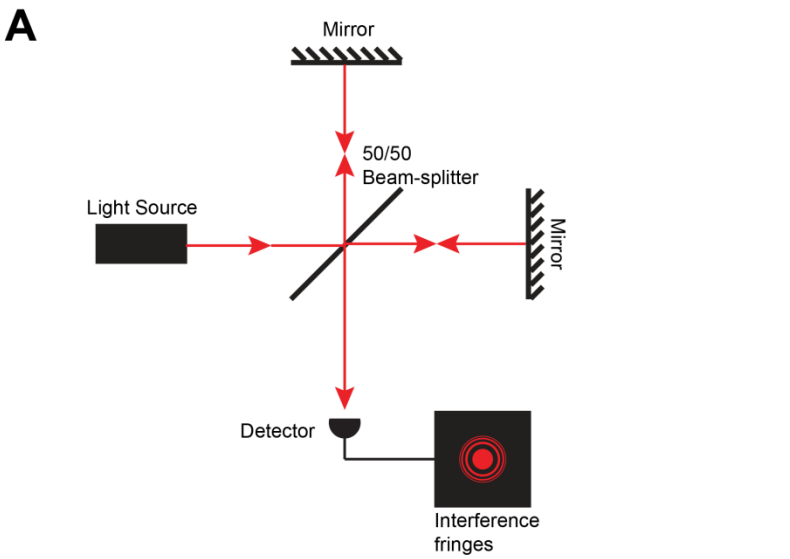
A
Mirror
50/50
Beam-splitter
Light Source
Mirror
Detector
Interference
fringes

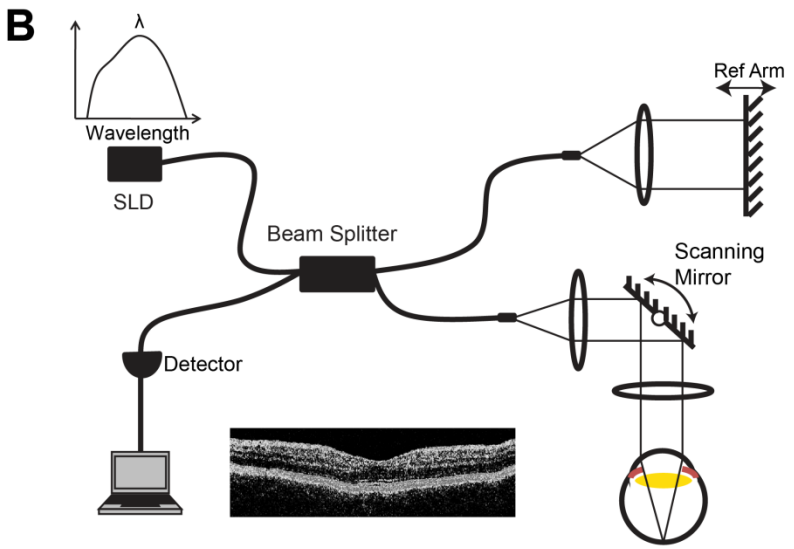
B
λ
Wavelength
SLD
Ref Arm
Beam Splitter
Scanning
Mirror
Detector

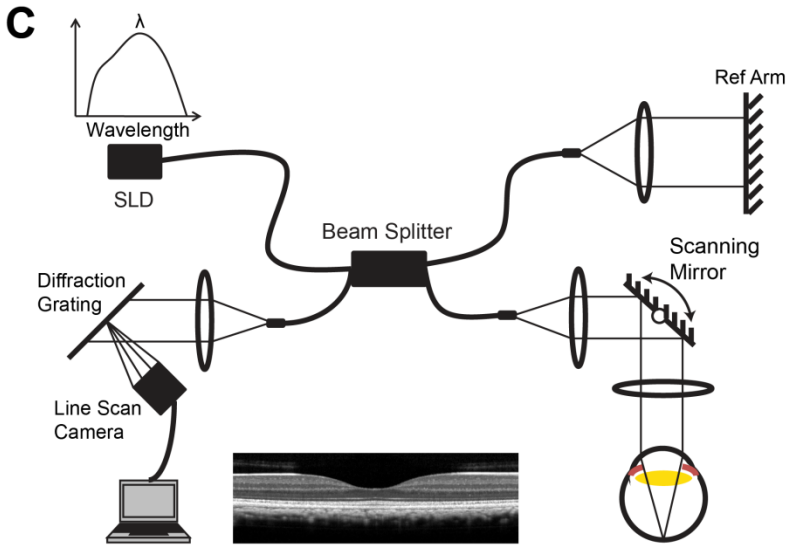
C
λ
Wavelength
SLD
Ref Arm
Beam Splitter
Scanning
Mirror
Diffraction
Grating
Line Scan
Camera

Figure 1-1. Optical Coherence Tomography.

A. A typical setup for a Michelson interferometer. Light from a coherent or partially coherence source is directed at a 50:50 beam splitter and reflected off mirrors. The interference from the reflected light can be displayed on a screen or focused on a detector as illustrated in this setup. B. The time domain OCT system reflects light off the tissue being imaged and a moving reference area. The reflected light is then captured by a detector, and transformed into an image after digital processing. C. The spectral domain system OCT system has a similar setup, but utilizes a diffraction grating and line scan camera and does not have a moving reference arm.

(Stratus OCT, Carl Zeiss Meditec Inc., Dublin, CA), there are several SD OCT systems available for clinical use. And although these systems use similar technology, morphological measures of similar retinal structures or layers cannot be compared between clinical instruments.[61,62,88-92]

CORRESPONDANCE OF OCT IMAGING AND RETINAL HISTOLOGY

The signal strength at each point within an OCT A-scan is dependent on the tissue reflectivity and the corresponding interference pattern from that location. In addition to changes in refractive index at the junction of retinal layers, each layer of the retina has its own signature reflectivity profile.[93] However, elements within the retina are not always homogenous, and it is likely that these differences are reflected in the OCT signal. For example, elements of photoreceptors can be found in at least four OCT B-scan layers including the outer segments, inner segments, outer nuclear layer, and outer plexiform layer. Several comparative histological studies have been performed for OCT B-scan layer identification using both TD and SD OCT systems.[93-96] In general, there is good agreement between these studies with similar retinal layer identification across species. However, the histological equivalence for *in vivo* scans in the non-human primate, the model used for three of the following chapters, is limited. While there is significant comparative anatomy work for the ONH,[97,98] there are no published reports for the macular region of the rhesus macaque monkey.

The visual system of the rhesus macaque monkey is often used in research because their anatomy and physiology are similar to humans. However, there are significant differences between the two species that need to be taken into consideration. For example, the rhesus monkey has a greater amount of pigment in the retina. Hence, most OCT segmentation algorithms fail at identifying the retinal pigment epithelium

(RPE), as it has similar reflectivity to the underlying choroid. It was therefore necessary that OCT scans acquired *in vivo* be compared to histology in this species. For this experiment, high resolution SD OCT scans (Spectralis HRA+OCT, Heidelberg Engineering, Heidelberg, Germany) were acquired through the optic nerve and fovea of a 6 year old rhesus monkey, at three separate visits. After the last scanning session, the eyes were enucleated, fixed in 2% paraformaldehyde and 1% glutaraldehyde and embedded in resin. 1 μm sections were then cut, stained with either cresyl violet or basic fuschin, and photographed. For the best corresponding histological and OCT sections, layers within the retina were manually segmented. For OCT sections, the segmentation was aided by the reflectivity profiles for each A-scan. Using an iterative cross correlation algorithm (Patel NB, et al. Optom Vis Sci 2009;86:E-abstract 090768), the best correspondence of layers was then determined. The retinal layers identified using this technique (Fig 1-2), were similar to those previously published and also corresponded well with those of human eyes.[99-101]

GLAUCOMA AND OCT TECHNOLOGY

ONH Analysis

The ONH is often considered the primary site for glaucomatous damage that subsequently leads to axonal loss. For example, early studies that investigated elevated intraocular pressure in the non-human primate eye illustrated a decrease in both orthograde and retrograde axoplasmic transport, that can be localized to the lamina scleralis, also known as the lamina cribrosa.[102] Similarly, histological studies in normal and glaucoma patients show significant changes in the ONH, even in the early stages of the disease process.[103] Hence, it is likely that *in vivo* structural measures of the ONH may provide useful information in the diagnosis and management of glaucoma.

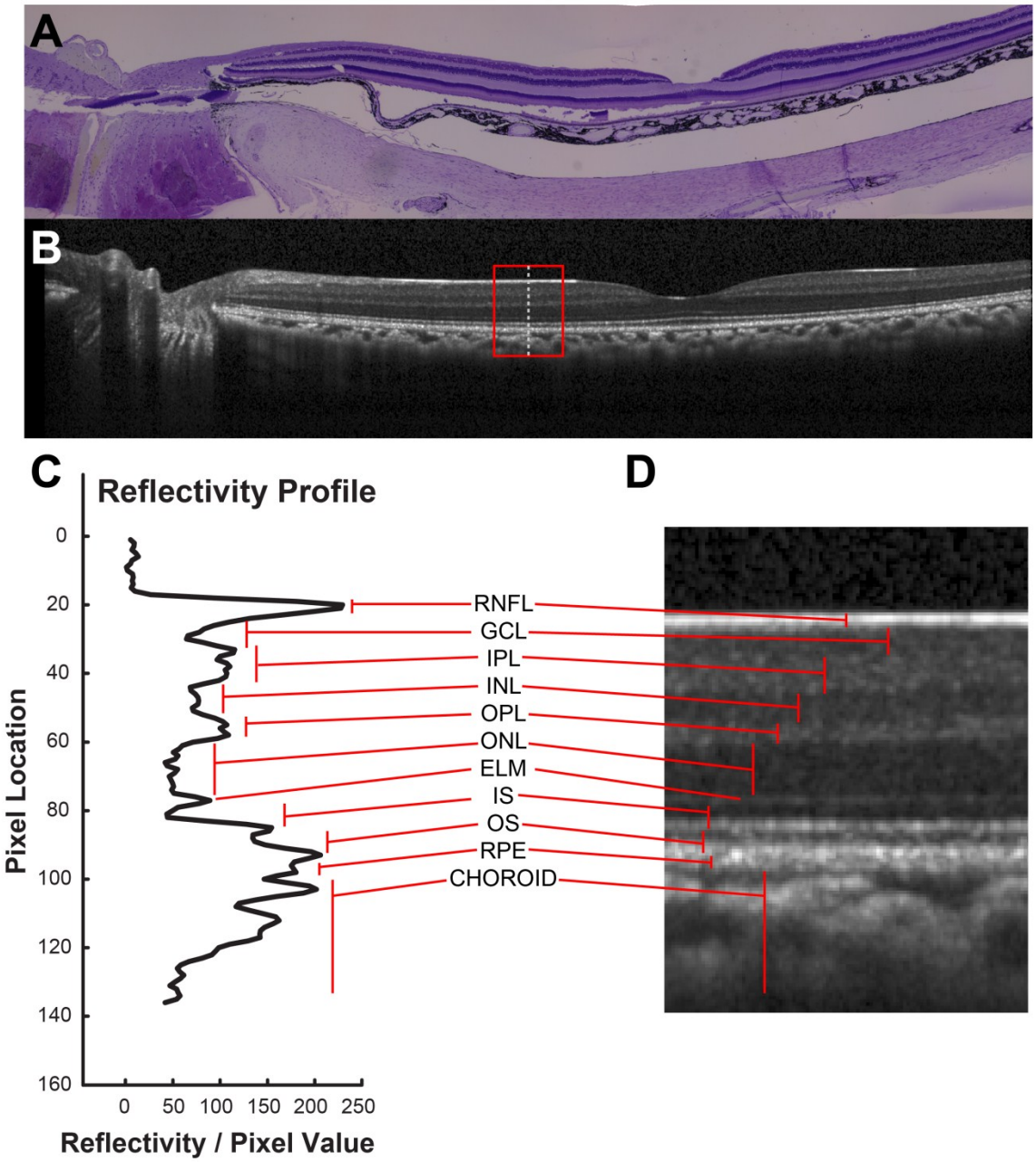
A
B
C
Reflectivity Profile
Pixel Location
0
20
40
60
80
100
120
140
160
0
50
100
150
200
250
Reflectivity / Pixel Value
RNFL
GCL
IPL
INL
OPL
ONL
ELM
IS
OS
RPE
CHOROID
D

Figure 1-2. **Correspondence between Histology and OCT**

A. Histological section through ONH and fovea of a 6 year old rhesus monkey stained with cresyl violet. B. SD OCT section through a similar region as that in A for the same animal. The boxed region (red) is enlarged in D, and the reflectivity profile for an A-scan (dashed line) is illustrated in panel C. Layer identification was a result of an iterative cross correlation algorithm that identified marked layers with most similar dimensions.

The ONH morphology is most commonly analyzed using radial B-scans centered on the ONH (Fig 1-3). In general, measures from these scans are repeatable with both TD and SD OCT systems in both normal and glaucoma patients.[104-107] From these studies, measures including the rim volume, vertical integrated rim area and rim area have good sensitivity and specificity at distinguishing a normal from a glaucomatous ONH.[107,108] However, ONH measures are not commonly assessed in the clinical setting as there are often inconsistencies in the reference plane used and there is only a limited amount of normative data available. With advances in enhanced depth imaging (EDI)[109-111] capabilities of SD OCT systems along with image post processing,[112] the more recent emphasis on ONH analysis has been on the location of the lamina cribrosa and the pre-laminar tissue in optic neuropathies. Specifically, changes in the lamina cribrosa geometry and position may provide important biomechanical information on the pathophysiology of axonal loss in glaucoma.[113] For example, in investigations in non-human primates with early high intraocular pressure induced glaucoma, there is a significant posterior displacement of the anterior lamina and thinning of the pre-laminar tissue, as determined with SD OCT.[114,115] Many of these findings correspond well with histological observations in the glaucomatous human ONH.[116] In human studies, EDI SD OCT scanning has been used to illustrate focal losses in the laminar structure of glaucoma patients.[117] However, even with current EDI OCT imaging, the lamina cribrosa can only be delineated in half of the ONHs scanned.[118] In addition, norms for pre-laminar tissue, anterior surface lamina depth and lamina cribrosa thickness as a function of age have not been determined.

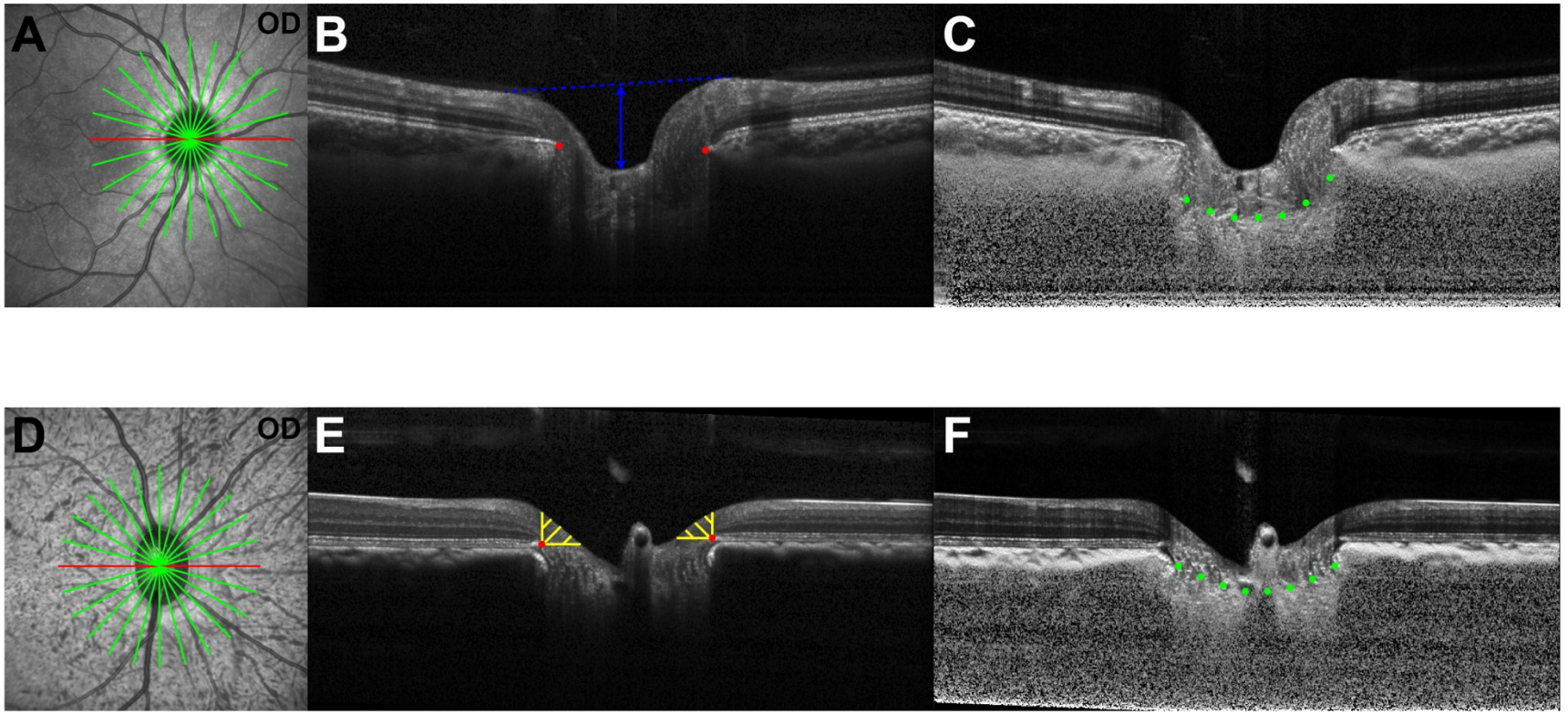
A
OD
B
C
D
OD
E
F

Figure 1-3. **Radial scan through optic nerve head.**

A radial scan pattern (A&D) is often used for morphological measures of the ONH. A-C are acquired from a human subject whereas D-F are from a rhesus monkey. The sections illustrated in B&E are the horizontal section through the ONH as illustrated by the red line in the SLO images. C&F are enhanced images using methods of compensation and contrast enhancement described by Girard et al (2011).[112] Red markings in B&D illustrate the opening of the basement membrane, a reference plane often used for morphological assessment. Cup depth is illustrated by the blue arrow in B, while the neural rim tissue is indicated by the yellow marked region in E. The green dots on the enhanced images C&F illustrate the anterior surface of the lamina cribrosa.

Macula Analysis

The central retina, that includes the fovea and surrounding tissues, has been of increasing interest for the diagnosis of glaucoma and glaucoma progression. Having the highest density of RGCs,[119] it is reasonable that there would be a decrease in total retinal or ganglion cell layer thickness early in the glaucomatous disease process.[57] Typical analysis of this foveal region includes a volume, or cube scan 10 to 15 degrees in diameter. In several investigations, although total macular thickness or volume measures were shown to be useful measures, they did not add to the diagnostic value of visual field, ONH or RNFL measures in glaucoma management.[120-126]

In theory, quantification of just the ganglion cell layer should have greater diagnostic value compared to total retina thickness, as the normal population variability for more outer layers is negated. While most automated algorithms cannot segment the RGC layer by itself, many will segment the RGC/inner plexiform layer complex, which often also includes the RNFL. As expected, analyses of these selective inner layers affected in glaucoma can be used to differentiate between early and advanced glaucoma patients.[120,127,128] However, as with total macular thickness and volume, inner retinal thickness or volume analyses also do not add to the current ability to diagnose and manage glaucoma.[129,130]

RNFL Analysis

The only current imaging methodology that samples the majority of axons from RGCs is the peripapillary RNFL scan. The B-scan analyzed is typically a 12 degree circular scan centered on the optic nerve, with a nominal scan circumference of 10.87 mm (Fig 1-4). This specific scan path is used by the majority of clinical OCT systems as it has the largest dynamic range with the smallest intra-subject variability in both normal

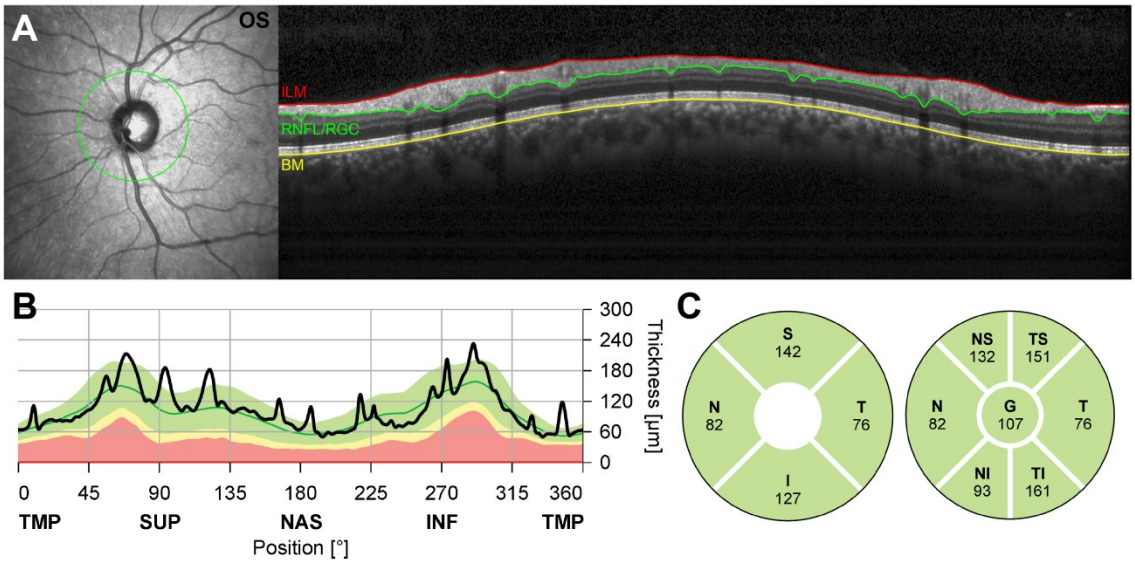

Figure 1-4. Standard 12 degree RNFL scan.

B-scan from a standard 12 degree diameter circular scan path of a healthy non-glaucomatous eye acquired using a Spectralis HRA+OCT SD OCT system. The scan represents the retina in a path from temporal – superior – nasal – inferior – temporal. B. Illustrates the RNFL thickness measures in microns quantified between the inner limiting membrane (ILM) and retinal nerve fiber layer/ganglion cell layer junction (RNFL/RGC). C. Quadrant and global thickness measures are often compared to a normative database and color coded (green $p > 0.05$,yellow $p < 0.05$, red $p < 0.01$).

and glaucomatous eyes.[131] To quantify the RNFL, an instrument based automated segmentation algorithm identifies the inner limiting membrane and the junction between the nerve fiber and ganglion cell layers. The RNFL thickness is then reported to the clinician/researcher as a TSNIT plot (A-scan thickness plot following a circular path from temporal, superior, nasal, inferior, and back to temporal), and average global or sector measures. These measures of the RNFL are shown to be repeatable and reliable in both normal and glaucomatous eyes.[132-135] In addition, RNFL measures have been used to estimate the number of axons within the eye (Equation 1-2, 1-3). For high resolution RNFL measures, acquired with a TD OCT system (512 A-scans/B-scan), the axon density (d), which is age dependent,[136,137] can be used to estimate the axonal count (a) when thickness data from each A-scan (h_x) is multiplied by the A-scan pixel width (21.2 μm/pixel).[138]

Equation 1-2

$$d\ (axons/\mu m^2) = (-0.007\ \times age) + 1.4$$

Equation 1-3

$$a\ (axons) = \left(\sum h_x\ \times 21.2\right) \times d$$

Although RNFL thickness is a useful measure in optic nerve health assessment, several limitations in the current imaging techniques and analysis prevent RNFL measures to be accurately used as structural endpoints for glaucoma diagnosis or progression. For example, an accurate assessment of RNFL thickness requires accounting for scan quality,[139,140] centration,[141,142] eye movement[143] and head tilt.[144] Hence, with current instrument based analysis, a significant change in thickness measures can only be detected when global measures either increase or decrease by 5-10 μm (~5-8% of total RNFL in healthy eyes).[132,135,145] However, studies involving

glaucoma patients with progressive field loss would indicate a need for more precise and accurate measures to detect a decrease in global RNFL measures that are approximately 1-2μm/year.[146-148]

Scan quality can be influenced by both modifiable (optical alignment, corneal hydration, averaging, and pupil dilation), and non-modifiable factors (media opacity, and preexisting retinal pathology). Several methodologies have been used to center scans including acquisition of volumetric data, and scan centration based on the neural canal opening.[97,141,143,149,150] Artifacts from eye movement and eye torsion, mainly due to head tilt, can be efficiently accounted for using image registration, and alignment to the fovea.[63,144]

Although the aforementioned factors are essential for accurate *in vivo* measures of retinal structures, thickness measures are also dependent on the optics and ocular biometry of the eye. For example, RNFL thickness measures in normal eyes with smaller axial lengths are usually larger than for longer or myopic eyes.[134,151-155] This relationship between axial length and RNFL thickness is a direct reflection of scan path on thickness measures. Specifically, for a fixed 12 degree diameter scan, the scan path would be further from the rim margin in longer eyes, where the RNFL is also thinner.[156-158] As the peripapillary region has a low density of ganglion cells, the observed relationship with axial length does not reflect on a change in axonal content, but rather a decrease in axonal density.[119]

Similarly, the proximity of the scan path to the ONH rim for anatomically large nerves may explain the positive correlation of RNFL thickness with nerve size (Fig. 1-5).[151,156,158] For example, in the African Descent and Glaucoma Evaluation Study (ADAGES), African Americans, who had larger optic disc areas compared to Caucasians, also had thicker RNFL measures.[159-161] However, it is not known if these

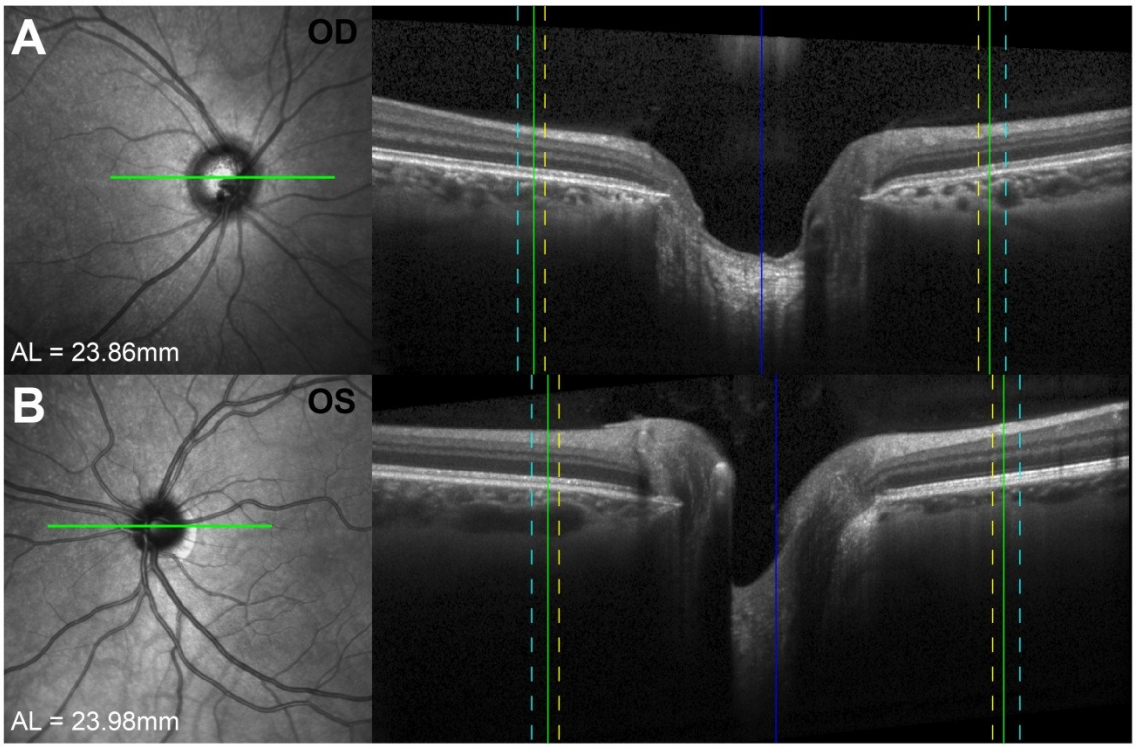

Figure 1-5. ONH size and RNFL thickness

Two eyes with similar axial lengths, but different sized optic nerves. The green lines illustrate the scan location for a 12 degree circular scan, while the yellow and blue dashed lines indicate the projected scan path if the axial length of the eye were 22.5 mm and 25 mm respectively. The deep blue vertical line illustrates the center of the ONH as determined by the basement membrane opening. Global RNFL thickness for these two subjects was 98 μm (A) and 87 μm (B).

differences are purely an artifact from the scan proximity to the optic nerve head (ONH) rim or if there are significant differences in RNFL axonal content based on ethnicity and ONH size. Histological data from non-human primates would suggest a mixed affect, as larger optic nerves often have more retinal ganglion cell nerve fibers.[162]

An evaluation of RNFL measures from standard 12 degree circular scans in the rhesus monkey is an ideal example for the influence of ocular magnification and ONH size on thickness measures. The axial length of the adult rhesus monkey (19 mm) is significantly shorter than that of the adult human (24 mm).[163] Hence, a 12 degree scan circumference, which is normally 10.9 mm in human eyes, is only 8.01 mm in the adult monkey eye. However, the RNFL TSNIT plot and average thickness measures are similar and comparable for the two species.[163,164] It is probable that the average RNFL thickness is similar in the two species, as the typical optic nerve of a rhesus monkey is significantly smaller making the scan distance from the rim margin comparable to that of humans.[98,162,164,165] It is also important to note that the RGC axonal content within the rhesus monkey eye is thought to be greater than that in humans.[162,166]

As illustrated by equation 1-2, the density of axons within the RNFL is age dependent, and is thought to be a result of age related changes in non-neuronal tissue. To use *in vivo* RNFL measures as a surrogate of retinal ganglion cell axonal content within the eye, the non-neuronal components need to be considered (Wheat, JL, et al. IOVS 2009;50:ARVO E-abstract 5826, Wheat, JL, et al. IOVS 2010;51:ARVO E-abstract 2104).[167,168] Although glial tissue and small vessels cannot be visualized using conventional *in vivo* SD OCT imaging technology, the major retinal vasculature often cast shadows on the underlying retina (Fig. 1-4). It is estimated that in a healthy eye, the major retinal vasculature contributes between 9-13% of the total RNFL content (Mardin CY, et al. IOVS 2009;50:ARVO E-abstract 3333).[63,167] With progressive loss of

neuronal tissue in glaucoma, an increase in the percentage contribution of retinal vasculature to the average, or global, RNFL thickness is expected. If the vascular content within the retina remains stable with disease progression, this component would only have to be compensated at baseline. However, changes in the major retinal vasculature have not been investigated using in vivo imaging. In addition, although vessel narrowing was not shown to be predictive of glaucoma or its progression in population based studies, the retinal vessel diameters in glaucoma patients were generally smaller than in control eyes.[169-172]

The main objective of the presented work was to investigate RNFL measures, using SD OCT technology, after correcting for retinal magnification and compensating for major retinal vasculature, in human and non-human subjects.

INNOVATIONS

There are two main innovations that will be investigated; 1) transverse scaling using a three surface schematic eye, and 2) custom scan paths that incorporate transverse scaling and are segmented with blood vessel compensation, for RNFL thickness and area analysis.

Retinal Scaling

Transverse scaling for OCT B-scans is dependent on the optical properties of both the scanning device and the eye itself.[173] Several methods have been described to calculate transverse scaling, with the most accurate methods taking into account corneal curvature, anterior chamber depth, lens thickness and axial length.[154,174-177] Using a three surface schematic eye the scaling of posterior segment retinal images can be accurately

calculated from the eye's nodal points.[174,175,178,179] Clinically, ocular measures including corneal curvature, anterior chamber depth, lens thickness, and axial length can be measured using non-contact optical biometry.[180-183] Although, optical biometers do not measure the crystalline lens curvature, age normative data have been published for both rhesus monkeys and humans.[163,184] Figure 1-6 illustrates a relaxed, unaccommodated three surface schematic eye of an adult emmetropic human eye (Fig 1-6A)[179] and an adult emmetropic rhesus monkey eye (Fig. 1-6B).[163]

RNFL Segmentation and Blood Vessel Compensation

Overall, RNFL thickness measures from all OCT systems, as determined with their proprietary automated segmentation, have good repeatability.[61,134,135,185,186] However, thickness measures acquired from the same individual on separate machines cannot be compared.[61,187,188] In addition, although OCT B-scans can be exported from the imaging device, custom scans and scans from other instruments cannot be imported into any current OCT system for thickness analysis. For the work in this dissertation, a custom segmentation algorithm written in commercial software (MATLAB, The Mathworks, Inc., Natick, MA) was developed for RNFL analysis of both instrument acquired and custom scan path B-scans. For this algorithm, B-scans are first de-noised using a Haar two dimensional stationary wavelet, and convolved with a Gaussian filter (SD = 4). As with most segmentation algorithms, the reflectivity profile of each A-scan is then analyzed to determine the location of the inner limiting membrane and the RNFL/RGC layer junction.[189,190] As most segmentation algorithms have some degree of error, the program allows for manual correction of erroneous layer identification which are most commonly located around the major retinal vasculature.

The Spectralis HRA+OCT, the SD OCT system used for the majority of these

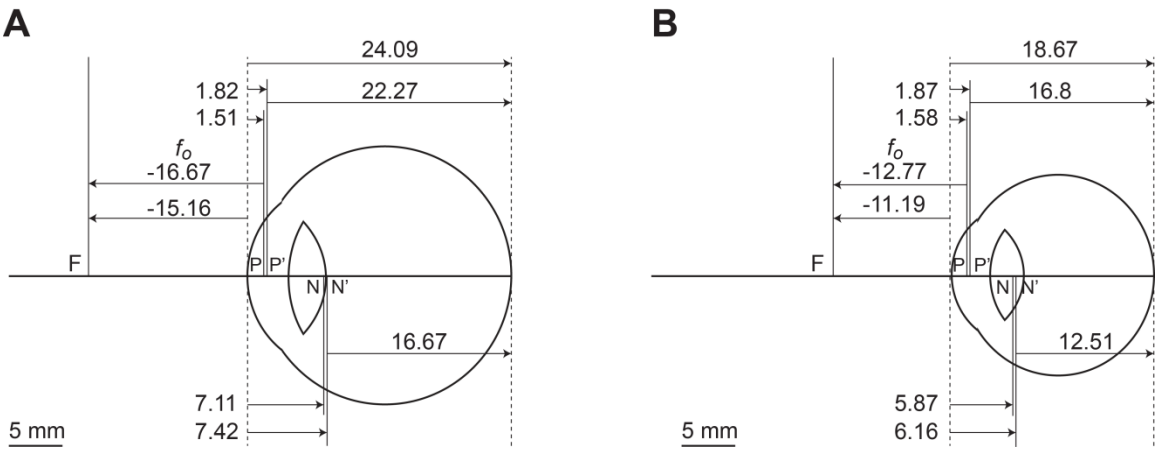

Figure 1-6. The three surface schematic eye.

Three surface schematic eyes of an emmetropic adult human[179] (A) and 4.8 year old rhesus monkey[163] (B). P and P' are the first and second principal planes while N and N' correspond to the first and second nodal points. Retinal scaling can be calculated using the distance from the second nodal point (N') to the imaging plane. Based on these schematic eyes, scaling for the adult human would be 291 μm/deg, and 218 μm/deg for the rhesus monkey eye.

experiments is a multi-laser system with real time image registration capability. With accurate retinal registration, A-scans can be averaged to increase the signal-to-noise ratio. The major retinal vessels within these scans should appear circular, when averaging frames during normal blood flow, if the pressure within the vitreous chamber is not greater than the systolic blood pressure. In addition, as the majority of retinal vessels are radially oriented to the optic nerve, OCT B-scans from circular or elliptical scan paths usually intersect vessels at right angles. Hence, after rescaling scans, retinal vessels can be fit with circles and removed from the RNFL (Fig. 1-7). RNFL thickness measures can then be transformed to an RNFL integral or area measure by incorporating the calculated transverse scaling of the eye. This methodology will be used to determine the RNFL thickness/area and vessel contribution; 1) in normal healthy human and non-human subjects, and 2) in the non-human primate, laser induced ocular hypertensive glaucoma model.

SCOPE OF DISSERTATION

This dissertation describes methodologies and experiments that were undertaken with the primary goal of improving structural measures of the posterior segment, as imaged with SD OCT technology. The research is a product of ongoing behavioral measures of vision studies in the lab of Dr. Ronald S. Harwerth (NIH EY001139). The results of this work include a methodology for RNFL analysis that takes into account the biometry of an eye and the shape of the optic nerve. In addition, chapter 6 illustrates the use of this precise method in investigating morphological changes in an experimental model of glaucoma.

Chapter 2 describes the role of axial length in retinal imaging with SD OCT. The subjects in this chapter included sixteen infant rhesus monkeys that were imaged at

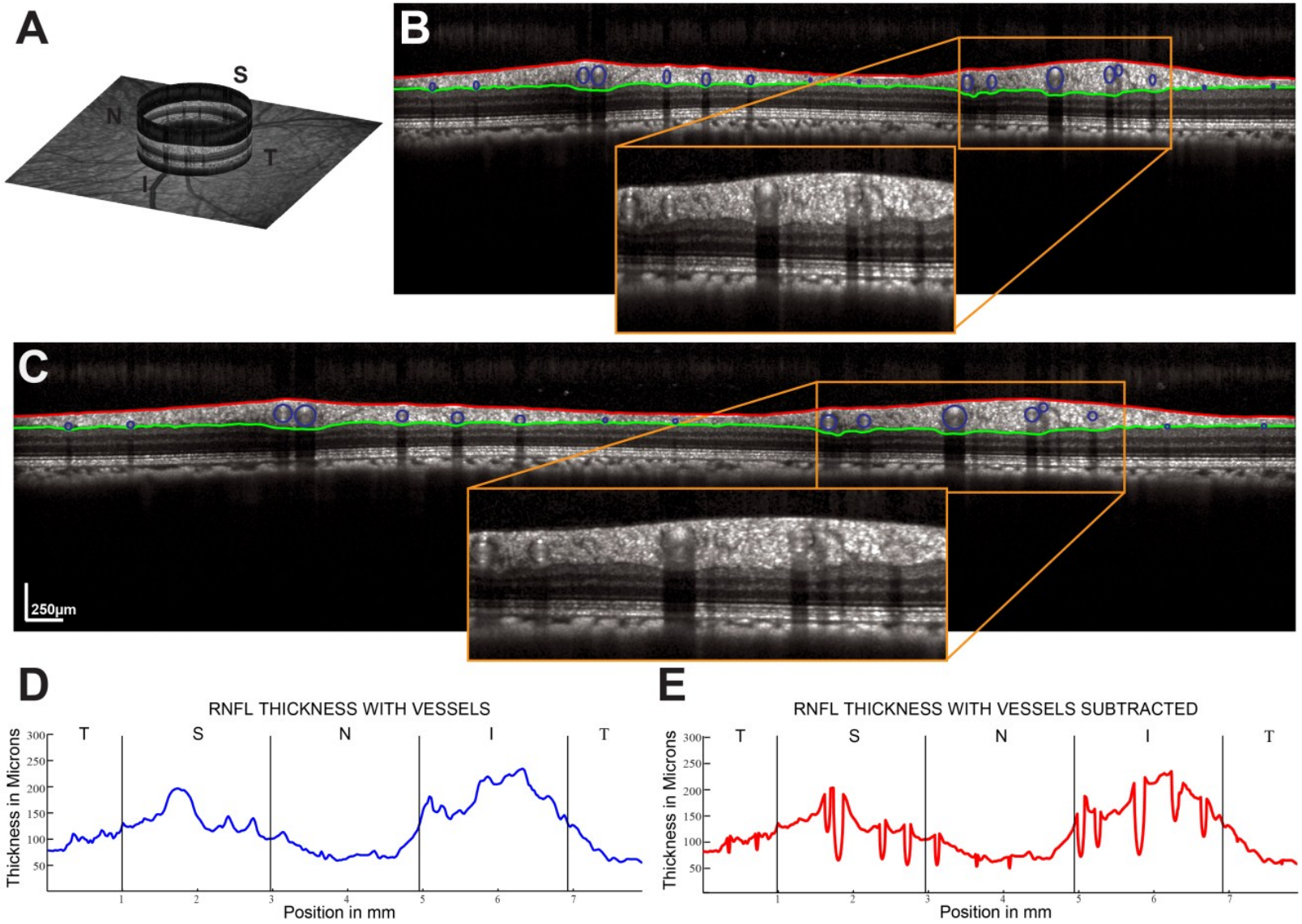
A
S
N
T
I
B
C
250µm
D
RNFL THICKNESS WITH VESSELS
T
S
N
I
T
Thickness in Microns
300
250
200
150
100
50
1
2
3
4
5
6
7
Position in mm
E
RNFL THICKNESS WITH VESSELS SUBTRACTED
T
S
N
I
T
Thickness in Microns
300
250
200
150
100
50
1
2
3
4
5
6
7
Position in mm

Figure 1-7. Custom RNFL anlysis.

A. SD OCT section illustrating the correspondence of major retinal vasculature and shadows within the B-scan. B. Unscaled, B-scan illustrating the elliptical shape of retinal vasculature within the RNFL. C. When scaled, retinal vessels within the B-scans take on a circular appearance. TSNIT plots before (D) and after (E) removal of major retinal vasculature. Note that only the thickness of the vessel within the RNFL is subtracted preventing negative RNFL thickness measures.

regular intervals from four weeks of age up until they were eighteen months old. While axial lengths in this species increase significantly within this period,[163] there is no change in the size of the ONH or the lateral distance between the optic nerve and the fovea.[191] Hence, the SLO images from these animals provided valuable data for changes in ocular magnification and validation of a three surface schematic eye for calculating transverse scaling. In addition, the OCT data were used to monitor changes in the retinal layers during the period studied. To the best of our knowledge, this is the first study to report longitudinal changes in the retinal layers for the period of infancy that was studied.

Although axial length is a major factor in determining ocular magnification,[174-176] the cornea contributes significant dioptric power to the optics of the eye. In chapter 3, the influence of anterior segment power on ocular magnification was investigated using standard 12 degree RNFL scans. Change in corneal power was accomplished by fitting human subjects with soft contact lenses ranging in power from -12 D to +8 D. In this chapter, using image registration and custom RNFL segmentation, the relationship between change in anterior segment power and RNFL thickness is attributed to changes in scan path. Image registration was also used to determine differences in ocular magnification and in validating the transverse scaling computed with a three surface schematic eye.

In chapter 4, the discrepancy between RNFL thickness measures between instruments is addressed. For this experiment two clinical SD OCT systems, the Cirrus HD-OCT (Carl Zeiss Meditec, Dublin, CA), and Spectralis HRA+OCT (Heidelberg Engineering, Heidelberg, Germany) were used for data collection on human subjects. While the Cirrus system interpolates a 12 degree circular scan from volumetric data through the optic nerve, the Spectralis uses a circular scan path to acquire the same scan. In addition, these instruments have different scan speeds and theoretical axial

resolutions. The chapter addresses the influence of; 1) scan centration on the ONH, 2) scan alignment to the fovea, and 3) segmentation algorithm on RNFL thickness measures.

The main focus of chapter 5 is the use of custom RNFL scans in the rhesus monkey. Specifically, significant differences in ONH size and ocular biometry would suggest that the standard 12 degree circular scan used for RNFL analysis in humans may not be ideal for the monkey eye. Hence, the purpose of this experiment was to investigate elliptical scan paths of varying sizes on RNFL measures in rhesus eyes. The same scaling methodologies and segmentation algorithms were used as described in chapters 2-4.

In chapter 6, changes in morphological measures are investigated for monkeys with laser induced experimental glaucoma. Incorporating transverse scaling methodologies, measures of the ONH, RNFL and macula were investigated in 47 healthy rhesus eyes and 6 experimental glaucoma eyes. The overall goal of this study was to determine the typical sequence of morphological changes in this experimental glaucoma model.

CHAPTER 2

THE EARLY MATURATION OF THE FOVEA IN MACACA MULATTA: SPECTRAL DOMAIN OPTICAL COHERENCE TOMOGRAPHY

The authors that contributed to this work include:

Nimesh B Patel, OD, Joe L Wheat, OD, PhD, Xunda Luo, M.Med, PhD, Li-Fang. Hung, B.Med, OD, PhD, Earl L Smith, OD, PhD, Ronald S Harwerth, OD, PhD.

ABSTRACT

Purpose: Changes in the anatomy of the fovea during infancy are important for understanding the early, normal development of vision. The present longitudinal study was undertaken to characterize the maturation of the fovea during the first year and a half of life in rhesus monkeys.

Methods: Starting at four weeks after birth, the retinas of the left eyes of sixteen infant monkeys were imaged using spectral domain optical coherence tomography (SD OCT). Retinal scans were repeated every 30 days during the first year of life and every 60 days thereafter. Volume scans through the fovea were registered, scaled using a three surface schematic eye, and analyzed to measure foveal pit parameters. The individual layers of the retina were manually segmented and thicknesses were measured over a transverse distance of 1250 microns from the center of the foveal pit.

Results: Significant changes in the extent of retina scanned were described using a three-surface schematic eye (R^2 = 0.88, slope = 1.003, $p<0.05$). During the first 18 months of life, the mean retinal thickness at the pit center increased by 21.4% with a corresponding 20.3% decrease in pit depth. The major changes occurred within the first 120 days, but did not stabilize until a year after birth.

Conclusions: In *Macaca mulatta* infants, the primary anatomical maturation of the fovea occurs within the first few months of life, as determined by longitudinal data from SD OCT measurements. The timelines for maturation of the fovea correspond well with the normal development of both lateral geniculate nucleus and cortical neurophysiology.

INTRODUCTION

In primates, the visual system is relatively immature at birth, with significantly reduced visual resolution, i.e., high contrast visual acuity often measuring less than 5 cycles per degree (cpd) in both humans and monkeys, compared to acuities of 30-40 cpd in adults.[192-197] The infant visual system improves rapidly over the first few months of life in both species, at about the same species adjusted relative rate,[192,198] but adult-like levels are not reached until about five years of age for children[195,199,200] or 40 weeks of age for monkeys.[201,202] The improvement of visual performance early in life has been attributed primarily to changes in the optics of the eye and retinal anatomy, along with neurologic maturation of the afferent visual pathway (lateral geniculate nucleus and visual cortex, reviewed in Simons[203] and Werner[204]). The majority of the investigations of early changes in the visual optics and development of the fovea pit have been in old world monkeys, because of their similarity to humans.

The optical characteristics of the monkey eye have been measured and modeled by schematic eyes,[205] double-pass ophthalmoscopy[206] and wavefront technology.[207] In general the optical properties of the primate eye, including clarity and higher order aberrations, continue to improve up to 13 to 21 weeks of age, but because the optics are relatively good at birth, it is not considered a significant limit on visual resolution.[206-208] In contrast, changes in ocular biometry, including axial length, corneal curvature and crystalline lens parameters, all of which have a significant influence on spatial resolution, develop over longer periods of early life. For example, the combination of relative retinal magnification, i.e., the extent of the retina stimulated per degree of visual angle, and cone spacing in the fovea pit predict a five-fold increase in spatial resolution during the first two years of life.[205,209,210]

The resolution limits, based on the density and characteristics of the photoreceptors in the foveal pit also have been investigated as an important component of the development of visual acuity. Although the future fovea of the monkey eye can be identified as early as fifty days post-conception,[209] it is relatively immature at birth, with only a single or bilayer of cuboidal or columnar cone cells in the neonatal macaque foveal pit.[211-213] The corresponding peak cone density at birth in monkeys is 31-41%,[213] whereas in humans it is only 17%[214] that of the adult fovea.[215] Within the first year after birth, peak cone density for monkeys increases from 43,000 cones/mm^2 to 210,000 cones/mm^2.[210] In humans, cone density has been measured at 36,294 cones/mm^2 at 5 days post natal, and has increased to 108,439 cones/mm^2 by 45 months of age, but is still not adult like (208,203 cones/mm^2).[214] The increase in cone density does not represent active mitosis[214,216] but is a direct result of cone migration as is evident by a decrease in the rod free zone.[209,210] In addition to an increase in density, the cone photoreceptors within the fovea become narrower (inner segment diameter of 2 μm) and longer (inner segments lengthen to 30-35 μm, while outer segments lengthen to 50-65 μm).[210,217] These changes in the photoreceptors are thought to improve both the waveguide characteristics and efficiency of photon capture.[218,219]

The present state of understanding of foveal maturation has been derived from histological studies. Although these data have provided excellent anatomical resolution, only a limited number of time points after birth have been investigated.[209,210,220,221] In addition, a normal threefold variability in cone density,[222,223] precludes the accurate construction of timelines for retinal maturation from anatomical studies. Consequently, to establish maturational rates and trends within the fovea, data from multiple time points for a larger number of subjects are needed. Such investigations are now possible with non-invasive, *in vivo* imaging with optical coherence tomography (OCT) technology.[86,93-

[95] Specifically, newer instruments based on spectral domain optical coherence tomography (SD OCT), provide sufficient resolution (nominally, 3.87 μm/pixel in the axial dimension) to identify the individual layers of the neural retina. However, as with most retinal imaging methodologies, the accuracy of SD OCT lateral or transverse measurements is dependent on the optics and ocular biometry of the eye. Although schematic eyes have been used to compute relative retinal magnification,[163,174-176,205,224-226] they have not been validated in a growing eye. Therefore, image-analysis algorithms were developed to analyze SD OCT data for retinal thickness measurements that were independent of the ocular dimensions of developing eyes in order to quantify postnatal anatomical changes in foveal morphology and neuronal layers within the central retina of macaque monkeys from 1 month to 18 months of life. Some of the results of these studies were presented in brief form (Patel NB, et al. IOVS 2009;50:ARVO E-abstract 6207).

METHODS

Subjects

The subjects for the study were sixteen healthy full-term infant rhesus monkeys (*Macaca mulatta*). Housing and rearing for the infants have previously been published.[227,228] All experimental and animal care procedures were reviewed and approved by the Institutional Animal Care and Use Committee at the University of Houston. The use of animals for these experiments confirmed to National Institutes of Health guidelines for the care and use of laboratory animals.

Animals used for the current study were also subjects for studies of refractive error development[229-231] and, therefore, only the left, control eyes were used for analyses, i.e., eyes that had no optical or surgical manipulation that could interfere with the normal

anatomy of the retina or optic nerve. The initial retinal scans were acquired at around thirty days of age (36 ± 6 days) and, subsequently, every thirty days thereafter for the first year of life. After a year of age the eyes were scanned at sixty-day intervals until the animals were at least 1.5 years of age (627 ± 27 days).

Animal Preparation

Animals less than a year of age were anesthetized with an intramuscular injection of ketamine (15-20 mg/kg) and acepromazine maleate (0.15-0.2 mg/kg), while animals over a year of age were administered ketamine (20-25 mg/kg) and xylazine (0.4-0.6 mg/kg). Body temperature was maintained between 37 and 38 degrees Celsius with a thermostatically controlled electric blanket (TC1000 temperature controller, CWE, Ardmore, PA). Heart rate and blood oxygen were monitored with a pulse oximeter (model 9847V; Nonin Medical Inc., Plymouth, MN). Prior to imaging the retina, pupils were dilated with topical tropicamide (1%) and phenylephrine (2.5%), and a custom plano powered rigid gas permeable contact lens was placed on the eye to maintain optical clarity. Head stabilization was achieved using mouth and occipital bars attached to a rotational mount, enabling appropriate eye alignment for scanning.

Optical Coherence Tomography

All scans were acquired by one of two trained operators (JLW, NBP), using a commercially available instrument (Spectralis HRA+OCT, Heidelberg Engineering, Heidelberg, Germany). This instrument has multiple laser sources allowing for simultaneous infrared scanning laser ophthalmoscope (IR SLO) and SD OCT imaging. IR SLO images are acquired using an 820 nm laser diode, whereas the illumination

source for SD OCT scans is a low coherence infrared (880 nm nominal wavelength) superluminescent diode (SLD). At a high resolution setting, the IR SLO captures frames at 5 Hz over a 30 degree field of view, whereas SD OCT A-scans are acquired at 40,000 Hz. Both imaging channels capture 512 samples per 10 degree scan length allowing an accurate registration of OCT scans to the SLO image. The built-in real-time image registration helps compensate for eye movements, and allows for successive intra-session scan averaging, increasing the signal-to-noise ratio. Based on the characteristics of the instrument optics, SLD bandwidth, and line scan camera, the resultant SD OCT images from the instrument have a digital axial resolution of 3.87 μm/pixel. The transverse resolution is dependent on the optics of the eye, as discussed in the following section.

All IR SLO images of the optic nerve and fovea were captured using a 30 degree scan angle, with the high resolution setting of the instrument. Although IR light from imaging systems is generally safe,[232,233] to minimize retinal exposure to the SLO and SLD light sources, SD OCT scans were limited to a 37 line raster scan centered on the fovea and covering a region 15 X 20 degrees, with averaging set at 9 frames. Total scan time was limited to 5 minutes per session.

Ocular Biometry and Relative Retinal Magnification

Ocular biometry measures used for determination of transverse scaling were from data collected for refractive error studies.[229-231] These measures were obtained every 2 to 4 weeks throughout the period studied and on separate days from retinal imaging. The methodology and details on biometric measurements have been described elsewhere.[228,234,235] Overall, changes in axial length, corneal curvature, anterior chamber depth, and lens thickness were similar to those previously reported in this species.[163,236]

As biometry measures rapidly change during the first few months of life,[163,236] linear interpolation was used to estimate biometry measures for each animal and scan date.

The normal development of anterior segment power and eye length of the infant eye results in changes in retinal image size, and transverse scaling of the retinal region scanned by imaging devices.[174,176] Specifically, as the eye lengthens, the area of the retina scanned increases when identical scan parameters are used. Several methodologies have been used to compute transverse retinal scaling,[173-176,237] but have not been validated in a growing eye. It is logical that the most accurate method for computing transverse scaling would require accounting for corneal curvature, axial length, anterior chamber depth and lens thickness. For this study a three surface schematic eye as described by Bennett and Rabbetts[179] was constructed for each eye and scan session to determine changes in retinal image size/transverse scaling. Briefly, the dimensions imaged by the IR SLO and SD OCT scans were calculated from the second nodal point to the retinal plane (N'M'), assuming a spherical surface (Equation 2-1).

Equation 2-1.

$$\text{Scan Length } (\mu\text{m/deg}) = \frac{1}{180}\pi(N'M')$$

Similarly, the transverse scaling for each 20 degree B-scan consisting of 1024 A-scans was computed using equation 2-2.

Equation2- 2.

$$\text{Transverse Scaling}(\mu\text{m/pixel}) = \frac{20}{360} \times \frac{2\pi(N'M')}{1024} = \frac{\pi(N'M')}{9216}$$

Scaling Validation

Changes in the extent of the retina imaged should correspond with those predicted by the schematic eye. To determine changes in retinal magnification, 30 degree SLO images centered on the optic nerve and fovea from a random scan date for each animal were used as baseline, and a baseline transverse scaling was computed using equation 2-1. The image series for each animal was subsequently registered to their respective baselines using a generalized dual bootstrap, iterative closest point algorithm (i2k retina, DualAlign, LLC, Clifton, NY).[238] Based on the change in image size (Fig 2-1A), the scaling for each scan date was determined using equation 2-3.

Equation 2-3.

$$Registered\ Image\ Scaling\ (\mu m/pixel) = \frac{\sqrt{Total\ Pixel\ Content\ in\ Registered\ Scan}}{\sqrt{Total\ Pixel\ Content\ in\ Baseline\ Scan}} \times Baseline\ Transverse\ Scaling$$

Of the 195 scan dates, 188 scans of both optic nerve and fovea SLO images were successfully registered. Image scaling for fovea scans predicted by image registration was compared to that computed by the three surface schematic eye for each scan session (Fig 2-1C). Overall, there was good agreement between the two methodologies (slope = 1.003, intercept = -1.958, R^2 = 0.88). In addition, to validate the registration technique, the square root of the registered scan's pixel content, corresponding to the length of the image, of both fovea and optic nerve SLO images were compared for all scan dates. Previous models of wide-field retinal imaging would predict minimal differences in retinal scaling for these two regions.[225] Similarly, there was good agreement for changes in image size for both optic nerve and fovea scans (Fig 2-1D, slope = 1.027, intercept = -47.67, R^2 = 0.98).

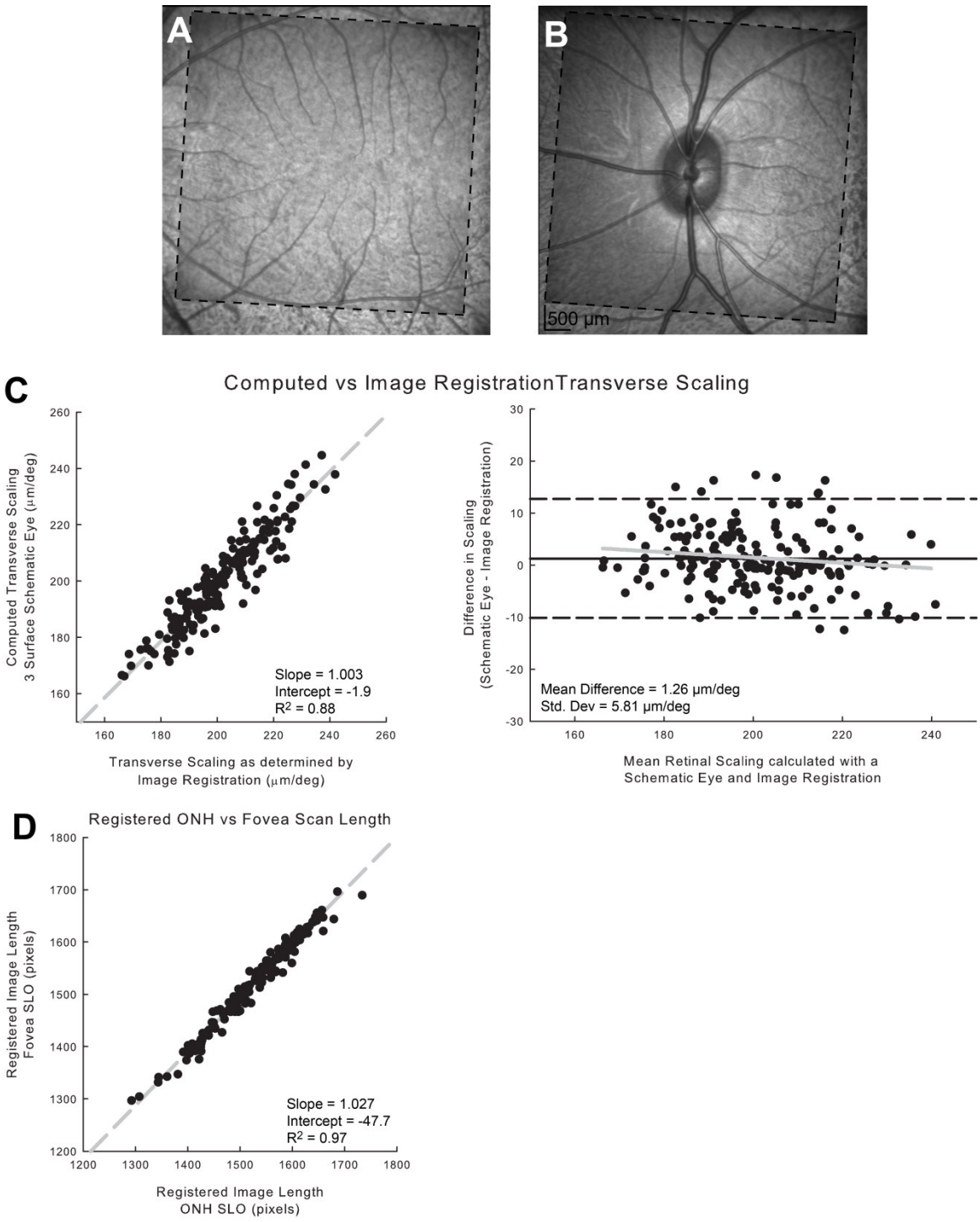

Figure 2-1. Retinal scaling with image registration and three surface schematic eye in eyes with increasing axial length.

A. Thirty degree IR-SLO images centered on the fovea from 51 days (dashed outline) and 289 days of age in registration. B. IR-SLO images of the optic nerve in registration from the same animal and scan dates as in A. C. Comparison of image scaling using image registration and the three surface schematic eye. The Bland-Altman plot illustrates the mean and difference between the two methodologies. The relationship between the differences and mean scaling (gray line) was not significant ($p = 0.06$). D. Validation of image registration technique, comparing IR-SLO image length from corresponding fovea and optic nerve registered scans.

Segmentation and Foveal Pit Morphology

Segmentation algorithms for most SD OCT systems are optimized for human eyes, and often fail at determining retinal layers in non-human primate eyes. Hence, a custom MATLAB (The Mathworks, Inc., Natick, MA) algorithm utilizing a canny edge detector,[239] along with A-scan longitudinal reflective profiles, was developed to identify the inner limiting membrane and retinal pigment epithelium (RPE) for each retinal B-scan. Total retinal thickness maps for the region scanned, were constructed using bilinear interpolation. Retinal curvature information for these thickness maps is lost as thickness measures are determined by the number of pixels between the two segmentation lines. In addition, the proprietary non-linear functions used to compensate for instrument and ocular optics[240] are optimized for human eyes. Hence, information from the RPE segmentation could not be used to determine retinal curvature. As a result, to ensure the most accurate thickness measures and computation of pit dimensions, all scans acquired were on axis within minimal tilt in the image plane.

For detection of the foveal pit, thickness maps were considered flattened to the RPE. Foveal pit shape characteristics were computed for each thickness map after rescaling to a 1:1 aspect ratio using the computed transverse scaling and the instrument determined axial scaling. The starting point depth of the pit was determined as the difference between the regional maximum and minimum thickness. To determine the center, points intersecting the pit slope at heights corresponding to one-half to seven-eighths of the pit depth were determined at one micron intervals. For each interval a least squares best fit circle was fit to the intersecting points (Equation 2-4). The centroid of these points was used as the center of the pit for all further calculations.

Equation 2-4

$r^2 = (x-h)^2 + (y-k)^2$, where r is the radius of a circle whose center is defined as (h, k) and whose circumference has points corresponding to (x, y).

The shape and slope characteristics of the foveal pit were determined using twelve interpolated radial sections through the center of the fovea. The first derivative of the total retinal thickness for each section was used to determine slope information and in locating the top and bottom of the pit. The maximum slope was identified by the peaks of the thickness differential, while the top and bottom of the pit were determined as points on either side of the maximal slope that approached a slope of zero (Fig 2-2B). The pit depths reported are the mean thickness differences between the top and bottom of the pit for the twelve radial sections. Based on the thickness contour, points corresponding to top and bottom of the pit were fit with least squares best fit circles. Similarly, points corresponding to the maximal slope for all radial sections were also fit with a circle (not illustrated in Fig 2-2). As thickness data were measured from images that were flattened to the RPE, an angular measure assuming a spherical eye was used to compute the chord distance for all radius measures.

Changes in Overall Retinal Thickness

Although the Spectralis HRA+OCT can align inter-session scans to track changes in retinal thickness, significant changes in relative retinal magnification with age precluded using the eye tracking system to register images across scanning sessions. Instead, commercial software using a generalized dual bootstrap, iterative closest point algorithm (i2k retina, DualAlign, LLC, Clifton, NY) was used to align the 30 degree SLO fundus images from successive scans. All subsequent image and thickness analyses were performed by custom MATLAB programs that incorporated the schematic eye transverse scaling computed for each scanning session. The scan location for each

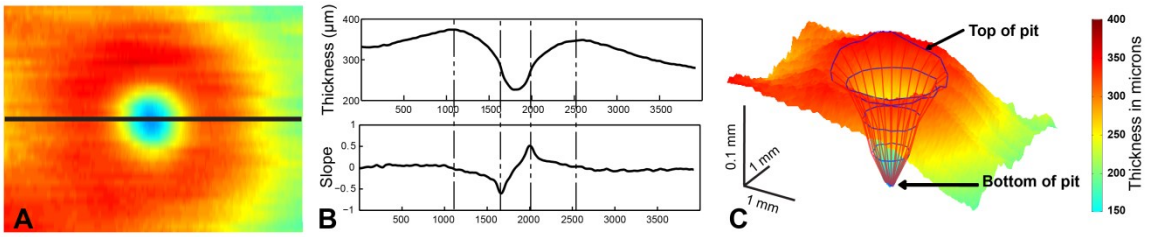

Figure 2-2. **Foveal pit analysis.**

A. Total retinal thickness map for a region 15º X 20º centered on the fovea (256 day old infant), B. Pit characteristics were determined using interpolated thickness data from the total thickness maps. For example, the top plot illustrates the thickness profile for a horizontal radial section through the thickness map as illustrated by the black line though A. Along with the thickness profiles from radial sections centered on the pit, slope data (bottom B) were used to determine pit characteristics and construct a skeleton to describe pit morphology. The dashed lines in B indicate the maximal slope locations and top of pit locations. C. Illustrated are the thickness map along with a skeletal reconstruction of the pit, including points used to fit the top and bottom of the pit.

OCT B-scan was determined from the raw SD OCT data files (.vol) and transposed onto the registered SLO image for thickness comparisons (Fig 2-3A-E). Average thicknesses were computed for superior, inferior, nasal and temporal regions from the center of the foveal pit (Fig 2-3E). For each quadrant average thickness measures were obtained for sectors, 0-50 μm, 50-100 μm, 100-250 μm, 250-500 μm, 500-750 μm, 750-1000 μm, 1000-1250 μm, and 1250-1500 μm from the fovea center. Average thickness measures for sectors were reported when greater than 75% of the sector overlapped the raster scan derived thickness map. In addition, a difference map was created by subtracting thickness values from baseline scans, and average sector thickness measures were recorded (Fig 2-3G-J).

Retinal layer thickness measurements

Retinal layers within OCT B-scans were identified based on previous histological studies.[93-95,241] To validate the relationship between histology and OCT imaging in the infant eye, the foveal region of a 10 day old rhesus monkey was scanned using the same scan protocol as that used for the longitudinal data. After a lethal injection of pentobarbital, the animal was perfusion fixed with 2% paraformaldehyde and 0.5% glutaraldehyde (pH 7.4). The retina corresponding to the scanned region was later dissected and embedded in epoxy resin. 1 μm sections were mounted and stained with Cresyl violet, and photographed using a DeltaVision (Applied Precision, Inc., Issaquah, WA) microscope system. In general, the relationship between OCT scans and histology (Fig 2-4A) was similar to previous reports.[93-95,241]

For the SD OCT data, the thicknesses of individual retinal layers were measured at the center of the pit and at eccentricities of 87 microns, 175 microns, and up to 1225

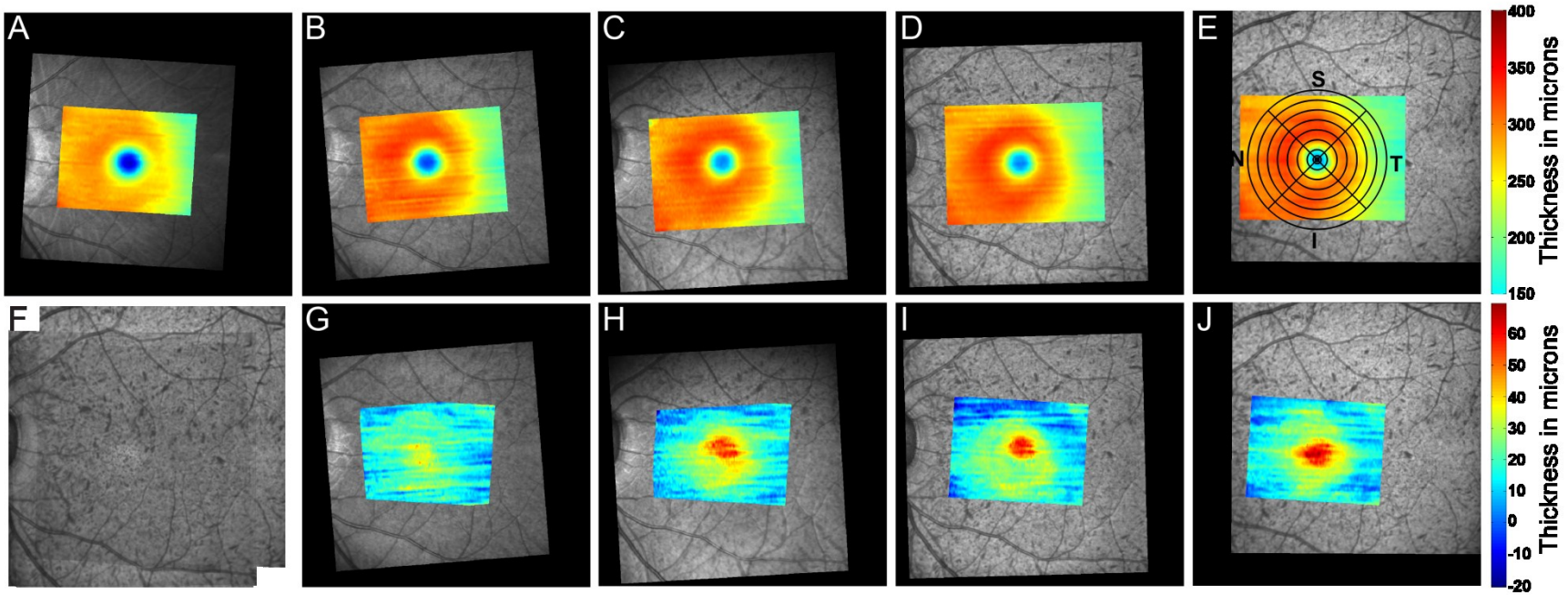

Figure 2-3. Change in total retinal thickness for one infant monkey.

Top row: Registered SLO images and corresponding total retinal thickness maps for one animal (A - 33 days, B - 67days, C - 137days, D - 468 days, and E - 649 days of age). Each scan is in registration, and the montaged IR-SLO image is illustrated in F. Bottom row G-J: Change in total retinal thickness from baseline measures at 33 days of age. Notice that as the animal ages, the portion of the retina imaged increases. A scaled grid was used to determine average thickness measures within quadrants of concentric circular regions which were used to determine overall retinal thickness changes with age.

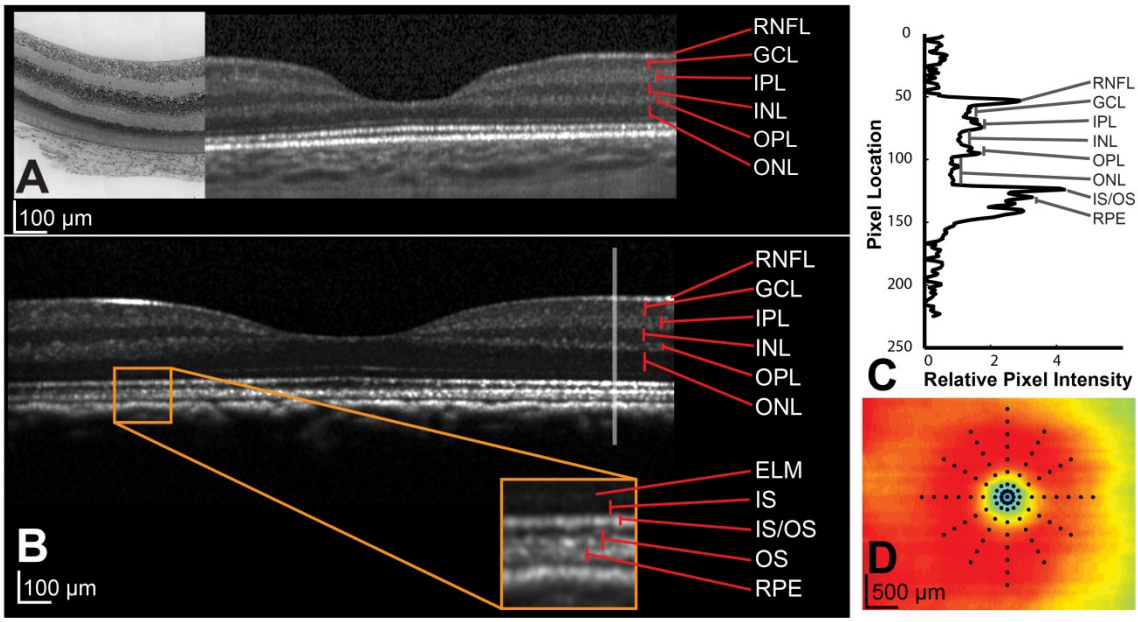

Figure 2-4. Identification of SD OCT retinal layers.

A. OCT section through fovea of a 10 day old infant with corresponding histology stained with Cresyl violet from the same animal. B. OCT section through the foveal region, of a 1.5 year old animal. C. Each layer was manually identified on the OCT B-scan with the assistance of reflectivity profiles, through the region of interest. The reflectivity profile illustrated is generated from the gray vertical line shown in B. D. For each eye, layer thicknesses at 89 points illustrated on the thickness plot were measured and monitored over time.

microns in 175 micron steps. A total of 89 locations along six radial regions corresponding to clock hours through the fovea center were sampled (Fig 2-4). To decrease bias retinal layer thickness measures were performed after all data collection had been completed. In addition, custom MATLAB programs were developed to randomly present the 89 sample locations for manual layer identification.

For each location, a B-scan section corresponding to 75 pixels on either side of the region of interest was interpolated from the raster volume data at one of six radial orientations. This B-scan and the longitudinal reflectivity profile (Fig 2-4C) through the region of interest were enlarged by a factor of six using bilinear methods to assist with accurate layer identification. The average layer thickness at each eccentricity was used for data analysis. All plots were created using MATLAB, or SigmaPlot (Systat Software, Inc., San Jose, CA), while all statistical analyses were performed using SPSS (IBM, Armonk, NY) and corrected for multiple comparisons. To determine the function that best described changes during the period studied, data from each subject were fit using both linear and non-linear functions. In general, linear, piecewise linear, and a three parameter exponential rise to maximum function ($y = a + b(1-\exp^{-cx})$) were used to fit the majority of data. Data were binned in 30 day intervals and repeated measures ANOVA with Bonferroni's correction for multiple comparisons were used to determine timepoints at which there were significant changes in thickness. A factorial ANOVA statistic was used to determine differences in thickness change across eccentricities.

RESULTS

Over the period studied, a total of 195 scans were acquired and used for data analyses, for the 16 infant rhesus monkeys. The animals all maintained good systemic

and ocular health during the period studied, with no major illnesses, ocular injuries or retinal pathology noted.

Retinal Scaling

Changes in relative retinal image size were best described using a three surface schematic eye. This scaling methodology was validated with predicted scaling changes as determined by image registration of both the fovea and optic nerve IR SLO scans (slope = 1.003, intercept = -1.958, R^2 = 0.88, p<0.01, Fig 2-1C). Overall, retinal image size was linearly related to axial length (Retinal Image/degree = 15.1XAxial Length - 60.2, R^2 = 0.97). As axial length increases at an exponential rate early in life, the relative retinal image size change with age was fit using a three parameter exponential rise to maximum equation (Ret Scaling = 163 + 52(1-$e^{-0.005XAge}$), R^2 = 0.59, p <0.01). For retinal scaling, the asymptote (a+b) along with the 95% confidence interval was calculated as 215 (202, 229) μm/deg.

Pit Morphology

Over the period studied, the average depth of the foveal pit decreased by 25 μm (14.6%). The individual and group data were best fit with an exponential decay model (Pit Depth = 145.8 + 43.8 × exp(-0.015 × Age in Days), R^2 = 0.24, p < 0.01, Fig. 2-5A). Repeated measures ANOVA using Greenhouse-Geisser estimates for sphericity indicated a significant change in depth over the first 150 days of age (F = 21.56, p < 0.01), corresponding to a time point when average pit depth was 150.4 μm.

The biomechanical models of pit development have attributed changes in morphology to retinal stretch,[211,221,242] suggesting that changes in pit depth are related to

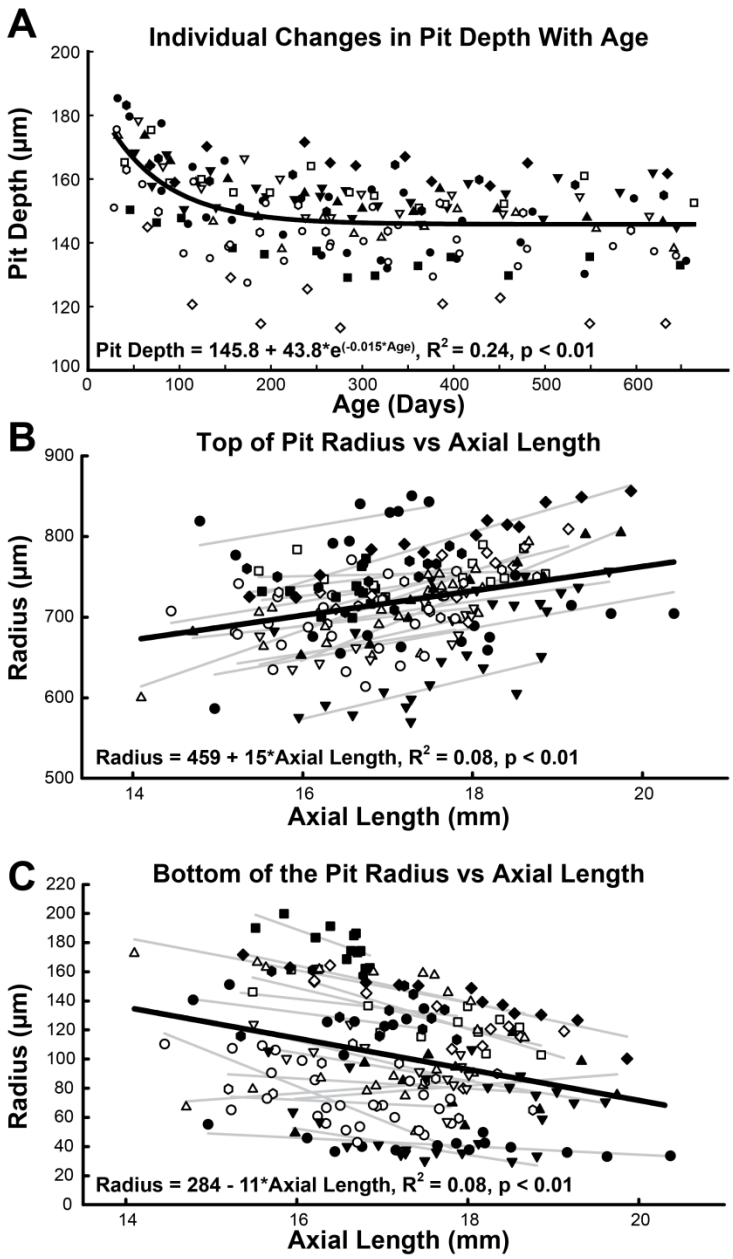

Figure 2-5. Axial length and pit morphology.

A. The pit depth decreased rapidly, reaching adult like depths prior to a year of age. Along with a decrease in pit depth, there was an increase in the top of the pit radius (B) and decrease in the bottom of the pit radius (C), that were both related to increases in axial length.

changes in axial length. Specifically, differences in the elastic modulus of the retinal layers resulting from the avascular zone are thought to be the determinant factors in pit shape development when subjected to retinal stretch and intraocular pressure.[211] The present data support that suggestion; the relationship between pit depth and axial length is generally linear (slope = 6.7 ± 0.95 μm/mm increase in axial length, $R^2 = 0.21$, $p < 0.01$). In addition, the decrease in pit depth should result in corresponding changes in the width of the foveal pit. As illustrated by Fig. 2-5B, there is an axial length related increase in the chord radius fit to points corresponding to the top of the pit radius (19.69 ± 10 μm/mm axial length, $p < 0.01$), and a decrease in radius for points corresponding to the bottom of the pit (10 ± 3 μm/mm axial length, $p < 0.01$, Fig 2-5C). However, there was no change in the chord radius for points fit to the maximum slope (1.71 ± 19.3 μm/mm axial length, $p = 0.72$). In addition, there is large variability in pit dimensions across animals as reflected by the coefficient of determination ($R^2 < 0.1$) for the best fit function to the data for both top and bottom of pit radii.

Total Retinal Thickness

Corresponding with changes in pit depth, the average retinal thickness for measures in the surrounding 500 μm of the pit increased up to 120 days of age (Table 2-1), with the largest change of 33 ± 9μm (19 ± 6%, Fig 2-6A, 2-7) noted within the central 50 μm (Repeated measures ANOVA, $F = 26.4$, $p < 0.01$). An analysis of the four quadrants, superior, inferior, nasal, and temporal, did not indicate any statistically significant difference in thickness change at eccentricities up to 1500 μm from the pit center when corrected for multiple comparisons (Fig. 2-6B, Table 2-2). Hence, for subsequent analyses of individual retinal layers, only the average layer thickness at each eccentricity was used. To illustrate changes in thickness, for total retinal thickness

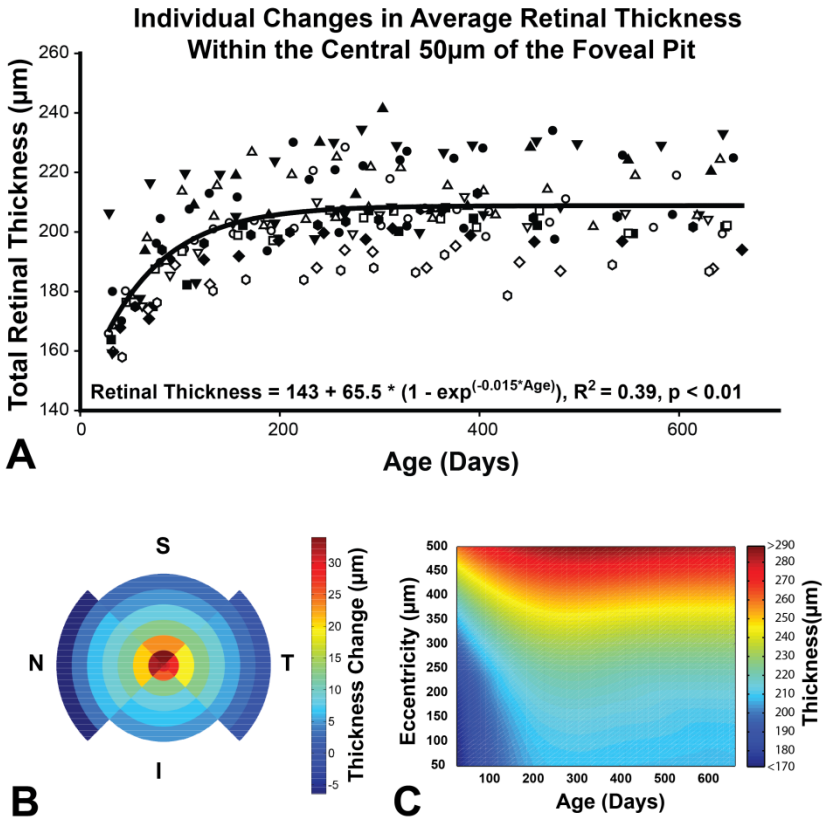

Figure 2-6. Change in total retinal thickness with age.

A. The average retinal thickness within 50µm of the pit increased by 20.9% with the majority of change occurring within the first 150 days after birth. The trend was similar for all animals and was best fit with an exponential to maximum function. B. The figure illustrates total retinal thickness change for each quadrant at the eccentricities illustrated in figure 2-3E. C. A surface plot illustrating changes in average thickness as a function of age and eccentricity up to 500 µm.

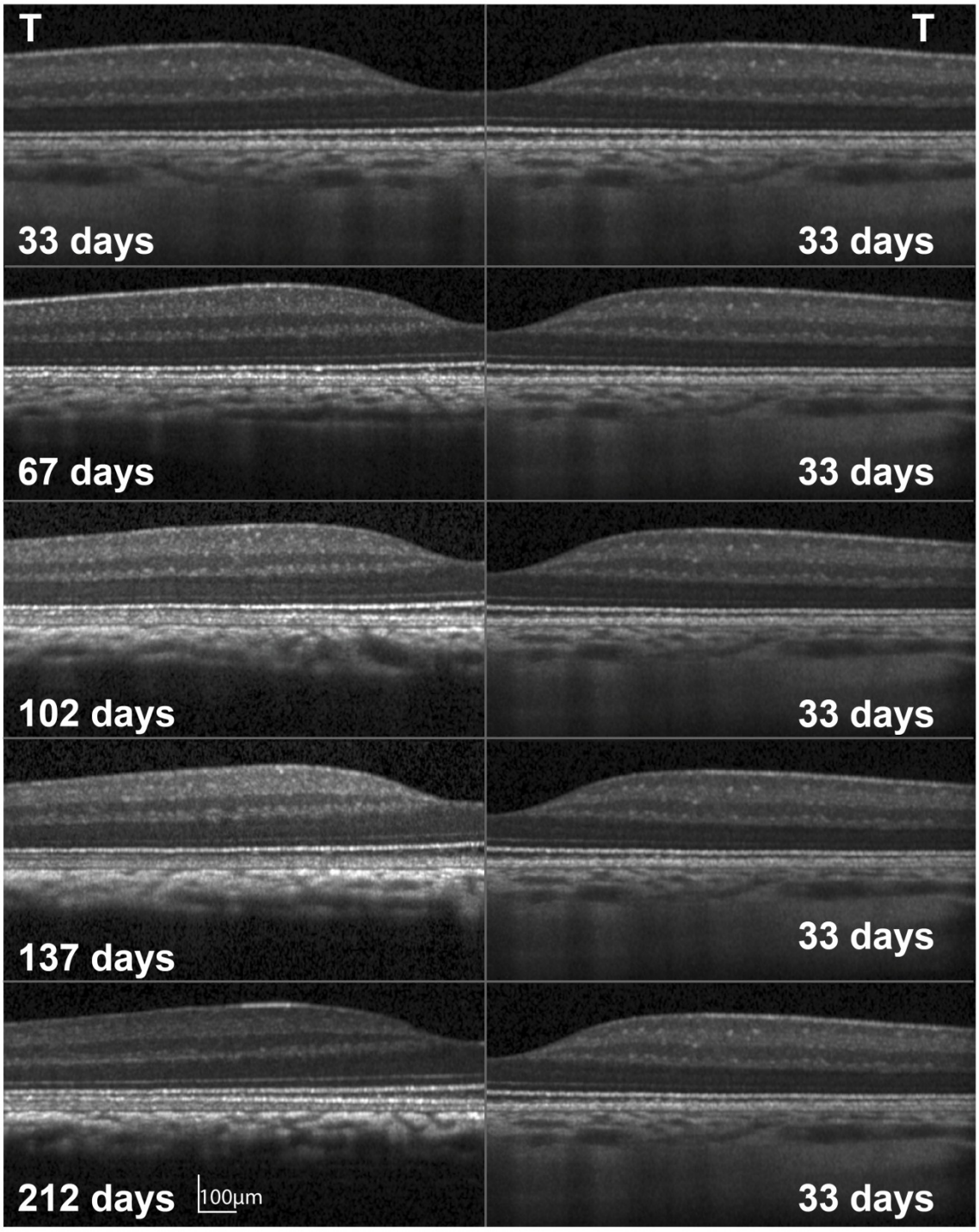
T
T
33 days
33 days
67 days
33 days
102 days
33 days
137 days
33 days
212 days
100µm
33 days

Figure 2-7. SD OCT sections through the fovea of one subject, illustrating changes in retinal thickness.

Scaled SD OCT images for one subject illustrating change in retinal thickness with age. For comparison, all sections are from temporal retina to the foveal pit center. The panels on the right illustrate the baseline scan at 33 days of age, while the left side of the figure has the follow up scan at ages illustrated in the bottom left corner of each panel. All follow up scans have been reflected along the vertical meridian. All scans were aligned to the retinal pigment epithelium.

Eccentricity (μm)	Mean Thickness (μm) at 36 ± 6 days	Mean Thickness (μm) at 628 ± 27 days	RMANOVA (F)	p
0-50	172.01 ± 12.5	207.21 ± 13.5	26.43	< 0.001*
50-100	174.81 ± 13.3	209.87 ± 14.6	26.78	< 0.001*
100-250	195.17 ± 24.9	226.89 ± 21.9	17.54	< 0.001*
250-500	268.72 ± 25.5	287.96 ± 19.4	8.40	< 0.001*
500-750	318.13 ± 19.9	328.34 ± 16.1	5.00	= 0.001
750-1000	328.46 ± 16.4	336.24 ± 14.7	3.58	0.03
1000-1250	323.14 ± 15.2	328.98 ± 13.9	2.94	0.06
1250-1500	312.46 ± 13.2	316.97 ± 13.1	2.64	0.05

Table 2-1. Average total retinal thickness.

Change in average total retinal thickness within the first 20 months of life. The reported thicknesses are averages for corresponding regions illustrated in Figure 2-6B. A significant increase in total retinal thickness was measured for regions within 500μm of the pit center. Significant values for repeated measures ANOVA, after correcting for Bonferroni's multiple comparison are noted by asterisks.

Eccentricity	Average Change in Total Retinal Thickness (μm) Superior	Inferior	Nasal	Temporal	Overall	P
0-50	32.9	31.1	32.1	31.6	31.9	0.96
50-100	33.6	30.2	32.9	30.6	31.8	0.72
100-250	34.0	25.5	32.3	27.8	29.9	0.058
250-500	23.1	12.6	20.7	19.1	18.9	0.033
500-750	12.7	8.2	11.6	12.7	12.7	0.259
750-1000	8.4	6.5	9.0	9.3	9.3	0.659
1000-1250	4.7	4.8	6.1	5.4	5.4	0.938
1250-1500	2.7	-	3.1	2.9	2.9	0.99

Table 2-2. Change in overall and sector average retinal thickness.

Change in overall average retinal thickness in the first 20 months of life. As indicated by the p values in the left column, changes in quadrant thickness over time for the regions investigated were not statistically significant.

(Fig 2-6C) or individual retinal layers (Fig 2-8 & 2-9), associated with eccentricity and age, a mean thickness plot was constructed using the surface fitting tool in MATLAB (Lowess fitting, Polynomial = linear, Span = 0.1, Robust = Bisquare).

Retinal Layer Thicknesses

Thickness measures for the retinal pigment epithelium (RPE) were best fit using a nonlinear piecewise, two segment function, where thickness measures increased for the first 289 ± 24 days of age followed by a steady decrease that continued until the end of the study. Although significant changes in RPE thickness with age were seen at all eccentricities (Repeated measures ANOVA, $F > 2.6$, $p < 0.04$, Fig 2-8, Sup Fig 2-11S), it is important to note that the maximum change in thickness did not exceed the digital axial resolution (3.87 μm) of the SD OCT instrument at any of the locations. However, as thickness measures were an average of twelve locations at each eccentricity, and similar thickness trends were noted at all eccentricities, it is possible that these measures reflect a real change.

At baseline, the outer segment layer was thickest within the center of the pit, measuring an average of 33.3 ± 4.5 μm ($F = 19.6$, $p < 0.01$, Fig 2-9A&B, Sup Fig 2-12S). Thickness measures illustrated in figure 2-9 are for the 87 μm eccentricity versus the center of the fovea, as this for the first location at which the average for 12 samples was used. For all eccentricities, the age-related change in thickness was best fit using an exponential rise to maximum function. The average age to reach 90% of maximal thickness, was used to compare the maturational rates across the regions analyzed. For the center of the fovea, the average age to reach 90% of the maximal outer segment layer thickness was 73.1 ± 37 days (Data for all eccentricities along with repeated measures ANOVA are reported in Table 2-3). Although the animals all had similar

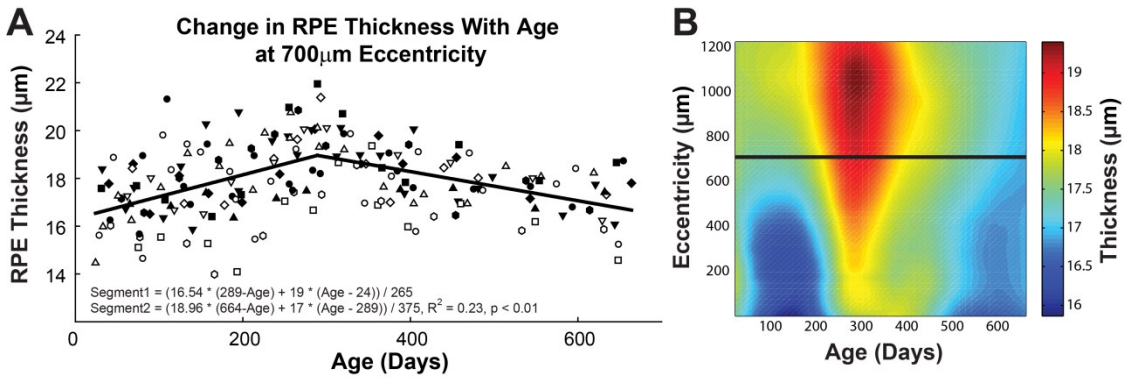

Figure 2-8. RPE thickness change with age.

At each eccentricity, the RPE thickness measured increased linearly, reaching peak thickness just prior to a year of age. Thickness after this point decreased linearly. A. Changes in RPE thickness are illustrated for each animal at 700μm eccentricity. The best fit to the data illustrates an increase in thickness till around 289 days of age followed by a reduction in thickness. B. Differences in thickness with age and eccentricity illustrate this trend with age at each eccentricity. The horizontal line through the plot illustrates the location for data presented in plot A

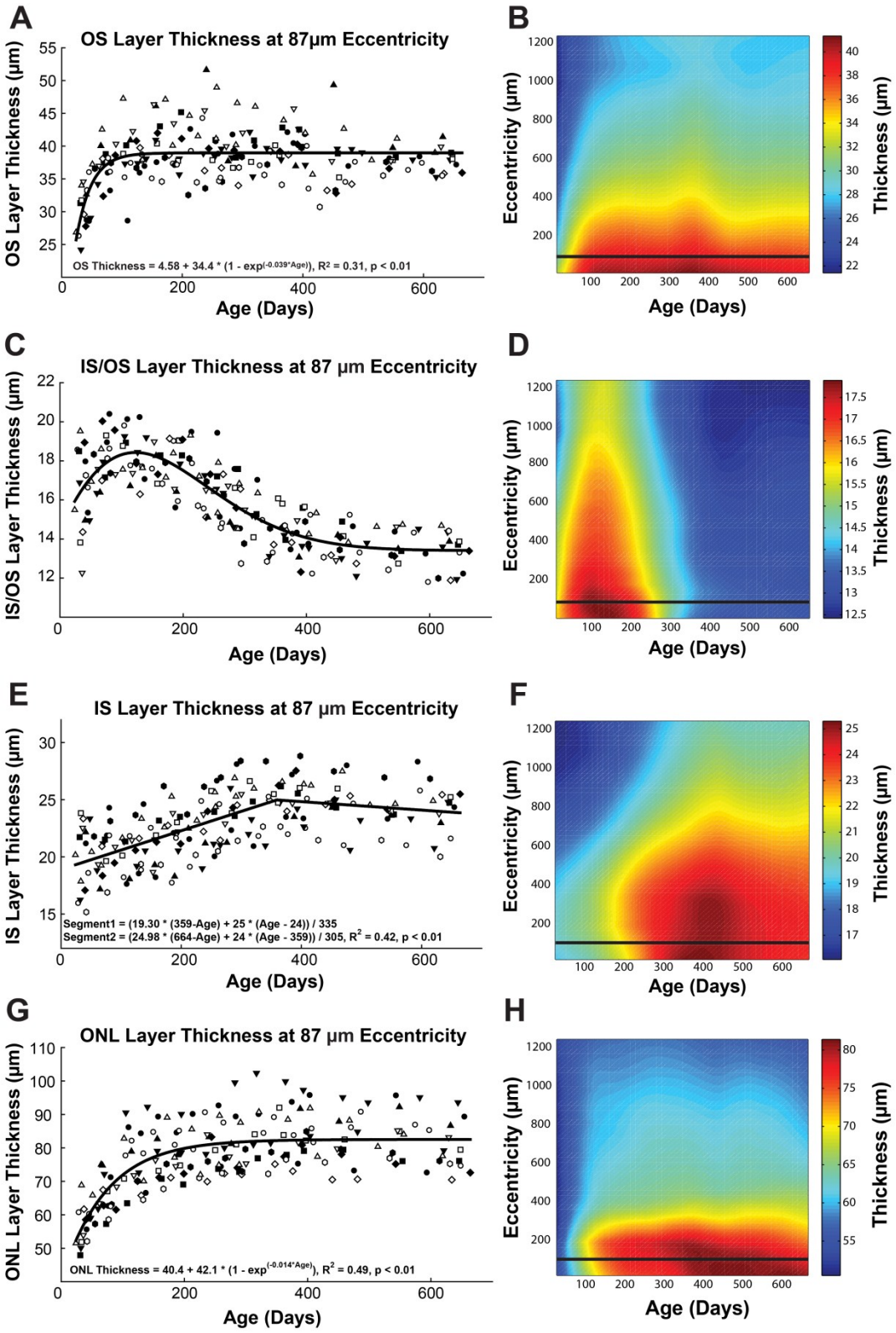

Figure 2-9. Changes in outer retinal layer thicknesses with age.

Outer retinal layers including the outer segments, inner segment/outer segment junction, inner segment, and outer nuclear layer, have significant changes in thickness with age. Plots A, C, E, and G, illustrate thickness changes for each of the 16 animals at an eccentricity of 87 μm. Although each of these layers show significant change in thickness, they all mature at different rates, with the outer segment layer thickness stabilizing at an earlier time point. Plots B, D, F, and H illustrate the relationship between thickness, eccentricity and age for each of the layers. The horizontal line through the plots indicate the location of the sampled data in A, C, E, and G.

Eccentricity (μm)	Thickness at 36 ± 6 days (μm)	Thickness at 628 ± 27 days (μm)	Mean Difference (μm)	Repeated Measures ANOVA (F)	P	Days to 90% of maximal thickness
Central	33.32 ± 4.53	39.52 ± 3.86	6.20 ± 5.8	6.897	< 0.01	73.1 ± 37.6
87	31.06 ± 3.86	37.69 ± 1.70	6.63 ± 4.6	8.298	< 0.01	70.2 ± 29.1
175	29.73 ± 3.73	32.97 ± 1.66	4.14 ± 4.4	8.101	< 0.01	65.5 ± 21.2
350	27.28 ± 3.89	32.97 ± 1.79	5.69 ± 4.4	7.026	< 0.01	69.4 ± 25.2
525	24.80 ± 3.71	31.19 ± 1.27	6.39 ± 4.2	7.681	< 0.01	78.7 ± 32.2
700	23.51 ± 3.52	29.76 ± 1.39	6.25 ± 4.1	9.376	< 0.01	79.0 ± 34.5
875	22.47 ± 3.63	29.02 ± 1.35	6.55 ± 4.4	10.351	< 0.01	82.3 ± 33.1
1050	21.40 ± 3.00	27.30 ± 1.17	5.90 ± 3.8	11.259	< 0.01	81.6 ± 35.3
1225	21.48 ± 3.53	28.18 ± 1.56	6.70 ± 3.6	11.462	< 0.01	91.9 ± 32.7

Table 2-3. Thickness change of the outer segment layer.

Eccentricity (μm)	Thickness at 36 ± 6 days (μm)	Thickness at 628 ± 27 days (μm)	Mean Difference (μm)	Repeated Measures ANOVA (F)	P	Days to maximal thickness
Central	20.32±4.36	23.67±3.11	3.35±3.8	19.233	< 0.01	394 ± 35
87	19.95±2.91	24.34±2.15	4.39±1.8	39.324	< 0.01	359 ± 29
175	20.29±2.68	24.38±2.06	4.09±1.4	51.429	< 0.01	385 ± 27
350	19.92±2.50	24.31±1.86	4.39±1.6	55.345	< 0.01	385 ± 26
525	18.54±2.27	22.85±1.90	4.31±1.3	48.501	< 0.01	355 ± 26
700	17.80±2.36	21.72±1.97	3.92±1.5	46.767	< 0.01	385 ± 30
875	16.87±2.33	20.98±1.92	4.11±1.3	53.851	< 0.01	391 ± 32
1050	16.16±2.09	20.24±1.69	4.08±1.3	47.954	< 0.01	392 ± 32
1225	16.11±1.72	20.06±1.64	3.95±1.8	25.838	< 0.01	385 ± 39

Table 2-4. Thickness change of the inner segment layer

Eccentricity (μm)	Thickness at 36 ± 6 days (μm)	Thickness at 628 ± 27 days (μm)	Mean Difference (μm)	Repeated Measures ANOVA (F)	P	Days to 90% of maximal thickness
Central	56.54 ± 6.7	81.91 ± 11.1	25.37 ± 9.4	27.168	< 0.01	140.07 ± 52.4
87	56.64 ± 5.3	79.71 ± 6.6	23.07 ± 7.8	51.109	< 0.01	123.19 ± 52.4
175	57.40 ± 5.1	75.60 ± 4.8	18.20 ± 7.3	26.156	< 0.01	111.13 ± 43.6
350	51.50 ± 4.8	63.53 ± 7.3	12.03 ± 6.0	9.71	< 0.01	89.40 ± 54.5
525	52.32 ± 5.0	61.47 ± 7.1	9.15 ± 5.3	8.37	< 0.01	77.63 ± 52.3
700	52.10 ± 4.3	60.76 ± 6.4	8.66 ± 6.0	6.9	< 0.01	64.63 ± 19.4
875	51.98 ± 3.9	59.72 ± 5.1	7.74 ± 5.0	6.083	< 0.01	64.00 ± 33.9
1050	52.88 ± 4.2	57.69 ± 5.8	4.81 ± 5.0	3.996	< 0.01	57.40 ± 31.2
1225	53.15 ± 3.9	56.17 ± 5.6	3.02 ± 4.8	0.045	0.09	64.00 ± 25.5

Table 2-5. Thickness change of the outer nuclear layer.

changes in thickness over the period studied, they matured at different rates as demonstrated by the large standard deviations for thickness measures at baseline (4.53 μm at center of the pit), and for the time to reach 90% thickness (SD = 37.6 days at center of the pit).

The thickness of the inner segment/outer segment (IS/OS) junction increased over the first hundred days, followed by a gradual reduction in thickness up to around 400 days after birth (Fig 2-9D). The change in thickness for each animal and eccentricity and grouped data was fit using a five parameter Weibull function (Fig 2-9C). Overall, there was a significant decrease in IS/OS thickness at all eccentricities averaging 3.4 ± 2.6 μm (Repeated measures ANOVA, $F > 16.1$, $p < 0.01$). Although the central fovea showed a greater reduction in thickness (4.2 ± 2.6 μm), compared to measures at an eccentricity of 1.2 mm (3.2 ± 2.5 μm), the difference was not statistically significant ($p = 0.17$).

Similarly, the mean thickness of the inner segment layer gradually increased by 4.06 ± 2.1 μm across all eccentricities measured (Fig 2-9F). Generally, the thickness of this layer increased up to a year or age (mean = 381.2 days), after which the thickness showed a slight thinning (Fig 2-9E&F). Table 2-4 summarizes the change in thickness, time to reach maximal thickness, along with the repeated measures ANOVA statistic for each eccentricity.

Of all of the retinal layers, the outer nuclear layer within 525 μm of the pit center had the largest increase in thickness during early maturation. The increase in thickness (mean = 25.37 μm, repeated measures ANOVA, $F = 27.18$, $p < 0.01$) was largest at the center of the pit and within 175 μm of the pit center, while thickness measures outside of 1050 μm were not significant (3.02 μm, repeated measures ANOVA, $F = 0.045$, $p = 0.09$, Table 2-5). Thickness changes for each animal were best fit using an exponential rise to

maximum function, which reached 90% of maximal thickness within the pit at 140 ± 52 days of age. The age to reach an asymptotic thickness, as illustrated by the time to reach 90% of maximal thickness, decreased with increasing eccentricity.

The change in thickness with age for the outer plexiform layer was not significant at all eccentricities (Sup Fig. 2-13S), except for measures at 350 μm from the center of the pit (repeated measures ANOVA = 2.6, p = 0.03). However, the change was only at one eccentricity measuring 3.75 ± 2.5 μm, comparable to that of the digital resolution of the SD OCT imaging system. Similarly, a slight yet significant change was noted for the inner nuclear layer, inner plexiform layer, and ganglion cell layer within the 350 μm eccentricity region.

The inner nuclear layer had significant changes with age at only the 350 μm and 525 μm eccentricities, both showing a linear increase in thickness over the period examined. At 350 μm the inner nuclear layer increased by 3.32 ± 2.3 μm, while at 525 μm the increase measured 2.52 ± 2.0 μm. The inner plexiform layer within 350 μm of the pit had increased in thickness, while thinning of this layer was noted outside this region. For eccentricities greater than 350 μm, the thickness of the INL showed a two-phase thickness change. From baseline the thickness decreased (at 350 μm, 2.7 ± 0.8 μm at 120 days of age), followed by a transient increase around day 256 ± 24 (at 350 μm, an increase of 2.1 ± 0.5 μm when compared to 120 days of age). Similar to the changes in the inner plexiform layer, the ganglion cell layer showed a slight, increase in thickness with age within 350 μm of the pit, while a decrease in thickness was noted at further eccentricities. At the 350 μm eccentricity, the ganglion cell layer thickness increased by 2.7 ± 0.8 μm, and was fit using an exponential rise to maximum function. Although, not clearly seen in the individual data, or surface thickness plot, when grouped into 60 day intervals, the ganglion cell layer outside 350 μm showed a decrease in

thickness within the first few months, followed by a transient thickening at around 368 ± 50 days. The thickness then stabilized within the following 60 days. All thickness changes were at, or less than, the 3.87 μm digital resolution of the SD OCT used to collect the data and only noted at specific eccentricities. Similarly, although the trends in retinal nerve fiber layer thickness were significant at 175 μm (4.7 ± 1.3 μm, $p < 0.01$) and 350 μm (3.61 ± 0.7 μm, $p < 0.01$) eccentricities, the thickness changes were within the digital resolution of the imaging system.

DISCUSSION

Although all retinal neural cells responsible for central vision are present at birth,[209,216,243,244] high contrast spatial resolution is relatively poor (5 cpd) in the infant rhesus monkey.[192,194,245] The rapid improvement in visual acuity over the first year of life has been attributed to both ocular and cortical factors.[193,205,218,220,246] The current knowledge on retinal maturation during this period has been based on histological data[209,210,220] which provides high resolution. However, the variability between individuals[223] precludes the use of histological data in the determination of accurate timelines. The present investigations used non-invasive *in vivo* SD OCT imaging during postnatal maturation to investigate changes in retinal image size and fovea characteristics from repeated measurements on infant rhesus monkeys.

The use of SD OCT measurements on a growing eye requires accurate compensation for the changes in transverse magnification associated with changes in axial length and the optical power of the cornea and crystalline lens. The three surface schematic eye constructed for calculations of retinal image size was verified by comparison to scaling changes required to obtain accurate image registration (Fig 2-1). In addition, the retinal image size for an average adult eye of the macaque monkey

based on this model was calculated as 215 μm/deg, which is similar to angular sizes previously reported.[178,247,248] Over the period studied, retinal image size increased by an average of 47 ± 16 μm/deg, or 28 ± 9%, with a resulting optical increase in the Nyquist limit. In addition, there are also significant changes in foveal pit morphology and neuronal densities within the central retina that also affect visual resolution.

The important changes in foveal pit morphology involved an increase in total retinal thickness within the foveal pit (65 μm) with a corresponding decrease in pit depth (44 μm). Concurrently, the characteristics of the pit also changed, with a decrease in radius at the bottom of the pit and an increase in radius of the top of the pit. In general, the majority of changes in thickness and width, which occurred within the first 120-150 days of age, were in agreement with the histological studies in the rhesus monkey where pit measures are shown to be adult like at 3-5 months of age.[209,210,221]

Early developmental changes in pit morphology have been modeled by finite element analysis (FEA),[211,221,242] which takes into consideration differences in inner and outer retinal tissue elasticity, and the dynamics of intraocular pressure and retinal stretch. Although there was significant inter-individual variability, the model is supported by the present data that illustrate a linear relationship between axial length, pit depth, and the width at both the top and bottom of the pit. Although, the timelines for pit depth are similar for histological and *in vivo* data, there were significant differences in the measures themselves. In particular, measures of pit depth in the present study were larger than those reported in the literature.[221] This discrepancy could be a reflection on differences in measuring techniques.

The increase in retinal thickness within the pit region follows a similar timeline to that of changes in the depth of the pit (Fig 2-5 – 2-7). Such increases in thickness could indicate either an increase in the cell size or cell quantity, but cannot be explained by cell

mitosis because the majority of neuronal cells within the central and peripheral retina are differentiated by embryonic day 150 in the *Macaca mulatta.*[216,243] Hence, this thickness increase is best explained by the centripetal cell migration and changes in cell morphology that were previously shown by histologic observations of age-related increases in photoreceptor cell density and of increasing lengths of the inner and outer segments of cones within the fovea.[209-211,221,242,249]

The majority of retinal thickness increase in the foveal pit occurs from changes in the outer nuclear layer, with a similar timeline to that of total retinal thickness, i.e., the rate of change (c) for the best fit exponential function ($y = a+b(1-exp^{-cx})$) was similar for both total retinal thickness (0.015) and outer nuclear layer (0.014). In addition, the majority of thickness increase for both total retinal thickness and outer nuclear layer is in the central 1mm of the fovea. Because it contains the cell bodies for photoreceptors, the increase in outer nuclear layer thickness is consistent with an increase in cone density during the period studied. Specifically, included in this area is the 15-20 μm region of highest cone density of 180,000 to 261,000 cones/mm^2, which drops off exponentially with increasing eccentricity.[210,221,249,250]

There is a discrepancy in thickness measures of the outer nuclear layer using *in vivo* methods (81.9 ± 11.1 μm within the center of the fovea, at 1.5yrs of age) versus those reported in histological sections (< 70 μm),[191] which is also evident in side-by-side comparisons of histological sections and SD OCT scans from identical locations of the same animal (Fig. 2-4A). The incongruity is likely a result of the methodology used for layer identification and characteristics of SD OCT imaging. Specifically, for SD OCT scans that are on-axis with the optics of the eye, the border distinction between the outer nuclear layer and Henle's fiber layer is significantly diminished.[251] Hence, the increased outer nuclear layer thickness is a result of including portions of Henle's fiber layer. This

is also evident by a localized peak sometimes found within the outer nuclear layer band of the reflectivity profile in well aligned scans (Fig. 2-4C) that is probably the junction between the outer nuclear layer and Henle's fibers. Nonetheless, the outer nuclear layer measured in SD OCT scans within the pit center should correspond to increases in peak cone density.

Based on previous histological studies using flat mount preparations, a significant increase in cone photoreceptor density[210] was expected during the period studied. Although not as precise as flat mount cell counts, microtome sections of neural tissue (analogous to SD OCT sections) have been used to estimate cell densities.[252] Hence, the resulting relationship between thickness from cross sections measures and the square root of photoreceptor density should be linear. Subsequently, for previously reported photoreceptor densities,[210] an exponential rise to maximum function can be constructed using the same rate of rise (0.014) as that of the ONL thickness (Cones/mm = $174.6 + 152.7(1-e^{-0.014 \times Age})$, $R^2 = 0.86$, $p < 0.01$). A linear equation was then derived using the best fit equations for cone density and ONL thickness (Cone Density = 4.07 X ONL Thickness - 3.06). Based on the predicted cone densities from SD OCT ONL thickness, a Nyquist limit was computed for each scan session, taking into account the retinal image size per degree visual angle as determined by the model schematic eye. Data from these calculations are presented in Fig. 2-10 and, for comparison, the best spatial resolution of lateral geniculate nucleus cells,[253] cortical cells,[254] and behavioral measures[245] are also shown. The spatial resolution calculated using this model are in good agreement with histological determined photoreceptor counts.[205,210] Based on SD OCT scans, the Nyquist limit at 30 days of age is estimated at 19 cpd, increasing to 35 cpd at 12 months of age. It is, therefore, apparent that the cone mosaic is not the

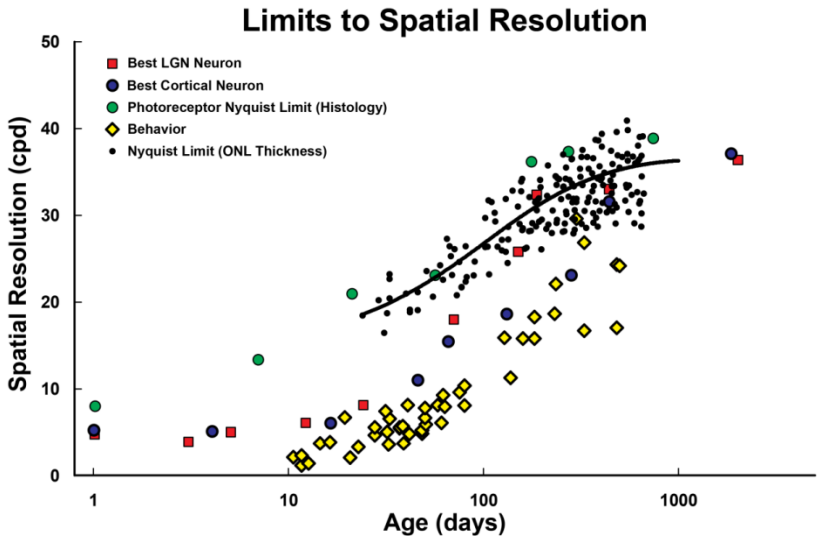

Figure 2-10. Estimates of nyquist limit from SD OCT ONL thickness.

Spatial resolution limits as determined using outer nuclear layer thickness are in good agreement with those predicted from histological cone density measures.[205,210] For comparison, spatial resolution data from behavioral studies[245] and recordings from the lateral geniculate nucleus[253] and cortical neurons[253] are also plotted.

defining limitation on behavioral measures of spatial resolution, but rather, resolution limits must be set by immaturities elsewhere within the retina or the visual pathway.

In addition to changes in the outer nuclear layer, there are also significant changes in both outer and inner segment layers, but these layers follow different time courses (Fig 2-9). For example, the outer segment layer thickness changed at greater than twice the rate of the outer nuclear layer, while changes in inner segment layer thickness were linear with age up to a year after birth. Although the outer segment layer was thickest in the pit region, the change in thickness was similar at all eccentricities measured. These results are in general agreement with histological observations of increase in photoreceptor outer segment length during the first two years after birth.[209] Similar to histological reports, the SD OCT measures reported are assuming scans were acquired on axis with the eye, with minimal or no tilt in the imaging plane.

During the period after birth there is a significant narrowing and lengthening of the photoreceptor outer segments.[214] These changes, especially the lengthening of the photoreceptor allows for more efficient photon capture.[219] For the present study, the cone outer segments at the center of the fovea pit increased in length from 28 μm at 30 days of age to 38 μm at 360 days of age. Based on photon capture probability equations ($p = 1 - e^{(-x/24.8)}$, where x is the length of the outer segment), this change in thickness would increase photon capture by only a factor of 1.16. Thus, although the increase in photon capture cannot explain the observed change in contrast sensitivity functions,[198] the timelines for the changes in outer segment thickness and peak contrast sensitivity are very similar.

The inner segment of the photoreceptor in SD OCT images consists of a portion commonly referred to as the IS/OS junction and the thickness up to the external limiting membrane. Through comparative histology studies, the IS/OS junction is thought to

include the ellipsoid and myoid of the photoreceptors.[95,255] That this SD OCT band is more than just a junction is supported by the significant thickness changes noted within the first year of life. Specifically, the IS/OS layer increases in thickness up to 120 days, followed by a gradual decrease and stabilizing after a year of age. The transient increase in thickness peaking at around 120 days of age may represent an increase in metabolic demand as the photoreceptors migrate, lengthen and mature. The inner segment layer measured from the IS/OS junction to the external limiting membrane increased linearly with age up to around 360 days after which a slight decrease in thickness was noted. The maximum thickness of 25.5 μm at the center of the pit is only slightly less than the inner segments length reported using histological methods (26-30 μm).[209] The thinner inner segment layer measures may represent the oblique orientation of these structures within the fovea and the exclusion of the IS/OS junction.

Similar to the inner segment layer, the retinal pigment epithelium also increased in thickness up to 300 days after birth. These changes corresponded with an increase in retinal pigmentation that although not quantified are clearly demonstrated in the reduced resolution of choroidal and deeper structures on SD OCT B-scans with age (Fig 2-7). The piecewise fit used to describe changes in this layer could represent changes in metabolic activity associated with maturation and photoreceptor migration. However, the current data cannot be used to determine if there is an associated increase in retinal pigment epithelial cell density within the period studied.

None of the SD OCT images from animals of any age provided evidence of an inner nuclear, inner plexiform, or ganglion cell layer within the central pit region. Although ganglion cells within the fovea have been reported in some non-human primates,[256-258] it was not evident in the *Macaca mulatta,* although the inability to visualize sparse cells in the infants may be a consequence of the resolution limits of SD

OCT imaging. For the period studied, biomechanical theories on pit maturation using FEA stretch models[221] would predict a transient thinning of the inner retinal layers within the fovea. Overall, such changes were not measured during the period studied. Significant thickness changes within the inner retina were confined to specific retinal layers and eccentricities and common maturational patterns could not be discerned. The minimal changes in the inner retinal layers during foveal maturation would indicate a large displacement between the photoreceptors that have migrated towards the fovea and the location of the ganglion cells receiving its signal. Specifically, although the outer nuclear layer increased in thickness at all eccentricities, the most significant changes were those inside 875 μm, which implies a constraint on the maximal possible displacement of inner retinal neurons, including ganglion cells, that receive input from a photoreceptor. This measure corresponds well with a peak displacement, from inner segment to ganglion cell, of 637 μm measured in human retinas.[259]

In conclusion, using SD OCT *in vivo* imaging, detailed timelines for anatomical maturation of the retina were achieved. In general, these structural changes followed similar timelines to those noted for function measures. However, significant differences in the magnitude of change are clearly evident. Future studies investigating both structural and functional properties e.g., the electroretinogram, may provide better insight to the role of retinal maturation in visual function.

Acknowledgements

The research was supported in part by NIH/NEI grants R01 EY001139, R01 EY003611, P30 EY007551, K23 EY018329, and K23 EY021761, and by a John and Rebecca Moores Professorship from the University of Houston.

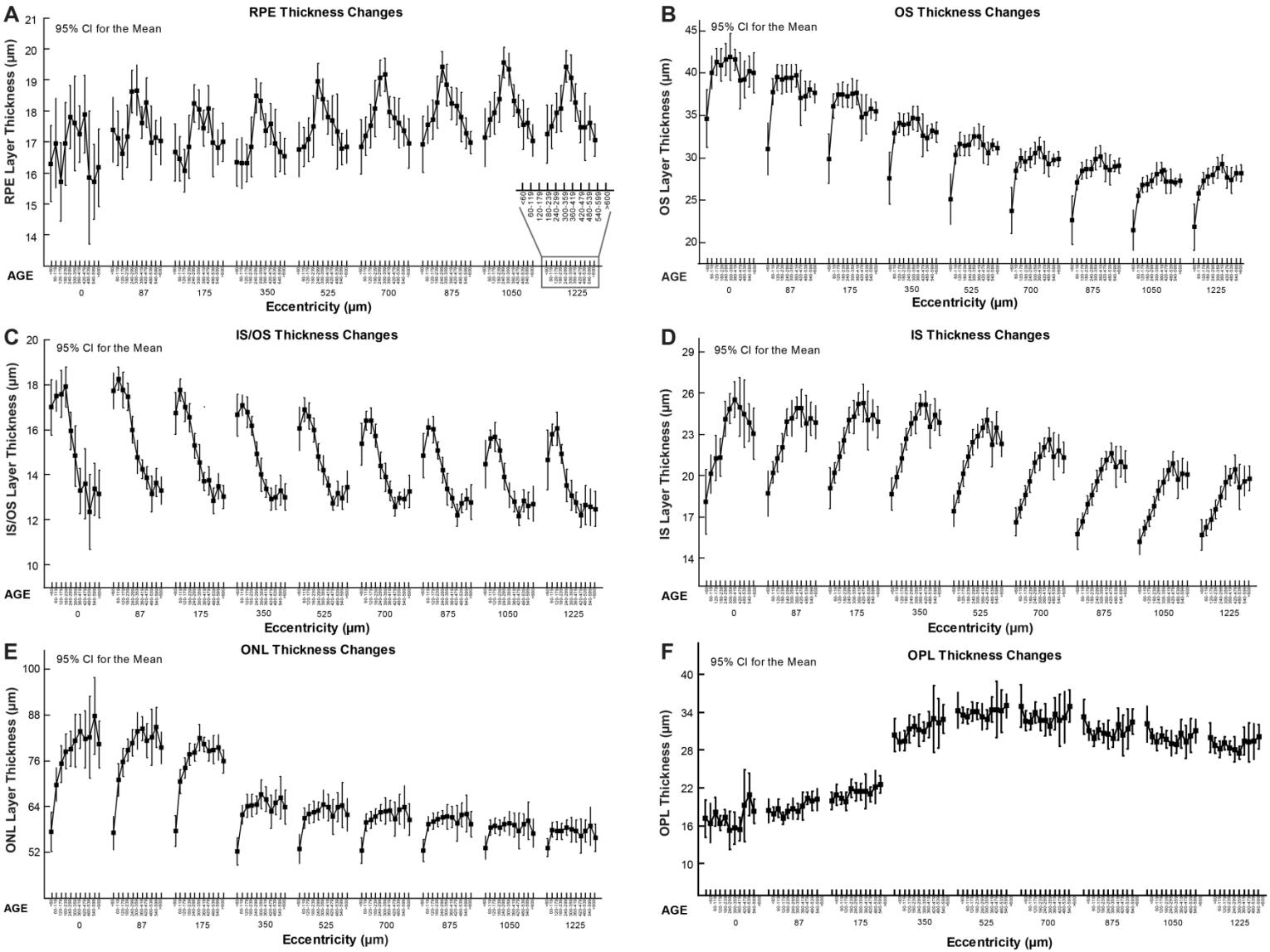
A
RPE Thickness Changes
95% CI for the Mean
RPE Layer Thickness (µm)
AGE
Eccentricity (µm)
B
OS Thickness Changes
95% CI for the Mean
OS Layer Thickness (µm)
AGE
Eccentricity (µm)
C
IS/OS Thickness Changes
95% CI for the Mean
IS/OS Layer Thickness (µm)
AGE
Eccentricity (µm)
D
IS Thickness Changes
95% CI for the Mean
IS Layer Thickness (µm)
AGE
Eccentricity (µm)
E
ONL Thickness Changes
95% CI for the Mean
ONL Layer Thickness (µm)
AGE
Eccentricity (µm)
F
OPL Thickness Changes
95% CI for the Mean
OPL Thickness (µm)
AGE
Eccentricity (µm)

Supplemental Figure 2-11S. Change in retinal layer thicknesses as a function of age.

Change in retinal thickness as a function of age and eccentricity (RPE, OS, IS/OS, IS, ONL, OPL). For each eccentricity (50μm-1750μm), the thickness measures are reported for data grouped into 60 day intervals (inset A).

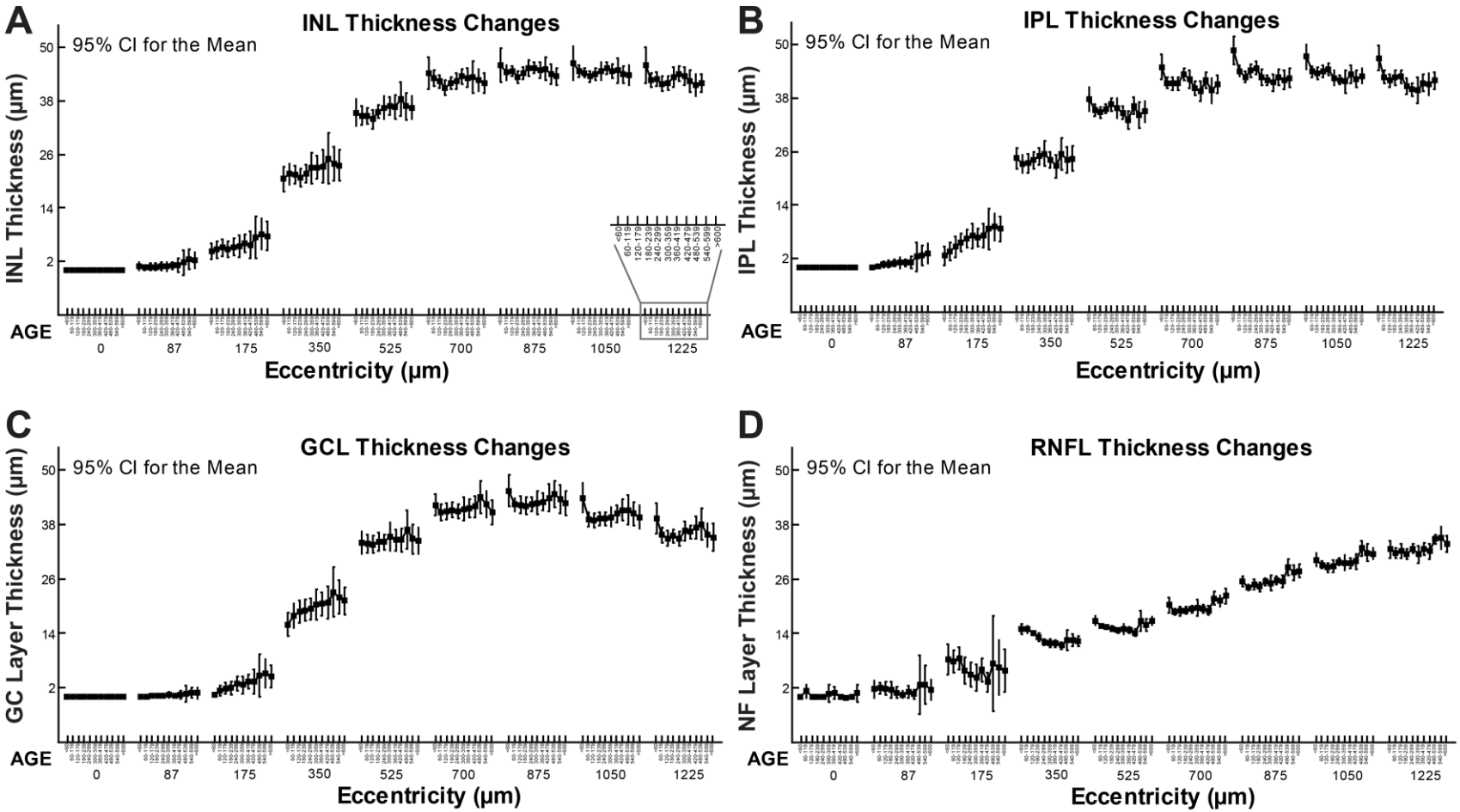
A
INL Thickness Changes
95% CI for the Mean
INL Thickness (µm)
50
38
26
14
2
AGE
0
87
175
350
525
700
875
1050
1225
Eccentricity (µm)
B
IPL Thickness Changes
95% CI for the Mean
IPL Thickness (µm)
Eccentricity (µm)
C
GCL Thickness Changes
95% CI for the Mean
GC Layer Thickness (µm)
Eccentricity (µm)
D
RNFL Thickness Changes
95% CI for the Mean
NF Layer Thickness (µm)
Eccentricity (µm)

Supplemental Figure 2-12S. Change in retinal layer thicknesses as a function of age.

Change in retinal thickness as a function of age and eccentricity (INL, IPL, GCL, and RNFL). For each eccentricity (50μm-1750μm), the thickness measures are reported for data grouped into 60 day intervals (inset A).

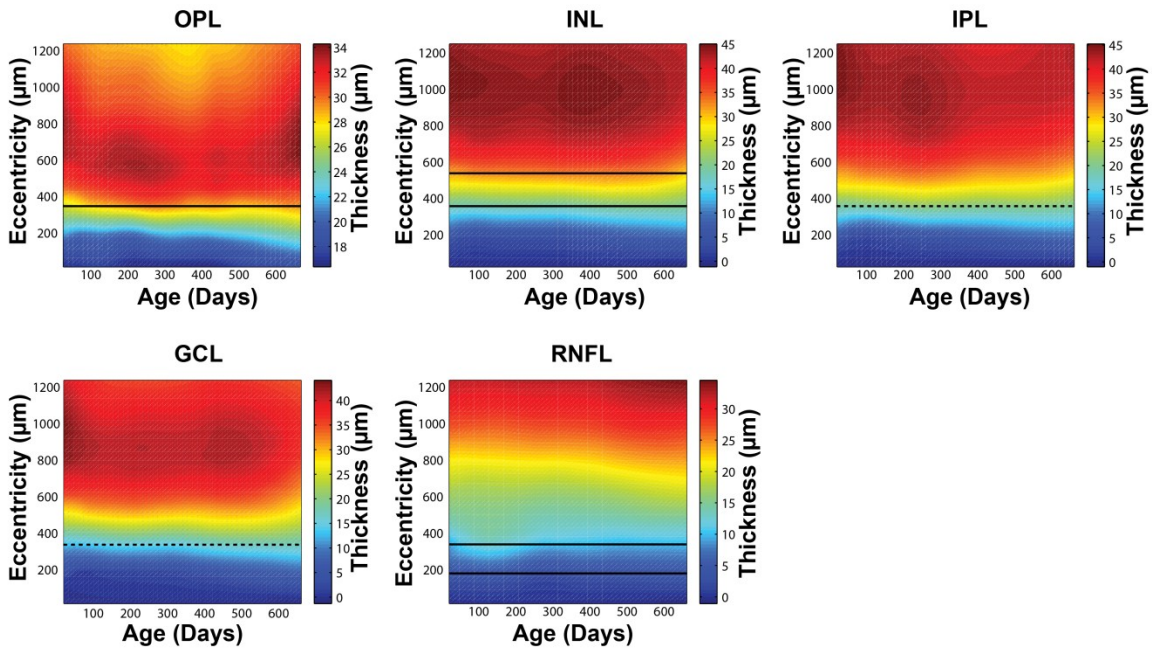

Supplemental Figure 2-13S. Change in retinal layer thicknesses as a function of age.

In general, there are minimal changes in the OPL, INL, IPL, GCL, and RNFL within the region and time period studied. Eccentricities at which statistically significant changes in the OPL and INL were measured are illustrated by the horizontal lines in the plots. The thickness of both the IPL and GCL decreased with age outside of 350µm (indicated by the dashed horizontal line) but increased in thickness closer to the center of the pit. Only a small change in RNFL thickness was noted, at 175 µm and 350 µm.

CHAPTER 3

INFLUENCE OF ANTERIOR SEGMENT POWER ON SD OCT RNFL SCAN PATH AND THICKNESS MEASURES.

The authors that contributed to this work include:

Nimesh B. Patel, OD, Brenda Garcia, BS, Ronald S. Harwerth, OD, PhD

ABSTRACT

Purpose: Retinal nerve fiber layer (RNFL) thickness measures with SD OCT provide important information on the health of the optic nerve. As with most retinal imaging technologies, ocular magnification characteristics of the eye need to be considered for accurate analysis. While effects of axial length have been reported, the effects of anterior segment optical power on RNFL thickness measures have not been fully described. The purpose of this study was to determine the influence of the optical power change at the anterior corneal surface, using contact lenses, on the location of the scan path and measurements of the thickness of RNFL in normal healthy eyes.

Methods: 15 normal subjects with less than 6D of ametropia and no ocular pathology were recruited. One eye of each subject was randomly selected for scanning. Baseline scans included raster cubes centered on the optic nerve and macula and a standard 12 degree diameter RNFL scan (Spectralis HRA+OCT). Standard 12 degree RNFL scans were repeated with 10 separate contact lenses, (Proclear daily, omafilcon A/60%) ranging from +8 to -12D in 2D steps. The extent of the retinal scan and RNFL thickness and area measures were quantified using custom MATLAB programs that included ocular biometry measures (IOL Master).

Results: RNFL thickness decreased (0.52μm/D, $r = -.33$, $p<0.01$) and the retinal region scanned increased (0.52%/D, $r=0.97$, $p<0.01$) with increase in contact lens power (-12 to +8 D). The normalized/percentage rates of change of RNFL thickness (-0.11/mm, $r=-0.67$, $p<0.01$) and image size (0.11/mm, $r=0.96$, $p<0.01$) were related to axial length. Changes in the retinal region scanned were in agreement with transverse scaling, computed with a three surface schematic eye ($R^2 = 0.97$, $p < 0.01$). RNFL area

measures, that incorporated the computed transverse scaling, were not significantly related to contact lens power (863μm^2/D, r=0.06, p=0.47).

Conclusion: Measurements of RNFL thickness by SD OCT are dependent on the optics of the eye, including both anterior segment power and axial length. The relationships between RNFL thickness measures and optical power are a direct reflection of scan path location with respect to the optic nerve head rim, caused by relative magnification. An incorporation of transverse scaling to RNFL measures, based on individualized ocular biometry, eliminated these dependencies.

INTRODUCTION

Glaucoma is group of progressive optic neuropathies that are characterized by losses of retinal ganglion cells (RGC) and associated visual field defects. An evaluation of the retinal nerve fiber layer (RNFL), which contains axons of RGCs, provides valuable information for the management of patients with glaucoma.[29,260] Traditionally, RNFL defects have been assessed by subjective methods (ophthalmoscopy and fundus photographs),[29-31] but recently objective measurements have become more common. For example, non-invasive, *in vivo* imaging technologies such as optical coherence tomography (OCT) can be used to quantify thicknesses of retinal layers.[86] The recent advances in this technology, spectral domain OCT (SD OCT), capture images at higher frequencies with axial resolutions approaching 4 μm.[261-264] The standard SD OCT scan used for evaluation of the RNFL is a circular scan, 12 degrees in diameter (nominally 3.47 mm), centered on the optic nerve head (ONH).[131,265] Thickness measures from these scans are generally presented as a continuous thickness plot following a scan path that starts on the temporal side of the ONH and progresses to the superior, nasal, inferior and back to temporal (TSNIT plot) side, with the data presented as global and sector average RNFL thickness.

In vivo RNFL thickness measures with OCT technology are generally repeatable, in both normal and glaucomatous eyes, with a test-retest variability of 4 to 8 μm.[132,135,145,266,267] However, several considerations are important in the acquisition and analyses of RNFL thickness. For example, to obtain precise and accurate measures, scans should be acquired through dilated pupils,[268] be well centered on the ONH[141,142] and have a high signal-to-noise ratio.[139,140] In addition, factors such as age,[134,136,269] refractive error[153,154,270] and axial length[134,151] need to be taken into consideration when

comparing to a normative database or evaluating variability between individuals. In general, eyes that are older, myopic and longer have thinner RNFL measures.

The systematic decrease in RNFL thickness with age is supported by histological analysis of RGC somas[271] within the inner retina and axonal counts within the optic nerve.[272,273] In contrast, thinner RNFL measures in longer myopic eyes do not correspond to a decrease in neuronal content, but are thought to be a result of optical magnification. Specifically, the extent of the retinal region scanned is related to the optics of the instrument and biometry of the eye scanned.[173] Hence, in longer eyes, a 12 degree circular scan path is further from the center of the optic nerve and its rim margin, where the RNFL is also thinner.[157,274] Therefore, the decrease in thickness within the peripapillary region does not reflect a change in axonal content, but rather a reduced axonal density in the peripapillary region.[119]

To compensate for magnification factors, a modified Littmann formula (t = p.q.s) has been commonly used to rescale RNFL thickness measures.[174,176] Using this methodology, an estimate of the RNFL thickness (t) can be computed from the magnification characteristics of the imaging system (p), the measured RNFL thickness using the standard scan (s), and a magnification factor (q) of the eye that incorporates axial length (q = 0.01306 X (Axial Length - 1.82)).[174,176] These methods have been used successfully to rescale RNFL thickness measures, with the assumption that the axonal content of the RNFL remains constant within the peripapillary region.[151,154,275] Although useful, the application of Littmann's formula only incorporates axial length in determining the magnification factor of the eye, assuming a constant for the position of the eye's second principal plane (P`).[174] Hence, the method does not consider individual differences in anterior segment optics, which may be especially important for accurate

measurements of RNFL thickness in patients who have had refractive and/or cataract surgery.

The influence of anterior segment power on RNFL thickness has been investigated by fitting subjects with varying powers of soft contact lenses. Although a significant relationship was not found with TD OCT,[276] RNFL thickness was related to contact lens induced refractive error with a higher resolution SD OCT[277] system. The general relationship between RNFL thickness and refractive error was similar to that with axial length. However, an optical basis for these findings was not determined. Therefore, in the present investigation of optical scaling anterior segment components, including corneal curvature, anterior chamber depth, and crystalline lens parameters, were included, in addition to axial length, in deriving RNFL measures from the analysis of SD OCT images.[175] Specifically, a three surface schematic eye[179] was used to quantify changes in the optical power of the anterior segment induced by soft contact lenses, and its influence on SD OCT RNFL scan path length and thickness measures.

METHODS

Subjects

Fifteen subjects with no history of ocular pathology were recruited for this study. All subjects were either students or staff at the University of Houston. The study adhered to the tenets of the Declaration of Helsinki, and all aspects of the study were reviewed by the Committee for Protection of Human Subjects at the University of Houston. Prior to collection of data, informed consent was obtained from all subjects.

Subjects were screened using a brief medical history, auto-refraction, visual acuity assessment, intraocular pressure measures, slit lamp examination and a dilated

fundus examination to ensure good ocular health. One eye of each subject was randomly selected for data collection. To ensure a uniform focal plane and to avoid exceeding the focus range of the imaging system, only eyes with refractive errors of less than 1D of astigmatism and 6D of ametropia were included.

Optical Coherence Tomography

Data were collected 30 minutes after instillation of 1% tropicamide and 2.5% phenylephrine. Baseline SD OCT scans with the Spectralis HRA+OCT (Heidelberg Engineering, Heidelberg, Germany, Software version 5.3.2) included; 1) a 97 line raster volume scan, 20 X 20 degrees centered on the optic nerve, 2) a 49 line raster volume scan, 20 X 20 degrees centered on the fovea, and 3) a standard 12 degree circular scan centered on the optic nerve. Scans were acquired with eye tracking, and averaging set at 16 frames for raster scans and 40 frames for circular scans. The infrared scanning laser ophthalmoscope (IR SLO) scan angle was set at 30 degrees for all scans acquired. Scans were repeated if image overlap was noted during averaging or if the image quality was < 25 dB. If scan quality was reduced due to ocular surface dryness, they were repeated at least two minutes after instilling a drop of artificial tear.

A series of 10 soft contact lenses (Proclear Daily, omafilcon A/60%, CooperVision Inc., Trumbull, CT) ranging in power from +8 to -12 D, were used to change the dioptric power of the anterior segment. To ensure adequate fit, each lens was allowed to settle on the eye for a minimum of 5 minutes and examined with slit lamp biomicroscopy. In addition, the refractive change induced by the contact lens was assessed by auto-refraction, and the SD OCT scan focus setting. With each contact lens, a 12 degree circular RNFL scan was acquired using identical settings to those at baseline, except for the scan focus, which was adjusted to achieve a sharp fundus

image. To assess test-retest repeatability, the last scan acquired was a standard RNFL scan without any contact lens. All scan data were exported in raw (.vol) files and analyzed using custom MATLAB (The Mathworks, Natwick, MA) programs.

Ocular Biometry and Scaling

Ocular biometry including corneal curvature, anterior chamber depth and axial length were measured at baseline, without any contact lenses, using a non-contact optical biometer (IOL Master, Carl Zeiss Meditec Inc., Dublin, CA). For scans acquired with contact lenses, the power adjustment was made by changing the radius of the anterior corneal surface. Crystalline lens parameters including thickness and curvature were interpolated from normative data.[184] The refractive index of the cornea, aqueous humor and vitreous humor were adjusted for the central wavelength (870 nm) of the SD OCT superluminescent diode.[278] Refractive index of the lens was computed with a ray tracing algorithm using the biometry and refractive data, assuming homogenous and spherical refractive surfaces. Using these parameters a three surface schematic eye as described by Bennett and Rabbetts[63,179,224] was constructed for each scan using a custom MATLAB program. Lateral or transverse scaling (μm/deg) was calculated from the second nodal point of the schematic eye, assuming a spherical retinal surface. Because axial scaling is dependent on the SD OCT imaging system and illumination source characteristics, no adjustments were made for the different contact lenses used.

Scaling Validation

The three surface schematic eye scaling methodology was validated with corresponding changes in retinal image size. To reduce bias, a custom automated

MATLAB program was used to randomly select one of the twelve RNFL scans from each subject as baseline. A baseline transverse scaling was then determined for this scan using a three surface schematic eye. Subsequently, for each of the 12 scans in the series, the 30 degree scanning laser ophthalmoscope (SLO) fundus image was extracted from the raw data (.vol files) and registered to the baseline fundus image using a generalized dual bootstrap, iterative closest point algorithm (i2k retina, DualAlign, LLC, Clifton, NY).[238] The lengths of the registered images, assuming a symmetric and square scanned region, were then used to compute a predicted/registered image scaling for each scan (Equation 3-1, Fig. 3-1A).

Equation 3-1.

$$Predicted\ /\ Registered\ Image\ Scaling = \frac{\sqrt{Total\ Pixel\ Content\ in\ Registered\ Scan}}{\sqrt{Total\ Pixel\ Content\ in\ Baseline\ Scan}} \times Baseline\ Transverse\ Scaling$$

This predicted/registered image scaling was then compared to the computed scaling. Overall, there was good agreement between retinal scaling computed using image registration and that computed using a three surface schematic eye ($Scaling_{Im\ Reg}$ = 1.01 X $Scaling_{3\ surface}$ - 1.8, R^2 = 0.97, Fig. 3-1B). Bland-Altman analysis demonstrated a mean difference of -0.006 μm/deg, and a 95% limits of agreement between -5.11 μm/deg and 5.10 μm/deg.

RNFL Segmentation and Analysis

RNFL B-scans were randomized, and a custom segmentation algorithm[63,224] was used to identify the inner limiting membrane and junction between the RNFL and RGC

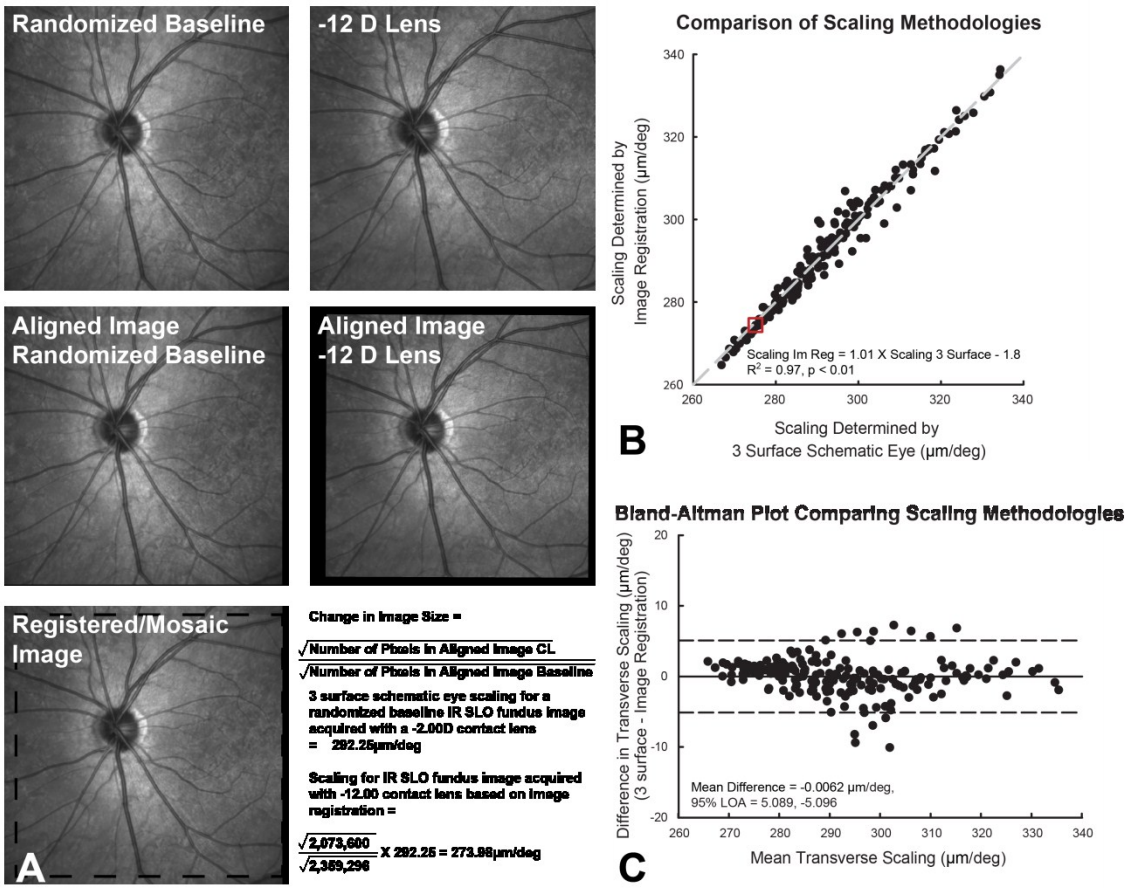

Figure 3-1. Retinal scaling with image registration and three surface schematic eye with changes in anterior segment power.

A. For each subject all 30 degree IR SLO images from RNFL scans were registered to a baseline scan that was selected at random. As demonstrated in this example, the square root of the number of pixels for each aligned image was used to determine the scaling of each scan based on the baseline. B. This plot illustrates the agreement between scaling determined by image registration and that computed using a three surface schematic eye. The data point in the center of the box is from the example shown in A. C. The limits of agreement determined by the 95% confidence interval of the mean difference for retinal scaling using a schematic eye and image registration.

layer. In brief, B-scan images (1536X496 pixels) were first de-noised using a Haar 2D stationary wavelet and convolved with a Gaussian filter (SD = 4). An iterative process was then used to identify intensity changes, corresponding to the layers of interest, within the signal profile of each A-scan. Any errors in layer identification, which were most commonly around shadows of major retinal vasculature, were manually corrected. To account for the non-neural retinal vasculature, B-scans were first rescaled to a 1:1 aspect ratio using the computed transverse scaling. The diameter of each major retinal vessel was determined from the corresponding shadows cast on the underlying retina (Mardin CY, et al. IOVS 2009;50:ARVO E-abstract 3333). The center of each vessel was manually marked, and a circular region matching that of the vessel was subtracted from the RNFL thickness (Fig 3-2C & D). RNFL thickness measures were transformed to area by multiplying the thickness for each A-scan by its calculated width. Prior to calculating global, quadrant and 30 degree sector (Fig 3-2C) thickness and area measures, the start of the TSNIT plot was shifted to align with a line passing from the center of the circular scan to the center of the foveal pit (Fig 3-3A). Methods used for identification of the fovea center, registration and alignment of the TSNIT plot have been described elsewhere.[63] In brief, the center of the fovea was identified using the center of concentric circles fit to the pit region at varying depths. The IR SLO images from the RNFL and macula scans were then registered. A line was then fit from the center of the circular scan to the foveal pit center.

Scan Path and RNFL Thickness

To investigate the relationship between scan path and RNFL thickness, identical paths to those of circular scans with contact lenses were interpolated from the baseline raster volume scan centered on the optic nerve for each subject. The IR SLO image and

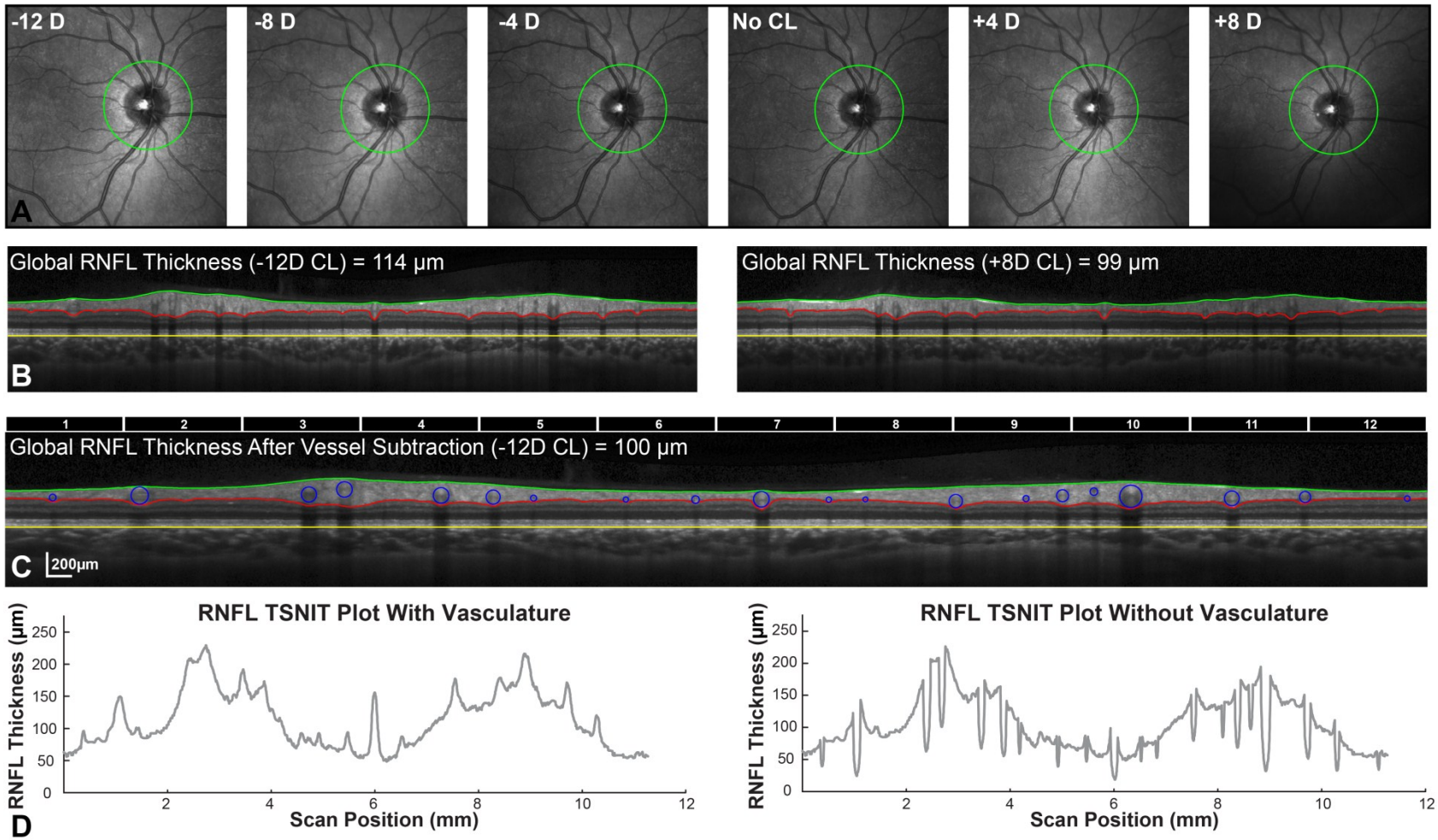
-12 D
-8 D
-4 D
No CL
+4 D
+8 D
A
Global RNFL Thickness (-12D CL) = 114 µm
Global RNFL Thickness (+8D CL) = 99 µm
B
1
2
3
4
5
6
7
8
9
10
11
12
Global RNFL Thickness After Vessel Subtraction (-12D CL) = 100 µm
C
200µm
RNFL TSNIT Plot With Vasculature
RNFL Thickness (µm)
Scan Position (mm)
RNFL TSNIT Plot Without Vasculature
RNFL Thickness (µm)
Scan Position (mm)
D

Figure 3-2. Illustration of the retinal region scanned and RNFL thickness of one subject with contact lens associated changes in anterior segment power.

A. 30 degree IR-SLO fundus images with RNFL scan path illustrate an increase in retinal region scanned with increase in contact lens power. B. The OCT B-scans acquired with a -12D and +8D contact lens demonstrate the change in RNFL thickness associated with scan path. C. Retinal vasculature was subtracted from the RNFL thickness after scans were rescaled to a 1:1 aspect ratio. The top portion of the figure illustrates the 30 degree sectors used for data analysis. D. Resulting TSNIT plots with and without vasculature were used to compute average thickness and area measures.

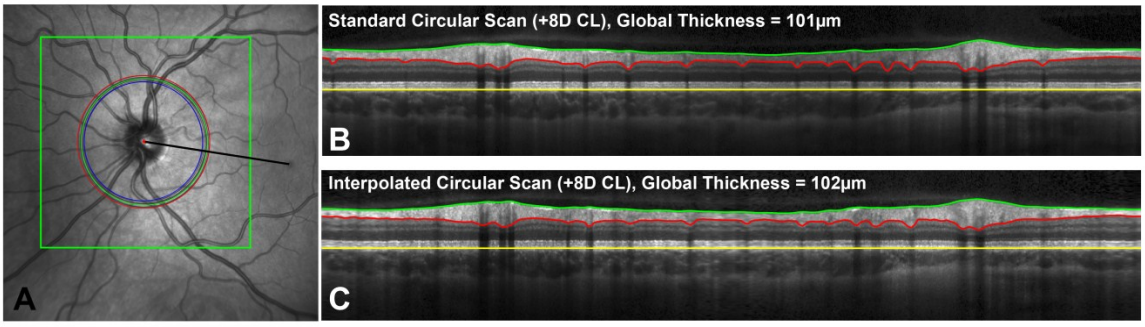

Figure 3-3. Changes in scan path with contact lenses, and the use of interpolated scans for RNFL thickness measures.

A. RNFL scan paths, acquired with contact lenses and at baseline, registered to the baseline 97 line raster scan (boxed region) centered on the optic nerve. The scan paths illustrated in blue, green and red correspond to scans with a -12D contact lens, no contact lens, and a +8D contact lens. The black line indicates the mean location for the line connecting the center of the optic nerve to the fovea to which TSNIT plots were aligned. B&C Illustrate the resultant OCT B-scans for the standard and interpolated scan with a +8D contact lens.

scan path for each RNFL scan was registered to the IR SLO image of the baseline raster volume (Fig 3-3A) using a generalized dual bootstrap, iterative closest point algorithm (i2k retina, DualAlign, LLC, Clifton, NY).[238] Using the registered scan path, an RNFL B-scan was then constructed using bilinear interpolation from the raster volume (Fig 3-3C). The resultant scans were segmented and analyzed using the same protocol as for the standard scan. To avoid bias, images were randomly imported into the program, and the user was unable to view the results of the registration process, or scan parameters used.

RESULTS

Of the fifteen subjects (mean age = 24.5 ± 2.5 yrs) recruited, nine right eyes and six left eyes were used for data collection. All eyes were healthy as determined by best corrected visual acuity, slit lamp biomicroscopy, intraocular pressures, and indirect ophthalmoscopy. Both the spherical equivalent refractive errors (range = +0.62 to -5.12 D) and axial lengths (range = 23.41 to 26.09 mm) were normally distributed (Shapiro-Wilk, $p>0.2$).

Global RNFL thickness measures without contact lenses at baseline measured 111.4 ± 9.0 μm. On repeat scan, approximately 2 hours after baseline, global RNFL thickness measured 111.1 ± 9.6 μm. The measurement error, or within subject standard deviation (S_w), was 1.19 μm. Based on this measurement error, 95% of global thickness measures should be within $1.96 \times S_w$ (2.33 μm) of the mean. Similarly, the repeatability, or difference between any two measures should not exceed $\sqrt{2} \times 1.96 \times S_w$ (3.31 μm) in 95% of samples from the same individual.[279] Major retinal vascular contribution was 12.6 ± 1.7 μm accounting for 11.4 ± 1.6% of the global RNFL thickness. The

repeatability for vascular contribution was 2.02 μm (Sw = 0.72 μm) or 1.7% of global RNFL thickness.

RNFL thickness

The contact lenses were effective at inducing a power change at the corneal surface as determined by both auto-refraction (slope = -0.94, R^2 = 0.99, $p < 0.01$) and SD OCT scan focus (slope = -0.95, R^2 = 0.99, $p < 0.01$). The mean scan quality was 35.3 ± 3.2dB, and was not significantly different for scans with and without contact lenses (p = 0.334). In addition, scan quality was not related to contact lens power (p = 0.6) or RNFL thickness (p = 0.3). Overall, the global RNFL thickness decreased linearly with increase in power (Fig 3-4A, slope = -0.52, 95% confidence interval -0.74 to -0.30, p<0.01). One subject (inverted filled triangles, Fig 3-4A) had significantly thicker RNFL measures, but followed similar trends to the rest of the subjects and had no detectable pathology on ophthalmoscopic examination and visual field testing. Hence, this subject was not excluded from data analyses. Repeated measures ANOVA with Greenhouse-Geisser correction demonstrated statistically significant differences for global, quadrant and sector RNFL thickness measures for the range of contact lenses used (global thickness, RMANOVA F(3.9, 55.9) = 82.4, p<0.001, Table 3-1). For global RNFL thickness, post hoc paired t-tests using an adjust p value of 0.004 for multiple comparisons, revealed a significant difference for contact lenses equal to or greater than +2D and less than -4D (Table 3-2). Based on the test retest repeatability for well centered scans (3.31 μm), thickness measures were significantly different for changes in anterior surface corneal power of greater than 6D.

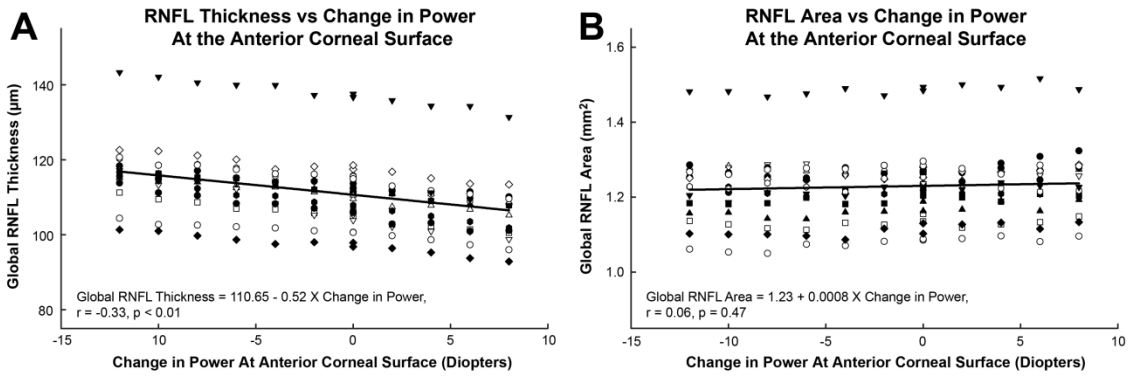

Figure 3-4. RNFL thickness and area as a function of contact lens power.

RNFL thickness (A) and area (B) as a function of the nominal power of the contact lens worn during the measurement. A. Global RNFL thickness with standard 12 degree circular scans decreased with increasing dioptric power at the anterior corneal surface. However, there is no significant change in Global RNFL area (B). The different symbols represent individual subjects.

	Change in Anterior Segment Power													
	-12	-10	-8	-6	-4	-2	Plano	Plano	2	4	6	8	Test Retest	RM-ANOVA
Global	116.8±9.4	115.3±9.6	114.6±9.4	113.5±9.3	112.3±9.4	111.8±9.0	111.4±9.0	111.1±9.6	109.3±9.5	108.4±9.0	107.0±9.7	106.0±8.8	3.3	**<0.001**
Temporal	83.8±8.5	82.2±8.9	81.8±9.7	82.0±9.0	81.4±9.6	80.7±8.4	80.6±8.4	79.9±9.1	79.9±8.6	79.4±8.6	78.5±9.9	78.4±8.7	4.7	**<0.001**
Superior	141.2±15.9	138.9±16.6	137.9±16.4	136.6±15.6	134.5±15.4	134.0±14.7	133.1±14.5	133.4±15.3	130.9±15.2	129.2±13.8	127.8±14.6	126.4±14.0	6.1	**<0.001**
Nasal	92.6±13.7	92.6±13.8	91.7±13.1	90.2±14.4	89.6±13.4	90.2±14.1	89.3±13.2	89.3±14.4	86.7±14.5	86.4±13.6	84.6±13.2	83.5±13.4	7.3	**<0.001**
Inferior	150.0±13.3	147.9±12.9	147.2±13.6	145.3±13.0	144.0±13.2	142.7±12.6	142.9±13.2	142.0±12.9	139.7±12.7	139.1±11.9	137.5±12.1	135.8±11.7	7.5	**<0.001**
S1	81.3±10.6	79.6±10.6	79.5±11.3	79.4±11.0	80.3±10.6	79.5±10.0	80.0±10.5	78.6±10.9	79.6±10.2	77.9±9.3	77.1±10.6	77.9±9.5	8	**0.036**
S2	119.2±21.2	117.4±21.9	115.7±21.5	115.8±21.8	115.5±22.1	113.6±21.6	114.7±21.2	113.4±20.9	113.2±22.3	111.1±21.2	110.7±21.2	110.7±19.8	6.7	**<0.001**
S3	168.6±16.7	165.3±16.8	164.5±16.6	163.5±17.2	161.0±17.0	160.1±16.4	159.1±16.0	159.9±17.4	157.6±16.9	155.8±16.0	154.6±17.5	153.5±17.6	10	**<0.001**
S4	124.6±26.4	122.7±27.4	121.3±25.8	120.4±24.6	117.3±23.2	117.2±22.2	116.2±21.1	117.3±22.4	113.9±22.2	112.4±19.9	109.9±20.3	108.1±20.3	9.2	**<0.001**
S5	127.3±25.8	126.1±24.8	124.7±25.5	122.3±26.2	121.6±24.9	122.5±23.8	119.3±24.1	119.6±23.9	116.8±21.6	115.2±23.3	112.7±22.6	111.4±23.8	11	**<0.001**
S6	91.8±14.1	91.9±14.3	91.2±13.9	89.7±14.8	89.5±15.5	90.0±16.7	89.9±14.2	89.5±15.0	86.4±16.0	86.7±14.4	85.3±14.1	84.2±15.0	10	**<0.001**
S7	73.9±10.8	74.0±11.4	73.8±11.0	72.7±12.8	71.9±10.8	72.5±11.8	72.7±10.6	72.3±11.6	70.6±12.2	70.3±11.9	69.1±12.0	68.1±11.6	6.2	**<0.001**
S8	107.7±19.1	107.1±18.5	107.0±18.0	104.3±18.6	103.4±18.4	103.8±18.2	102.1±18.2	102.1±18.6	98.1±19.1	98.0±17.8	95.5±17.7	93.8±17.5	7.9	**<0.001**
S9	136.8±17.4	134.2±17.6	134.4±18.4	130.9±18.2	130.3±19.5	129.2±17.2	128.7±17.4	127.9±19.3	126.7±18.4	124.6±16.9	123.0±17.1	120.7±17.6	15	**<0.001**
S10	182.1±17.2	180.0±16.5	177.3±18.2	176.9±17.2	174.8±17.9	173.4±18.3	174.4±19.3	172.8±18.4	169.5±18.0	170.6±16.2	168.3±17.0	166.5±17.4	12	**<0.001**
S11	121.8±22.8	120.1±24.3	120.3±24.8	120.6±23.3	118.9±24.7	116.0±23.6	117.3±23.2	118.0±23.8	117.2±23.0	116.7±23.8	116.0±24.5	115.8±24.7	8.4	**<0.001**
S12	66.8±7.7	65.5±7.5	65.1±9.4	64.9±6.7	63.2±7.6	63.7±7.1	62.1±7.8	61.5±7.7	61.6±6.6	62.0±7.2	62.0±8.7	60.6±7.8	6.5	**<0.001**
Vessel	13.3±1.9	13.1±1.3	12.8±1.4	13.2±1.3	13.0±1.6	12.7±1.6	12.6±1.7	12.8±1.6	12.0±1.8	12.5±1.6	12.3±1.3	11.9±1.6	2	**0.001**

Table 3-1. Mean RNFL thickness with contact lens.

Mean global, and sector RNFL thickness measures with each contact lens. Test-retest/repeatability measures are calculated using thickness data with no contact lenses. Significant changes in thickness were noted for each measure as indicated by repeated measures ANOVA.

Contact Lens Power	Mean Difference (µm)	Std. Deviation (µm)	Paired t-test, p value
-12	5.69	2.18	<0.001
-10	4.35	1.99	<0.001
-8	3.67	1.82	<0.001
-6	2.49	1.94	<0.001
-4	1.47	1.45	0.001
-2	0.68	1.08	0.029
No lens	-0.17	0.88	0.453
2	-1.74	0.89	<0.001
4	-2.64	1.15	<0.001
6	-3.75	1.39	<0.001
8	-4.95	1.34	<0.001

Table 3-2. Mean differences of RNFL measures with contact lenses.

Mean differences of global RNFL measures compared to baseline scans without any lens.

Major retinal vascular contribution

RNFL thickness measures after removal of major retinal vasculature, decreased at a rate of 0.46 μm (95% CI, -0.67 to -0.24) per diopter increase in contact lens power. Overall, the slopes for RNFL thickness change with and without retinal vasculature were not significantly different (p= 0.69). However, there was a slight, but statistically significant, decrease in the major retinal vascular thickness contribution with increase in dioptric power (slope = -0.06 μm/D, R^2 = 0.06, p = 0.001). The mean, maximum thickness change in vascular contribution was 1.4 μm, and less than the test retest variability. Subsequently, the percent vascular contribution to the RNFL across the range of contact lens powers was not significantly different (RMANOVA, F(6.3, 88) = 0.965, p = 0.46).

RNFL circular scan path

The calculated circumference of RNFL scans decreased with increase in anterior surface corneal power (slope = 60.1 μm/D, R^2 = 0.40 , p<0.001, Table 3-3). The registered scan paths transferred onto their corresponding baseline raster SLO images, illustrate these changes in scan location (Fig 3-3A). With an increase in scan length, there was a corresponding linear decrease in global RNFL thickness (slope = -7.7 μm/mm, R^2 = 0.22, p<0.001). In addition, RNFL thickness measures from interpolated B-scans, matching the registered scan paths, were in good agreement with those of the standard circular scans (Fig. 3-5, Mean difference = -0.15μm, 95% LOA = 1.61 μm, -1.91 μm). The within subject standard deviation for global RNFL thickness measures from interpolated and standard scans was 0.41 μm, corresponding to a repeatability of 1.14 μm. These data provide evidence that the relationship between RNFL thickness

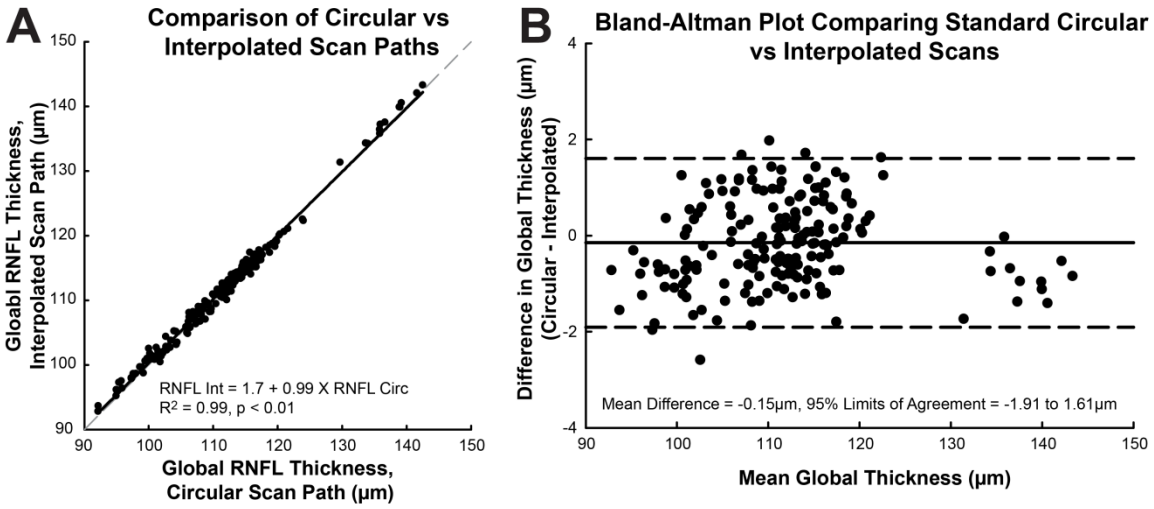

Figure 3-5. Agreement between interpolated and circular scans.

A comparison of the RNFL thickness measurements derived by interpolation from raster scans and direct measurements from circular scans. A. Correlation of the thickness measures from standard circular and interpolated scans. The gray dashed line represents a 1:1 relationship. Results of a linear regression analysis are presented as an inset. B. Bland-Altman analysis of the limits of agreement between the thickness measures from raster scans and circular scans. Dashed lines represent the 95% limits of agreement.

Change in Anterior Segment Power (D)	Scan Circumference (mm)	Std. Deviation	CV (%)
-12.00	10.51	0.42	4.02
-10.00	10.59	0.43	4.03
-8.00	10.68	0.43	4.04
-6.00	10.77	0.44	4.05
-4.00	10.88	0.44	4.08
-2.00	10.99	0.45	4.10
0	11.11	0.45	4.07
+2.00	11.24	0.47	4.18
+4.00	11.39	0.48	4.23
+6.00	11.55	0.50	4.30
+8.00	11.73	0.52	4.37
Maximum Change	1.22	0.11	9.02

Table 3-3. Calculated scan diameters for each contact lens.

Calculated mean scan circumference for the 12 degree circular scan with each contact lens.

and changes in corneal power is a result of differences in scan diameter and subsequently scan path.

Anterior Corneal Surface Power and Axial Length

Although the trends in scan circumference and RNFL thickness measures were similar across subjects, there were significant inter-individual differences (Fig 3-4). The inter-subject variability is also evident from the increase in standard deviations for global thickness changes with larger contact lens powers (table 3-2), and the high coefficient of variation for the maximal change in scan diameter. To reduce the effects of inter-subject variability and to determine the main effects of the optical power of the cornea, the data for each subject were transformed to a percentage of baseline thickness measures (Fig. 3-6A). Similarly, using the same registration protocols as those for scaling validation, a percentage metric was used to describe the extent of the retinal region scanned with each contact lens using the pixel content from registered SLO images (Fig. 3-6B). Interestingly, the subject considered an outlier in the untransformed data (Figs. 3-4A & B) falls in the middle of the normalized data.

The data for each subject were analyzed by linear regression to obtain the slope for the best-fit line passing zero reference associated with the baseline (no contact lens) condition. The slopes of the functions ranged from -0.29 to -0.76 (Fig 3-6A), with a mean slope of -0.44 (-0.47, -0.41). Data for each quadrant and clock hour sector analyzed are presented in table 3-4. Similarly, the slopes for the percentage of retinal region imaged ranged from 0.38 to 0.72 (Fig 3-6B), with a mean slope of 0.49 (0.47, 0.51). The slope of the linear regression for RNFL thickness and retinal region scanned as a function of optical power were opposite in sign, but were similar in magnitude (mean difference = 0.04 ± 0.08, $p = 0.04$). In addition, as illustrated in Fig. 3-6C, the rates of change with

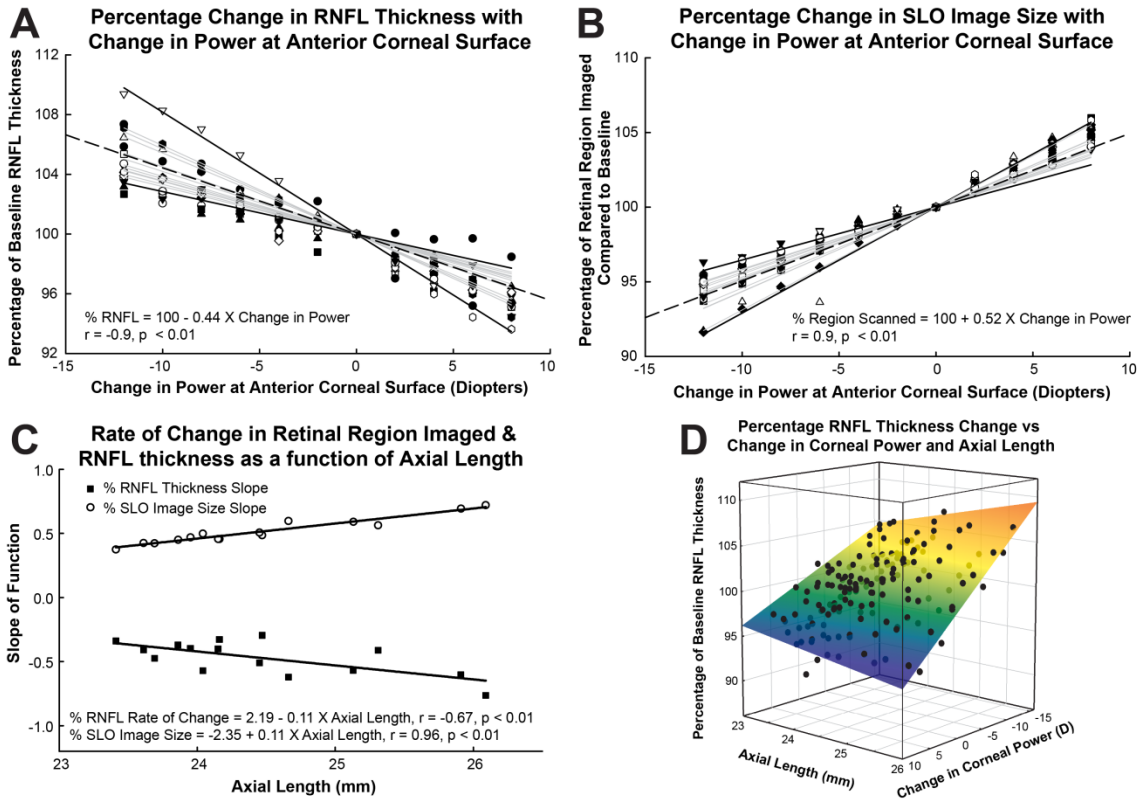

Figure 3-6. Relationship between axial length, change in anterior segment power and RNFL thickness.

When expressed as a percentage of baseline, there are significant differences in the rate of change for both RNFL thickness (A), and the region of the retina scanned (B). The gray lines are linear regressions through the origin for each subject. The solid black lines in A and B represent the largest and least slope, while the dashed black fit illustrates the mean fit for the data. The rates of change were linearly related to axial length (C). The surface plot (D) illustrates these differences associated with axial length and change in power at the anterior corneal surface.

	Slope % RNFL Thickness/D		Slope % RNFL Area/D	
	Slope	95% CI	Slope	95% CI
Global	-0.45	-0.48, -0.43	0.05	0.03, 0.07
Temporal	-0.33	-0.43, -0.23	0.17	0.09, 0.24
Superior	-0.45	-0.49, -0.41	0.01	-0.03, 0.06
Nasal	-0.49	-0.56, -0.41	0.00	-0.07, 0.07
Inferior	-0.51	-0.55, -0.46	0.00	-0.04, 0.04
S1	-0.38	-0.50, -0.28	0.13	0.02, 0.24
S2	-0.33	-0.43, -0.23	0.18	0.09, 0.27
S3	-0.41	-0.47, -0.34	0.07	0.00, 0.15
S4	-0.52	-0.59, -0.44	-0.08	-0.17, 0.01
S5	-0.56	-0.64, -0.48	-0.14	-0.26, -0.03
S6	-0.47	-0.56, -0.37	0.01	-0.07, 0.11
S7	-0.38	-0.50, -0.26	0.07	-0.02, 0.17
S8	-0.65	-0.76, -0.54	-0.17	-0.27, -0.07
S9	-0.66	-0.75, -0.58	-0.14	-0.22, -0.06
S10	-0.48	-0.56, 0.41	0.02	-0.04, 0.09
S11	-0.20	-0.33, -0.08	0.26	0.15, 0.36
S12	-0.31	-0.46, -0.15	0.06	-0.09, 0.23

Table 3-4. Slope values for percent RNFL thickness and area with change in anterior corneal surface power.

Slope values for percent RNFL thickness and area measures for global, quadrant and sector measures with change in anterior corneal surface power.

axial length, followed a similar trend for percent RNFL thickness (slope = -0.11, R^2 = 0.45, p <0.02) and percent retinal image size (slope = 0.11, R^2 = 0.92, p <0.01). Overall, changes in dioptric power at the corneal surface had a larger effect on retinal image size and RNFL thickness, in longer eyes. Equations 3-2 & 3-3 describe the percentage change in retinal region scanned and RNFL thickness as a function of axial length (AL, in mm) and change in corneal power (ΔK, in Diopters) with contact lenses.

Equation 3-2

% Retinal Region Scanned = 100 - 2.35.ΔK + 0.11.ΔK.AL

Equation 3-3

% RNFL Thickness = 100 + 2.19.ΔK - 0.11.ΔK.AL

RNFL Area

The average global RNFL area, for the fifteen subjects without any contact lenses was 1.231 ± 0.095mm^2, and 1.100 ± 0.091mm^2 after vessels were removed. In contrast to RNFL thickness measures, the global, quadrant and sector RNFL areas did not vary with dioptric power changes at the corneal surface (Global RNFL area, slope = 0.0008mm^2/D, p = 0.47, Fig 3-4B). When expressed as a percentage of baseline RNFL area, the rate of change was 0.06 ± 0.06/Diopter. In addition, the relationship between individual rates of change and axial length was not statistically significant (p = 0.727).

DISCUSSION

An accurate and precise analysis of the retinal nerve fiber layer can provide important information on the health of the optic nerve. With significant advances in non-invasive imaging technology, the RNFL can be imaged and quantified at increasingly

higher resolutions, and with improved repeatability using OCT technology. However, as with most ophthalmic imaging systems, the OCT scan path is dependent on the optics of the eye and imaging device.[173] For example, the RNFL circular scan path for most myopic eyes is further from the optic nerve rim margin, compared to an emmetropic or hyperopic eye. These differences in scan location can have a significant impact on the measured RNFL thickness that decreases with increasing distance from the rim margin.[156,157] Several studies in both adults and children have reported a relationship between refractive error and RNFL thickness (0.9 to 1.6 μm/D).[134,153,155,270] Similarly, for standard RNFL scans, thickness measures decrease with increasing axial length (-2 to -3 μm/mm).[134,151,153-155] As there is a strong relationship between axial length and refractive error, it is not surprising that these slopes are similar when converted using a 1 mm axial length to 3D refractive error ratio determined by schematic eye calculations.[179]

As the change in RNFL thickness for eyes with moderate ametropia is linearly related to axial length,[134,151,153-155] and the distance from the rim margin, thickness measures can be rescaled to match those of an emmetropic eye. Specifically, several investigators[151,153,154] have used a modified Littmann's formula[174] that incorporates a magnification factor of the eye to make this correction. However, these formulas only take into account the axial length of the eye with the assumption that the inter-individual variations in optics of the anterior segment have a minimal effect on the eyes principal points. Along with an increasing prevalence of myopia,[280] advances in both refractive[281-283] and cataract[284] surgery necessitate investigation of anterior segment power and its effect on ocular magnification and *in vivo* imaging. In addition, the equivalent power of the eye as determined by the cornea, crystalline lens, and the separation of the two structures,[179] is age dependent with possible implications on age related changes in the RNFL.[184,285-287]

Recently, using contact lenses, the effects of changes in anterior segment optics on RNFL thickness has been investigated with time domain[276] and spectral domain[277] OCT. Whereas a significant relationship was not found with the time domain system, the RNFL thickness was linearly related to contact lens induced refractive error (0.5 μm/D) when a spectral domain instrument was used. The discrepancy between the two studies is probably a result of differences in; 1) controlling for accommodative effects, and 2) the axial resolution and segmentation algorithms used by the two imaging systems.[288,289]

The present study used a custom segmentation algorithm[63,224] to investigate the relationship between contact lens associated anterior segment power changes and RNFL thickness, with and without compensation for major retinal vasculature. In general, the relationship between global RNFL thickness and dioptric power change at the cornea (-0.52μm/D) followed similar trends to those previously reported by Lee et al.[277] The major retinal vascular contribution for scans at baseline was 11.5±1.6%, and similar to those previously reported (Mardin CY, et al. IOVS 2009;50:ARVO E-abstract 3333).[63,167] Subtraction of this non-neuronal component did not significant affect the relationship of the RNFL thickness with anterior segment power (-0.46 μm/D). Although not clinically significant, the decrease in the vascular thickness contribution with increase in power should be considered as imaging technology continues to improve and compensation for non-neuronal factors becomes standard in RNFL analysis.

The outcomes of the present study provide evidence that the relationship between RNFL thickness and contact lens power is a direct result of changes in ocular magnification. As illustrated by the registered scan paths used for RNFL B-scans interpolation (Fig 3-3), the scan circumference got larger with an increase in contact lens power. The accuracy of the image registration process and subsequent scan path location was validated by the agreement and repeatability of RNFL thickness measures

from the interpolated and corresponding standard circular scans (Mean difference = -0.15μm, S_w = 0.41 μm). In general, the repeatability was better than that determined for the test retest without contact lenses (Mean difference = 0.31μm, S_w = 1.19μm). Hence, these data reiterate the importance for an accurate, in registration scan placement for follow up scans,[141,142] which was not the case for RNFL scans acquired without contact lenses. The present findings are also in agreement with test retest RNFL thickness data from normal and glaucoma eyes that show improved repeatability with image registration compared to using the customary, well-centered scans.[145]

When RNFL thickness data were expressed as a percentage of the baseline, there were significant inter-individual differences in the rate of change. Specifically, longer eyes had larger percentage deviations in RNFL thickness across the contact lens powers. This finding was supported by corresponding differences in individual rates of change for the retinal region scanned as determined by image registration. In principle, these results are in agreement with differences in image size for model eyes of varying axial length and refractive error, as imaged with a time domain system.[173] Hence, the percentage change formulas (Eq. 2 & 3) can be used to compare intra-individual RNFL thickness measures associated with changes in dioptric power at the corneal surface. However, the formulas generated by the present data included a narrow range of axial lengths, limited by the inclusion criteria of the study. In addition, the formulas cannot be applied for optical power changes at locations other than the anterior corneal surface, such as with cataract surgery.

An accurate measure of the scan circumference can provide useful information when comparing thickness measures between individuals or to a normative database. For this study, individualized three surface schematic eyes were used to calculate the transverse scaling and scan diameter. Overall, this method was accurate at determining

changes in the retinal region imaged as illustrated by the good agreement with the registered SLO fundus images. Although the RNFL thins with increasing distance from the rim margin,[157] the axonal content within the peripapillary region should be relatively similar, as only a small percentage of the RGC population resides in this region. Hence, it is not surprising that the RNFL area, calculated by multiplying thickness measures by the SD OCT scan length, did not show any significant change across the 20 D range of contact lenses used. Subsequently, these RNFL area measures can be used to predict RNFL thickness at predetermined scan diameters. However, the relationship holds true only for a limited distance from the optic nerve. For example, in highly myopic eyes, the scan path can pass through regions with high ganglion cell densities and where RNFL thickness change is not linearly related to the distance from the rim margin. This limitation can be overcome by incorporating ocular biometry, prior to scan capture, and adjusting the scan angle, resulting in a fixed scan diameter at the retinal surface. Whereas these adjustments need to be made prior to scan capture for standard circular scans, they can be made during post-processing in cases where B-scans are interpolated from volumetric raster data.

In conclusion, this study illustrates the use of image registration and retinal scaling in describing the relationship between RNFL thickness and ocular biometry. A three surface schematic eye that includes anterior segment power and axial length can accurately determine scaling and scan dimensions. As imaging technology and RNFL segmentation algorithms improve, it is necessary to incorporate the optical properties of the patient's eye in determining the scan characteristics for thickness/area analysis.

Acknowledgements

The research was supported in part by NIH/NEI grants R01 EY001139, P30 EY007551, T35 EY007088, and K23 EY021761, and by a John and Rebecca Moores Professorship from the University of Houston.

CHAPTER 4

AGREEMENT BETWEEN RETINAL NERVE FIBER LAYER MEASURES FROM SPECTRALIS AND CIRRUS SPECTRAL DOMAIN OPTICAL COHERENCE TOMOGRAPHY

This chapter was accepted for publication in the journal Optometry and Vision Science (OVS) on August 25th, 2011, and published May 2012, 89(5):652-666. It has been included in this dissertation with permission from Wolters Kulwer Health, the publishers of OVS via Copyright Clearance Center (License Number 2886741251882).

The authors that contributed to this work include:

Nimesh B. Patel, OD, Joe L. Wheat, OD, PhD, Aldon Rodriguez, BS, Victoria Tran, BS, Ronald S. Harwerth, OD, PhD

ABSTRACT

Purpose: An assessment of the retinal nerve fiber layer (RNFL) provides important information on the health of the optic nerve. There are several non-invasive technologies, including spectral domain optical coherence tomography (SD OCT), that can be used for *in vivo* imaging and quantification of the RNFL, but often there is disagreement in RNFL thickness between clinical instruments. The purpose of this study was to investigate the influence of scan centration, ocular magnification, and segmentation on the degree of agreement of RNFL thickness measures by two SD OCT instruments.

Methods: RNFL scans were acquired from 45 normal eyes using two commercially available SD OCT systems. Agreement between RNFL thickness measures was determined using each instrument's algorithm for segmentation and a custom algorithm for segmentation. The custom algorithm included ocular biometry measures to compute the transverse scaling for each eye. Major retinal vessels were identified and removed from RNFL measures in 1:1 scaled images. Transverse scaling was also used to compute the RNFL area for each scan.

Results: Instrument-derived global RNFL thickness measured from the two instruments correlated well (R^2 = 0.70, $p<0.01$) but with significant differences between instruments (mean of 6.7 μm; 95% limits of agreement of 16.0 μm to -2.5 μm, intraclass correlation coefficient = 0.62). For recentered scans with custom RNFL segmentation, the mean difference was reduced to 0.1 μm (95% limits of agreement 6.1 to -5.8 μm, intraclass correlation coefficient = 0.92). Global RNFL thickness was related to axial length (R^2 = 0.24, $p<0.01$), whereas global RNFL area measures were not (R^2 = 0.004, $p = 0.66$).

Major retinal vasculature accounted for 11.3±1.6% (Cirrus) or 11.8±1.4% (Spectralis) of the RNFL thickness/area measures.

Conclusion: Sources of disagreement in RNFL measures between SD OCT instruments can be attributed to the location of the scan path and differences in their retinal layer segmentation algorithms. In normal eyes, the major retinal vasculature accounts for a significant percentage of the RNFL and is similar between instruments. With incorporation of an individual's ocular biometry, RNFL area measures are independent of axial length, with either instrument.

INTRODUCTION

During the past two decades, there have been important advances in technology for non-invasive imaging of the eye. These technologies have become standard in the diagnosis and management of ocular pathologies, especially those of the posterior segment. In 1991, with the advent of optical coherence tomography (OCT), it became possible to image retinal layers with about 8 μm resolution.[86] More recent advances, spectral domain optical coherence tomography (SD OCT), have increased image capture speed and resolution (nominally down to 4 μm).[261-263,290,291]

SD OCT technology is an important tool for assessing optic neuropathies.[131,138,292-296] Specifically, the most common assessed structural measure for optic nerve health, is the retinal nerve fiber layer (RNFL), quantified using a standard circular scan 12 degrees in diameter centered on the optic nerve. The analysis of the RNFL thickness is based on a quantification of number of pixels of each A-scan image and a pixel-to-micron calculation across each A-scan in the scan path. Thickness measures from each A-scan are often plotted following a path from temporal, superior, nasal, inferior, and back to temporal, and commonly referred to as a TSNIT plot. These measures are further quantified as average thickness measures for the entire B-scan, TSNIT plot, and/or sector-based averages. However, several factors including scan quality, scan centration, and the specific segmentation algorithm are known to influence thickness measures derived from SD OCT images.[139-141] In general, for each instrument, the *in vivo* RNFL thickness measures are reliable with good repeatability in both normal and diseased eyes.[132,133,135,145,297] In addition, significant changes in RNFL can be detected when the TSNIT average changes by 4 to 8 μm, dependent on the specific technology and instrument used.[135,188,266]

With increasing clinical utility, several commercially available SD OCT instruments have become available. In theory, the thickness measures quantified from well-centered scans of similar dimensions should be identical across instruments. However, both total retinal thickness measures and RNFL thickness measures are significantly different between instruments and cannot be used interchangeably.[61,185,186] To efficiently monitor patients, it is essential that thickness data from current and future instruments be compatible and comparable, especially in monitoring chronic conditions such as glaucoma. The purpose of this study was to investigate factors including scan centration, scan path and segmentation on the discrepancy between RNFL thickness measures between SD OCT systems.

Across SD OCT instruments, there are two strategies for acquiring B-scans for RNFL analysis. The more common methodology involves sampling from a circular scan path centered on the optic nerve. Alternatively, with scan speeds achieved by most SD OCT technology, volumetric data centered on the optic nerve head can be acquired and circular scan data interpolated to produce OCT B-scans that correspond to a 12 degree diameter circular scan path.[141,143,224,298] The two methodologies produce TSNIT measures and either can be used with real-time or offline image registration for signal averaging to improve signal-to-noise ratios for improved retinal layer segmentation. For example, the Cirrus HD OCT (Carl Zeiss Meditec, Dublin, CA) interpolates scans from volumetric data centered on the optic nerve, whereas the Spectralis SD OCT (Heidelberg Engineering, Heidelberg, Germany) uses a circular scan path to capture RNFL B-scans. Although RNFL thickness measures from both techniques are correlated, significant differences have been reported for global and quadrant thicknesses.[61,297] The most notable difference comparing these two techniques has

been in the nasal quadrant for which the agreement has a significant linear relationship (slope = 0.7, intercept = -42.13 μm).[297]

In addition to the technology of image acquisition, other factors such as axial length, size and shape of the optic nerve head, age, and non-neuronal content should be considered in evaluating global (average) or quadrant measures of RNFL thickness.[134,154,155,224,299] Specifically, RNFL thickness measures are thinner in eyes that are older, longer, and have a smaller optic nerve size. It is well established that RNFL thickness changes that occur with age are a reflection of the associated loss of retinal ganglion cells, corresponding to between 0.3 and 0.6% loss/yr.[136,271-273,300] The relationship of RNFL thickness and axial length has been attributed to ocular magnification, and the location of the scan path and, after compensation for ocular magnification, cross-sectional area measures of the RNFL are not related to axial length.[154,224,275,301] Both histological and *in vivo* studies in human and non-primates suggest a relationship between optic nerve head size and total axonal content within the optic nerve.[156,162,302] The RNFL also has significant non-neuronal components, including glial and vascular tissue (Mardin CY, et al. IOVS 2009;50:ARVO E-abstract 3333).[167,168] In addition, with glaucomatous disease progression, an increase in glial tissue and decrease in vascular components have been noted (Wheat JL, et al. IOVS 2009;50:ARVO E-abstract 5826).[169,171,303] Thus, there are many biometric and biological factors that need to be included in assessing OCT measurements of RNFL thickness, especially for management of clinical patients.

As OCT technology evolves, for RNFL measures to be used as a diagnostic tool in optic neuropathy diagnosis and management, it is essential that measures can be compared across instruments. This is especially true for chronic conditions such as glaucoma where both neuronal and non-neuronal changes take place over several

years. The present investigation was undertaken to address these discrepancies by comparing RNFL thickness measures acquired using two SD OCT instruments that use different methodologies to capture the 12 degree circular TSNIT scan. The influence of segmentation, ocular biometry, and the major retinal vessel content to RNFL thickness measures using both technologies was investigated. Some of the results of these studies have been presented briefly elsewhere (Patel NB, et al. IOVS 2011; 52: ARVO E-abstract 173).

METHODS

Subjects

Fifty healthy subjects, aged 21-68 years, with no prior history of ocular pathology were recruited for this study. All subjects were patients, students, or staff at the University of Houston, University Eye Institute. The study adhered to the tenets of the Declaration of Helsinki, and all aspects of the study were reviewed by the committee for protection of human subjects at the University of Houston. Informed consent was obtained from all subjects.

Before enrollment, subjects were screened using visual acuity, standard automated perimetry 24-2 visual fields, intraocular pressure measures, slit lamp examination and dilated fundus evaluation to ensure good ocular health. One randomly selected eye from each subject was used for data analysis. Of these, five eyes that had either undocumented pathology or excessive eye movements during SD OCT scanning were excluded from data analysis.

Optical Coherence Tomography

SD OCT scans were acquired from subjects at least 30 minutes after pupils were dilated with 1% tropicamide and 2.5% phenylephrine. Three scan patterns/protocols were used to acquire high-resolution scans using the Spectralis HRA+OCT (Heidelberg Engineering, Heidelberg, Germany, Software version 5.1.3) that included (1) 12 radial scans centered on the optic nerve head, (2) a 12 degree circular scan centered on the optic nerve head, and (3) a 49 line raster scan, 20X20 degrees centered on the fovea. For noise reduction, B-scan averaging was set at 16 frames for all scan protocols. Scans were repeated if image overlap was noted as frames were being averaged or if the scan had excessive noise, determined as an image quality of < 20 dB (signal to noise ratio). A maximum of three attempts were made to obtain good scans when needed. The unaltered scan data were exported in raw (.vol) files, for analysis using custom MATLAB (The Mathworks, Natwick, MA) programs.

Two scan protocols using the Cirrus HD OCT (Carl Zeiss Meditec Inc., Software version 5.0.0) scans were acquired on all subjects; (1) the high-resolution macular cube scan centered on the fovea, and (2) 200 X 200 A-scans centered on the optic nerve. Scans were repeated if motion was detectable on the *en face* reflectance image or when the scan quality was < 8/10. A maximum of three attempts were made to obtain good scans when needed. The scan data were exported as raw (.dat,.bin,.img,.txt) files using the Carl Zeiss Meditec, Research Browser (version 5.0.0.326).

Ocular Biometry and Scaling

Axial lengths, corneal curvatures, and anterior chamber depths were measured using the IOL Master (Carl Zeiss Meditec). Transverse scaling for each eye was computed using a three-surface schematic eye, using methods described by Bennett

and Rabbetts.[174,175,179] Lens parameters including lens thickness and curvature were interpolated from normative data.[184] Refractive indices for the ocular components were calculated for a wavelength of 855 nm, corresponding to the mean of the central wavelengths for the Cirrus (840 nm) and Spectralis (870 nm) OCT sources.[278,304] The constructed schematic eyes were used to compute the transverse scaling at the retina assuming a spherical retina as previously described.[224] Transverse scaling was used to compute the circumference of the scan path, which was then used to compute the RNFL estimated integral or area.[224,275]

Instrument Algorithm Based RNFL Analysis

The raw data exports from the Cirrus and Spectralis SD OCT RNFL scans were used to determine the global, quadrant, and sector thickness data. The 30 degree sector was centered on the temporal quadrant and subsequent sectors were numbered in a clockwise manner referenced to the OD (Fig. 4-4D). The influence of scan centration was investigated using the raw export data from the Cirrus HD OCT that contained RNFL segmentation data for the entire 200 X 200 A-scan region. To investigate the influence of scan alignment using Cirrus HD-OCT data, custom MATLAB programs were used to interpolate RNFL thickness profiles for scans displaced up to 500 μm from the center of the nerve. The mean change in global RNFL thickness from these interpolations for all subjects in this study is illustrated in figure 4-1 and follows systematic trends previously noted.[140-142]

To evaluate the influence of scan path differences on sector and global thickness differences, RNFL scans with identical locations were compared. This was achieved by aligning the two scans and interpolating RNFL scans from the RNFL thickness map from the Cirrus data that were identical to that of the Spectralis RNFL scan path. The Cirrus

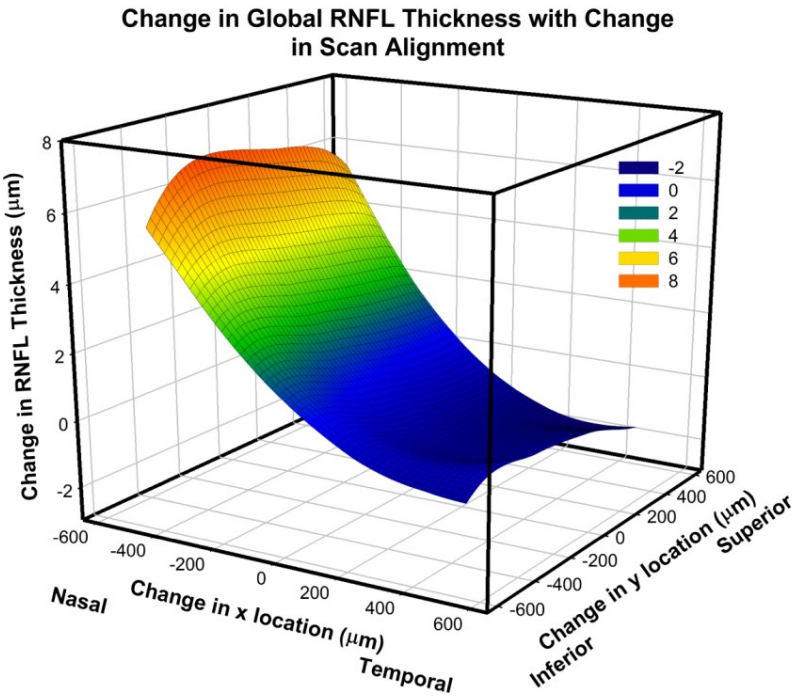

Figure 4-1. The effect of scan misalignment on RNFL thickness.

The contour map represents the average change in RNFL thickness for 54 eyes, all referenced to the right eye and the center of the optic nerve. Global RNFL thickness can vary by 14.8 ± 5.3 µm within 1 mm of the center of the scan, median = 14.6 µm, range = 5.7 µm - 29.0 µm.

fundus image used for registration was constructed from the volume data where the pixel intensity for each A-scan from the 200 X 200 scanned region was averaged to create a 2-D image (Fig 4-2B). This reflectance image was registered to the infrared scanning laser ophthalmoscope (SLO) image from the Spectralis scan using a generalized dual bootstrap iterative closest point algorithm (i2k retina, DualAlign LLC, Clifton, NY).[238] The scan path, extracted from the Spectralis raw data export, was mirrored on the Cirrus reflectance image and used to determine the RNFL thickness as quantified by the instrument's algorithm (Fig. 4-2E). In addition, the aligned images were used to determine the differences in ocular magnification, which was calculated as the square root of pixel content ratio between the two fundus images, assuming a scan angle of 30 degrees for the Spectralis and 20 degrees for the Cirrus (Eq. 4-1).

Equation 4-1.

$$\text{Difference in Ocular Magnification} = \frac{\sqrt{\text{Number of Pixels Spectralis SLO}}}{\sqrt{\text{Number of Pixels Cirrus Reflectance Image}}} \times \frac{20}{30}$$

Custom RNFL Torsional Alignment

All SD OCT instruments have chin and forehead rests, which allow horizontal and vertical eye alignment but not torsional alignment. Previous studies have shown that significant cyclotorsional eye movements occur during fixation, especially with reduced visual stimuli as occurs during OCT imaging.[305,306] Torsional eye movements can influence quadrant and sector RNFL thickness measures and identification of thinning, especially with respect to the normative TSNIT plot. Although the Spectralis software aligns RNFL scans to the macula, it is highly dependent on (1) accurate centration of the scan and (2) accurate fixation by the patient when scan acquisition and averaging is started. Hence, alignment using anatomical landmarks may provide for

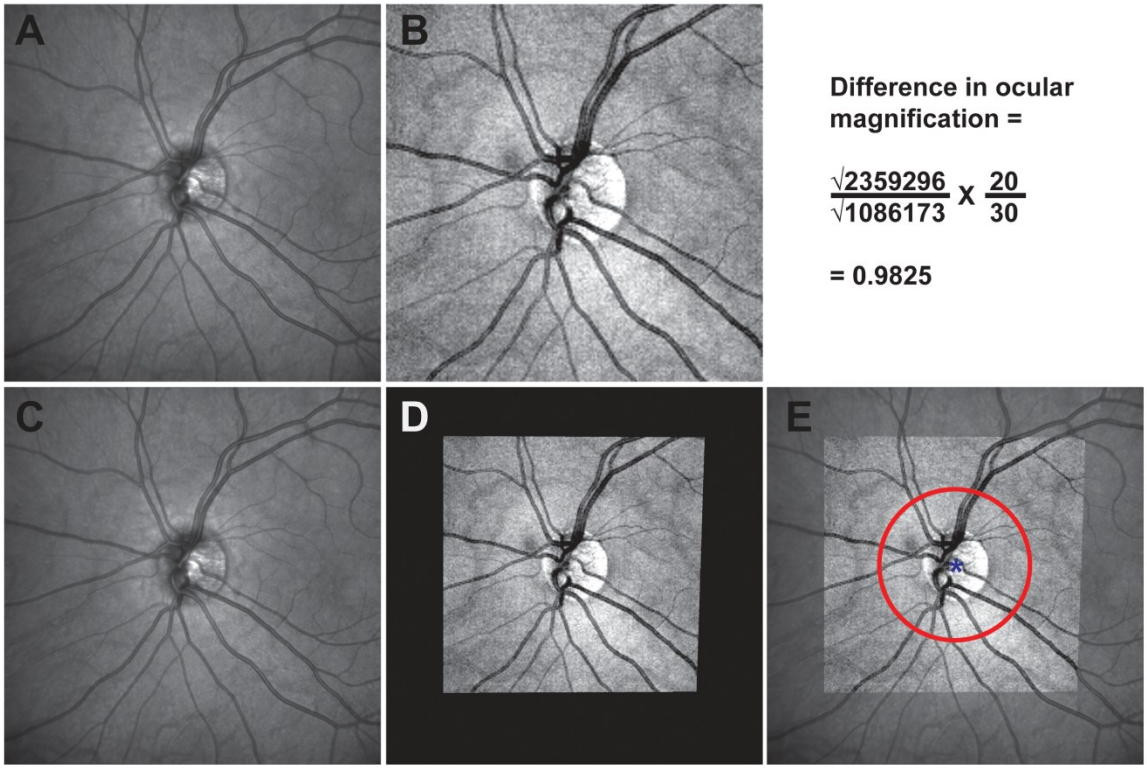

Figure 4-2. Registration methods for Spectralis and Cirrus scan paths.

The 30 degree SLO image from the Spectralis HRA+OCT(panel A) and the mean reflectance image from the Cirrus HD OCT volume scan centered on the optic nerve (panel B) were aligned (panels C & D) and registered (panel E) to provide identical scan paths for 12 degree circular scans with each instrument. The difference calculation for ocular magnification for this data set is illustrated above figure E.

better repeatability. Torsional eye position was compensated for by aligning the center of the optic nerve to the foveal pit for each subject. The center of the fovea was identified as the thinnest region within the raster scan of the macular region. This center was refined by fitting the thickness profile of the pit region with best fit circles from 30 to 75% of the pit height and using the geometric mean of these as the refined pit center (Patel NB, et al. IOVS 2009;50:ARVO E-abstract 6207). The neural canal opening was manually identified using radial scans through the optic nerve. The neural canal opening was fit with an ellipse, which was used to determine the center of the optic nerve.[98,224] The SLO images for the scans centered on the optic nerve and on the macula were registered using the i2k Retina software. All RNFL scans were subsequently referenced to the line fit between the centers of the fovea and optic nerve as illustrated in figure 4-3.

Custom RNFL Segmentation

The standard Cirrus 12 degree circular scan used for RNFL thickness analysis consist of 512 A-scans interpolated from a 200 X 200 A-scan volume, spanning a nominal region of 20 X 20 degrees. In contrast, the Spectralis, high-resolution 12 degree circular scan, consists of 1536 A-scans acquired in a circular path. In addition, the scan depth of the Cirrus is up to 2 mm, whereas the maximum depth for Spectralis images is 1.92 mm. To match the scans, using the image registered data, the Cirrus volume scans were interpolated to obtain 1536 A-scans and cropped to a maximum height measuring 1.92 mm to match the same locations obtained for Spectralis circular scans.

A custom MATLAB program identified the inner limiting membrane and junction between the RNFL and ganglion cell layer. To enhance layer visibility, images were first de-noised using a Haar 2-D stationary wavelet and convolved with a Gaussian filter with

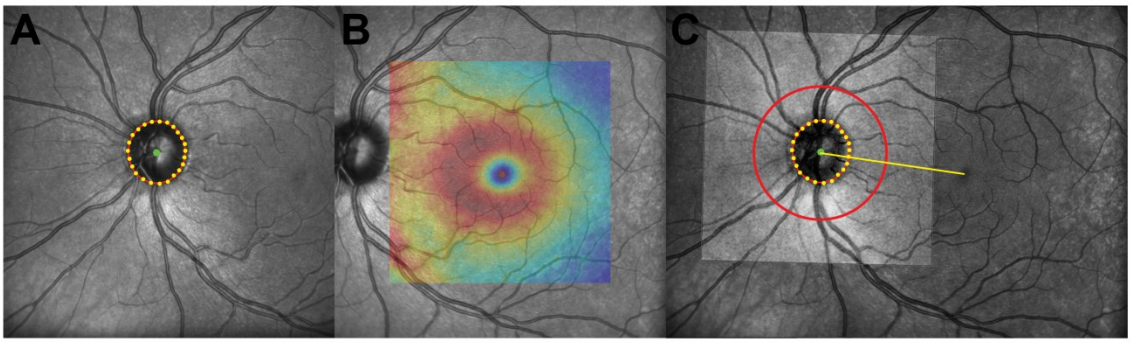

Figure 4-3. Procedures to align scans to a line from the ONH to the fovea.

Procedures to correct the SD OCT images for torsional eye movements by identifying a reference line connecting the center of the ONH to the center of the fovea pit. A. First locations of the opening of the neural canal (NCO) were identified on 12 radial B-scans through the optic nerve and were transferred onto the infrared scanning laser ophthalmoscope (SLO) image, and fit with an ellipse. B. Second, the center of the fovea pit was identified in the retina thickness map as the region with the thinnest retina (darkest blue color) and geometric center of the pit was identified from the geometric center of a series of iso-thickness circles best fit to the pit thickness at varying heights. C. An example of the registered foveal and optic nerve SLO images illustrating the line through the NCO and foveal pit center that was used as reference for torsional alignment of the retinal images.

a SD of 4. Signal intensity profiles for each A-scan were then used to identify the RNFL, as previously described.[224] Errors in segmentation, that were most common around retinal vessels, were corrected manually. To reduce bias, a total of four RNFL scans from the Cirrus, with different scan centers, were segmented and analyzed by the user who was unaware of which scan was from the registered scan path.

The RNFL B-scan from the Spectralis is an averaged image for up to 16 B-scans. The time taken to capture these scans often spans several diastolic and systolic phases. If retinal vessels change significantly in size during these phases, the non-neuronal retinal vessel content within the RNFL would be different between averaged and non-averaged scans. To account for the retinal vasculature, B-scans were first scaled to a 1:1 aspect ratio using the computed transverse scaling from the three-surface schematic eye. The borders of the shadows cast by the retinal vasculature were identified and marked. The center of each vessel within the retinal tissue was then manually identified. The thickness of the RNFL within the circular region marked by the vessel center and shadow borders was subtracted from the total thickness and determined as the RNFL vascular contribution (Fig. 4-4). The RNFL area for each A-scan was computed as the RNFL thickness multiplied by its width. The average RNFL thickness and sum of RNFL areas, with and without retinal vasculature, for the 1536 A-scans were used for data analysis.

Statistical Analysis

Measurement bias and variability for RNFL thickness for global and quadrant measures were investigated using mean versus difference plots (Bland-Altman).[307,308] Although RNFL thickness measures from separate OCT systems correspond well, there are significant differences between the measures. For example, the slope and intercept

for linear functions fit to registered TD and SD OCT systems are dependent on the region/sector of the RNFL being compared.[143] Similar results have been reported for RNFL thickness measures from separate SD OCT systems.[61,62] These findings can be attributed to differences in 1) instrument segmentation algorithms, and 2) individual variability in ocular anatomy. Specifically, scan centration,[141,142] signal strength[140,309] and ocular magnification,[173] need to be taken into account when evaluating RNFL thickness. Hence, to assess RNFL thickness reliability, intraclass correlation coefficients, using a two way mixed model with absolute agreement, was used.[310] In addition, agreement for global, quadrant and sector thickness measures was assessed using paired t-tests.

RESULTS

RNFL Thickness - Instrument Algorithm.

For the 45 eyes included in the data analysis, the average image quality for RNFL scans was 30.6 ± 4.93 dB and 9.0 ± 0.82 for the Spectralis and Cirrus scans, respectively. In general, the high signal strength and quality of the scans decrease the variability in thickness measures resulting from segmentation errors.[140,311] Hence, signal strength was not considered a covariant for comparisons of instrument and custom segmentation. The average RNFL global thickness measurement was 97.9 ± 7.9 μm for the Spectralis and 91.2 ± 8.4 μm for the Cirrus. The agreement of RNFL measures using each of the two instruments was assessed using Bland-Altman plots, the ICC, and paired t-tests. Bland-Altman plots provide a graphical method for comparing the two methodologies. The mean difference, and 95% limits of agreement can be used to assess if the difference between two methodologies are clinically acceptable.[308] ICC measures for comparison of thickness measures were calculated using a two-way mixed, absolute agreement model (SPSS, IBM, Armonk, NY). The ICC is a measure of

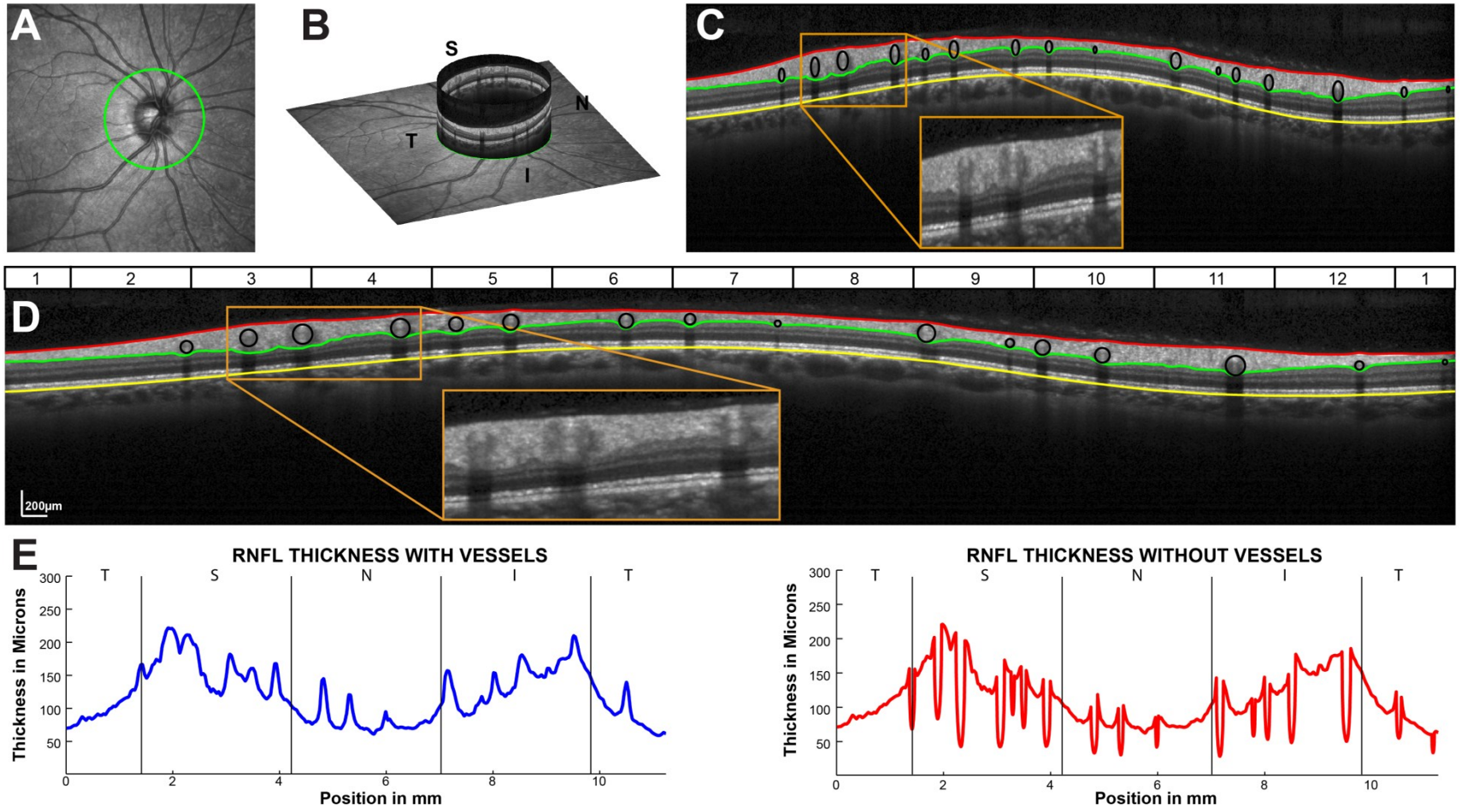
A
B
S
N
T
I
C
1
2
3
4
5
6
7
8
9
10
11
12
1
D
200µm
E
RNFL THICKNESS WITH VESSELS
T
S
N
I
T
Thickness in Microns
300
250
200
150
100
50
0
2
4
6
8
10
Position in mm
RNFL THICKNESS WITHOUT VESSELS
T
S
N
I
T
Thickness in Microns
300
250
200
150
100
50
0
2
4
6
8
10
Position in mm

Figure 4-4. Segmentation methodology with vessel compensation.

The identification and removal of the major vasculature from the RNFL. A&B. An example of the RNFL B-scan image illustrating the locations of vessels. C&D Shadows in RNFL B-scans identify major retinal vessels in B-scan images of Spectralis scans in the unscaled image (C) and after rescaling the B-scans to 1:1 μm (D) where the retinal vessels can be identified as circular structures within the scan. E. RNFL thickness plots demonstrating the effect of removing the vessel contribution to RNFL thickness. It should be noted that only portions of the vessel within the RNFL segmentation were subtracted to create the thickness plot and in subsequent calculations of RNFL and area measures.

reliability, calculated by comparing the between-subject variances to overall variance. In general, agreement is considered good, when the within subject variance is a third of the between-subject variance (ICC ≥0.75).[312] Paired t-tests were also used to test the hypothesis that the difference in RNFL thickness measures from the two instruments is 0.

On the basis of these statistics, there was overall poor agreement of RNFL thickness between the two instruments, with the least agreement for the nasal quadrant (Table 4-1). Similarly, Bland-Altman plots (Fig. 4-5) indicate significant thickness differences in all quadrants, along with a systematic discrepancy for nasal quadrant thicknesses (slope = 0.51, intercept = -27.19, R^2 = 0.34, p <0.01). The mean bias and limits of agreement for each measure are illustrated in the insets in figure 4-5. In addition, the SD of thickness differences for each quadrant, except for the temporal quadrant was at least half the SD for thickness measured from each instrument.

Scan Alignment

Various methods are used to center the RNFL scan on the optic nerve. For example, the Spectralis relies on the user to visually center the scan on the optic nerve. A circular guide, the size of an average optic nerve, is projected on the real time SLO image to aid in centering. In addition, when an internal nasal fixation target is used, the scan is referenced to the center of the optic nerve and fixation. Alternatively, the Cirrus obtains a 200 X 200 volume scan of the optic nerve and an automated process is used to determine the geometric center of the optic nerve head after the rim margin has been identified. The RNFL scan is interpolated from the volumetric data at a fixed distance from the center of the optic nerve head. These volumetric data can also be used to investigate the effect of scan alignment, which for the eyes included in this study,

	Cirrus		Spectralis			95% confidence intervals		Paired t-test
	Mean (µm)	Std Dev	Mean (µm)	Std Dev	ICC	Lower	Upper	
Global	91.17	8.42	97.92	7.94	0.623	0.456	0.797	<0.001
Temporal	63.71	12.96	72.79	12.71	0.765	-0.074	0.864	<0.001
Superior	115.03	14.94	118.52	12.98	0.734	-0.054	0.938	0.022
Nasal	65.89	10.06	74.56	15.88	0.559	0.552	0.847	<0.001
Inferior	120.08	16.39	125.21	15.21	0.764	0.119	0.78	0.001
Sector 1	49.57	8.7	58.81	10.87	0.631	0.544	0.876	<0.001
Sector 2	77.15	19.18	85.73	17.53	0.853	-0.071	0.887	<0.001
Sector 3	125.78	21.95	134.4	23.92	0.78	0.068	0.957	<0.001
Sector 4	114.12	24.88	112.97	22.18	0.797	0.491	0.895	0.613
Sector 5	105.17	16.77	108.18	18.31	0.794	0.658	0.883	0.075
Sector 6	80.23	17.45	90.59	23.26	0.743	0.653	0.882	<0.001
Sector 7	55.31	9.79	62.95	15.5	0.414	0.256	0.893	<0.001
Sector 8	62.12	10.6	70.13	16.12	0.571	0.11	0.64	<0.001
Sector 9	95.75	18.21	99.21	18	0.701	0.182	0.776	0.1
Sector 10	134.94	26.79	137.62	27.59	0.801	0.517	0.824	0.301
Sector 11	129.53	26.72	138.45	25.62	0.885	0.666	0.885	<0.001
Sector 12	64.4	15.79	73.37	15.84	0.759	0.465	0.959	<0.001

Table 4-1. Instrument algorithm RNFL thickness measures.

Instrument algorithm RNFL thickness measures for quadrant and clock hours for Cirrus and Spectralis SD OCT. Along with the paired t-test statistic, the intraclass correlation coefficient (ICC) with 95% confidence intervals provides a measure of agreement for the two segmentation algorithms.

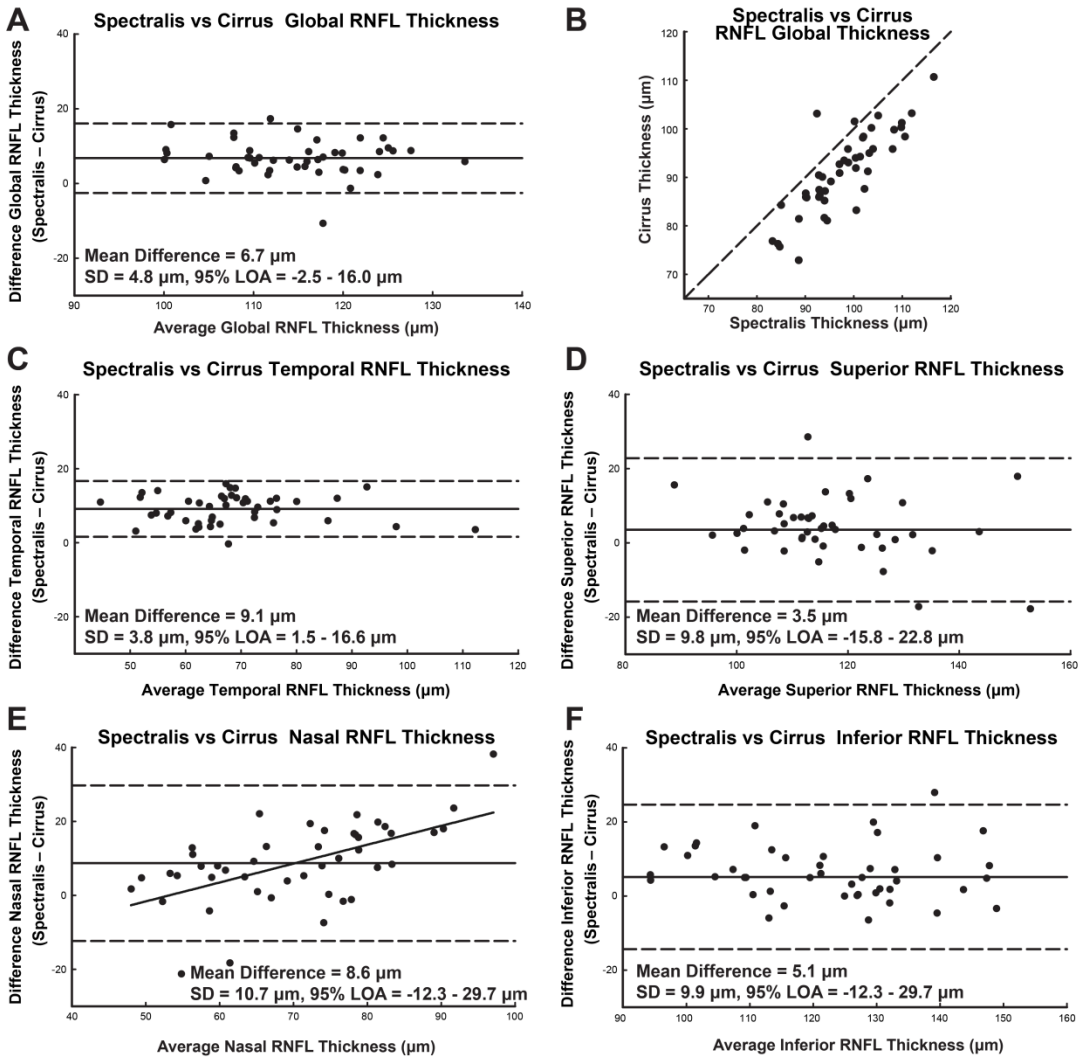

Figure 4-5. Agreement between instrument segmentation RNFL thickness for Spectralis SD OCT and Cirrus HD OCT.

The limits of agreement determined by the 95% confidence interval of the mean for RNFL thickness by Spectralis and Cirrus SD OCT instruments, using the manufacturer's thickness algorithms. A. The Bland-Altman plot for the agreement between global thickness measurements. B. Thickness measures from the two instruments and their deviation from the 1:1 line. C-E. Bland-Altman plots to illustrate the limits of agreement for each quadrant, demonstrating that the relationship between the thickness difference

and average thickness is not statistically significant, except the nasal quadrant (E, slope = 0.51, intercept = -27.19, R^2 = 0.34, $p < 0.01$).

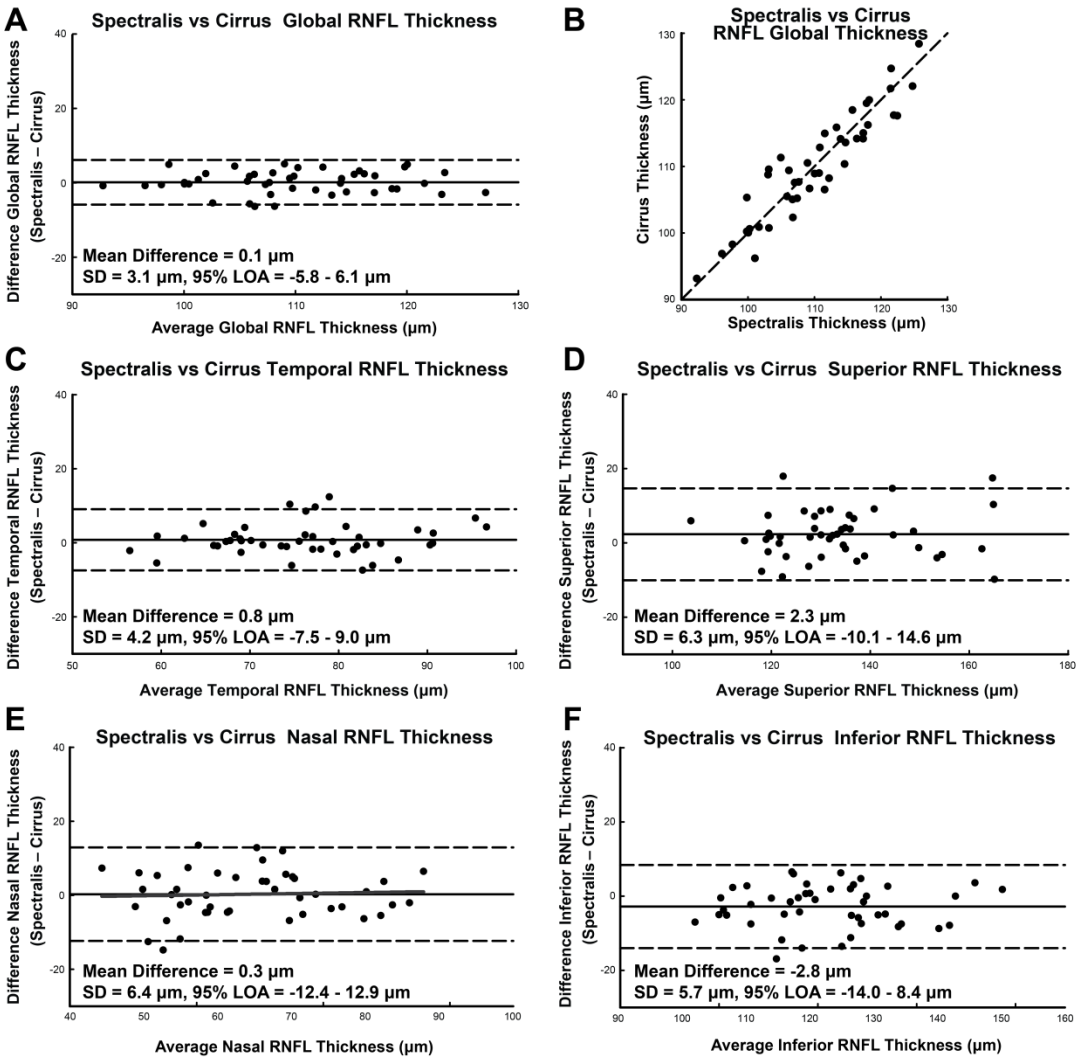

Figure 4-6. Agreement between custom segmentation RNFL thickness for Spectralis SD OCT and Cirrus HD OCT.

The limits of agreement between RNFL thickness by Spectralis and Cirrus SD OCT instruments, using custom algorithms for scaling, rotation, registration, and segmentation, but without vessel compensation. Other details are as in Fig. 4-5. The Bland-Altman analysis for RNFL thickness via custom image analysis demonstrates well correlated measurements and high ICCs for all quadrants with no statistical relationship between the thickness difference and average thickness. E. For the nasal quadrant, the

difference in thickness measures between instruments did not have a systematic trend (slope = 0.02, intercept = -1.9, $R^2 < 0.01$, p = 0.75).

resulted in an average maximum change in thickness of 14.8 ± 5.3 μm (Fig. 4-1) for misalignments of the scan by up to 500 μm.

The SLO fundus image from the Spectralis and reflectance fundus image from the Cirrus were successfully registered for all the subjects using a generalized dual bootstrap iterative closest point image registration algorithm.[238] The difference in scan center location between the two instruments, using the registered images, was 117.7 ± 70.2 μm. Realignment of the Cirrus scan to match that of the Spectralis had a minimal effect on the thickness differences (Table 4-2). In addition, using the modeled average thickness data from varying scan alignment (Fig. 4-1), the differences in scan location measured was predicted to account for only 0.45 ± 0.4 μm of the thickness differences.

Along with horizontal and vertical misalignments, torsional differences between the fundus images from the two instruments were also evident. The TSNIT thickness plots were shifted according to the average angular difference between the two images. To realize the greatest match, the plots were also shifted to the point with the highest cross correlation. The average rotational difference, using these methods, was 6.4 ± 3.8 degrees. Realignment using all three dimensions improved the ICC for each quadrant (Table 4-2).

Custom Segmentation and Retinal Vascular Contribution

The custom segmentation program consistently measured a larger RNFL thickness for both Spectralis (11.4 ± 3.7 μm) and Cirrus (18.8 ± 3.5 μm) scans compared to the instrument algorithms. In addition, these custom measures were significantly different ($p < 0.01$) for most quadrants and sectors for both instruments. However, the agreement for RNFL thickness measures, as determined by ICC and paired t-test, comparing custom segmentation to the instrument algorithm, was better for Spectralis

scans (Table 4-3). Overall, the agreement between instruments improved with custom segmentation. For the Bland-Altman plot, the SD were (1) less than with the instrument algorithm, (2) less than half the SD for the range of thicknesses for each measure. Good agreement for RNFL measures were also indicated by ICC and t-test statistics. For global RNFL thickness, the mean difference was 0.1 ± 3.1 μm, ICC = 0.96, p= 0.59 (Table 4-5).

The major retinal vasculature accounted for ~11% (11.8 ± 1.5% Cirrus, 11.3 ± 1.6% Spectralis) of the global RNFL thickness (Table 4-4). Superior and inferior quadrants had the greatest major retinal vascular contribution with the temporal quadrant having the least (Table 4-4). Differences for major retinal vascular contribution were insignificant for the segmentations from the two instruments ($p > 0.05$, $\beta < 0.18$ for all quadrants). Although there was very good agreement in vascular contribution, the vascular location in the registered B-scans were not always identical. In addition, some small vessels were clearly visible in one B-scan, but not the other, as illustrated in figure 4-7.

Ocular Biometry and RNFL Area

For the healthy eyes included in this study, axial lengths ranged from 22.3 mm to 27.9 mm and were normally distributed with a mean of 24.7 ± 1.32 mm. The global RNFL thickness, as determined by the instrument algorithm, decreased with increase in axial length, with a slope of -3.1 μm/mm for the Spectralis ($p < 0.01$) and -3.1 μm/mm forthe Cirrus ($p < 0.01$) (Fig. 4-8). Although thickness measures between instruments were significantly different, the slope of the function was not ($p = 0.95$). Similarly, for the custom segmentation data, the slope of RNFL thickness vs. axial length was -3.0 μm/mm ($p < 0.01$, $R^2 = 0.24$, Fig. 4-8B).

	Cirrus					
	Global Thickness (µm)	**Std. Dev.**	**ICC**	**Paired t-test**	**Cross Correlated ICC**	**Paired t-test**
Global	90.83	8.42	0.645	<0.001	0.645	<0.001
Temporal	62.95	11.85	0.721	<0.001	0.837	<0.001
Superior	111.59	13.71	0.794	<0.001	0.886	<0.001
Nasal	66.85	11.03	0.574	<0.001	0.649	<0.001
Inferior	124.26	16.64	0.904	0.054	0.905	0.056

Table 4-2. Average thickness for identical scan paths.

Average thickness and ICC for scans centered to match that of Spectralis 12 degree circular scans.

	CIRRUS				SPECTRALIS			
	Instrument Global Thickness (µm)	Custom Global Thickness (µm)	ICC	Paired t-test	Instrument Global Thickness (µm)	Custom Global Thickness (µm)	ICC	Paired t-test
Global	91 ± 8	110 ± 9	0.227	<0.001	98 ± 8	110 ± 8	0.405	<0.001
Temporal	64 ± 13	76 ± 10	0.515	<0.001	73 ± 13	77 ± 10	0.803	<0.001
Superior	115 ± 15	133 ± 14	0.407	<0.001	119 ± 13	135 ± 15	0.463	<0.001
Nasal	66 ± 10	88 ± 13	0.249	<0.001	75 ± 16	89 ± 14	0.539	<0.001
Inferior	120 ± 16	143 ± 15	0.361	<0.001	125 ± 15	140 ± 15	0.6	<0.001
Sector 1	50 ± 9	59 ± 6	0.303	<0.001	59 ± 11	60 ± 6	0.542	0.52
Sector 2	77 ± 19	83 ± 13	0.588	0.005	86 ± 18	84 ± 12	0.692	0.231
Sector 3	126 ± 22	138 ± 27	0.636	<0.001	134 ± 24	138 ± 29	0.768	0.233
Sector 4	114 ± 25	140 ± 24	0.405	<0.001	113 ± 22	144 ± 21	0.404	<0.001
Sector 5	105 ± 17	119 ± 22	0.54	<0.001	108 ± 18	123 ± 23	0.594	<0.001
Sector 6	80 ± 17	110 ± 24	0.334	<0.001	91 ± 23	112 ± 24	0.57	<0.001
Sector 7	55 ± 10	78 ± 16	0.204	<0.001	63 ± 15	77 ± 15	0.486	<0.001
Sector 8	62 ± 11	77 ± 11	0.304	<0.001	70 ± 16	76 ± 12	0.593	0.001
Sector 9	96 ± 18	111 ± 16	0.469	<0.001	99 ± 18	111 ± 17	0.684	<0.001
Sector 10	135 ± 27	152 ± 25	0.603	<0.001	138 ± 28	147 ± 25	0.836	<0.001
Sector 11	130 ± 27	166 ± 23	0.375	<0.001	138 ± 26	162 ± 21	0.525	<0.001
Sector 12	64 ± 16	84 ± 15	0.42	<0.001	73 ± 16	86 ± 16	0.6	<0.001

Table 4-3. Instrument algorithm vs Custom RNFL thickness measures.

Instrument algorithm vs Custom RNFL thickness measures for quadrant and clock hours for Cirrus and Spectralis SD OCT.

	Spectralis			Cirrus			Paired t-test (p), vascular contribution
	Thickness with vessels (µm)	Thickness without vessels (µm)	% Vascular contribution	Thickness with vessels (µm)	Thickness without vessels (µm)	% Vascular contribution	
Global	110 ± 8	97 ± 7	11.8 ± 1.5	110 ± 8	97 ± 7	11.3 ± 1.6	**0.076**
Temporal	77 ± 10	74 ± 9	4.0 ± 2.5	76 ± 10	73 ± 9	3.8 ± 2.9	**0.617**
Superior	135 ± 15	116 ± 12	14.3 ± 3.0	133 ± 14	115 ± 13	13.4 ± 2.9	**0.054**
Nasal	89 ± 14	80 ± 11	10.0 ± 3.4	88 ± 13	80 ± 11	9.7 ± 3.5	**0.558**
Inferior	140 ± 15	120 ± 14	14.6 ± 2.6	143 ± 15	123 ± 14	14.2 ± 2.4	**0.223**

Table 4-4. Major retinal vascular contribution to RNFL thickness.

Major retinal vascular contribution to RNFL thickness. Vascular contribution to the RNFL is similar for the two instruments as illustrated by the paired t-test statistic.

	Cirrus		Spectralis		95% Confidence Interval			Paired t-test (p)
	Mean (µm)	Std Dev	Mean (µm)	Std Dev	ICC	Lower	Upper	
Global	109.9	8.03	110.16	8.07	0.921	0.861	0.956	0.591
Temporal	75.82	9.58	76.72	10.01	0.902	0.823	0.945	0.591
Superior	132.64	14.34	135.03	14.52	0.893	0.801	0.942	0.165
Nasal	88.33	13.36	88.72	13.6	0.884	0.799	0.935	0.015
Inferior	143.16	14.78	140.49	15.1	0.91	0.816	0.953	0.689
Sector 1	58.96	5.76	59.61	5.54	0.774	0.625	0.869	0.004
Sector 2	83.39	12.66	83.58	12.35	0.885	0.799	0.935	0.258
Sector 3	138.24	27.97	137.62	28.56	0.944	0.901	0.969	0.835
Sector 4	140.44	23.79	144.12	21.01	0.853	0.742	0.917	0.665
Sector 5	119.24	21.79	123.37	23	0.902	0.802	0.949	0.042
Sector 6	109.55	23.97	112.48	23.77	0.861	0.76	0.921	0.004
Sector 7	78.45	15.88	77.15	14.88	0.858	0.757	0.919	0.121
Sector 8	77	11.34	76.55	11.55	0.647	0.438	0.79	0.293
Sector 9	111.67	15.75	111.44	17.35	0.831	0.712	0.904	0.756
Sector 10	151.78	25.38	147.28	24.67	0.942	0.842	0.974	0.874
Sector 11	165.7	22.6	162.48	21.41	0.897	0.813	0.943	<0.001
Sector 12	84.37	14.61	86.24	15.61	0.903	0.828	0.946	0.03

Table 4-5. Custom algorithm RNFL thickness measures.

Custom algorithm RNFL thickness measures for quadrant and clock hours for Cirrus and Spectralis SD OCT. Along with the paired t-test statistic, the intraclass correlation coefficient (ICC) with 95% confidence intervals provides a measure of agreement for the two segmentation algorithms. Thickness measures are before compensation for major retinal vasculature.

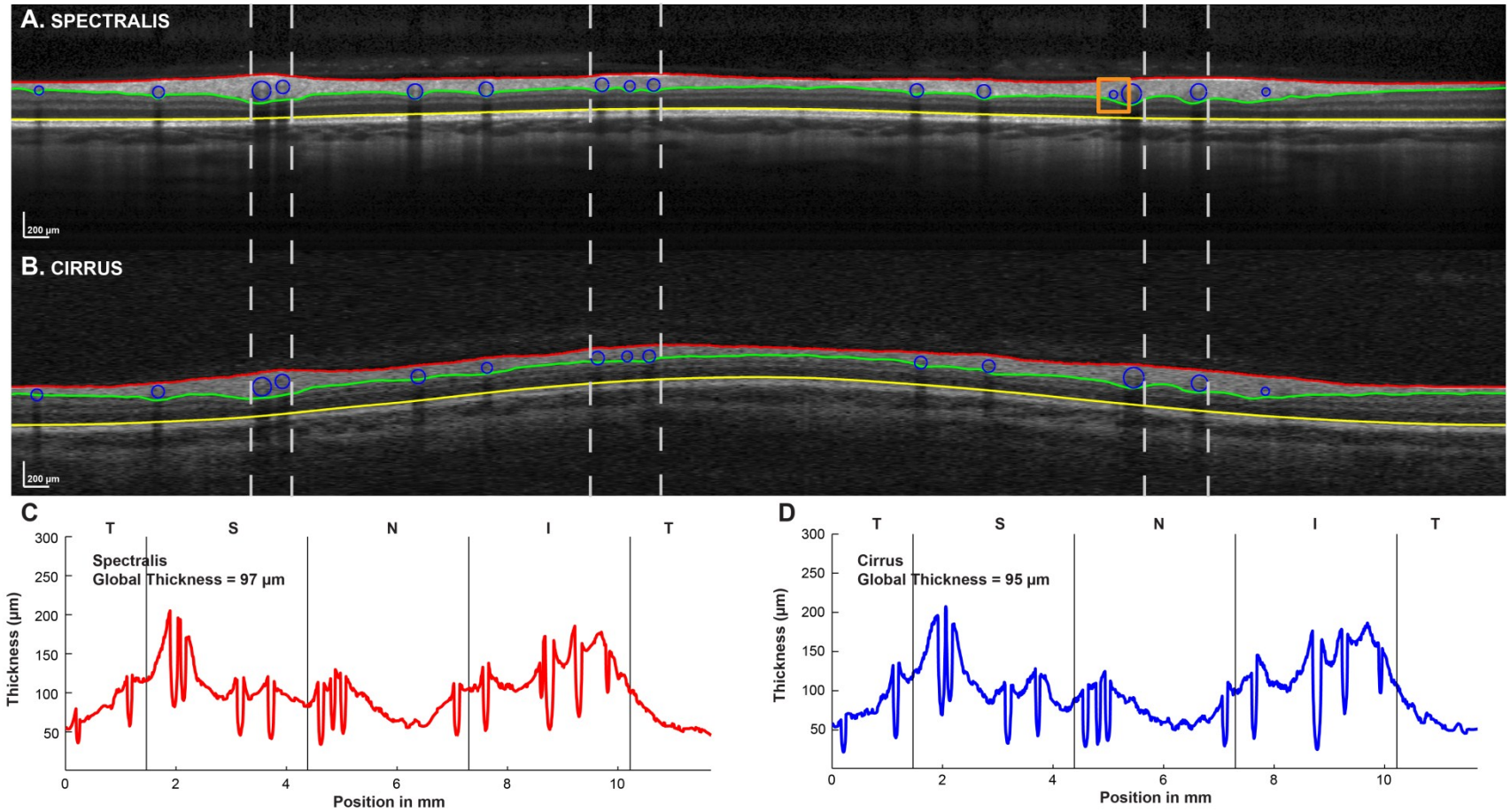
A. SPECTRALIS
200 µm
B. CIRRUS
200 µm
C
T
S
N
I
T
Spectralis
Global Thickness = 97 µm
Thickness (µm)
Position in mm
D
T
S
N
I
T
Cirrus
Global Thickness = 95 µm
Thickness (µm)
Position in mm

Figure 4-7. Differences in B-scans from Spectralis and Cirrus OCT

Examples of TSNIT functions for Spectralis SD OCT and Cirrus HD OCT after incorporating vessel identification and compensation in the B-scans, and with identical scan paths from the two instruments. The B-scans for the Spectralis (A) and Cirrus (B) are presented with white vertical dashed lines illustrating the location of some of the major retinal vessels in the two images. Although the vessels localized well, there were some small misalignments. Overall, a similar number of vessels were identified in both B-scans, but with some smaller vessels being missed in one or the other B-scan occasionally, as illustrated by the orange box in A. The TSNIT plots for both Spectralis (C) and Cirrus (D) instruments show dips at similar locations and nearly equal global thicknesses after compensation for the major retinal vasculature.

A significant relationship between axial length and ocular magnification ratio, as determined using the registered fundus images, would indicate differences in the optics of the two imaging devices ($R^2 = 0.41$, $p < 0.01$, Fig. 4-8C). For the majority of the scans, the region of the retina scanned per degree of scan angle was smaller for Spectralis images and was similar for only significantly longer eyes. However, this difference did not alter the location of the scan paths significantly, as illustrated by the similarity in RNFL thickness at all axial lengths using the custom segmentation (Fig. 4-8B).

The thinner RNFL measures for longer axial lengths should not reflect on a difference in retinal ganglion cell axonal content, but rather illustrates changes in RNFL thickness and density associated with distance from the optic nerve rim margin.[156-158] However, the cross-sectional area of the RNFL should be independent of scan distance from the optic nerve head rim margin within the peripapillary region were a low density of ganglion cells are present.[119] RNFL area measures were computed by multiplying the scan circumference, as determined using the computed transverse scaling, and the global RNFL thickness.[224,275] The RNFL area was not related to axial length (Spectralis: $p = 0.69$, Cirrus: $p = 0.66$) and was similar for the two instrument (Fig. 4-8D).

DISCUSSION

High-resolution imaging of retinal structure has become standard in clinical care and several technologies, including scanning laser polarimetry, confocal SLO, and OCT are available to image and measure structures of the posterior segment of the eye. However, only OCT provides cross-section images of the retina to visualize and quantify the individual retinal layers. Recent advances in this technology, SD OCT, enable imaging of the eye at high speeds with axial resolutions down to 4 μm.

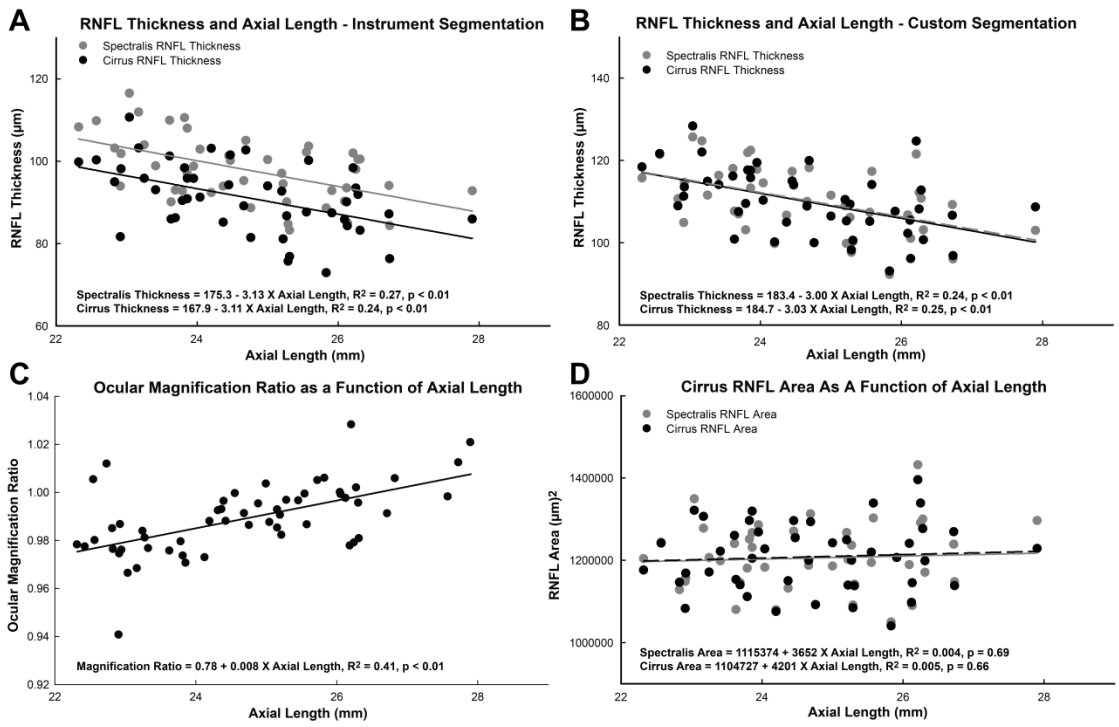

Figure 4-8. RNFL thickness and area as a function of axial length.

Relationships between RNFL measurement parameters and axial length using Spectralis SD OCT and Cirrus HD OCT instruments. A. The relationship between RNFL thickness and axial length was significant for both instruments, with similar slopes for linear regression, but with an approximately constant difference between instruments across the range of axial lengths. B. With custom segmentation, the relationship between thickness and axial length was not significantly different for the two instruments. C. The relationships between the ocular magnification ratio and axial length were significantly different between the two instruments. D. The differences in ocular magnification did not have a significant influence on the RNFL area computations and the RNFL area was not statistically related to axial length.

Although there are several clinical SD OCT instruments which all use similar technology and capture comparable images, clinical studies have shown that the thickness measures of retinal structures are significantly different between instruments.[61,143,187,297] In studies comparing RNFL thickness measures from the Spectralis SD OCT and Cirrus HD OCT, although measures from both instruments were repeatable, a significant difference was reported between instruments.[297] Similar to the present study, a linear relationship was reported for the agreement for the nasal quadrant (slope = 0.70).[297] The principal finding of this investigation is that the underlying sources for the differences in measurements are related to software applications for image segmentation and data analysis procedures, rather than in the data acquisition. Therefore, to detect changes, such as progressive glaucomatous neuropathy, either an identical instrument would need to be used for follow-up or the raw data would need to be analyzed by algorithms that include ocular biometry and identical image segmentation across instruments.

The present investigation was based on the agreement in RNFL thickness between two specific SD OCT instruments, i.e., the Cirrus HD OCT and Spectralis HRA+OCT. The selection of the two SD OCT systems was rooted in the different scanning protocols used to acquire the standard circular B-scan used for RNFL quantification. Although the Spectralis uses a circular scan path, which the user centers on the optic nerve, the Cirrus interpolates the scan from a 200 X 200 A-scan cube centered on the optic nerve. In addition, the Spectralis allows for real time image registration and averaging of B-scans to increase the signal to noise ratio. Thus, although the specific results apply to these clinical instruments, the overall results should be generalized to other SD OCT instruments.

In agreement with previous studies,[61,106,187,297] it was shown that for eyes with no history of optic neuropathy, there were significant differences in the RNFL thickness measures between the Spectralis SD OCT and Cirrus HD OCT systems, using the instrument-based analysis. The 95 % agreement for global thickness was better than that for average quadrant thickness measurements using the instrument image analysis algorithm (Fig. 4-5). However, the limits of agreement for global thickness measures (-2.5-16.0 μm) had a range half that of the total range of thickness measures for either instrument (37.8 μm Cirrus, 33.3 μm Spectralis). In addition, the difference in thickness measures for the nasal quadrant was related to the average thickness measures of the two instruments. However, the mean difference in thickness measures for the global and quadrant thicknesses were different from previously reported results.[61,106,187] The differences could be a reflection on differences in subjects or in the instrument software versions. For example, previous studies have investigated both normal and glaucoma subjects, but only healthy eyes were included in the present study. In addition, both instruments have undergone several software upgrades from the previous studies. However, the more important sources of discrepancy in thickness measures were scan alignment, ocular magnification, and segmentation. The influence of scan alignment and centration has been investigated using both time-domain and SD OCT systems.[141-143] The general finding of these studies is that a misalignment of the scan, in either the horizontal and vertical direction has a significant impact on both the shape of the TSNIT thickness plots and global RNFL thickness measures. A similar pattern, with up to 14 μm of global RNFL thickness change, was noted when the center of the RNFL scan was displaced for the Cirrus data (Fig. 4-1). However, centering the Cirrus scan to match that of the Spectralis had only a small increase in agreement of global RNFL thickness (Table 4-2).

The relatively small improvement in agreement between instruments with only adjustment for scan centration can be explained by differences in torsional eye position during scanning movements of the eyes. Specifically, although a head tilt does not change global thickness, it has a significant effect on the shape of the TSNIT plot.[144] This redistribution of thickness along the TSNIT plot results in significant differences in both sector and quadrant thicknesses and associated changes in the thickness distribution with respect to normative data. By taking into account torsional eye alignment differences, and their influence on the scan path, there were substantial improvements in the agreement of quadrant thickness measures for the two instruments (Table 4-2), although, the thickness measures from the two instruments were still significantly different. Although referencing RNFL scans to the center of the optic nerve and the internal fixation target, as is done with Spectralis RNFL scans, improves alignment, detection of these landmarks using anatomical features may be useful in individuals with poor fixation.

It is logical that although there can be slight differences in the characteristics of the various OCT instruments, the images from these systems should be similar, with comparable RNFL thickness.[313,314] This result was demonstrated by the significant improvement in instrument agreement for RNFL thicknesses with B-scans that were registered, aligned to the fovea, and analyzed by the same segmentation protocol (Fig. 4-6, Table 4-5). The Bland-Altman plots illustrated a smaller SD for all quadrants, compared with instrument analysis. The largest SD was in the nasal quadrant, which also had the greatest improvement in thickness agreement and had the largest number of segmentation errors requiring manual correction. The failure of the program to accurately segment this region is probably due to the reduced signal in the nasal quadrant that is attributable to the characteristics of the optical scan angle.[315] Overall,

the custom segmentation results in larger RNFL thickness measures compared to either instrument algorithm. This increased thickness can be attributed to the method by which the algorithm dealt with retinal vasculature. Although most instrument algorithms tend to "skip" across retinal vessels, the custom algorithm outlines each vessel that contributes to the RNFL and has no smoothing artifact (Figs. 4-4 and 4-7). Hence, agreement between custom and instrument segmentation was greatest for the temporal quadrant which also had the smallest contribution from major retinal vasculature.

For an accurate assessment of the axonal content within the RNFL, the non-neuronal content within the layers should be excluded. Although glial tissue cannot be visualized using current technology, the major retinal vasculature cast shadows within the B-scan, and can be accounted for (Mardin CY, et al. IOVS 2009;50:ARVO E-abstract 3333).[167] After the SD OCT scans had been rescaled to a 1:1 aspect ratio, the custom algorithm allowed the user to manually select the center of each vessel identified, and subtract the vessel area from the scan image.[224] Using this technique, major retinal vasculature contribution to RNFL thickness in healthy eyes was ~11% and similar for the two instruments (Table 4-2). These measures were in agreement with those reported by Mardin et al. (11%), but are slightly less than reported by Hood et al. (13%).[167] The vascular contribution is actually larger than that reported in this study, because there were instances where vessels were noted in the B-scan of one instrument but not in the other (Fig. 4-7), and small vessels and capillaries cannot be visualized and excluded.[316,317]

An additional factor that is necessary to consider when analyzing the RNFL thickness is ocular biometry. Specifically, the thickness of the RNFL measured using the traditional 12 degree circular scan is a function of axial length.[134,157,224] This relationship with axial length was similar for both instrument- and custom segmentation for both

systems (Fig. 4-8), which is a direct reflection of the projection of the scan path in relationship to the optic nerve rim margin for different sized eyes. Although the RNFL thickness decreases as the scan path increases in distance from the rim margin, the thickness change is related to retinal ganglion cell axon density rather than the number of axons within the region.[119,157,224] It is then logical that the area of the RNFL within the scanned region, which reflects the axonal content, is poorly correlated with axial length (Fig. 4-8). Similarly, an alternative method to compensate for thickness changes with scan distance from the nerve is to rescale RNFL thickness measures using axial length as illustrated by Kang et al.[154]

Both RNFL area and rescaling of RNFL thickness computations require consideration of the optics of the eye and instrument being used.[173-175,318] Although biometry of the eye is measured efficiently and accurately using non-contact low coherence reflectometry, the optical properties of the scanning laser devices are proprietary and usually unknown to the clinician or researcher. The influence of instrument optics on ocular magnification can be investigated for the same eye imaged using both instruments with image registration (Fig. 4-2). Using these methods, a significant difference in ocular magnification, related to axial length was noted for the Cirrus and Spectralis SD OCT systems (Fig. 4-8C). However, these differences were not large enough to cause any appreciable divergence in the scan path, as noted by the similarity in thickness and area measures for varying axial lengths (Fig. 4-8).

In conclusion, the results of these investigations have demonstrated the utility of methods for comparing measurements of retinal morphology across SD OCT instruments. Specifically, images captured using two different SD OCT instruments (Cirrus and Spectralis) were shown to be similar when similar image processing methods were used. The apparent differences in RNFL thickness with the embedded

instrument algorithms, previously reported in the literature and confirmed by this study, are explained by differences in scan path and segmentation methodologies. Thus, the results demonstrate the importance of considering both scan centration and differences in torsional eye position when comparing quadrant thickness measures between instruments. In addition, with application of a common methodology for transverse magnification and segmentation of the retinal layers, the RNFL thickness measures, with and without compensation for major retinal vessels, will be comparable between instruments. Finally, by incorporating ocular biometry, the scaled measures of RNFL area are independent of axial length.

Acknowledgments

This study was supported by R01 EY001139 (RSH), K23 EY018329 (JW), T35 EY007088, P30 EY007551, Optometric Glaucoma Society Ezell Fellowship (NBP), John and Rebecca Moores Professorship (RSH).

CHAPTER 5

RETINAL NERVE FIBER LAYER ASSESSMENT: AREA vs. THICKNESS MEASUREMENTS FROM ELLIPTICAL SCANS CENTERED ON THE OPTIC NERVE.

This chapter was published in the journal Investigative Ophthalmology and Visual Science on November 10th, 2010, and published April 2011, 52(5): 2477-2489.

The authors that contributed to this work include:

Nimesh B. Patel, OD, Xunda Luo, M.Med, PhD, Joe L. Wheat, OD, PhD, Ronald S. Harwerth, OD, PhD

ABSTRACT

Purpose: An evaluation of the retinal nerve fiber layer (RNFL) provides important information on the health of an optic nerve. Standard measurements of the RNFL consider only thickness, but an accurate assessment should also consider axial length, size of the optic nerve head (ONH), blood vessel contribution, and distance of the scan from the ONH margin. In addition, although most primate ONHs are elliptical, the circular scan centered on the ONH is the mainstay in both clinical and research analyses. The purpose of this study was to evaluate thickness and area measures of RNFL cross sections when axial length and ONH shape are included.

Methods: Circular, raster and radial scans of left-eye optic nerves were acquired from 40 normal rhesus monkeys (*Macaca mulatta*) using spectral domain optical coherence tomography. The disc margin was identified by manually selecting the RPE/Bruch's membrane opening and ONH border tissue. With a pixel-to-micrometer conversion computed from a three-surface schematic eye, RNFL scans were interpolated at 300 to 600 μm (in 50 μm steps) from the edge of the ONH. The thickness and area of the RNFL at each distance were obtained by custom programs. Blood vessels in the RNFL were selected and removed from the overall RNFL measures.

Results: The average RNFL thickness decreased systematically from 149 ± 12.0 μm for scans 300 μm from the disc margin to 113 ± 7.2 μm at an eccentricity of 600 μm ($p < 0.05$). In contrast, the cross-sectional areas of the RNFL did not vary with scan location from the disc margin (0.85 ± 0.07 mm^2 at 300 μm compared to 0.86 ± 0.06 mm^2 at 600 μm). Blood vessels accounted for 9.3% of total RNFL thickness or area, but varied with retinal location. On average, 17.6% of the superior and 14.2% of the inferior RNFL was

vascular, whereas blood vessels accounted for only 2.3% of areas of the temporal and nasal RNFL regions.

Conclusions: In nonhuman primates, with appropriate transverse scaling and ONH shape analysis, the cross-sectional area of the RNFL is independent of scan distance, up to 600 μm from the rim margin, indicating that the axonal composition changes little over this range. The results suggest that, with incorporation of transverse scaling, the RNFL cross-sectional area, rather than RNFL thickness, provides an accurate assessment of the retinal ganglion cell axonal content within the eye.

INTRODUCTION

Glaucoma is a multifactorial group of optic neuropathies that ultimately leads to permanent vision loss if left untreated.[66] It has been estimated that by the year 2030, approximately 37 million individuals will be blinded by this disease.[319] The diagnosis of primary open-angle glaucoma is typically made from a clinical examination of the optic nerve and the nerve fiber layer and an evaluation of visual field sensitivity.[29,30,320,321] A major emphasis over the past few decades has been on early diagnosis and detection of disease progression, both of which require accurate and precise data to detect subtle optic neuropathy and assess changes over time.

Although functional assessment of vision is commonly used to evaluate optic neuropathies, inter-subject and intra-subject variability can make detecting small defects or changes difficult.[164] Recent advances in imaging instruments allow for more objective measurements of various ocular diseases, and under optimum conditions, the measurements are far more precise. The most popular imaging modality, optical coherence tomography (OCT), uses low coherence interferometry to acquire high-resolution images of the retina.[86] A recent advance in this technology, spectral domain OCT (SD OCT) with eye tracking technology, provides faster, higher-resolution scans than the prior time domain methods (TD-OCT).[263,291,322,323] The resulting images are analyzed to provide thicknesses, and in the case of optic nerve diseases, the thickness of the retinal nerve fiber layer (RNFL) is commonly used to detect disease and monitor progressive changes.

The standard scan used to assess the RNFL is a circular one, 12 degrees in diameter, centered on the optic nerve.[131-133] Analysis usually involves a RNFL thickness profile of the entire scan, along with sectorial and global (average) thicknesses that are compared to age-matched normative data. Several studies have shown these methods

to be repeatable in both normal and glaucoma patients.[132,133,135] However, scan quality and placement have been shown to be important in thickness analysis, and control of these sources of error should be considered.[139-142,298]

In addition, to improve the accuracy of RNFL measures, factors such as axial length and the size and shape of the optic nerve head (ONH) should be considered.[134,153-156,274,275] Several studies (including the present study), demonstrate significant correlations between RNFL thickness measures and axial length.[134,154,155] For example, for 12 degree circular scans, the physical scan diameter increases with increasing axial length, because of ocular magnification factors (see Fig. 5-7).[174,176] As a result, the RNFL is usually thinner in eyes with longer axial lengths because the scans are farther from the ONH rim margin.[157,274] However, the variation in thickness with proximity to the rim margin should not represent a change in axonal content, but rather it should be a reflection of the convergence of axons to the ONH.

Rhesus monkeys are often used in vision research as they can be trained for psychophysical tasks and have ocular and brain anatomy similar to that in humans.[163,198,324-328] Specifically, the non-human primate glaucoma model has provided invaluable insight into biochemical, functional, and structural changes that occur with glaucoma disease progression.[165,327-331] However, several differences between human and monkey eyes are important in the accurate assessment of structural content. Although the RNFL thickness profile and average thickness measures, using OCT technology, are similar to those in humans, the non-human primate has a significantly shorter axial length (19 mm) compared to that of humans (24 mm).[163,164,178] Hence, a standard 12 degree circular scan that has a circumference of 10.9 mm in humans would measure 8.01 mm in an adult *Macaca mulatta* eye. It is probable that the RNFL thickness profile is similar in the two species, as the optic nerves of rhesus monkeys are

significantly smaller than those in humans, making the scan distance from the rim margin similar to that of humans.[98,162,164,165]

The inherent variation in density of RGC axons in the RNFL with proximity to the ONH causes uncertainty when RNFL thickness measurements are based on circular scans of a fixed angular diameter unless transverse magnification effects are considered. In addition, the ONHs of both human and non-human primates are typically elliptical in shape, with the vertical meridian being larger than the horizontal[98,332] and, although non-human primates have significantly smaller ONH areas than humans, slightly larger quantities of axons normally pass into their neural canals.[98,162,165,302,333-337] Thus, there is a combination of ocular factors affecting the assessment of optic neuropathy from RNFL measures in non-human primates: smaller nerves with a larger quantity of axons, a shorter axial length, and the elliptical ONH shape.

For accurate assessment of the axonal content within the RNFL, the non-neuronal components (blood vessels and glial tissue) should be excluded from the total thickness. Although glial tissue cannot be accounted for by current OCT imaging systems, blood vessels within the RNFL cast shadows in B-scans (Mardin CY, et al. IOVS 2009;50:ARVO E-abstract 3333).[167] It is also interesting to note that the majority of the moderate- to large-caliber retinal blood vessels are in the superior and inferior sectors of the retina where the RNFL is thickest.[167]

Altogether, it is apparent that there are several optical and scanning factors that are likely to affect the accuracy of RNFL measurements for detecting and evaluating the stage of optic neuropathy by current OCT technology. These factors should be considered when using structural measures in non-human glaucoma models, where the shape of the eye is significantly different from that of the human. Therefore, the present investigation was undertaken to evaluate the effects of ocular biometry (refractive

components and axial length), ONH characteristics (shape and area), and major retinal vessel area, on RNFL measurements by SD OCT in rhesus monkeys of various ages. Some of the results of these studies have been presented in abstract form (Patel, NB, et al. IOVS 2010;51:ARVO E-abstract 2104).

MATERIAL AND METHODS

Subjects

To include a large range of axial lengths, 40 rhesus monkeys ranging in age from 28 days to 23 years of age, the majority (32 monkeys) of whom were less than 2 years of age, were included in this study. Seven of these animals were scanned multiple times over their first year of life, starting at 1 month of age. All animals had good systemic and ocular health, and only left eyes were included in the present study, which were the normal control eyes for other ongoing studies.[164,229-231] Experimental and animal care procedures were reviewed and approved by the Institutional Animal Care and Use Committee of the University of Houston. The use of animals for these experiments adhered to the ARVO Statement for the Use of Animals in Ophthalmic and Vision Research.

Optical Coherence Tomography

SD OCT scans were acquired from animals under anesthesia. Animals less than a year of age were anesthetized with an intramuscular injection of ketamine (15-20 mg/kg) and acepromazine maleate (0.15-0.2 mg/kg), whereas animals over a year of age were administered ketamine (20-25 mg/kg) and xylazine (0.8-0.9 mg/kg). The monkey's pupils were dilated to at least 4.5 mm with 1% tropicamide and 2.5%

phenylephrine. Corneal hydration to preserve optical clarity was maintained by custom-designed, gas-permeable contact lenses. The animal's head was stabilized using mouth and occipital bars attached to a rotational mount, enabling appropriate eye alignment for scanning.

All scans were acquired by one of two of the authors using spectral domain optical coherence tomography (JLW, NBP; Spectralis HRA+OCT; Heidelberg Engineering, Heidelberg, Germany). For this study, three high resolution scan patterns centered over the optic nerve were acquired: the standard RNFL thickness scan using a 12 degree diameter circular pattern (1536 A Scans/B scan), twelve 20 degree radial B-scans (1024 A-scans/ B scan), and a 20 X 20 deg horizontal raster grid comprised of 49 B-scans (1024 A-scans/ B-scan). For speckle noise reduction, B-scan averaging was set at 16 frames for all scan protocols. The scan data were exported in raw (.vol) files, and converted to 16-bit/pixel B-scan images, using custom programs written in commercial software (MATLAB; The Mathworks, Inc., Natick, MA).

Ocular Biometry and Scaling

Biometric data, including corneal curvature, anterior chamber depth and axial length, were measured for each monkey by a laser interferometer (IOLMaster; Carl Zeiss Meditec Inc., Dublin, CA). Crystalline lens parameters, including lens thickness, refractive index, and posterior and anterior lens radius, were interpolated from published normative data for monkey eyes.[163]

For each eye, data for transverse scaling were derived from a three-surface schematic eye, constructed using methods described by Bennett et al.[174,179] The model eye assumed a single-surface corneal (n = 1.336), homogenous refractive index for all optical structures (aqueous, crystalline lens and vitreous), and spherical refractive

surfaces. The constructed eyes were used to calculate scan lengths and scaling factors at the posterior pole, based on the distance of the second nodal point to the retina, assuming a spherical retina.[178]

Equation 5-1.

$$Retinal\ Scaling,\ L = \frac{\pi}{180} \times N'R$$

Where *L* is the length of retina in micrometers per angular degree from the nodal point, and *N′R* is the distance from the second nodal point to the retina.

For high-resolution Spectralis HRA+OCT scans (Heidelberg Engineering), the length of a 30 degree scan image is comprised of 1536 pixels. Hence, a 20 degree B-scan is 1024 pixels in length, and a 12 degree circular scan has a diameter of 614 pixels. The transverse scaling for each pixel was calculated as:

Equation 5-2.

$$Transverse\ Scaling = \frac{L}{1536/30}$$

For example, the second nodal point (N') for an animal 5 years of age, with a corneal curvature of 5.8 mm, axial length of 18.01 mm, and anterior chamber depth of 3.35 mm, is 5.82 mm from the cornea, when a scan focus setting of +1.2 D is used. The calculated distance from the second nodal point to the retina is 12.19 mm, and the length of the retina scanned for each angular degree from the second nodal point is *L* = 212.8 μm/deg (equation 5-1). Scaling for this example is similar to and agrees with that of previously published four-surface schematic models for adult macaque eyes.[178] The transverse scaling (equation 5-2) for this example would be 4.16 μm/pixel, and a 20

degree B-scan would measure 4.26 mm (1024 pixels × 4.16 μm/pixel), and the circumference of the standard 12 degree scan would be 8.02 mm (π × 614 pixels × 4.16 μm/pixel). Axial scaling was determined from the instrument specifications (1 pixel = 3.87 μm). Each OCT B-scan was rescaled such that the length and width of each pixel was equal (see Figs. 5-4E, 5-5C).

In the seven animals observed longitudinally, we verified the use of the three-surface schematic eye for ocular magnification. Changes in the transverse scaling were compared with changes in the extent of the retina imaged with the scanning laser ophthalmoscope (SLO). SLO images from follow up scans were registered using a generalized dual bootstrap iterative closest-point algorithm (i2k retina software; DualAlign LLC, Clifton, NY). The square root of the total-image pixel content in the registered images was used to determine the length of the registered image and change in ocular magnification. Overall, there was a good relationship between the two scaling methodologies (Fig. 5-1, $R^2 = 0.97$, $p < 0.01$).

Interpolated Scan Validity – Circular Scans

It was necessary to develop and validate methods to create custom scans to investigate elliptical scan patterns. It is logical that custom B-scans scans could be created from a grid of raster scans using interpolation methods. For example, the Cirrus HD-OCT (Carl Zeiss Meditec, Dublin, CA), uses a cube of 200 X 200 A-scans to interpolate its standard RNFL circular scan. Using interpolation of circular scan paths from volume scans, the influence of scan decentration and comparability to TD-OCT methodology has been investigated.[141,143,298] Overall, these methods result in repeatable and reliable measurements of RNFL thickness.[187] However, scan interpolation from a

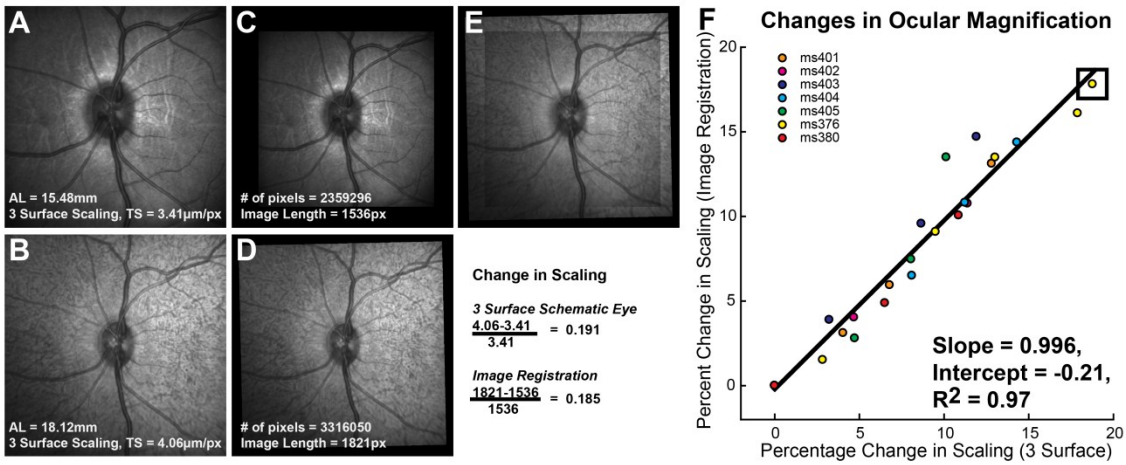

Figure 5-1. Retinal scaling with image registration and three surface schematic eye in eyes with increasing axial length.

A. Baseline 30 degree SLO image centered on the optic nerve were used to register subsequent SLO images (B). The pixel content of the aligned scans (C, D), needed for accurate registration (E), were used to compute the change in ocular magnification. F. The change in ocular magnification computed from image registration agrees with the change calculated using the 3 surface schematic eye.

cube with lower resolution in the vertical dimension (i.e., 49 lines in the 20 X 20 deg raster; 1024 pixels/raster line) should be validated. Therefore, to investigate the validity of interpolated B-scans, standard circular scans and corresponding interpolated B-scans acquired on the same day were compared (Fig. 5-2). The interpolation of a scan that is identical to the standard circular scan (Fig. 5-2A) requires transfer of the scan dimensions and coordinates of the circular scan on to the raster scan (Fig. 5-2A). The infrared SLO fundus images from the circular scan (Fig. 5-2A) and raster scan (Fig. 5-2B) were registered using a generalized dual bootstrap iterative closest-point algorithm (i2k retina; DualAlign LLC, Clifton, NY).[238] Subsequently, the center and radius of the circular scan were extracted from the raw data file, and identical coordinates were determined on the registered raster fundus image. A-scans from identical locations to the standard circular scan were interpolated from the raster cube using linear interpolation (Fig. 5-2B). The similarity of the B-scan images and the RNFL thickness values were used for comparison.

For a more analytical comparison to determine whether the methods of extracting circumpapillary RNFL thicknesses from raster data caused substantive alterations of the images, the fidelity of interpolated circular scans was assessed by comparing differences in regional intensities in the retinal images. Individual A-scans from the interpolated B-scan were registered to the standard or random scans by shifting each A-scan to the location with the highest cross correlation.

The results of the image analyses, illustrated in figure 5-2, demonstrate that when the extracted circle scan (I_{Rc}) (Fig. 5-2B) is subtracted from the standard scan (equation 5-3) of the same monkey (I_c) (Fig. 5-2A), the difference image (I_d) (Fig. 5-2C) contains little data. On the other hand, when the extracted scan (Fig. 5-2E) is subtracted from the standard scan of one of 10 randomly selected animals (Fig. 5-2D), the

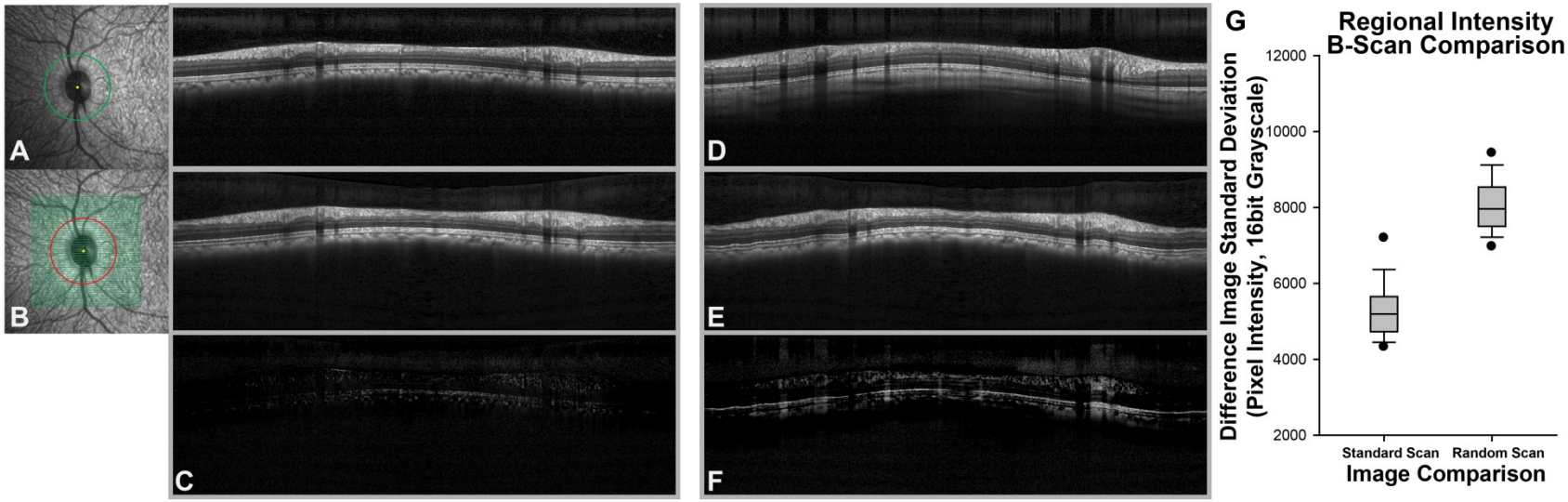

Figure 5-2. Standard vs interpolated RNFL scans.

A. SLO image with the standard scan pattern for RNFL analysis with high resolution B-scan from standard RNFL scan. B. SLO image of raster scan with registered interpolated standard circular scan pattern. Individual A-scans of interpolated B-scans (B) were registered to the standard circular RNFL scan (A) and the difference image (C) was used for analysis. Similarly A-scans of interpolated B-scans were registered (E) to a random standard RNFL scan from another animal (D), and subtracted (F). The plot (G), illustrates the difference image standard deviations between the two groups.

difference scan (Fig. 5-2F) contains many larger values. To quantify the comparisons of same or different subjects, the standard deviations of pixel values across the difference images (Fig. 5-2C, 5-2F) were used for statistical analysis. For 16-bit images, the units for each pixel range from 0 (black) to 65,535 (white):

Equation. 5-3

$$I_d = abs(I_c(x,y) - I_{Rc}(x,y))$$

The standard deviations should be smaller for similar images, and it was found that the SDs of difference images (I_d) were significantly less when interpolated B-scans were compared to standard scans from the same eye (5321.2 ± 851) than when compared to a random standard scans (8296.7 ± 1563, $p < 0.01$). These standard deviations represent a coefficient of variation (CV) of 8.1% for comparison to a scan from the same eye and 12.7% for a scan from a random eye.

Although the intensity data demonstrate that the standard and interpolated scans are qualitatively comparable, it is also important to compare RNFL thicknesses measures to determine whether the segmentation routines retain the retinal morphology information. The data presented in Fig. 5-3A, illustrate that global RNFL thickness measures from interpolated scans and standard scans are correlated highly ($R^2 = 0.98$, $p < 0.01$). The Bland-Altman analysis (Fig. 5-3B) also demonstrates agreement of measures, with a mean difference of 0.26 μm and 95% limits of agreement of -2.6 to 3.1μm. In addition, the intraclass correlation (ICC) for global thickness measures was 0.99 and >0.75 for all of the 12 clock hour sectors (Table 5-1). Based on these results, calibration equations were not required, as they are for systematic differences between time domain and spectral domain RNFL measures obtained with similar methodologies.[143] Overall, the statistical analysis confirms that the interpolated scans

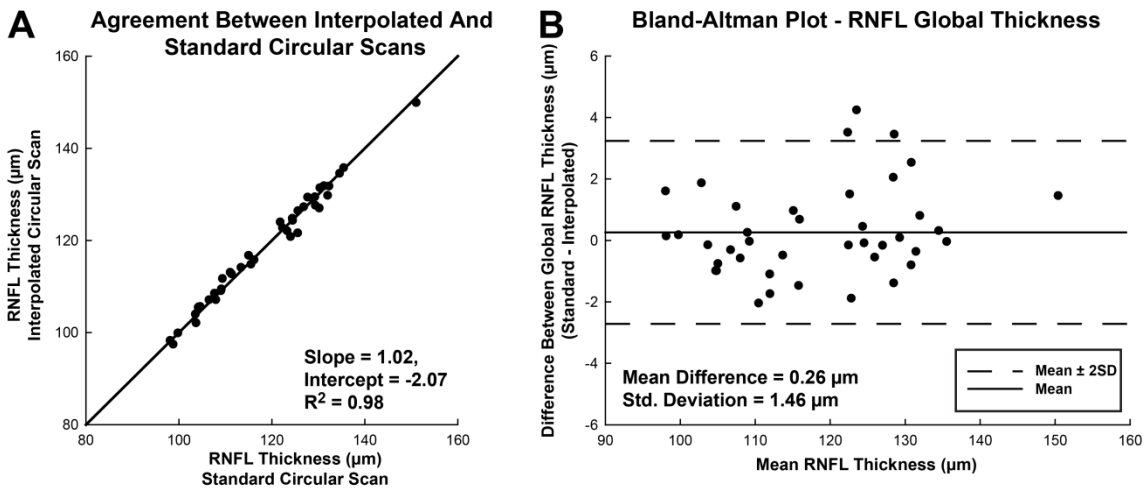

Figure 5-3. Agreement of RNFL thickness from standard and interpolated scans.

A. Global RNFL thickness agreement between standard and interpolated 12 degree circular scans. B. Bland-Altman plot comparing RNFL thickness of circular versus interpolated scans.

	12 Degree Circular Scan		Interpolated Scan		
Clock hour	**Mean Thickness (μm)**	**SD**	**Mean Thickness (μm)**	**SD**	**ICC**
1	85.2	13.4	84.3	13.8	0.97
2	128.4	20.8	128.9	20.7	0.98
3	163.6	21.9	162.9	22.0	0.99
4	124.8	22.4	124.3	22.2	0.99
5	101.3	16.6	100.5	14.9	0.94
6	75.3	11.2	74.0	9.9	0.88
7	63.0	8.0	62.6	6.7	0.86
8	104.7	15.5	105.4	16.7	0.97
9	162.1	26.4	164.4	26.7	0.98
10	208.2	28.5	210.0	27.8	0.99
11	134.4	21.9	132.7	21.9	0.97
12	69.9	13.3	67.6	12.2	0.96
Global	118.4	12.5	118.1	12.1	0.99

Table 5-1. RNFL thickness from standard and interpolated scans.

Comparison of RNFL thickness measures from standard circular RNFL scans and corresponding interpolated RNFL scan.

have excellent quantitative agreement with standard scans using SD OCT technology and similar agreement should hold for elliptical scans extracted from raster data.

Scan Interpolation and Analysis: Elliptical Scans

For construction of elliptical scans, the shape and size of the optic nerve had to be determined. Locations along the ONH rim margin were marked manually by identifying the border tissue and RPE\Bruch's membrane, as visualized in the radial B-scans centered on the optic nerve (Fig 5-4A, yellow and red asterisk). When necessary because of obstruction of features from shadows of blood vessels, points were selected directly on the raster scan infrared SLO fundus image.[98,150] For the purposes of this study, both boundaries were fit with a best-fit ellipse, and the ellipse for the neural canal opening (NCO) was used for scan interpolation (equation 5-4 and Fig. 5-4B). The ONH outline was then transferred to the raster scan image (Fig. 5-4C) after the fundus images of the radial and raster scans had been aligned using the retinal registration software (i2k Retina; Dual-Align, LLC). The major and minor axes of the fitted ellipse were used to calculate the area of the nerve and as the reference to create larger ellipses (equation 5-4). Concentric ellipses with eccentricities of 300 to 600 μm from the ONH rim margin in 50 μm steps (Fig. 5-4D) were constructed by increasing the lengths of major and minor axes in equal increments.

Equation 5-4.

$$\frac{(x-h)^2}{a^2}+\frac{(y-k)^2}{b^2}=1$$

$$Ellipse_{area}=\pi \times a \times b$$

$$Ellipse_{center}=(h,k)$$

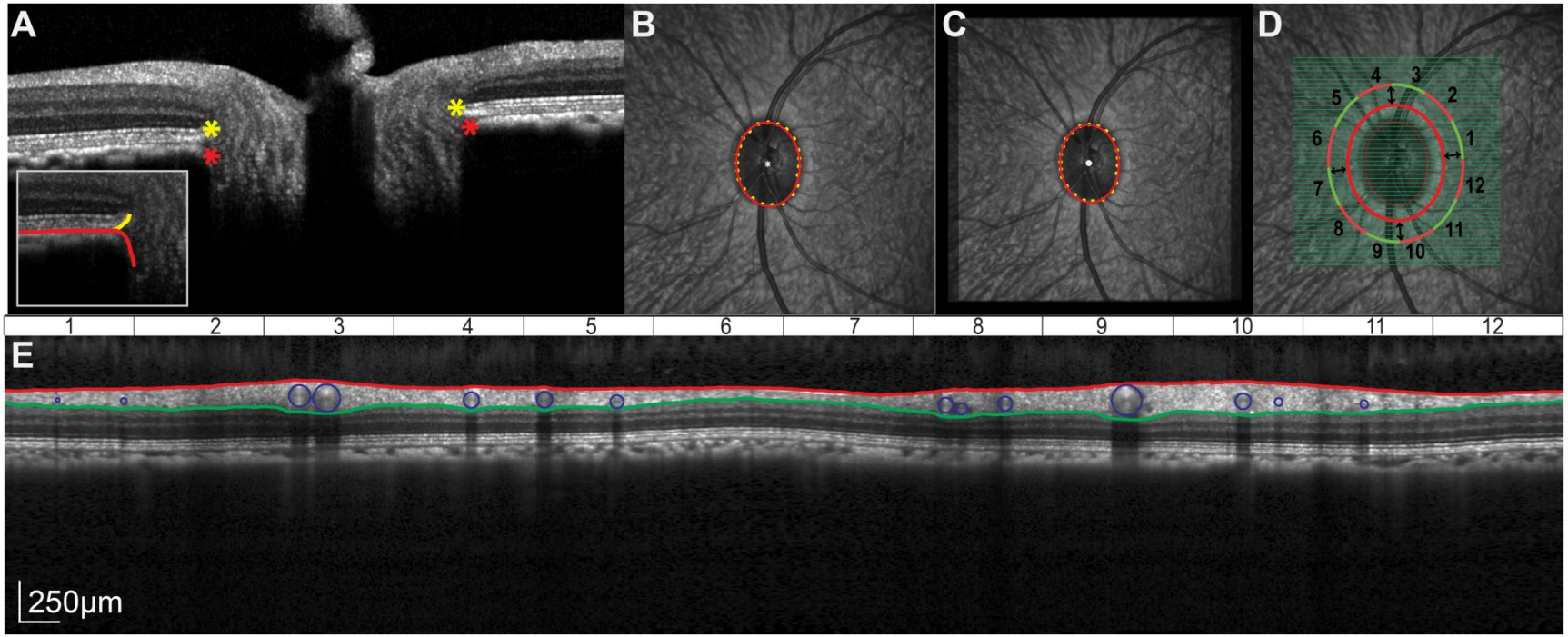

Figure 5-4. Identification of the ONH rim, and methodology for interpolating elliptical RNFL B-scans.

A. The border tissue and RPE\bruch's membrane were marked (yellow and red asterisk) on radial scans. B. The corresponding NCO points on the IR-SLO image were plotted and fit with an ellipse. C. The ONH best fit ellipse was registered to the raster scan SLO. D. Scans 300-600 µm from the ONH rim edge were interpolated from radial scans. E. B-scans were analyzed using the same algorithm as that for standard scans.

Where (*h*, *k*) represents the center of the ellipse, (*a*, *b*) represent the major and minor ellipse axis, and (*x*, *y*) are point coordinates on the ellipse. The circumference of each constructed ellipse was estimated using Ramanujan's approximation (equation 5-5).[338]

Equation 5-5.

$$Circumference_{ellipse} \approx \pi(a+b)\left(1+\frac{3\left(\frac{a-b}{a+b}\right)^2}{10+\sqrt{4-3\left(\frac{a-b}{a+b}\right)^2}}\right)$$

Data for the B-scans corresponding to each of the elliptical scan paths were interpolated from the raster B-scan data, with a resolution of 1536 interpolated A-scans (i.e., the number of A-scans acquired with the standard high-resolution circular scan). The elliptical B-scans were scaled to 1 pixel:1 μm, based on the length of the B-scan corresponding to the computed circumference of the ellipse, as illustrated by the example (Fig. 5-4E) of an OCT scan derived for an ellipse 600 μm from the ONH rim.

RNFL Quantification

Borders to segment the RNFL for both standard and interpolated scans were determined using custom-written computer programs (MATLAB; The MathWorks). To improve RNFL segmentation, B-scans were denoised using a Haar two-dimensional stationary wavelet, and convolved with a Gaussian filter with an SD of 4. Signal intensity profiles for each A-scan from the original B-scan (Fig. 5-5A) and denoised B-scan were used iteratively to determine the inner limiting membrane and RNFL/ganglion cell layer (GCL) junction. The ILM, shown by the red line (Fig. 5-5B) was determined as the first peak in each A-scan intensity profile (Fig. 5-5A), whereas the RNFL/GCL junction was defined as the subsequent region with a dampening of reflectivity,

illustrated by the green line (Fig. 5-5B). Small errors in segmentation, especially noted in regions were the RNFL signal was poor and around the major retinal vasculature, were manually corrected.

The cross-sectional images in figure 5-5 illustrate the effect of appropriate transverse scaling by comparison of the unscaled image (Fig. 5-5B) and the scaled image (Fig. 5-5C). After B-scans are scaled to 1pixel:1μm, the vascular structures within the retinal nerve fiber layer, identified by the shadows cast on the underlying layers, are the expected circular shape, instead of the vertical ovals in the unscaled images (cf., insets in Figs. 5-5B, 5-5C).[167] For further image analysis, the borders of each shadow were manually marked along with the center of the visible vessels within the B-scan. A circular region with a center marked for that of the vessel and a diameter equivalent to the width of the shadow was used to determine the vessels' contribution to the RNFL thickness or area. To prevent negative values for RNFL measures, only portions of the circle within the borders of the ILM and RNFL/GCL junction were used. An example of the contributions of blood vessels to RNFL thickness is presented in figure 5-5D by RNFL TSNIT data for the scaled images before (left panel) and after the subtraction of blood vessels (right panel). The effect of removing the blood vessels is apparent by inspection of the insets for figures 5-5B and 5-5C, the inferior sector that illustrates the relative thinning of the TSNIT data (Fig. 5-5D) in the specific regions of blood vessels.

For analysis of thickness or area, global thickness was determined by the average RNFL thickness measured from all A-scans within the B-scan and sector thicknesses were based on the average RNFL thickness from A-scans within each of the 12 clock-hour regions. RNFL areas were calculated by multiplying the average RNFL thickness, in micrometers, by the length of the scan or of a sector of the scan, in micrometers.[275]

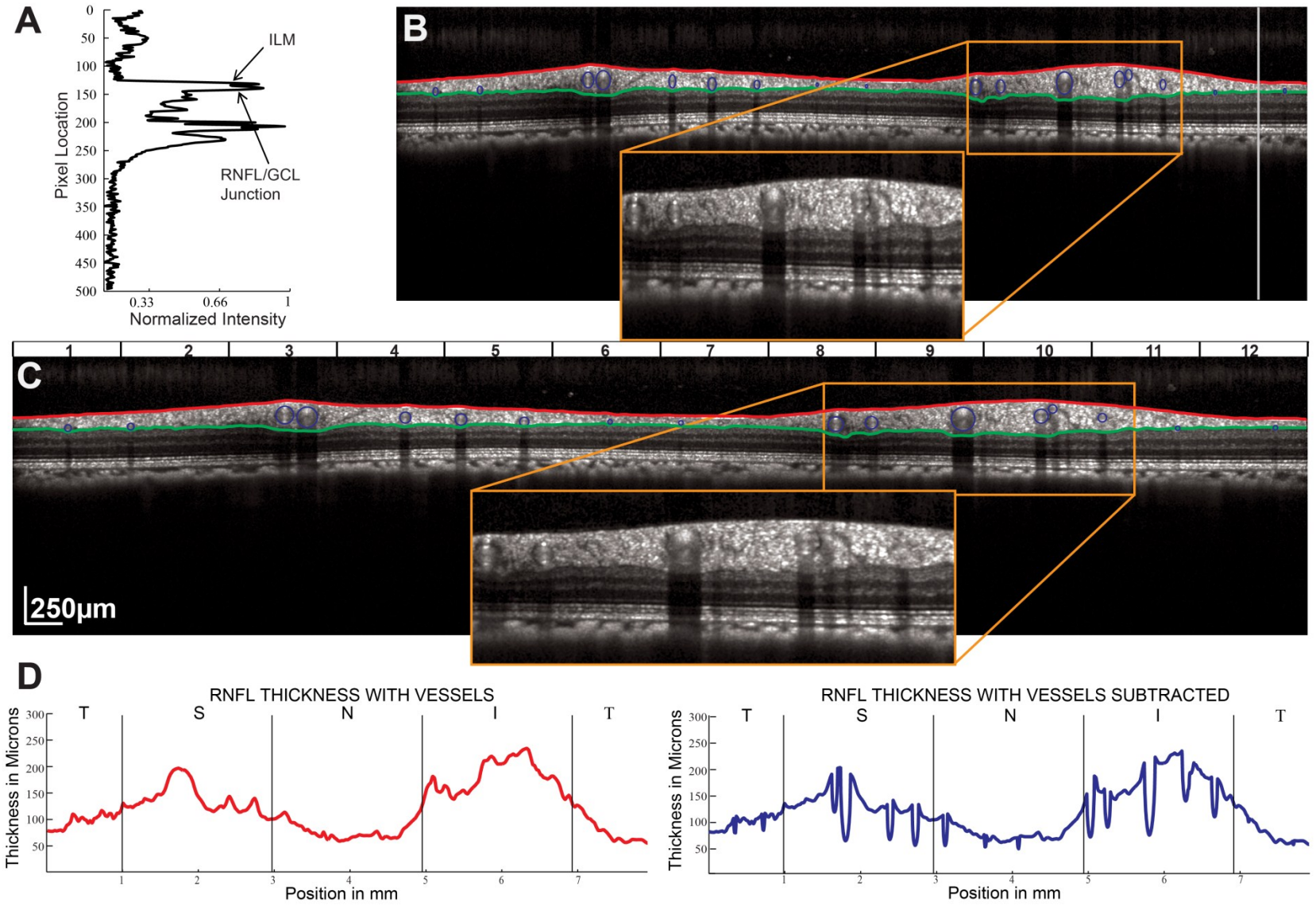
A
Pixel Location
Normalized Intensity
ILM
RNFL/GCL
Junction
B
C
250µm
D
RNFL THICKNESS WITH VESSELS
RNFL THICKNESS WITH VESSELS SUBTRACTED
Thickness in Microns
Position in mm
T
S
N
I
T

Figure 5-5. Segmentation methodology with vessel compensation.

A-scan reflectivity profiles (A), from RNFL scans (B) were used to determine the ILM and RNFL/GCL junction. The reflectivity profile illustrated is from the A-scan corresponding to the white line in the B-scan. Retinal vessels are illustrated for both the scaled and unscaled B-scans. Major retinal vessels within the RNFL of the scaled B-scan were identified by their shadows and fit with circles (C). Standard TSNIT curves were created for both with and without vessel subtraction (D). RNFL measures were computed for the 12 sectors illustrated.

RESULTS

RNFL Thickness Measures

Axial lengths for the rhesus monkeys in this study ranged between 14.5 and 19.9 mm and were normally distributed with a mean of 17.28 ± 1.38 mm. These values were appropriate for the ages of the animals used for the study.[163] The influence of ocular magnification is clearly demonstrated by the relationship between global RNFL thickness and axial length. With the standard scan used without transverse scaling, the animals with longer eyes had significantly thinner RNFLs ($R^2 = 0.57$, $p < 0.01$; Fig. 5-6A), with a linear regression slope of -6.33 μm/mm. Similarly, the global RNFL thickness of each of the seven longitudinally observed infant animals decreased systematically as their eyes lengthened (Fig. 5-6B) at rates that varied from -6.3 to -16.1 μm/mm, with a mean of -9.6 μm/mm (Table 5-2). An example of the change in the relationship between the standard scan location with respect to the ONH as the axial length increases during normal growth is presented in figure 5-7 for one young monkey (ms404, see Fig. 5-6B). It is apparent that the distance of the OCT scan from the ONH rim increases with axial length. Therefore, the change in RNFL thickness with axial length is likely to be a methodological artifact rather than a reflection of the neuronal composition. Specifically, the axonal content of the RNFL should not vary over a short period of aging or with axial length, and thus it is likely that the measurements represent an effect of scan location.

The importance of the scan path distance to the rim of the ONH is exemplified by the thickness measures from the elliptical scans (Fig. 5-6C). The means of the population data at each scan distance illustrate a decreasing global RNFL thickness with increasing eccentricity (300 to 600 μm) from the ONH rim margin ($R^2 = 0.9$, $p < 0.01$; Fig 5-6C). The systematic and consistent relationship is strongly supported by the ICC of 0.34 for global thickness versus scan distance. The significant differences in mean

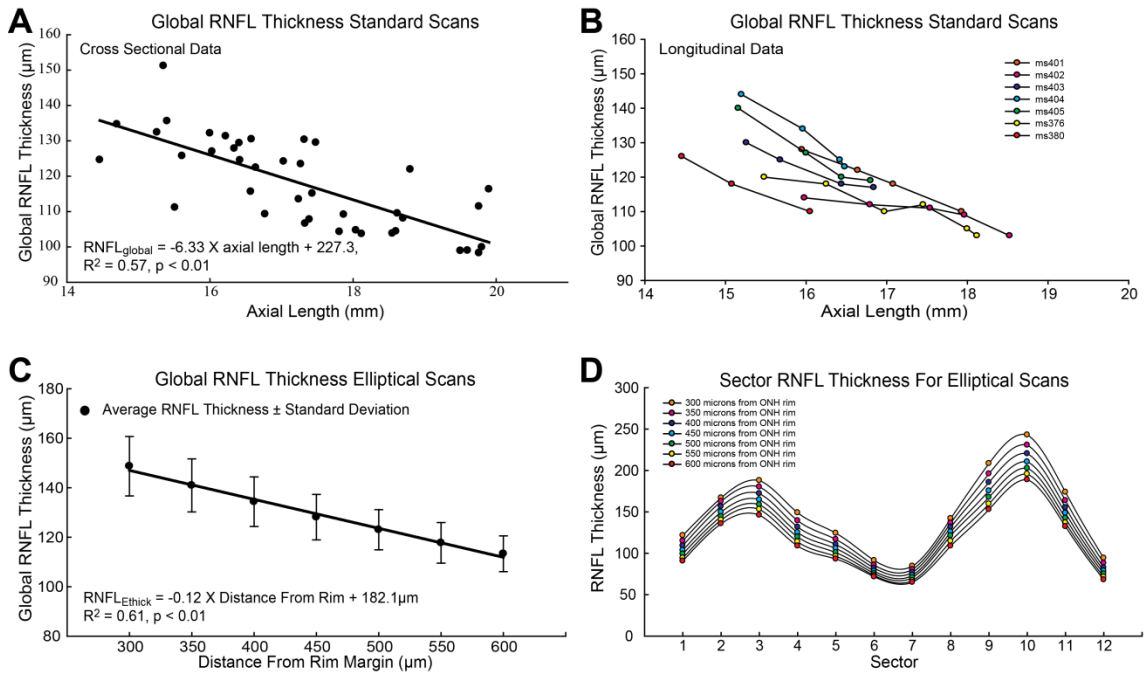

Figure 5-6. Influence of axial length and scan path on RNFL thickness.

Global RNFL thickness from standard circular scans (with no transverse scaling) decreases systematically with increase in axial length, in both cross sectional (A) and longitudinal (B) data. A systematic decrease in RNFL thickness also occurs with increasing distance from the rim margin using custom elliptical scans (C). This change in thickness is noted in all sectors of ellipses evaluated (D).

Animal	Slope (µm/mm)	Intercept
ms401	-13.5	343.4
ms402	-9.9	268.5
ms403	-8.4	257.8
ms404	-16.1	390.0
ms405	-9.1	273.3
ms376	-6.3	218.8
ms380	-3.8	176.2

Table 5-2. Relationship between RNFL thickness and axial length.

Linear fit parameters for global 12 degree RNFL thickness change with increase in axial length in seven animals followed longitudinally.

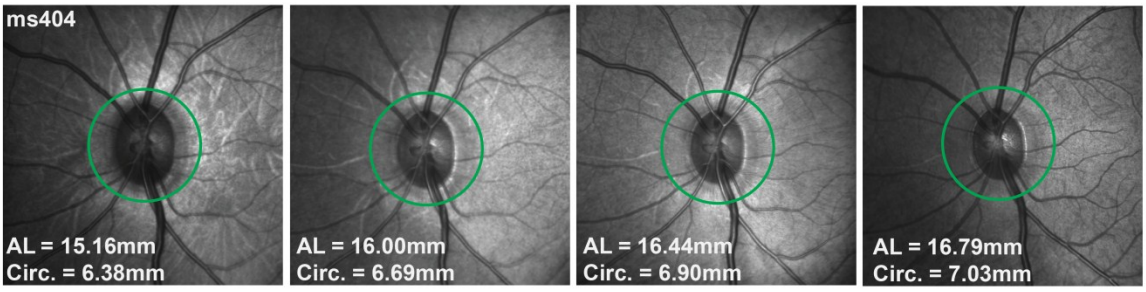

Figure 5-7. Changes in RNFL scan path location for one infant monkey.

Standard RNFL scan path for an infant rhesus monkey at four separate scanning sessions.

thickness as a function of scan location were confirmed by repeated-measures ANOVA ($F(2.19, 85.4) = 1014.1$, $p < 0.01$). The results of the ICC and ANOVA analyses for each of the 12 clock-hour sectors (Fig. 5-6D) were in agreement with the global thickness results.

Although RNFL thickness varied with scan eccentricity (Fig. 5-6C), when the elliptical scans were placed a constant distance from the ONH rim the relationship between RNFL thickness and axial length for any given eccentricity was not significant (Table 5-3, Figs. 5-8A, 5-8B). In fact, the global RNFL thickness measures with elliptical scans located 550 μm from the ONH rim were similar to the 12-degree circular scans (Fig. 5-8C), although the cross-sectional variability of the circular scans was larger (CV = 11.0%) than that of the elliptical scans (CV = 6.9%, Fig. 5-8D.) . In addition, the residuals for the best fit for elliptical scans 500 μm from the rim margin had a smaller variance (51.32) than for 12 degree scans (81.74). Thus, these data support the hypothesis that the relationship between RNFL thickness and axial length occurs because the proximity of standard OCT scan paths to the ONH rim vary with axial length.

Vascular Component

In the assessment of glaucomatous neuropathy, especially for the assessment of progression, it may be important to separate the neuronal and non-neuronal components of the RNFL. To determine the extent of one non-neuronal vascular component, the major retinal vasculature visible within the high-resolution OCT images were identified and removed from the thickness and area measures. Across the 40 subjects, the major retinal vascular contribution to the mean RNFL thickness for standard scans was 10.2 ± 2.5 μm (Table 5-4). The amount of blood vessel contribution to RNFL thickness was

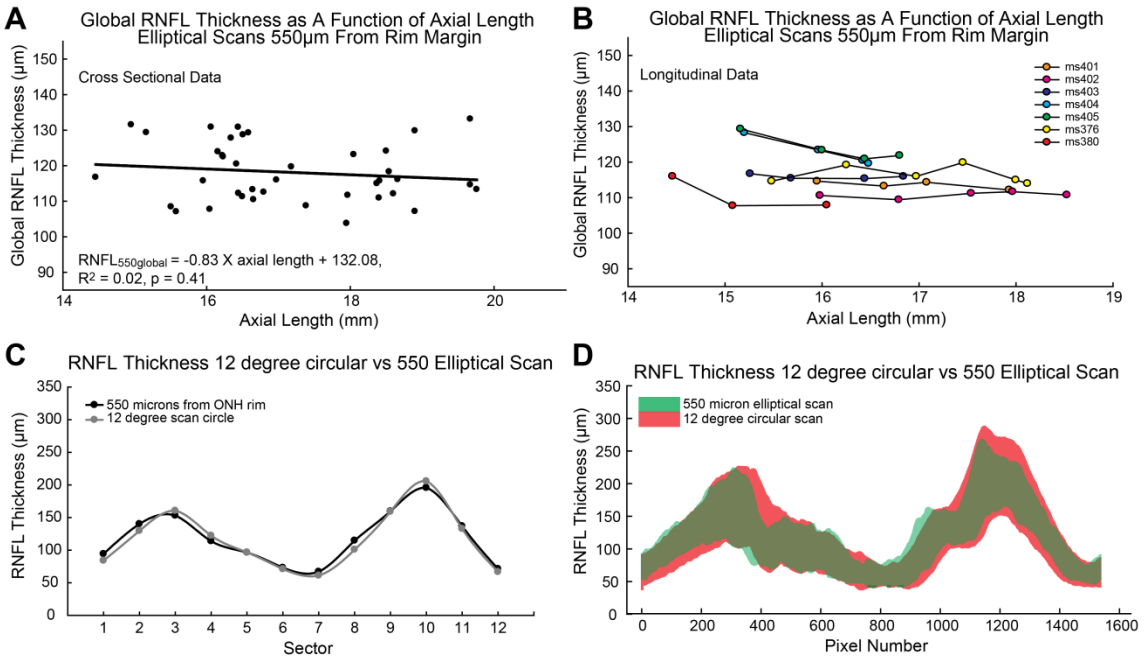

Figure 5-8. Relationship between a constrant 550 µm elliptical scan path and RNFL thickness.

Elliptical scans are not correlated with axial length. The plots illustrate the relationship of global RNFL thickness with axial length for the 550 µm elliptical scan for both the cross sectional (A) and longitudinal data (B). The 550 µm distance elliptical scan is most similar to the 12 degree circular scan (C). 550 µm scans have less variation in thickness than with standard 12 degree scans (D). Illustrated are the 95% confidence limits for TSNIT plots for both scan types (D).

Scan Distance From Rim	Slope (µm/mm)	R^2	P
300	-1.95	0.04	0.2
350	-1.24	0.02	0.36
400	-1.35	0.03	0.29
450	-1.16	0.03	0.31
500	-0.94	0.02	0.36
550	-0.96	0.02	0.35
600	-0.65	0.01	0.47

Table 5-3. RNFL thickness from elliptical scans and axial length.

Best linear fit data for global RNFL thickness from elliptical scans and axial length.

Scan	RNFL Global Thickness (μm)	Change in Thickness with Vessel Removal	Percentage Change	RNFL Global Area (μm^2)	Change in Area with Vessel Removal	Percentage Change
300	148.9	13.5	9.1	850270.7	77083.3	9.1
350	141.2	12.9	9.1	851055.7	77943.4	9.2
400	134.5	12.4	9.2	852463.1	79143.2	9.3
450	128.3	11.8	9.2	853083.7	78861.5	9.3
500	123.1	11.4	9.3	857399.1	79905.5	9.3
550	117.9	11.2	9.5	857837.5	81573.3	9.5
600	113.5	10.6	9.3	860812.7	80515.7	9.4
12^o	115.2	10.2	8.8	846114.3	72893.4	8.6

Table 5-4. RNFL area from elliptical scans and axial length.

Thickness and area changes in global RNFL measures after vessels have been eliminated from the RNFL. Data for elliptical scans 300 to 600 μm from the rim margin and the standard 12 degree circular scan.

larger for the superior and inferior portions, compared to the temporal and nasal RNFL, and these segments were most affected by the removal of vessels (Fig. 5-9, Table 5-5). For elliptical scans, removing the major retinal vasculature resulted in a greater reduction of global RNFL thickness for scans closer to the rim margin (repeated measures ANOVA, $F(4.55, 182) = 37.371$, $p < 0.01$). However, the proportional change in RNFL measures was not altered significantly with scan distance (repeated measures ANOVA, $F(6, 240) = 0.998$, $p = 0.43$).

Area Measures

The next logical refinement of RNFL assessment was to translate the thicknesses to RNFL area values. RNFL area measures should provide a better quantification of axonal content, which should not change with the region scanned in a given eye and should provide an accurate assessment of axonal losses with age or glaucoma. The cross-sectional areas were calculated by multiplying the mean RNFL thickness by the ellipse circumference for circular scans determined by the scan radius and for elliptical scans by using Ramanujan's approximation (equation 5-5).[338] Similarly, for sector area measures, the average thickness was multiplied by the length of the scan for that sector.

For standard RNFL circular scans, the correlation between RNFL area and axial length was not significant ($R^2 = 0.07$, $p = 0.11$), although there was a slight trend for larger global RNFL area measures with increasing axial length. In agreement with the results for circular scans, cross sectional RNFL areas for the custom elliptical scans did not change significantly with increasing distance from the ONH rim margin (Fig. 5-10A, $R^2 = 0.002$, $p = 0.49$). The ICC for global RNFL area measures was 0.97 for the seven eccentricities from the ONH rim analyzed. Repeated-measures ANOVA with

Sector	Vessel Contribution (μm)	Percentage RNFL thickness
1	1.1 ± 1.8 μm	1.25
2	4.3 ± 5.1 μm	3.35
3	29.9 ± 11.7 μm	18.63
4	17.0 ± 11.5 μm	13.88
5	8.8 ± 5.6 μm	9.13
6	3.8 ± 4.3 μm	5.30
7	1.4 ± 2.1 μm	2.28
8	5.7 ± 6.1 μm	5.69
9	19.3 ± 13.5 μm	12.17
10	27.1 ± 14.1 μm	13.19
11	2.4 ± 4.0 μm	1.80
12	1.4 ± 2.1 μm	2.07
Global	10.2 ± 2.5 μm	8.80

Table 5-5. Vessel contribution to sector thickness for standard RNFL scans.

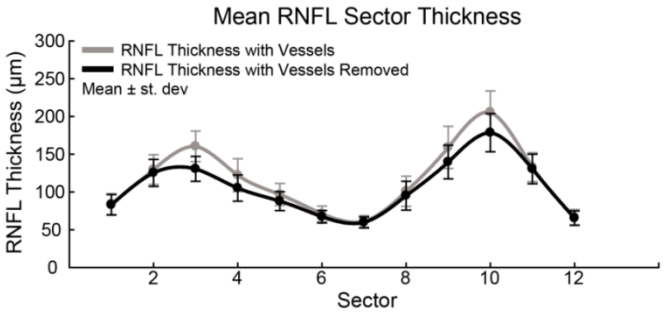

Figure 5-9. **Vessel contribution to RNFL thickness.**

Vessel contribution to the RNFL thickness is greatest in the superior and inferior scanned portions. Illustrated are the average RNFL thickness, with and without vessel compensation, for each sector.

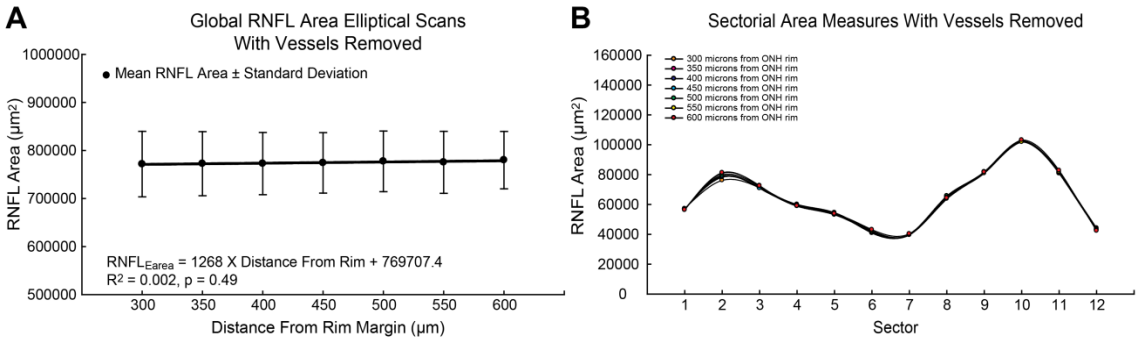

Figure 5-10. RNFL area as a function of scan path.

Area measures for global and sector RNFL show no significant difference with increasing eccentricity from the ONH rim.

Greenhouse-Geisser estimates for sphericity also indicated no significant relationship between global RNFL area measures for the seven elliptical scan distances ($F(3.899, 152) = 1.732$, $p = 0.15$). Area measures for all 12 sectors analyzed showed similar results (Fig. 5-10B). CV measures of variance, were similar for both thickness and area measures for elliptical scans. A significant reduction in variation is also achieved for the standard scan when using area measures (Table 5-6). These findings are in line with the premise that the variation in thickness with eccentricity from the OHN rim is a result of changing the length of the scan, and thus scans with smaller circumferences have larger thicknesses to encompass a constant number of axons entering the ONH. In addition, within the peripapillary region analyzed in this study, the ganglion cell density is relatively low, and a large change in axonal content was not expected.[119] However, when the scan eccentricity is significantly large, axons from cell bodies more proximal to the ONH will not be included in the measure, and the RNFL area is smaller.

ONH Parameters

The transverse scaling should provide a more accurate measurement of the ONH size. The ONHs of all of the animals imaged were better described as ellipses than circles, with the major axis oriented vertically. The average major and minor axis dimensions were 0.688 ± 0.057 mm and 0.522 ± 0.044 mm, respectively, with a mean ratio of vertical/horizontal axes of 1.32 ± 0.06. ONH areas were calculated from the fitted ellipse ($A = a \times b \times \pi$) that should be a close approximation to the opening of the neural canal. Although the ranges of ages and axial lengths of the 40 monkeys were quite broad, the intersubject variability of ONH area measures was small. The mean ONH area was 1.14 ± 0.18 mm^2 with a range of 0.78 to 1.48 mm^2. The ONH size was statistically related to RNFL global area ($R^2 = 0.18$, $p < 0.01$; Fig. 5-11), but not to axial

Scan	Without Vessel Compensation				With Vessel Compensation			
	Global Thickness (µm)	CV (%)	Global Area(µm^2)	CV (%)	Global Thickness (µm)	CV (%)	Global Area(µm^2)	CV (%)
300	148.7	8.1	848628	8.4	135.1	8.2	771566	8.8
350	140.9	7.6	849681	8.1	128.2	7.9	772506	8.6
400	134.3	7.4	851540	7.8	121.9	8	772659	8.4
450	128.1	7.2	852310	7.8	116.4	7.4	774132	8.1
500	123	6.6	857253	7.5	111.5	7.2	777299	8.1
550	117.7	6.9	856979	7.6	106.5	7.5	775311	8.3
600	113.3	6.4	860773	7.3	102.6	6.8	779986	7.6
12 Degree	115.2	11	846114	7.5	105.3	11	773221	7.9

Table 5-6. Variability in RNFL measures for standard vs. elliptical scans.

Less variability in RNFL measures are noted after appropriate transverse scaling is computed for each eye. Data for elliptical scans 300 to 600 µm from the rim margin and the standard 12 degree circular scan.

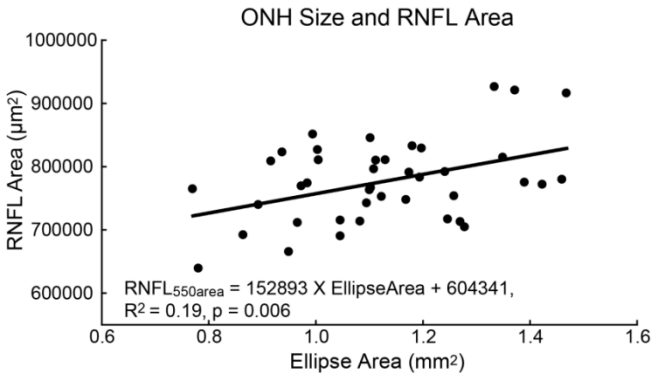

Figure 5-11. The relationship of RNFL area with size of the optic nerve.

length (R^2 = 0.06, p = 0.14). This result is not surprising, as we would expect larger optic nerves in eyes with a greater number of RGC axons.

DISCUSSION

The results demonstrate the importance of appropriate transverse scaling and the use of elliptical scans for the assessment of the retinal nerve fiber layer. As an example, the data showed a significant relationship between axial length and RNFL thickness using the standard 12-degree circular scans (with no transverse scaling). Although this result is in agreement with several studies in both human and non-human primates,[134,154,155,331,339] it is unlikely that it represents neuronal differences between longer and shorter eyes. In fact, the effect of ocular biometry was well explained by the differences in ocular magnification between subjects (Figs. 5-6A, 5-7), when axial length was eliminated as a factor by scaling the circular scan and expressing the results as RNFL areas. In essence, the relation between RNFL thickness and axial length occurs because a fixed angular scan covers a larger retinal region in longer compared to shorter eyes and RNFL tissue further from the ONH margin is thinner.[156,157,274,275] The thinning associated with scan distance, however, does not reflect on a change in axonal content, but, rather, it is the change in axonal density with proximity to the optic nerve.[119,157]

The influence of ocular magnification is exemplified in the rhesus monkey, whose smaller eyes have higher equivalent powers. Overall, the slope of the relationship between RNFL thickness and axial length of the grouped data (-6.3 μm/mm) is significantly different from the (-2 to -3 μm/mm) regression slopes noted in human eyes.[134,153,154,340] Although, the major factor in ocular magnification is axial length, the longitudinal data from the seven animals illustrate the need to consider corneal

curvature, anterior chamber depth, and ocular lens parameters. In these seven infants, even though area measures were similar between animals, the RNFL thickness relationship with axial length was significantly different between animals (Table 5-2). These differences in slope data could be explained by the different maturational rates of the ocular components in these animals.

Changes in RNFL thickness with increasing distance from the center of the optic nerve have been reported in a study which SD OCT technology was used in the non-human primate.[331] Similarly, the present findings indicate a linear change in thickness up to 600μm from the rim margin. In addition, eyes with a larger global RNFL area have a greater change in RNFL thickness at increasing eccentricity ($R^2 = 0.16$, $p = 0.01$), with similar trends in each sector. However, this relationship becomes non-linear when larger eccentricities are analyzed, as illustrated in RNFL thickness data up to 1050μ from the rim margin in four animals (Fig 5-12). It is important to note that the standard 12 degree circular scan path is within the region where changes in RNFL thickness follow this linear relationship.

Furthermore, systematic differences in scan paths and ocular magnification of various OCT systems may explain the differences in RNFL measures, using essentially similar technologies.[187,341,342] For example, Kang et al. illustrated a method of minimizing the relationship of RNFL thickness and axial length by accounting for ocular magnification based on the optical properties of the Cirrus HD OCT. In addition, using circular scans of varying size, Bayraktar et al.[275] have shown significant changes in RNFL thickness, but minimal changes in RNFL area with an increase in OCT scan diameter. Similarly, in nonhuman primates, RNFL area measures for elliptical scans 300 to 600 μm from the rim margin show no significant change. This finding is logical, as a reduction in axonal content is not expected in the regions analyzed. In accordance, we

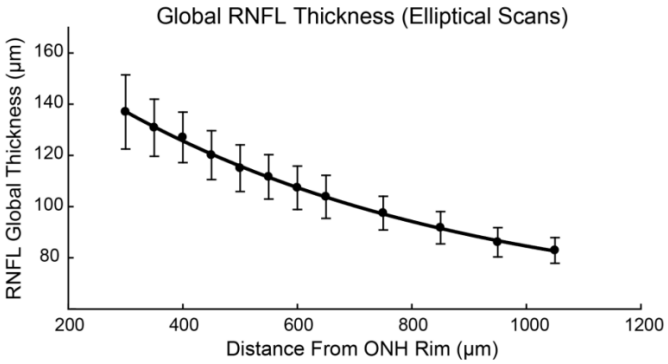

Figure 5-12. Change in global RNFL thickness using custom elliptical scans with increasing eccentricity from the rim margin.

may find fewer discrepancies between various OCT technologies by accounting for ocular magnification.

For OCT measurements of the RNFL to be a good surrogate for the population of RGC axons, the contribution of non-neuronal components to the RNFL thickness or area should be considered.[50,136] The two main non-neuronal components within the nerve fiber layer include retinal blood vessels and neuroglia. With current OCT technologies, we are unable to account for glial components of the RNFL. However, retinal vessels within the retina are often seen as circular or elliptical structures that cast shadows on the underlying retina, and several retinal vessels usually pass through the nerve fiber layer in the region of the retina analyzed for RNFL thickness. After rescaling of OCT B-scans, many of these vessels take on a circular appearance and this circular region can be subtracted from the total area. In the present study, retinal vasculature accounted for 9.3% of the total RNFL area in healthy nonhuman primate eyes. In human subjects, Hood et al. predicted a ~13% contribution of retinal vasculature to the total RNFL thickness.[167] The differences between the two studies could be due to methodology or species being studied. Nonetheless, retinal vascular components make up a significant portion of the nerve fiber layer and, in glaucomatous eyes, the contribution may be larger, even though retinal vessels are thought to decrease by up to 15% in diameter.[167,343,344] For example in animals with optic nerve transection, as the RNFL thickness deceases, retinal blood vessels are seen to emerge in the thickness plots as spikes.[345] These spikes in the TSNIT plot can be removed using methodology presented in this article, providing a better measure for the neuronal content within the RNFL. However, it is important to note that although the major retinal vessels are accounted for by the methods described, smaller vessels, which make a significant contribution to RNFL measures, cannot be accounted for by the current technology.[316,317]

RNFL area measurements should be linearly related to the number of RGC axons if, in addition to the vasculature, the non-neuronal glial components can be excluded from the area calculation (Wheat JL, et al. IOVS 2007;48:ARVO E-abstract 491), (Wheat JL, et al. IOVS 2009;50:ARVO E-abstract 5826).[138] Such measures could reduce the variability noted in structure-function relationships. A previous nonhuman primate study indicated that the glial content in the nerve fiber layer is no less than 18%.[168] Although significant variations in glial content and activation are known to occur, especially with optic nerve and retinal disease processes, an estimate of 20% to 30% is reasonable to use for estimating axonal content in young, healthy eyes.[346-348] Several studies have also investigated axonal diameters of retinal ganglion cells. At the optic nerve, the mean axon diameter measures 0.84 ± 0.07 μm, with a cross-sectional area of 0.55 μm^2.[166,337] A reasonable estimate of the total axonal content in these healthy eyes can then be determined as:

$$Estimated\ total\ Number\ of\ Axons\ in\ the\ RNFL = \frac{RNFL\ Area\ with\ vessels\ removed\ \times (1 - Estimated\ Fraction\ of\ Glial\ Tissue\ in\ the\ RNFL)}{Cross\ sectional\ area\ of\ a\ single\ axon\ fiber}$$

In the RNFL cross sectional areas, the axonal content of healthy rhesus primates is estimated at 1,126,953 ± 92198 axons, using a 20% glial estimate, and similar to that previously reported.[162,166,337,349]

Transverse scaling provides accurate data for the determination of the ONH shape and size. The size of the optic nerve for macaque monkeys (1.44 ± 0.19 μm^2) was similar to reported data using histological methods.[98,162,165] Although a relationship between disc size and axial length have been reported in humans, this relationship was not seen in rhesus monkeys ($p = 0.14$).[152,350-352] However, the relationship between the

size of the ONH and the RNFL area was significant and similar to relationships noted in previous human and nonhuman studies.[156,162]

In conclusion, the investigation of SD OCT assessment of the RNFL suggests that scaled measures of the RNFL area can improve the interpretation of the retinal ganglion cell axonal content in the retina. After rescaling, RNFL thickness plots within the peripapillary region for scans of fixed distance from the rim margin can be constructed based on area measures. Although obtaining RNFL area measures requires the inclusion of ocular biometry data, there are fast noninvasive methods available for these measurements.[180,353,354] The results also demonstrate the importance of using custom scans, especially in nonhuman primates, the majority of whom have an elliptical optic nerve.[98,332] Finally, while the use of an animal model with smaller eyes provides evidence that the methods of transverse scaling will be robust to normal ocular variations, the methods should be applied to normal human subjects and glaucoma patients to determine whether there is clinical utility for the diagnosis and management of glaucomatous neuropathy.

Acknowledgments

The research was supported in part by NIH/NEI grants R01 EY001139(RSH), P30 EY007751, and K23 EY018329(JLW) and by a John and Rebecca Moores Professorship.

CHAPTER 6

ELEVATED INTRAOCULAR PRESSURE RELATED STRUCTURAL CHANGES IN THE RETINA

The authors that contributed to this work include:

Nimesh B. Patel, OD, Ronald S. Harwerth, OD, PhD

ABSTRACT

Purpose: A spectral domain optical coherence tomography (SD OCT) assessment of the retina and optic nerve head (ONH) provides important information for the clinical diagnosis and management of glaucoma. The clinical signs of glaucoma can be replicated in an experimental model of the disease, using non-human primates that have similar ocular anatomy and physiology to humans. However, there are substantive differences in ocular biometry and ONH characteristics in the eyes of humans and monkeys that need to be considered to apply clinical instruments to experimental glaucoma. The purpose of this study was to adapt SD OCT technology to quantify morphological changes at the posterior segment caused by experimental glaucoma in rhesus monkeys and to investigate the temporal relationships of clinical signs of progression of optic neuropathy in glaucoma.

Methods: Normative data were collected from 47 normal monkeys ranging in age from 1.9 to 23 years of age. Unilateral ocular hypertension was induced in 6 animals by an Argon laser scarification of the trabecular meshwork. SD OCT scans were acquired using the Spectralis HRA+OCT. Transverse retinal scaling for SD OCT data was calculated with a three surface schematic eye using the ocular biometry data acquired with an IOL Master. The total retinal thickness from radial scans centered on the optic nerve and macula were used for morphological analysis. Retinal nerve fiber layer (RNFL) area measures, both with and without removal of major retinal vascular, were determined from custom elliptical scan paths that were 550 μm from the ONH rim margin.

Results: There was no significant relationship between any of the scaled measures and axial length ($p>0.1$). Cup depth (coefficient of variation (CV) = 27.2%) and neural rim volume (CV = 22.9%) had the least variability in the normative data, and were the first measures to show signs of significant change in eyes with experimentally induced ocular hypertension. Significant reductions of the RNFL area did not occur until after the neural rim volume had decreased by about 60%. Thinning of the retina in the macula area was delayed considerably compared to the cupping of the ONH or thinning of the RNFL and, although the change in macula volume was linearly related to changes in sectorial RNFL area measures ($R^2 = 0.61$, $p < 0.02$), it did not exceed the variability of the normative data. The percentage vascular contribution to the RNFL area increased with decreasing area ($R^2 = 0.64$, $p < 0.01$), but the overall vessel area contribution decreased with increasing disease severity ($R^2 = 0.33$, $p < 0.01$).

Conclusions: The early structural changes in ONH morphology were correlated to the cumulative IOP, which provides support for a biomechanical paradigm for neuronal damage in experimental glaucoma. The custom measures of the RNFL area demonstrated excellent repeatability, with changes subsequent to OHN cupping and providing a larger dynamic range of measurement. With disease progression, the portion of retinal vasculature increased, but the overall area contribution of blood vessels to the RNFL decreased. Although total macula volume measures are repeatable, it was the last morphological measure to show significant change during the progression of experimental glaucoma and, therefore, may be most applicable to clinical assessment of glaucoma at late stages.

INTRODUCTION

Glaucoma is a group of progressive optic neuropathies that can result in irreversible blindness, especially if not treated.[66] Although there is no cure, early detection and adequate intraocular pressure reduction can slow the progression of glaucoma.[355-357] As the world's population ages and the prevalence of glaucoma increases, a major emphasis should be placed on the early detection of this potentially blinding disease. At present, clinical diagnosis and management are based on assessment of the intraocular pressure, visual field testing and an ophthalmoscopic examination of the ONH and RNFL.[29,30,358]

In general, structural damage to retinal ganglion cells (RGCs) results in a corresponding reduction in visual sensitivity.[22,46,359,360] In addition, the loss of visual sensitivity usually follows the accurate path of the axons of the RGCs in the RNFL.[26,361] Although visual field testing is the current "gold standard" in glaucoma assessment, it has a relatively high inter- and intra-subject variability, making it difficult to detect small changes, often requiring confirmatory testing.[33,34,164] Similarly, there is also significant variability in the subjective, ophthalmoscopic examination of the optic nerve and RNFL.[36,37]

In the past two decades, a new procedure has been developed for assessing retinal neuropathy by non-invasive, *in vivo,* imaging with optical coherence tomography (OCT) to obtain an objective structural assessment of the posterior segment of the eye. With this technology, the morphology of the ONH is most commonly assessed using radial scans centered on the ONH, while the thickness of the RNFL is quantified using a 12 degree (nominally 3.74 mm) circular scan. RNFL thickness measures from these scans are repeatable and reliable in both normal and diseased eyes.[131-135] Advances in technology, such as spectral domain optical coherence tomography (SD OCT), allow for

faster scan speeds (up to 40,000 Hz) and higher resolution images (~3 μm) with minimal motion artifact. With this technology, volume scans are often utilized for analyses of the ONH and macula regions.

Because it has the highest density of ganglion cells,[119] the retina in the macula area has become of increasing interest for both glaucoma diagnosis and management. With loss of RGC bodies from glaucoma, it is reasonable that there would be a corresponding thickness change in the RGC layer.[57] Such changes with disease progression would result in a decrease in overall retinal thickness and volume,[121] and several investigators have attempted to relate disease stage to macular thickness and/or volume.[120-124] Although results from these studies have been promising, it has not been demonstrated that they add diagnostic value, compared to RNFL thickness measures using the standard circular scan centered on the optic nerve.[125,126,129,130] Hence, an investigation of RNFL and macula thickness at multiple time points in disease progression may provide insight into the relationship between the two measures.

The rhesus monkey is often used to study both structural and functional changes associated with laser-induced ocular hypertension (experimental glaucoma).[46,327,328] In this model of glaucoma, elevated intraocular pressure results in increased optic nerve cupping[362] and losses of RNFL and visual sensitivity.[164] Although the general anatomy of the monkey eye is similar to that of the human, several differences between the two species need to be considered in applying methods and instrumentation for optical imaging of retinal structure, which were designed for human eyes, to assess the effects of experimental glaucoma in eyes of monkeys. For example, non-human primates, have a significantly shorter axial length (19 mm) than that of humans (24 mm)[163,164] and a 12 degree SD OCT circular scan, which is nominally a 10.9 mm circumference in human eyes, is only 8.01 mm in an adult *Macaca mulatta* eye. Also, because the smaller eye of

the non-human primate has a higher equivalent optical power than that of a human eye, ocular biometry has a larger effect on the scan path in the monkey eye. Specifically, the relationship between RNFL thickness and axial length has a steeper slope in eyes of monkeys (-6.33 μm/mm)[224] than humans (-3.00 μm/mm)[63] for standard 12 degree circular scans, when the same imaging and segmentation protocols are used.

Anatomically, the ONH of the non-human primate is also smaller and more elliptical[98] compared to that of a human.[302,363] Hence, the scan path of the standard RNFL scan is also significantly further from the rim margin of the ONH for temporal and nasal measures compared to those superior and inferior. In addition, although the monkey optic nerve is smaller, the number of axons passing through the neural canal opening is similar, if not greater, than in human eyes.[162,166,302,333] For the most accurate measures of the RNFL thickness, it is important that both ocular biometry and the shape of the optic nerve be taken into account. When RNFL scans are interpolated from SD OCT raster volume scans centered on the ONH, a scan path 550 μm from the rim margin results in thickness measures that are similar to those from a 12 degree circular path in an adult emmetropic animal.[224] In addition, RNFL area measures, computed by multiplying thickness measures by the scan length, should provide information that is directly related to the axonal content within the nerve fiber layer.

Although RNFL thickness and/or area measures include information on the axonal content, the RNFL also has significant non-neuronal tissue that contributes to the total thickness or area, which varies with the patient's age and stage of disease. Specifically, the retinal vasculature[167,316] and glial tissue[168] within the RNFL constitute a significant portion of the *in vivo* measured thickness. However, the anatomical changes related to glial and vascular tissues, and their contribution to the RNFL thickness over the course of progression of glaucoma, have not been thoroughly defined. Although glial

and small vasculature in the RNFL cannot be imaged with SD OCT systems, the major retinal vasculature casts shadows on the underlying tissue and can be quantified (Mardin CY, et al. IOVS 2009;50:ARVO E-abstract 3333).[167]

The purpose of this study was to determine the changes in the ONH morphology, parapapillary RNFL thickness, and total retinal thickness in the macular area over the time course of experimental glaucoma in the non-human primate using SD OCT technology. The methodology involved custom algorithms for correcting for transverse magnification based on the optical properties of each monkey's eye, construction of elliptical SD OCT scan paths at defined distances from the ONH rim, segmentation of the individual retinal layers, removal of non-neuronal tissue in the RNFL and morphological assessment of the ONH and macula. Each of the structural signs of glaucomatous neuropathy was then correlated to cumulated daily pressure to evaluate IOP effects.

METHODS

Subjects

Normative data were collected from healthy rhesus monkeys ranging in age from 1.9 years to 23 years of age. Longitudinal data were collected from 6 monkeys with unilateral, laser-induced ocular hypertension. All animals maintained good systemic health throughout the experimental period. Data from only one eye of animals was used to create the normative database, while both eyes of the ocular hypertensive animals were analyzed. Experimental and animal care procedures were reviewed and approved by the Institutional Animal Care and Use Committee of the University of Houston. The use of animals for these experiments confirmed to the National Institutes of Health guidelines for the care and use of laboratory animals.

Animal Preparation

The monkeys were anesthetized with an intramuscular injection of ketamine (20-25 mg/kg) and xylazine (0.8-0.9 mg/kg) and treated with a subcutaneous injection of atropine sulfate (0.04 mg/kg). Throughout the experiment, body temperature was monitored and maintained using a thermal blanket (TC1000 temperature controller, CWE, Ardmore), while heart rate and pulse was monitored with a pulse oximeter (model 9847V; Nonin Medical Inc, Plymouth, MN). Additional details on animal anesthesia and monitoring have been previously published.[54,164,224] The animal's pupils were dilated with topical 1% tropicamide and 2.5% phenylephrine, and the head was stabilized using mouth and occipital bars, which were also used for eye alignment during scanning. An eyelid speculum was used to keep the eye open and a plano power, custom designed rigid gas permeable lens was placed on the eye to prevent corneal dehydration, and to maintain optical clarity. For experiments that included fluorescein angiography, the medial surface of the lower leg was shaved and cleaned with 70% isopropyl alcohol. Using a 23 gauge infusion set, 0.1-0.2 ml of 10% sodium fluorescein was administered intravenously, and the animal was monitored for anaphylaxis during the procedure.

Laser Induced Ocular Hypertension

Ocular hypertension in six animals was induced by argon laser scarification of the trabecular meshwork[325,326] using a standard ophthalmic slit lamp based laser system (HGM PC endo, HGM, Salt Lake City, UT). The laser was set to deliver 1.0 W of power with a 50 μm spot size and 0.5 second pulse duration. Contiguous argon laser burns were applied to the trabecular meshwork via a laser gonioscopy lens designed for a monkey's eye (Ocular Kaufman, Ocular Instruments, Bellevue, WA). The initial treatment involved 270 degrees of the drainage angle. Retreatment to elevate

intraocular pressures (IOP) was performed at 4-week intervals and included only 180 degrees of the drainage angle. This protocol has been used successfully to elevate intraocular pressure in the non-human primate, resulting in optic neuropathy and associated function loss, similar to that found with glaucoma.[22,46,324,327,364] On average five laser treatments were necessary to elevate and maintain IOP in the six ocular hypertensive animals in this study. IOP measurements were made using a Tono-Pen XL (Reichert, Inc., Depew, NY) at each scanning session, within ten minutes of administering anesthesia.[365]

Optical Coherence Tomography

All SD OCT scans were acquired using the Spectralis HRA+OCT system, with the high resolution setting (Heidelberg Engineering, Heidelberg, Germany). SD OCT scans used for data analysis included; 1) 12 line, 20 degree radial scan centered on the optic nerve, 2) 49 line, 20 X 20 degree raster scan centered on the optic nerve, and 3) 15 X 20 or 20 X 20 degree raster scan centered on the fovea. The signal to noise ratio was improved by setting B-scan averaging to at least 16 frames. To investigate the normal RNFL axonal map, high density, 193 line raster scans 30 X 20 degrees in size were captured at multiple locations within the central 30 degrees of the fovea in eight animals. These high density scans were acquired with eye tracking, but with averaging of B-scans turned off. The OCT scan data were exported as raw (.vol) files and analyzed using custom software (MATLAB; The MathWorks, Inc., Natick, MA).

Ocular Biometry and Retinal Scaling

Biometry data including corneal curvature, anterior chamber depth and axial

length were obtained using an IOL Master, non-contact optical biometer (IOLMaster, Carl Zeiss Meditec Inc., Dublin, CA). The crystalline lens thickness and curvature were interpolated from published normative data.[163] The refractive index of the lens was computed using a ray tracing algorithm from the measured biometry and SD OCT scan focus setting. These parameters were incorporated into a three surface schematic eye using methodology described by Rabbetts and Bennett.[179] The transverse retinal scaling was calculated from the second nodal point to the retina, assuming a spherical retinal surface. No adjustments were made to axial scaling, which is dependent on the specifications of the imaging system itself. Specifics of the transverse scaling methodology and validation have been detailed elsewhere.[224]

Optic Nerve Head Analysis

The dimensions or the optic nerve head (ONH) rim margin were determined by marking the RPE/Bruch's membrane opening (BMO), also the neural canal opening (NCO)[98,150], on each side of the ONH in 12 radial B-scans and fitting the resulting 24 points with an ellipse (see Fig 6-1A). The segmentation of the inner limiting membrane (Figs 6-1C, red line) and basement membrane (Figs 6-1C, green line) for each scan based on the instrument algorithm was examined and manually corrected when necessary. A spline fit was used to define the ILM surface in regions of the neural canal opening that were obscured by blood vessels. However, the majority of instrument-based segmentation errors were in the identification of the RPE-BM border, which has a similar reflectivity profile to that of the underlying choroid, in the adult rhesus monkey. Thickness data from this segmentation were used to create a mesh grid (Fig. 6-1B), of total retinal thickness as references for calculations of morphological ONH parameters. The rate of thickness change (e.g., where the slope of the thickness profile approached

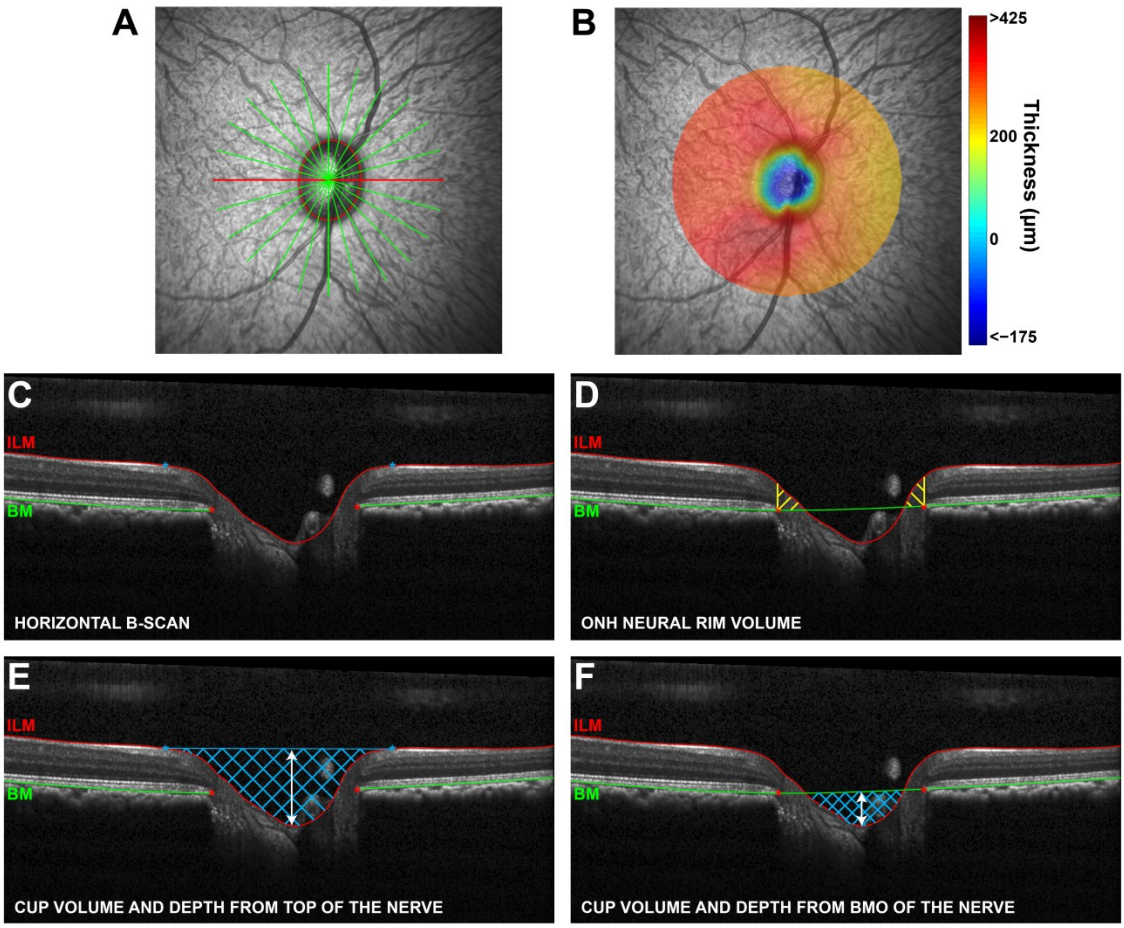

Figure 6-1. Morphological analysis of the ONH using radial SD OCT scans.

A. 30 degree scanning laser ophthalmoscope image along with the scan locations for radial scans used for morphological analysis. The mesh grid (1B) was constructed using the total retinal thickness data from each radial B-scan after correcting and errors in segmentation of the ILM and BM. The horizontal B-scan (red scan path in A) is illustrated in 1C-F. C. The termination of Bruch's membrane at the ONH was marked in each radial scan (red asterisk) and used to delineate the Bruch's membrane opening (red ellipse in 1A). The top of the nerve (blue asterisk) was identified as the location where the first derivative of the total thickness profile approached zero. These landmarks were used to determine ONH neural rim volume (yellow region in D), cup

volume and depth from the top of the nerve (E) and cup volume and depth referenced to the BMO (F).

zero) was used as references for the top and bottom of the ONH cup. The ONH cup depth and volume were quantified with respect to both the top of the ONH and the BMO as reference planes (Fig. 6-1C, E&F). The neural rim volume was quantified as the total tissue included by the vertical line from the point of the NCO and the surface of the ILM in the radial B-scans (Fig. 6-1D).

Retinal Nerve Fiber Layer Analysis

The scanning laser ophthalmoscope (SLO) image from the radial scan was registered to the SLO image from the raster scan centered on the optic nerve using a generalized dual bootstrap iterative closest-point algorithm (i2k retina; DualAlign LLC, Clifton, NY). Subsequently, using this registration transformation, points corresponding to the ONH BMO, as determined using radial scans, were transposed onto the raster scan. From this ONH BMO, an ellipse 550 μm from the rim margin was calculated and used to interpolate an RNFL B-scan from the raster data. The ILM and RNFL/RGC layer borders were identified with a custom MATLAB algorithm.[39] Errors in segmentation, mostly around shadows of major retinal vasculature, were manually corrected. These shadows along with vessels on the SLO image were used to identify the major retinal vasculature in the RNFL. The width of each vessel, along with the manually selected center, was used to demarcate and subtract out a circular region within the RNFL. Specifics for the scan interpolation and segmentation methodology have been presented elsewhere.[63,224]

Although horizontal and vertical eye position can be controlled with the mouth and occipital bars, torsional eye position varies between scanning sessions, especially for monkeys under anesthesia. To compensate, all scans were referenced to a line connecting the centers of the ONH and fovea.[40] The raster scan centered on the fovea

was used to identify the center of the foveal pit. Specifically, the thinnest and thickest regions within the macula was first identified, and circles were best fit to regional thickness measures, within the center of the scan, corresponding to 30 to 60% of the total retinal thickness (Patel NB, et al. IOVS 2009;50:ARVO E-abstract 6207). The average center of the best fit circles was used to describe the center of the foveal pit. This landmark was transposed on to the raster scan SLO image using i2k Retina registration software.

For the six ocular hypertensive animals scanned multiple times, an identical scan path was constructed for each analysis. Specifically, the SLO image and scan path from the baseline scan were registered to each follow up scan. Prior to scan interpolation, the scan path was realigned to the fovea. In instances where the automated registration failed, the ONH rim margin was marked again on the follow up radial scan and registered to the raster scan, from which a RNFL scan path 550 μm from the ONH rim margin was constructed as described above.

Macular Volume

For each raster volume data set, the B-scans along with the instrument segmentation of the ILM and RPE basement membrane (BM) were evaluated for errors. As with radial scan analysis, the majority of segmentation errors were in identification of the RPE-BM. To reduce bias, the B-scans in each volume data set were randomly presented to the user. A thickness map for the central retina scanned was then constructed from the thickness profiles between the ILM and RPE-BM for each raster B-scan. For data analysis, only thickness information from a circular region 3 mm in diameter and centered on the fovea was used (dashed regions Fig 6-9). Total retinal volume was calculated as the mean thickness in this region multiplied by the area

analyzed (7.07 mm^2).

RNFL Axonal Pathway Analysis

To relate macular volume to RNFL area, it was important to know the course of RGC axons from the macular area to the ONH. Although individual axonal fibers cannot be resolved with an SD OCT system, fiber patterns can be appreciated in an *en face* view. For the highest transverse resolution of *en face* images, high density raster volume OCT data are used. Adjacent B-scans in the volume data are then aligned and scans are interpolated at various depths in the image plane. To visualize the RNFL, scans are aligned to the ILM prior to scan interpolation. Due to hardware and software limitations, the maximum scan density used was 193 B-scans within a 30 X 20 degree region. Hence, multiple overlapping scans were necessary to cover the central 60 degrees of the retina. Using image registration, images from equal depths were created for this region of interest.

The image series created for the various depths was used to trace the RGC axon pathway from the retina to the optic nerve for 8 normal rhesus monkey eyes (Fig. 6-2). A circular region 3 mm in size was centered on the fovea and used to determine the maximal extent of the nerve fiber from the region (Fig 6-2I). The intersection of the nerve fiber trace from the maximal extent of the macula region sampled and an ellipse 550 μm from the ONH rim margin was used to determine the corresponding region sampled in the RNFL measures. Overall, the angular subtense to the center of the optic nerve was 51.7±7 degrees for the superior arcade and 50.7±5 degrees for the inferior arcade.

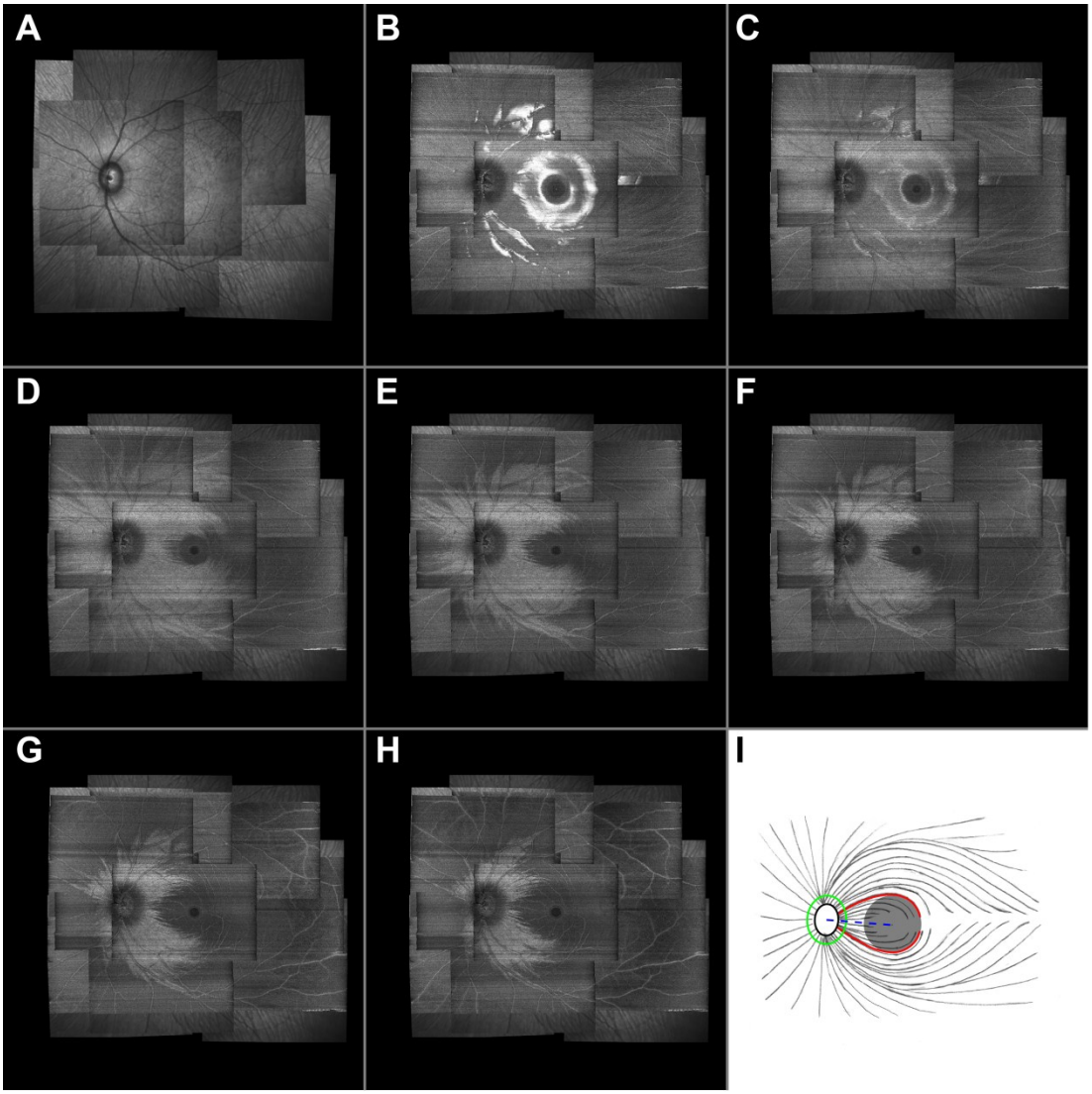

Figure 6-2. RNFL pathway in the retina.

Montage of nine infrared scanning laser ophthalmoscope images within the central 60 degree of the retina. Starting at the inner limiting membrane interface, B-H illustrate the nerve fiber layer at various depths in the SD OCT volume. Each image in the series is interpolated at a depth 7.73 μm greater than the previous. I. Illustrates the nerve fiber layer tracing produced from the image series B-H. This tracing was used to estimate the sector of the RNFL (green ellipse) sampled within the central 3mm of the foveal pit (gray

region). The outer limits of the nerve fiber layer from this region of interest are outlined in red.

RESULTS

Normative data was collected from 47 animals ranging from 1.9 years to 23.7 years of age (mean age = 9.1 ± 6.4 years). Axial lengths in these animals measured between 15.2 mm and 21.1 mm (average = 19.3 ± 1.2 mm). The mean age of the six animals with unilateral ocular hypertension was 7 years and 1 month. Intraocular pressure data from both the control and laser-treated eyes are illustrated in figure 6-3. Time points at which laser treatments were applied are marked with a red asterisk. Laser treatments needed to achieve a sustained IOP elevation ranged from 3 to 10 sessions. The IOP difference between the two eyes (gray region Fig. 6-3A-F) was used to calculate a cumulative IOP,[366] expressed as mmHg.days, and referenced to the first laser treatment. The longest follow up was 822 days, while the shortest was 181 days after the first laser treatment. Figure 6-3G illustrates the cumulative IOP as a function of days after laser treatment. The slope trends for individuals subjects provides comparative information on the stability and changes in IOP.

Optic Nerve Head Analysis

Data for the mean, standard deviation and CV for ONH cup parameters for control (normal) eyes are illustrated in table 6-1. The relationships between scaled ONH cup parameters and axial length were not statistically significant ($p>0.1$) for any parameter. Of the 47 animals analyzed, the ONH cup depth for 9 animals did not reach the level of the BMO. However, all animals had finite ONH cup depth and volume values when the measurement was referenced to the top of the ONH (see Fig. 6-1). Hence, the coefficient of variation was larger for all ONH cup measures referenced to the BMO, than when referenced to the top of the ONH. Both the ONH cup depth (slope = 233.4 $\mu m/mm^2$, $R^2 = 0.15$, $p < 0.01$), and ONH cup volume (slope = 0.32 mm^3/mm^2, R^2 =

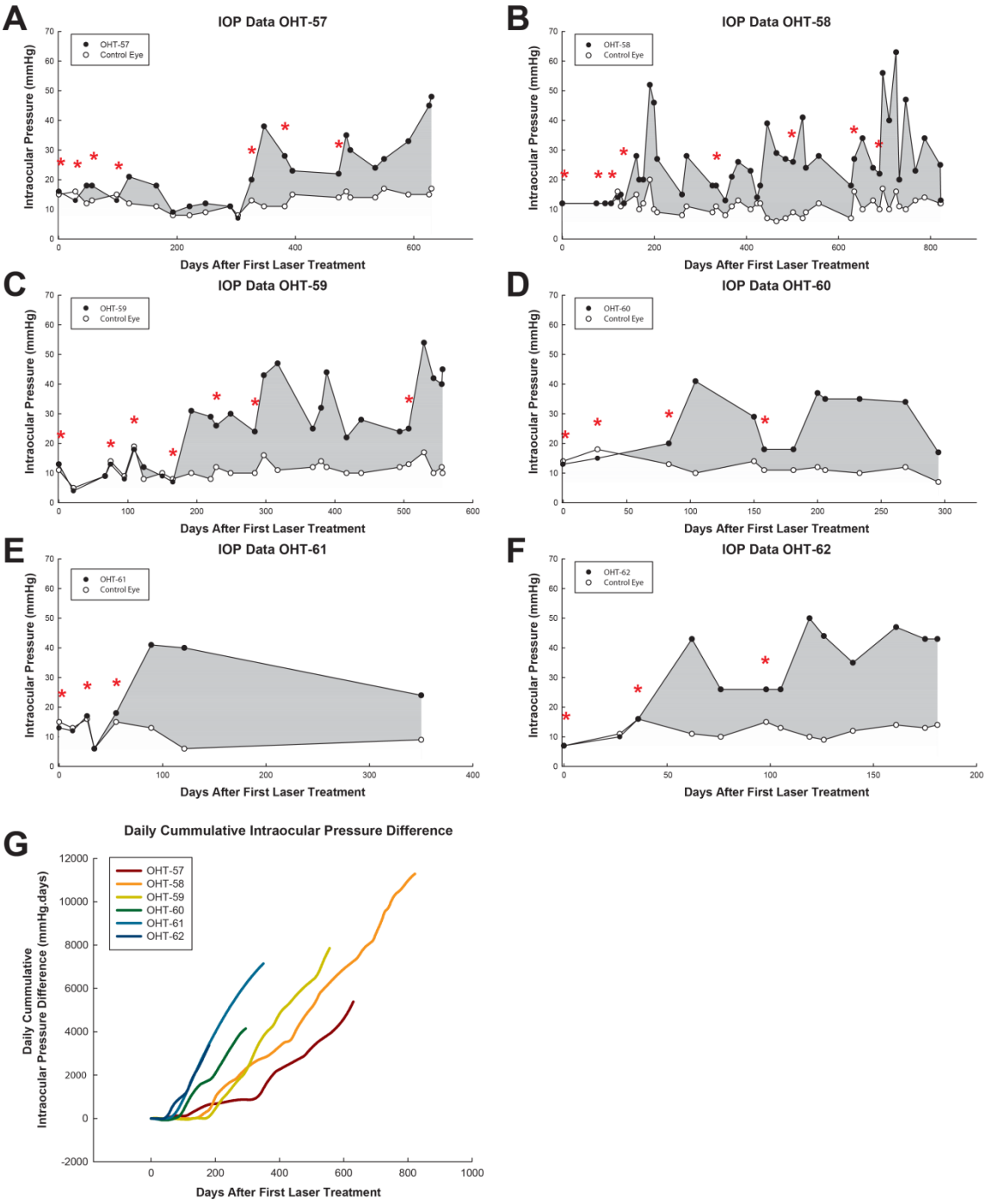

Figure 6-3. IOP data for ocular hypertensive and control eyes.

The red asterisk represent the days when laser treatment was performed. The IOP difference between the two eyes (shaded region), was used to calculate the integrated intraocular pressure (G).

	NORMATIVE DATA n = 47			OHT Control Eyes n = 5
	Mean	Standard Deviation	CV (%)	Repeatability ($2.77 \times S_w$)
Rim Volume (mm^3)	0.298	0.068	22.9	0.012
Cup Volume at BMO (mm^3)	0.009	0.015	162.3	0.005
Cup Volume from Top (mm^3)	0.224	0.107	47.7	0.017
Cup Ratio	0.075	0.08	111.8	0.012
Cup Depth from BMO (µm)	126.4	113.3	89.6	17.6
Cup Depth from Top (µm)	462.9	125.9	27.2	25.6

Table 6-1. Morphological measures of the optic nerve.

Morphological measures of the optic nerve referenced from the top of the nerve and the basement membrane opening. Repeatability was assessed using the repeat scans on the control eyes of 5 ocular hypertensive animals.

0.44, p <0.01) measured from the top of the ONH were linearly related to the size of the BMO. However, there was no relationship between BMO area and either ONH rim volume (p = 0.09) or axial length (p = 0.49).

Of the control eyes in the six ocular hypertensive animals, one animal had only two acceptable ONH scans and was excluded from the ONH analysis. The repeatability of ONH cup measures was assessed using the within-subject standard deviation (S_w) from the control eyes ($2.77 \times S_w$).[279] Specifically, based on the measurements error, or within subject standard deviation (S_w), 95% of measures should be within $1.96 \times S_w$. Hence, the repeatability, or difference between any two measures from the same individual should not exceed $\sqrt{2} \times 1.96 \times S_w$ for 95% of measures. Although there was significant inter-subject variability in the normative data there was good repeatability for all ONH morphological measures (Table 6-1).

For the analyses of the effects of experimental glaucoma, the two parameters (rim volume and cup depth from the top of the nerve) that had the smallest coefficients of variation in the normative data were used for assessing change. Disease state was determined as the first time point at which a measure exceeded two times the standard deviation of the normative data (95% confidence limit), while progression or a significant change was determined as the time point at which the morphological measure exceeded the normal intra-subject repeatability (mean - $2.77 \times S_w$). These data along with the cumulative IOP at the respective time points are illustrated in figure 6-4 and tables 6-2&3 for each animal. For every animal, the cup depth increased linearly with cumulative IOP (range of slopes = 0.01 to 0.10 µm/mmHg.days). However, only 9.3% of the variation was explained by the best linear regression fit for all ocular hypertensive eyes (p = 0.03). This trend and variability in cup depth are illustrated in figure 6-5 for three ocular hypertensive animals. Specifically, animals with shallow cups showed larger overall

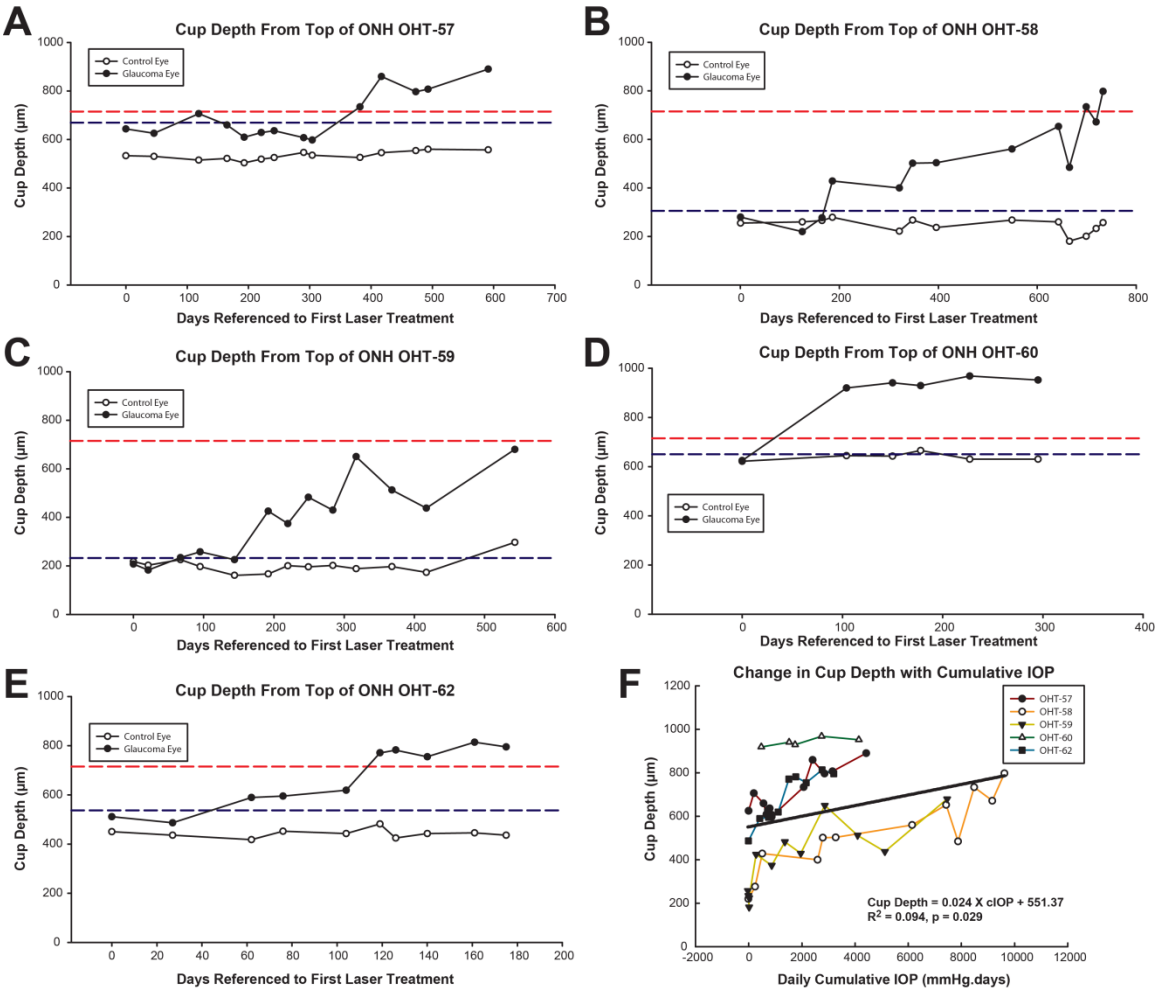

Figure 6-4. ONH cup depth for ocular hypertensive and control eyes.

A-E. ONH cup depth for control eyes (open circles) and ocular hypertensive eyes (closed circles) as a function of time. The red dashed line illustrates the 95% confidence interval for the normative data. The blue dashed line illustrates the cup depth needed to exceed the test retest repeatability from the subject's baseline measures. F. Cup depth increased linearly for each animal with cumulative daily IOP, with significant variability in slope measures.

OHT-59

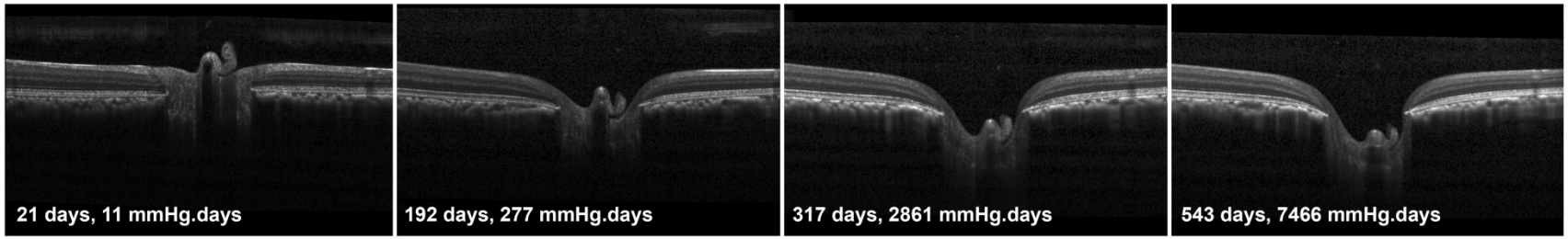

OHT-60

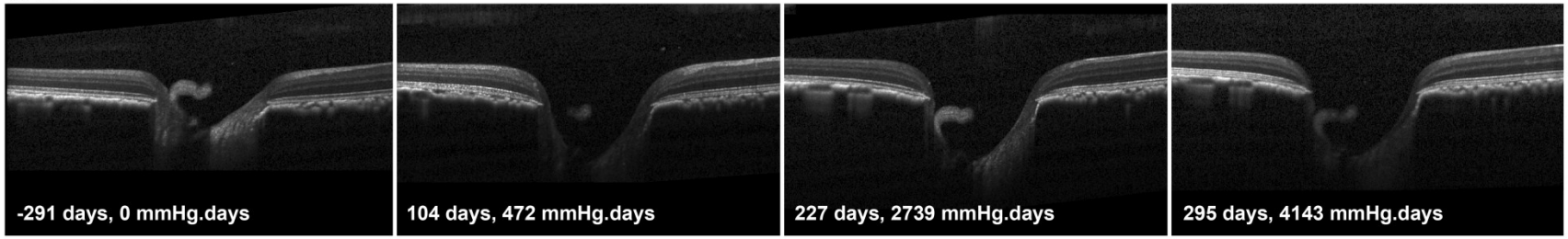

OHT-62

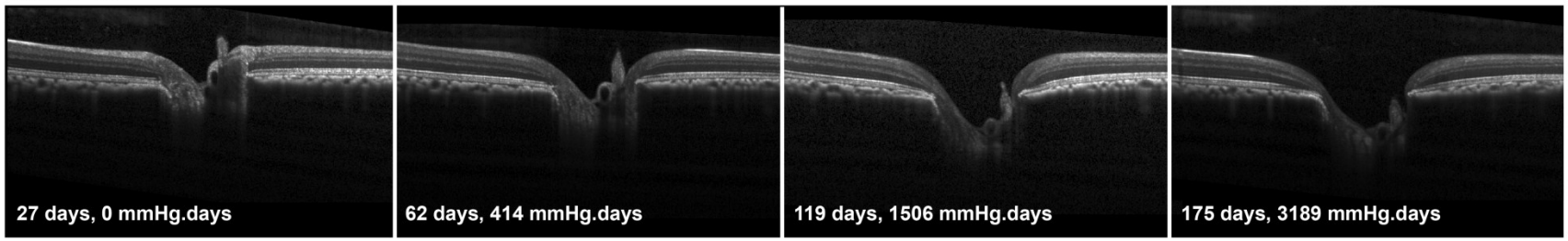

Figure 6-5. Variability in physiological ONH cupping and changes with IOP. Horizontal radial B-scans for three ocular hypertensive eyes at 4 time points, the first image being prior to any significant increase in intraocular pressure. The B-scans illustrate the variability between animals and the changes in cup depth and rim volume associated with the duration of elevated pressure and the cumulative daily IOP.

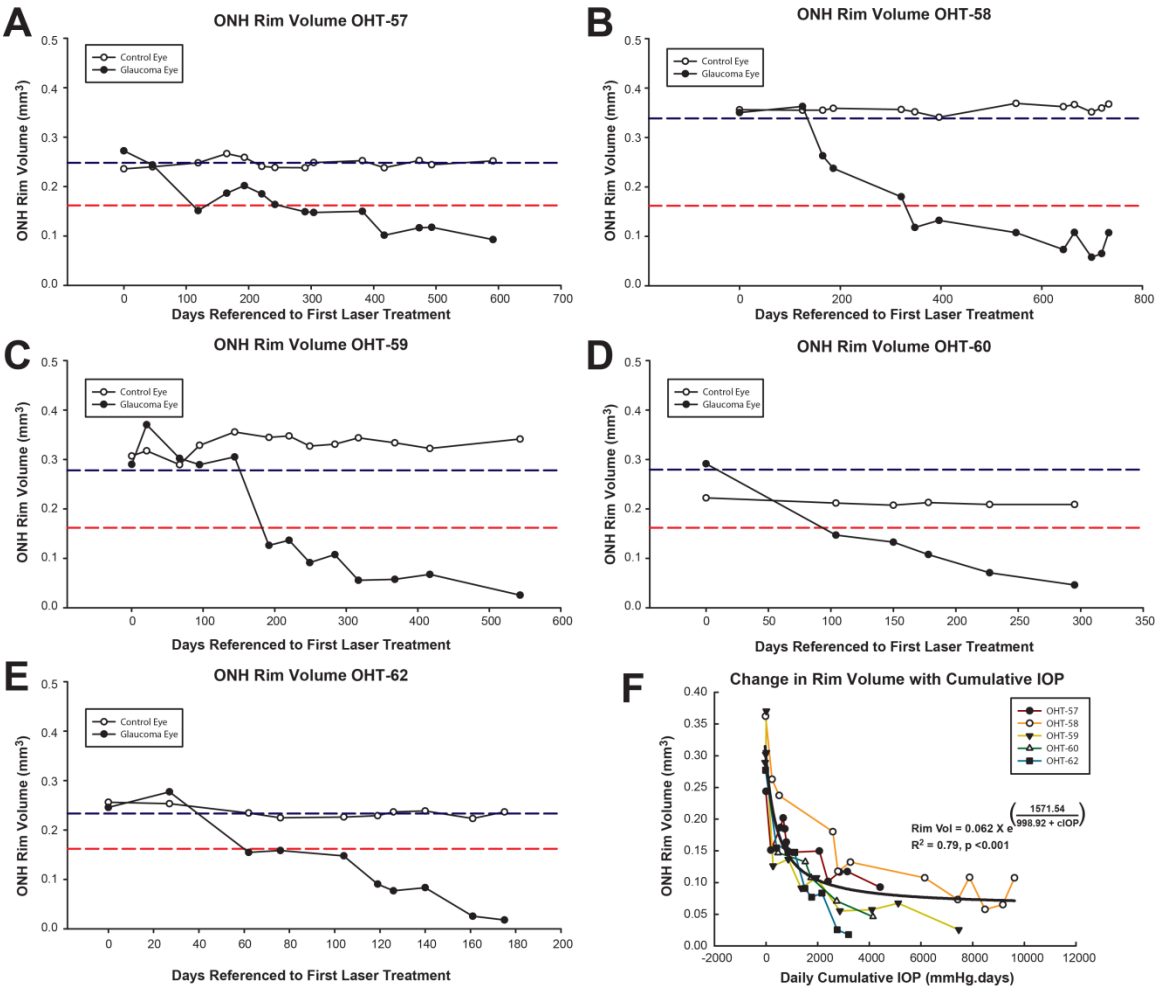

Figure 6-6. ONH rim volume for ocular hypertensive and control eyes.

A-E. ONH rim volume for control eyes (open circles) and ocular hypertensive eyes (closed circles) as a function of time. The red dashed line illustrates the 95% confidence interval for the normative data. The blue dashed line illustrates the cup depth needed to exceed the test retest repeatability from the subject's baseline measures. Overall, all five animals showed a significant change in rim volume within 200 days of the first laser treatment. F. An exponential decay model best describes the change in rim volume as a function of cumulative daily intraocular pressure.

CUP DEPTH FROM TOP OF ONH (µm)	First scan at which measures exceeded test-retest		First scan at which measures exceeded 95% CI of normative data	
	Days after first laser treatment	Cumulative daily IOP(mmHg.days)	Days after first laser treatment	Cumulative daily IOP(mmHg.days)
OHT-57	119	192	382	2065
OHT-58	168	266	699	8478
OHT-59	67	0	Not Reached	
OHT-60	104	472	104	472
OHT-62	62	414	119	1506

Table 6-2. Cup depth in ocular hypertensive eyes.

Days after first laser treatment and cumulative IOP for first detection of progression and time points for when data were first outside the 95% limits of the normative data for the cup depth from the top of the ONH. Zero cumulative pressures indicate no change in IOP from baseline.

ONH RIM VOLUME (mm^3)	**First scan at which measures exceeded test-retest**		**First scan at which measures exceeded 95% CI of normative data**	
	Days after first laser treatment	Cumulative daily IOP(mmHg.days)	Days after first laser treatment	Cumulative daily IOP(mmHg.days)
OHT-57	46	0	119	192
OHT-58	125	0	348	2786
OHT-59	192	278	192	278
OHT-60	104	472	104	472
OHT-62	62	414	62	414

Table 6-3. Rim volume in ocular hypertensive eyes.

Days after first laser treatment and cumulative IOP for first detection of progression and time points for when data were first outside the 95% limits of the normative data for the ONH Rim Volume. Zero cumulative pressures indicate no change in IOP from baseline.

changes than those who had physiologically large cups at baseline. The ONH neural rim volume was less variable and also decreased systematically with increasing cumulative IOP. Specifically, these data were best fit using an exponential decay model (Fig. 6-6, $R^2 = 0.78$, $p < 0.01$). Based on these results, only neural rim volume was used for further analysis of ONH morphology.

Retinal Nerve Fiber Layer

The mean global RNFL thickness for the normative data was 124.95 ± 8.92 μm and 113.53 ± 8.45 μm after removal of the major retinal vasculature, corresponding to global area measures of 953127.3 ± 72420 μm^2 and 865939.3 ± 67645.2 μm^2 (9.16 ± 1.12% vascular contribution). RNFL area measures did not show a significant relationship with axial length ($R^2 = 0.04$, $p = 0.11$). In general, animals with greater global measures also had a larger vascular thickness/area contribution ($R^2 = 0.23$, $p = 0.001$). Consequently, the percent vascular contribution to RNFL area was similar across the range of RNFL measures for normal healthy eyes ($R^2 = 0.05$, $p = 0.13$). Repeatability of RNFL measures, based on the control eyes of the 6 ocular hypertensive animals, was 4.0 μm for global thickness and 31408 μm^2 for area measures after removal of major retinal vasculature.

A decrease in RNFL area was measured in all six ocular hypertensive eyes. Table 6-4 illustrates the time points and cumulative IOP measures for when RNFL measures decreased past the test-retest repeatability and the 95% confidence interval of the normative data. Although all animals showed progressive loss, RNFL area measures for subject OHT-57 did not fall below the 95% confidence interval of the normative data. As illustrated in figure 6-7G, RNFL area measures decreased exponentially with increase in cumulative IOP ($R^2 = 0.39$, $p < 0.01$).

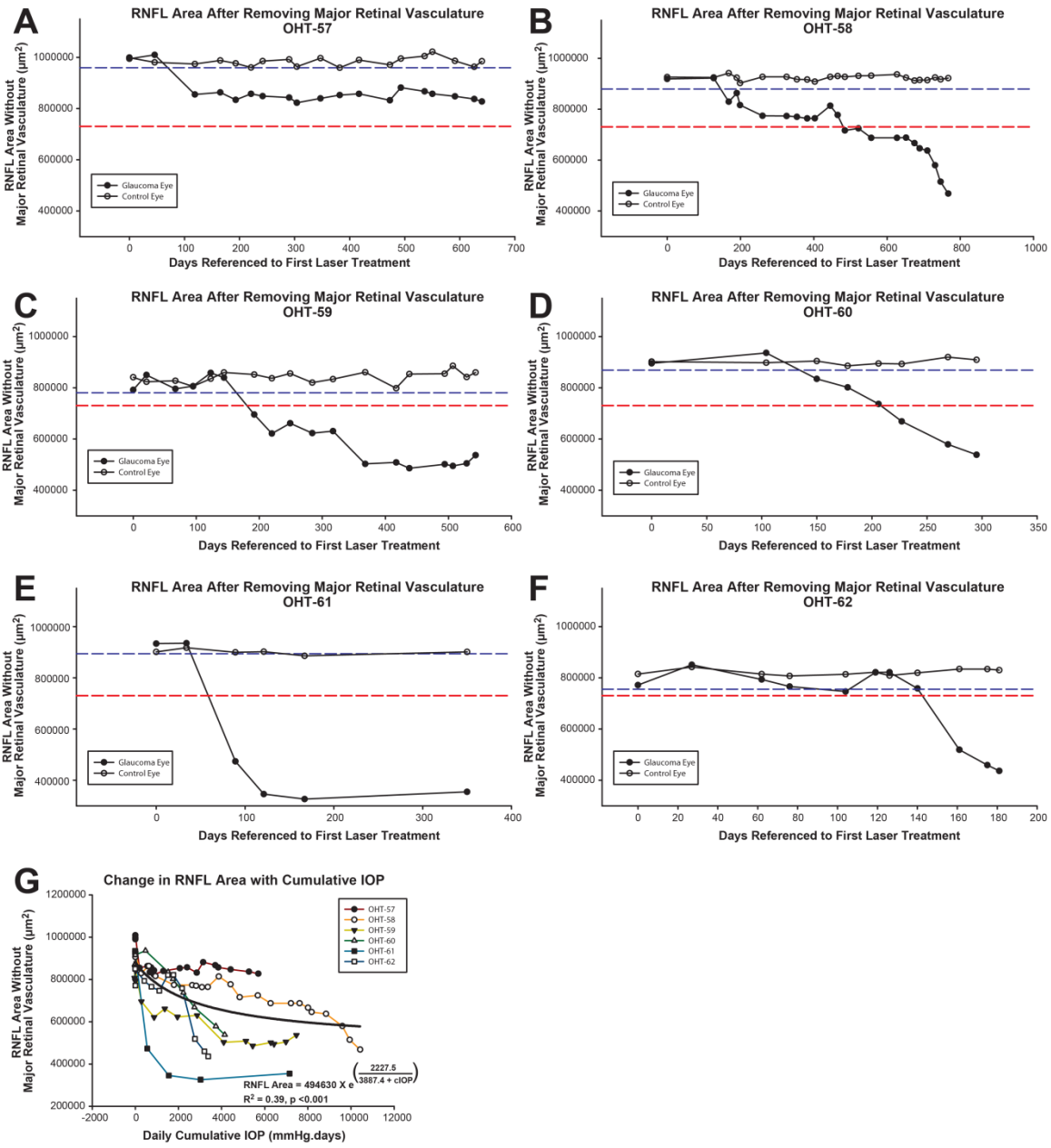

Figure 6-7. Global RNFL area for ocular hypertensive and control eyes.

A-F. Global RNFL area measures after subtraction of major retinal vasculature for control eyes (open circles) and ocular hypertensive eyes (closed circles) as a function of time. The red dashed line illustrates the 95% confidence interval for the normative data. The blue dashed line illustrates the RNFL area needed to exceed the test retest

repeatability from baseline measures. All animals showed a decrease in RNFL area, however, the RNFL area for OHT-57 did not decrease past the normative data. G. The decrease in RNFL area with cumulative daily IOP was best fit using an exponential decay model.

RNFL Area (μm^2)	First scan at which measures exceeded test-retest		First scan at which measures exceeded 95% CI of normative data	
	Days after first laser treatment	Cumulative daily IOP(mmHg.days)	Days after first laser treatment	Cumulative daily IOP(mmHg.days)
OHT-57	119	192	Not Reached	
OHT-58	168	266	485	4840
OHT-59	192	278	192	278
OHT-60	150	1522	227	2739
OHT-61	89	556	89	556
OHT-62	104	1108	161	2759

Table 6-4. RNFL area in ocular hypertensive eyes.

Days after first laser treatment and cumulative IOP for first detection of progression and time points for when data were first outside the 95% limits of the normative data for the RNFL area.

The major retinal vascular contribution to global RNFL measures for the six ocular hypertensive eyes at baseline was within the 95% confidence interval of the normative data (Fig. 6-8A&B). With loss of RNFL, there was no appreciable change in the location of the major retinal vasculature. Specifically, the location and number of peaks and troughs in the RNFL TSNIT plots with and without vessel subtraction were similar across scan sessions (Fig. 6-8C). As anticipated, there was an increase in the percent vascular contribution to the global RNFL measures with disease severity (Fig. 6-8B, $R^2 = 0.64$, $p < 0.01$). However, the overall vascular area contribution decreased with increasing disease severity (Fig. 6-8A, $R^2 = 0.33$, $p < 0.01$). Figure 6-8D illustrates the segmentation and vascular caliber for an identical section of the RNFL B-scan for one subject at various stages of RNFL loss. Although the vessels in these B-scans appeared circular, there were varying degrees of changes in vessel caliber associated with disease progression (data not shown). However, the major retinal vessels for each animal were well perfused as illustrated by the fluorescein angiographies performed at the last scan session (Fig. 6-8C,&E). In addition, no signs of optic atrophy of retinal anoxia were ever noted during the period studied.

Macula Volume

For the normative data, the mean macula volume within the central 3 mm of the fovea measured 2.24 ± 0.11 mm^3, corresponding to a coefficient of variation of 5.05%. As with other morphological measures, there was no significant relationship between macula volume and axial length ($p = 0.49$). Repeatability of this measure, based on the control eyes of the six ocular hypertensive animals was 0.06 mm^3. For the ocular hypertensive eyes, there were significant changes in the total retinal thickness for the region scanned. Figure 6-9 illustrates total retinal thickness maps and the associated

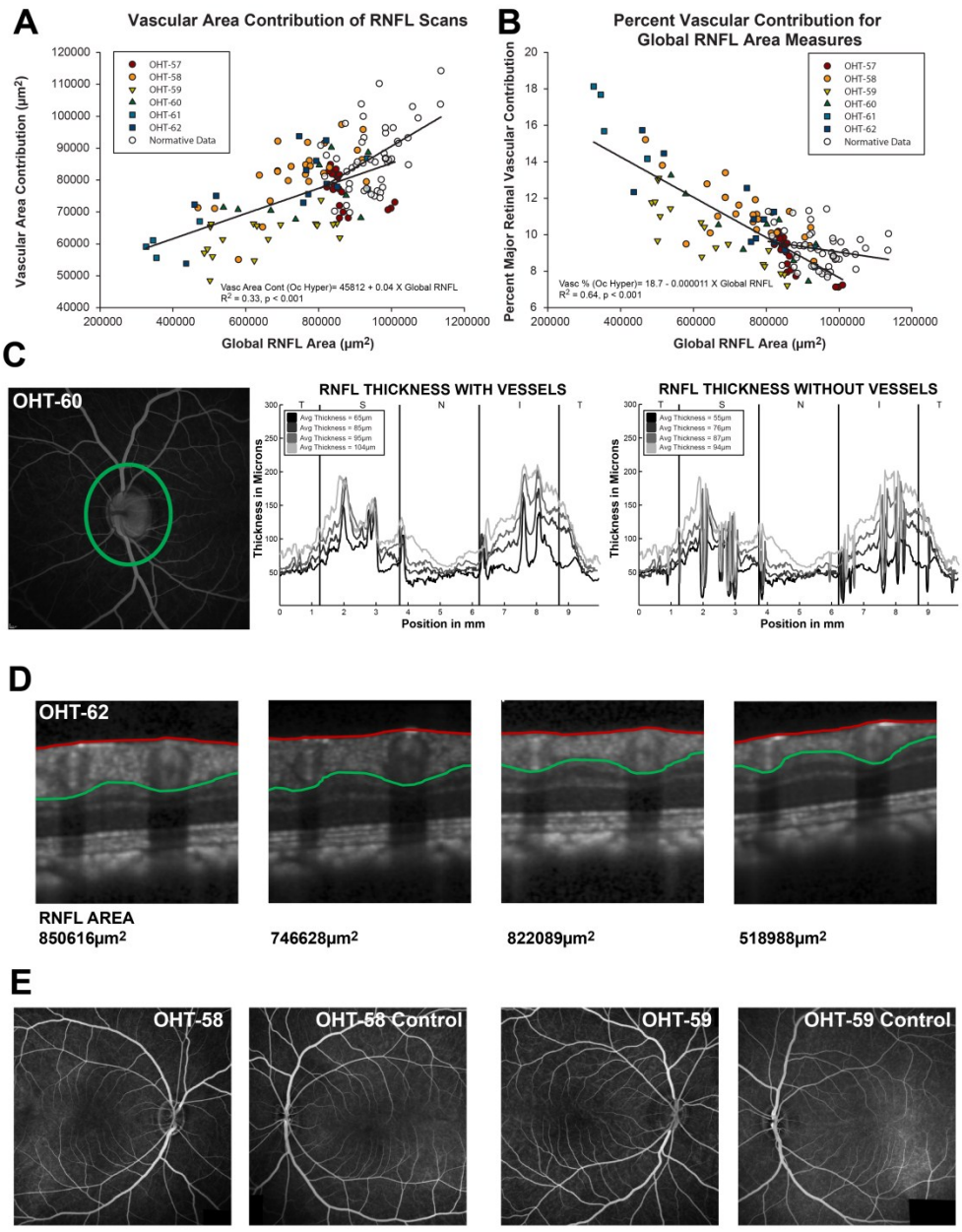

Figure 6-8. Changes in retinal vasculature with loss of RNFL.

A. Vascular area contributions for normal and ocular hypertensive eyes. The normative data are represented by open circles while each colored symbol represents a separate ocular hypertensive subject. B. The percent vascular contribution to the global RNFL area for the data presented in 7A. C. TSNIT plots for an ocular hypertensive eye at various stages of RNFL loss. The major retinal vasculature is located in sections

corresponding to the peaks and toughs within the plots. The fluorescein angiography images, with the scan paths illustrated, are included for comparison with the TSNIT plots. D. A portion of the superior RNFL B-scan for an ocular hypertensive eye at various stages of RNFL loss. The image illustrates the segmentation and shape and size of two major retinal vessels within the RNFL. E. Good retinal perfusion was documented through fluorescein angiographies performed at the final scan time point.

OHT-59
Baseline
21 days, 11 mmHg.days
192 days, 277 mmHg.days
317 days, 2861 mmHg.days
543 days, 7466 mmHg.days
Total Retinal Thickness (µm)
>375
275
175
<100
Change in Retinal Thickness (µm)
>20
0
-30
<-60
OHT-62
Baseline
27 days, 0 mmHg.days
62 days, 414 mmHg.days
119 days, 1506 mmHg.days
175 days, 3189 mmHg.days
Total Retinal Thickness (µm)
>375
275
175
<100
Change in Retinal Thickness (µm)
>20
0
-30
<-60

Figure 6-9. Changes in total retinal thickness with glaucoma progression.

A&B. Macula thickness maps for two ocular hypertensive eyes, at various stages of disease. The SLO images and thickness maps are aligned to that of the baseline scan for comparison. The dashed circular region represents the 3 mm zone used for calculating the macula volume. The top row illustrates the total retinal thickness while the bottom row for each image series represents the total retinal thickness change from baseline.

thickness change from baseline for two animals. Although the macula volume of all the ocular hypertensive eyes decreased as a function of cumulative IOP (Fig. 6-10G), and showed progression, none of these measures fell outside the 95% confidence interval of the normative data. In addition, the time it took to reach a measurable difference in macula volume was longer than that for ONH morphology or RNFL area measures (Table 6-5).

Relationship between morphological measures

For comparison of ONH, RNFL and macula morphology, measures were first converted to standard scores (z scores) using both within subject standard deviation and the standard deviation of the normative population. Standard scores based on the within subject standard deviation illustrate the ability to detect progression, while scores based on the standard deviation of the normative data describe when measures fall outside the normal population and disease can be detected. These data for each animal were plotted as a function of cumulative daily IOP and fit using an exponential decay model (Fig. 6-11). Based on these plots and the individual data (Tables 6-2:5), statistically significant changes were first measured for the ONH rim volume, followed by the RNFL area. Changes in the macula volume were realized later in the disease process and did not exceed the variability within the normal population.

Axons in the RNFL also form the rim volume of the ONH. Hence, there should be a relationship between the two morphological measures. Figure 6-12 illustrates the relationship between ONH rim volume and global RNFL area. Overall, the rim volume shows a significant decrease prior to changes in the RNFL. The best fit to the data was with an exponential rise to maximum model (Fig. 6-12, $R^2 = 0.64$, $p < 0.01$). Based on this best fit equation, as the neural rim volume approaches zero, the residual RNFL area

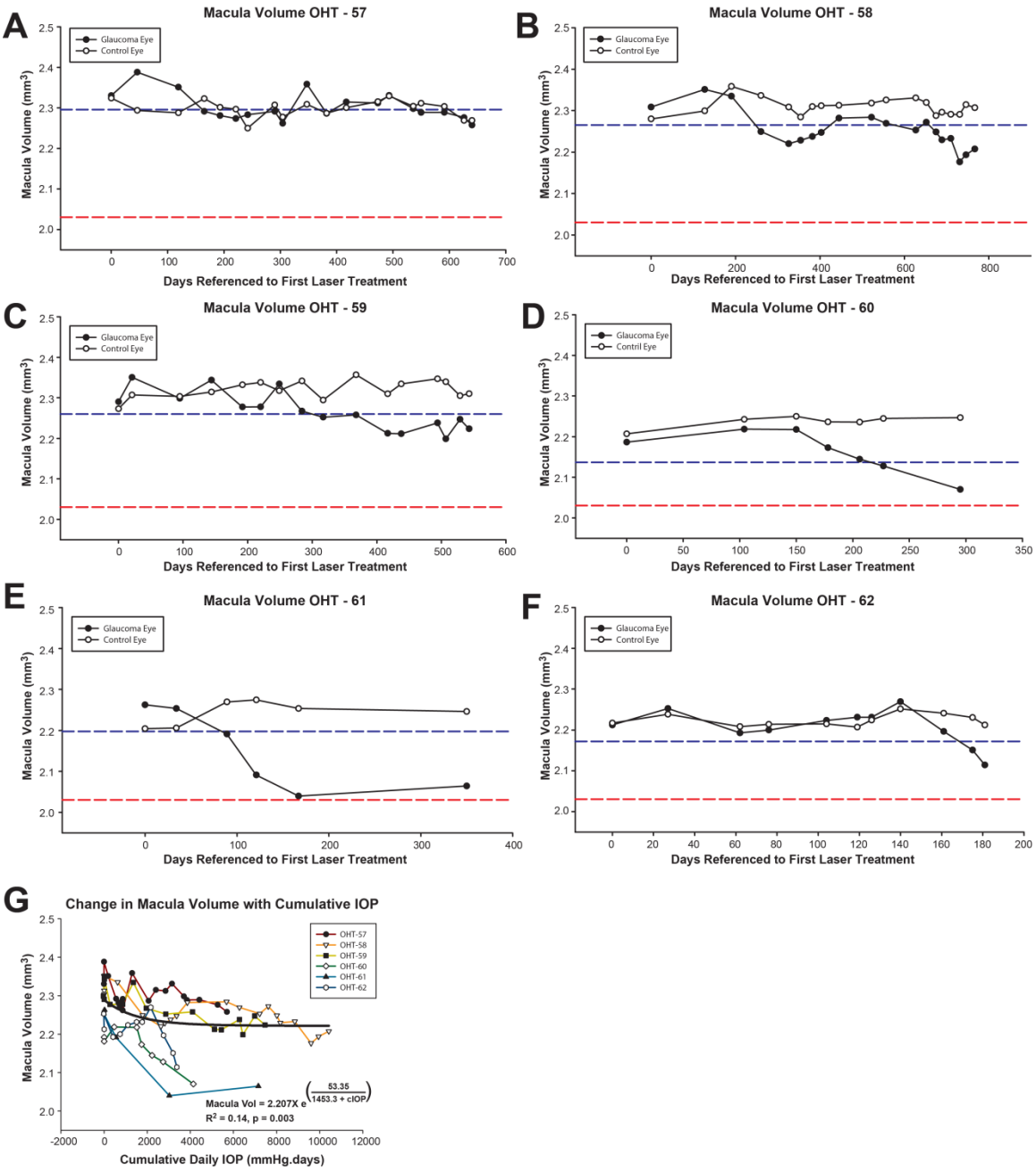

Figure 6-10. Macula volume for ocular hypertensive and control eyes.

A-F. Macula volume within the central 3 mm circular region for control eyes (open circles) and ocular hypertensive eyes (closed circles) as a function of time. The red dashed line illustrates the 95% confidence interval for the normative data. The blue dashed line illustrates the macula volume needed to exceed the test retest repeatability

from the individual's baseline measures. Although all animals showed change, none exceeded the 95% confidence interval for the normative data. G. The decrease in macula volume with cumulative daily IOP was best fit using an exponential decay model.

Macula Volume (mm^3)	First scan at which measures exceeded test-retest		First scan at which measures exceeded 95% CI of normative data	
	Days after first laser treatment	Cumulative daily IOP(mmHg.days)	Days after first laser treatment	Cumulative daily IOP(mmHg.days)
OHT-57	193	668	Not Reached	
OHT-58	260	1786	Not Reached	
OHT-59	317	2862	Not Reached	
OHT-60	227	2739	Not Reached	
OHT-61	121	1551	Not Reached	
OHT-62	175	3199	Not Reached	

Table 6-5. Macula volume in ocular hypertensive eyes.

Days after first laser treatment and cumulative IOP for first detection of progression and time points for when data were first outside the 95% limits of the normative data for the macula volume.

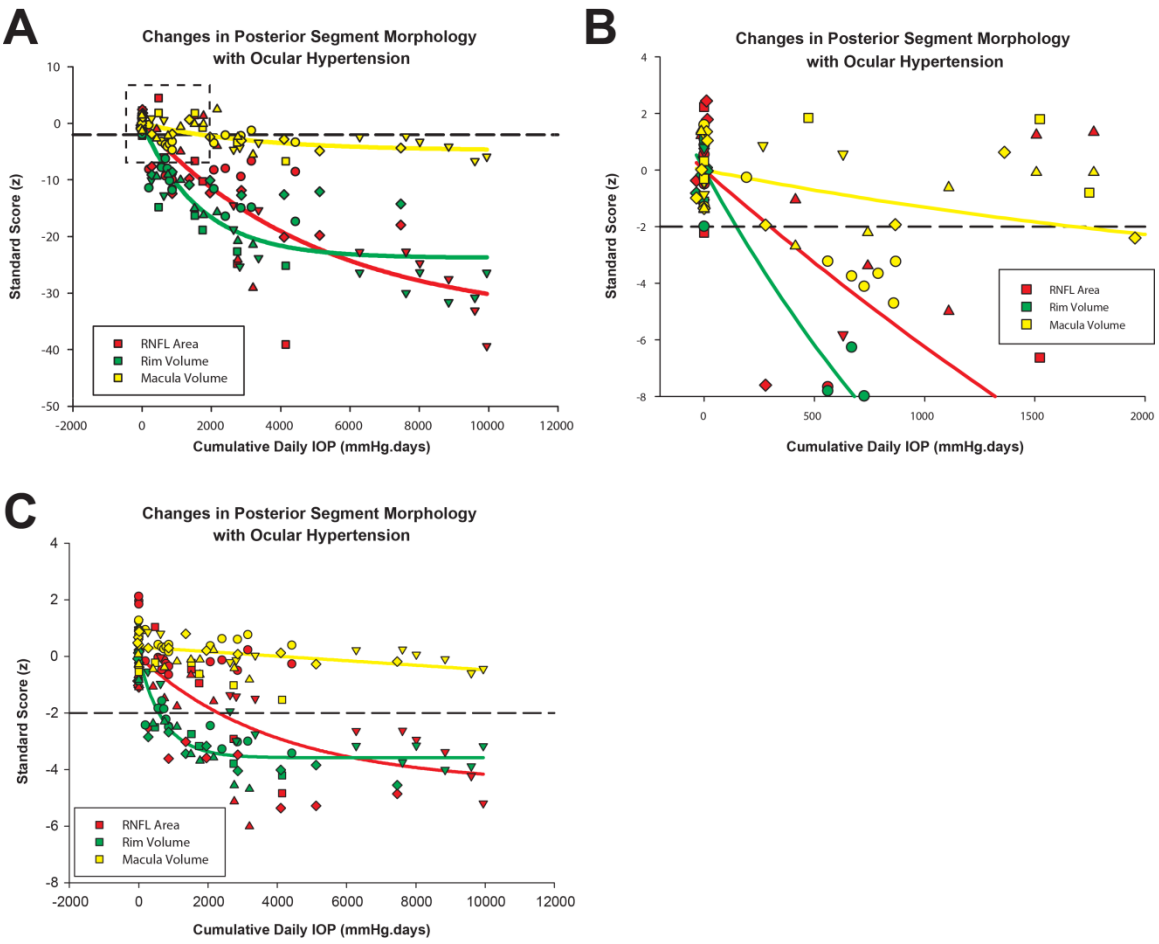

Figure 6-11. Morphological changes in the posterior segment plotted as standard scores.

A. Standard scores based on within subject standard deviations plotted as a function of integrated daily IOP. The dashed line represents 2 standard deviation units, a point at which progression could be identified. Data within the dashed boxed region are illustrated in B. C. The general trend in morphological changes remained the same when standard scores were based on the standard deviation for the normative data.

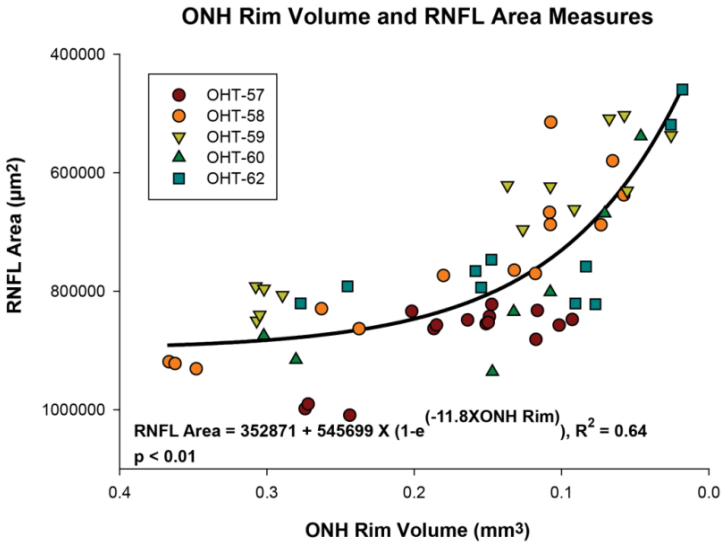

Figure 6-12. The relationship between ONH rim volume and RNFL area.

ONH rim volume decreased prior to changes in RNFL area measures for all animals included in this study. The axes of the plot are reversed to illustrate the effects of disease progression on each measure.

would measure 352,871 μm^2, corresponding to a global thickness measure of 46.2 μm for a 550 μm elliptical scan path from the optic nerve rim margin.

Any decrease in macula volume is most likely a result of RGC loss within the region.[57] Hence, a decrease in macula volume should be correlated to changes in the RNFL area corresponding to the papillomacular bundle. The 3 mm circular region sampled for macula measures corresponded to a 102.4 degree sector of the temporal retinal nerve fiber layer as discussed in the methodology (Fig. 6-2). As expected, the changes in these two morphological measures were well correlated and the best-fit function was linear (Fig. 6-13, $R^2 = 0.61$, $p < 0.01$).

DISCUSSION

High resolution imaging of the posterior segment provides important diagnostic information for the health of the eye. Although several imaging techniques are often used to assess the retina and ONH, only SD OCT provides sufficient resolution to identify and quantify the thickness of each of the retinal layers in cross-section images. With the resolution of modern imaging technology, it is necessary to include the optical and biometric properties of the patient's eye to achieve accurate measurements for patient management and clinical research. In the present investigations, methods have been developed and applied to include relative retinal magnification, accurate segmentation, morphological analysis of the ONH, and contributions of major retinal vasculature to the RNFL.

The rhesus monkey is often used for vision research because their visual system is both anatomically and functionally similar to that of the human. However, several differences in ocular anatomy between the two species needed to be taken into consideration. Specifically, the rhesus monkey has, 1) a shorter eye with higher

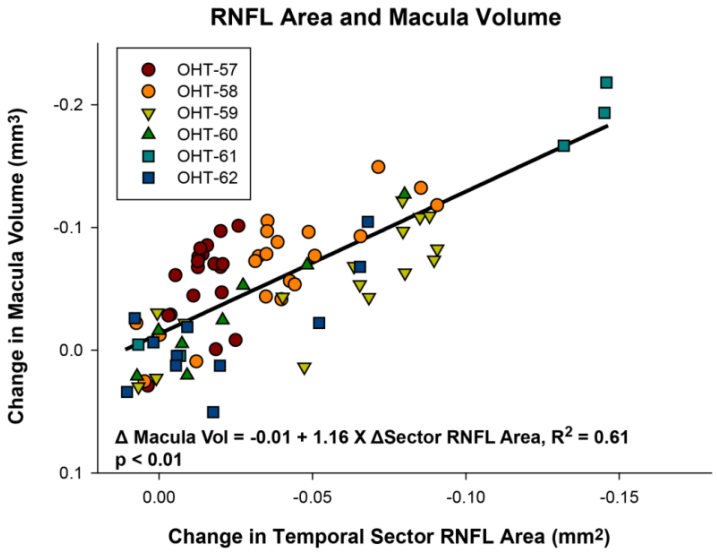

Figure 6-13. The relationship between macula volume and RNFL area.

The change in macula volume is linearly related to changes in the corresponding sector RNFL area.

equivalent power,[163,178] 2) the optic nerves are smaller, yet may contain a larger number of axons,[162,166] and 3) the optic nerve has a prominent elliptical shape.[98,224] The influence of ocular biometry on SD OCT was modeled using a three surface schematic eye which accurately described changes in retinal magnification associated with variation in axial length. Similarly, when retinal scaling was used to construct a custom elliptical RNFL scan path, global thickness measures were not related to ocular biometry, as compared to the significant relationship with standard 12 degree circular scans.[224] Although these previous studies provided significant data on the normal anatomy of the posterior segment, most subjects were juvenile (<2 yrs of age). Hence, to analyze morphological changes associated with ocular hypertension, it was essential to collect normative data for adult animals with a similar age range.

In addition to the typical measurements of RNFL thickness[224] and macula volume, methodologies for optic nerve head analysis were also implemented in the present study. In general, measures referenced to the basement membrane opening (BMO), corresponding to the neural canal opening (NCO),[98,150] and the top of the optic nerve were investigated. Of these measures, the neural rim volume and ONH cup depth from the top of the ONH were the least variable in the normal population and had very good repeatability. Although there are no reports on the cup depth from the top of the optic nerve head in non-human primates, the average rim volume was similar to previous reports in this species.[114] Overall, these *in vivo* measures show similar features and trends compared to human eyes. For example, eyes with larger BMO areas also had a deeper physiological ONH cup depth and cup volume, corresponding to larger clinically observed cup to disc ratio in human patients.[23] Although larger optic nerves are often thought to have more axons,[162,224] the neural rim volume was not related to the size of the BMO and, therefore, these present data are not in agreement with previous

reports of a relationship between ONH size and neural rim area.[367,368] This discrepancy illustrates the importance of a three dimensional volume measure compared to a one or two dimensional area or thickness measure in assessing neural rim characteristics.

ONH morphological measures had the earliest sign of progression in the eyes with experimental glaucoma. Although, for each individual, the ONH cup depth decreased linearly with cumulative intraocular pressure, the large inter-subject precludes a generalizable relationship. In contrast, the decreases in ONH rim volume were similar across animals and showed more consistent trends with cumulative IOP. This finding is in agreement with current clinical practice, where a greater emphasis is placed on observation of the neural rim tissue than on the cup to disc ratio itself.[23] In addition, the neural rim volume had decreased by up to 60% from baseline measures prior to RNFL area measures falling outside the normative data. These results are in agreement with morphological changes of the optic nerve reported in early glaucoma in non-human primates.[114] Hence, the non-linear relationship between ONH rim volume and RNFL area provides support for the biomechanical hypothesis/paradigm of glaucoma.[113]

It is possible that the ONH changes measured are a direct reflection of compliant biomechanical forces on the optic nerve.[115,369] To mitigate this problem, animals were sedated with xylazine,[365] and a drop of 1% apraclonidine was instilled in the ocular hypertensive eye, both of which are effective at reducing the intraocular pressure to physiological levels. However, it is essential that the differences in ONH rim volume and RNFL area measures be verified in the clinical population, sampling from normal, glaucoma suspects and patients with various forms of glaucoma, and at every stage of the disease. This is especially of importance, as intraocular pressure is only a risk factor for glaucoma,[356,370-373] and patients considered to have normal tension glaucoma,[357,374] demonstrate progressive optic neuropathy regardless of having normal IOP measures.

The parapapillary RNFL thickness is the most common SD OCT measure in the management of optic nerve pathologies. Both the dynamic range[265] and repeatability[131-135] of this measure make it ideal for diagnosing and monitoring progressive and non-progressive optic nerve pathologies. For example, although ONH rim volume was the first to show significant changes in the ocular hypertensive eyes, and hence important for disease detection, it was also the first measure to asymptote (Fig. 6-6F, 6-11A&C). In contrast, RNFL area measures continued to change over a larger period of time (Fig. 6-8, 6-11A&C). In addition, having a small intra subject standard deviation, SD OCT RNFL area measures are better for detecting progression once disease has been identified.

The RNFL, as imaged and quantified using SD OCT, has both neuronal and non-neuronal components. These non-neuronal components include both glial[136,168] and vascular[167,316,345] tissue. Although glial tissue and small retinal vasculature cannot be resolved by current SD OCT imaging systems, the major retinal vasculature cast shadows[167] and can be visualized within the scan. The results of the present study illustrate the importance of accounting for major retinal vasculature when assessing the RNFL. In the healthy rhesus eyes, the major retinal vascular contribution was 9.2%, and similar to those previously reported in juvenile animals.[224] For the ocular hypertensive eyes, although the percent vascular contribution increased (up to ~18%), there was a significant decrease in the vascular area itself. Based on the best fit to the vessel area data (Fig. 6-7A), this decrease to end stage disease measured a 25.5% change. In human subjects, previous reports indicate a difference in vessel diameter of up to 15%[167,169,170,344] when comparing healthy eyes to the eyes of glaucoma patients. When the decrease is transformed to an area measure it is a 28% difference, which is similar to the present findings. Hence, the reduction in vascular contribution is likely a result of

a change in vessel caliber, as illustrated in Fig 6-7D. Although the vessel walls could not be visualized accurately enough to measure vessel caliber, an investigation of the vessel shadow width in these animals resulted in a similar decrease with disease progression (22.6%, data not shown), (Patel NB, et al. WGC 2011;E-Abstract FP16).

The relationship between ONH neural rim volume and RNFL area after vessel compensation (Fig. 6-12) provides useful data regarding non-neuronal components in the RNFL. Based on a neural rim volume of 0 mm^3, the best fit to these data would suggest a residual RNFL area of 352,871 μm^2. It is likely that this residual RNFL area (39.3%) represents glial and microvascular components within the RNFL. Although this estimate is similar to previous reports,[168] histological studies will be required to verify this measure. In addition, the present SD OCT data do not provide insight into changes in these non-neuronal components as a function of disease state.

The macular region in primates has the highest densities of both cone photoreceptors and retinal ganglion cells.[119,223,250] In the non-human primate, using SD OCT technology, the RGC layer has been reported to be thickest within a 1 mm radius of the foveal pit (Patel NB, et al. IOVS 2009;50:ARVO E-abstract 6207). Hence, for progressive optic neuropathies, it is likely that there will be a corresponding change in the macula morphology. Although total foveal volume within the central 3 mm, had good repeatability, it was the last of the morphological measures investigated to show progression (Fig. 6-9). In addition, none of the animals exceeded the normal variability of the normative data.

The decrease in macula volume corresponded well with changes in temporal (102.4 degree sector) RNFL area (Fig. 6-13). The best fit linear regression to these data had an intercept of approximately zero, providing support that the total retinal volume change within the central 3 mm is associated with only inner retinal loss. Although not

quantified in the present study, it is likely that isolation and measurement of the RGC layer itself would provide a better diagnostic measure. For example, studies in human subjects have reported differences in the retinal ganglion cell/inner plexiform layer in the macular region in both early[120,127] and advanced[124,128] glaucoma patients.

In conclusion, the findings of this study provide support for the use of multiple SD OCT determined scaled morphological measures for the diagnosis and management of primary open angle glaucoma associated with an elevated intraocular pressure. While ONH rim volume measures were the first to show change, RNFL area had the largest dynamic range. The data also provide evidence that for the most accurate RNFL measures, it is important to compensate for the major retinal vasculature. Although the total macular volume did not exceed the normative data, these measures may be important, especially in monitoring changes in patients with advanced to end stage disease.

CHAPTER 7

DISCUSSION, SUMMARY AND FUTURE DIRECTIONS

GENERAL DISCUSSION

Glaucoma defines a group of optic neuropathies that can lead to irreversible blindness if left untreated. In 2002, it was estimated that 37 million individuals worldwide were blinded by this disease, with 82% of these patients being over the age of 50.[319] As the world's population ages, by the year 2020, 79.6 million individuals will have the disease, of which 74% will be diagnosed as open angle glaucoma.[375] In the United States, glaucoma is a significant public health problem, affecting 2.2 million individuals, and is one of the leading causes of irreversible vision loss.

Having an elusive cause, the diagnosis or management of glaucoma usually relies on direct assessment of the optic nerve head (ONH), evaluating the retinal nerve fiber layer (RNFL) and/or measuring the sensitivity across the visual field. Although classical visual field defects are the hallmark sign of glaucoma, inter-individual and intra-individual variability make the detection of small changes or defects difficult, generally requiring multiple confirmatory tests.[33,34,164] Advances in imaging technology, specifically SD OCT provides an objective, non-invasive *in vivo* examination of the RNFL and ONH with nominal axial resolutions between 5-7 μm that may improve the diagnosis and management of glaucoma. However, for RNFL measures, several factors including age, ethnicity, axial length, signal strength, non-neuronal factors and scan centration need to be considered.[134,136,140,142,268] The series of experiments in this dissertation investigate ocular biometry, scan centration, segmentation and major retinal vasculature in RNFL analysis.

SUMMARY OF FINDINGS

SD OCT Layer Identification

The preliminary studies comparing histological sections to high resolution SD OCT images through similar regions provided a good correlation for retinal layers as illustrated in figure 1-2. However, there were some notable discrepancies. Specifically, the outer nuclear layer (ONL) thickness was significantly thicker while the outer plexiform layer (OPL) was significantly thinner in SD OCT sections. In addition, the iterative cross correlation methods used could not find a good histological correlate for the bright band in OCT sections, commonly labeled as the inner segment/outer segment (IS/OS) junction.

For the studies in foveal maturation (chapter two), the layers identified by cross correlation and the IS/OS junction[99,241] were used for data analysis. Overall, the SD OCT data from this study provided valuable insight into changes in foveal morphology from one to eighteen months of age. Specifically, using repeated measures on the same animal, accurate timelines were determined for each retinal layer and eccentricity evaluated. In general, the *in vivo* measures for the macular region corresponded well with and added to histological data previously published.[191,209,210,221]

The maturational changes in retinal layers, as visualized by SD OCT, provided additional insight on the identity of each layer. For example, there were significant changes in the IS/OS junction during the period studied. Hence, it is unlikely that this bright band in OCT cross sections represents a junction between the inner and outer segments. However, it does provide support for the band corresponding to the ellipsoid of the inner segments.[22, 23] In addition, thickening of this layer was most notable at time points at which metabolic demand in the outer retina would also be greatest. [95,255]

The histological comparison with the SD OCT scan section of a 10 day old (Fig 2-4) exemplified the discrepancy in ONL thickness. As with the histological comparison in the adolescent monkey (Fig 1-2), the OPL was significantly thinner than in the histological section. Hence, the monkey SD OCT ONL includes OPL and Henle fibers, similar to that in human scans.[251] However, the ONL thickness within the center of the pit, where the ONL and Henle fibers should be proportional, was used effectively at estimating the cone density and subsequently the Nyquist limit[376] for each scan session (Fig. 2-10).

Transverse Scaling of *in vivo* Images

The Littmann[176] or modified Littmann formulas (t=p.q.s)[174] are the most common methods used for determining transverse or lateral scaling for in vivo images, including fundus photography and scanning laser imaging. As, changes in axial length are calculated to have a nine times larger effect on ocular magnification compared to refractive changes associated with the cornea and crystalline lens,[377] this methodology does not take into account variability in anterior segment optics and assumes a static location for the first principal point.[174] However, the most accurate scaling methodologies should consider as many refractive elements as possible.[175] The first two experiments in this dissertation validate the use of a three surface schematic eye[179] for transverse scaling.

The influence of axial length on the extent of the retina scanned was investigated in chapter two. For the sixteen animals followed with SD OCT imaging, a three surface schematic eye accurately described changes in the ocular magnification as determined through image registration of successive SLO images. The rhesus monkey eye was

ideal for this experiment, as it has a higher equivalent power, and therefore small changes in axial length result in significantly large changes in retinal magnification.

In chapter three, the effects of anterior segment power on ocular magnification and RNFL thickness were investigated. Changes in dioptric power at the anterior corneal surface corresponded to both changes in ocular magnification and subsequently scan path location and RNFL thickness measures. In addition, the rate of change in ocular magnification with contact lens dioptric power was directly related to axial length. These observed changes were accurately described using the three surface schematic eye. Overall, the results from the experiments described in chapter two and three validate the use of a schematic eye for calculating transverse retinal scaling.

SD OCT RNFL Segmentation

For assessment of optic neuropathy, a 12 degree circular scan centered on the ONH is the most common method implemented for measurements of the peripapillary RNFL thickness. Measures of global RNFL thickness from these scans are shown to be repeatable and reliable in normal and diseased eyes[131-135] and are often used as a surrogate for axonal content within the eye.[47,48,50,138] However, thickness measures are dependent on the specific clinical instrument and the segmentation algorithm used. Specifically, although RNFL thickness measures are derived from similar scans, the global RNFL measures from one clinical instrument cannot be used interchangeably with another.

A custom, semi-automated segmentation algorithm that compensates for major retinal vasculature was investigated in human subjects as described in chapters three and four. In addition, the algorithm using image registration and methods to detect the fovea center, as described in chapter two, aligned the RNFL scans to a line connecting

the center of the optic nerve and the fovea. In both experiments, the vascular contribution to the global RNFL thickness was approximately 11.5%. These measures are in agreement with those reported by Mardin et al (11%), (Mardin CY, et al. IOVS 2009;50:ARVO E-abstract 3333), but less than those reported by Hood et al (13%).[167] In chapter three, the standard circular RNFL scan was repeated at the end of the experiment with no contact lenses. Based on these well centered circular scans, the intra-subject standard deviation was 1.19 μm, corresponding to repeatability measures of 3.31 μm, and comparable to instrument based RNFL analysis (1.5-5 μm).[88,266,378-380] However, when the scan path was registered and interpolated from raster scans centered on the optic nerve, the repeatability improved to 1.19 μm, illustrating the importance of scan path in addition to scan centration on RNFL measures.

The custom segmentation algorithm was then used to investigate differences in thickness measures between two commercial instruments (Spectralis and Cirrus). Whereas the Cirrus HD OCT interpolates a circular scan from a 200 X 200 A-scan scanned region centered on the ONH, the Spectralis uses the traditional circular scan path to acquire the same data. Although subjects were scanned sequentially by the same operator, there were significant differences between the instrument-determined RNFL measures of the two instruments (mean = 6.7 ± 4.8 μm), and similar to those reported by Leite et al.[61] However, when identical scan paths and the same segmentation algorithm were used, the measures were in good agreement (mean difference = 0.1 ± 3.1 μm). The results of this study also illustrate the influence of ocular magnification on RNFL thickness measures.

In both human subject experiments, a three surface schematic eye was used to calculate the transverse scaling. When transverse scaling was incorporated, the relationship between RNFL measures and anterior segment power or axial length was

not significant. Specifically, RNFL area[275] measures calculated by multiplying the scan circumference by global thickness were independent of ocular biometry. In turn, the RNFL area should correspond well with the RNFL axonal content when the thickness contributions of non-neuronal factors, including microvasculature and glial tissue, have been excluded.

SD OCT RNFL Measures in the Rhesus Monkey

The standard 12 degree circular scan has been used to describe RNFL changes in the monkey experimental laser induced ocular hypertension glaucoma model. However, several factors including differences in ocular biometry and ocular anatomy should be considered. For example, the adult eye of the rhesus monkey is significantly shorter than that of the human, and also has a higher equivalent power. In addition, whereas the human ONH is slightly larger in the vertical than horizontal dimension, the monkey optic nerve is particularly elliptical in shape. Hence, the standard RNFL circle-scan may not be appropriate for this species.

In chapter five, RNFL measures were investigated in the rhesus monkey using both, a standard circular scan, and custom elliptical scan paths that matched the shape of each subject's ONH. The same segmentation algorithms as those used for chapters three and four were used for RNFL quantification. The major retinal vasculature accounted for only 9.3% of global thickness measures in monkeys, which is less than in humans. Thickness measures from the standard circular scans were linearly related to axial length, with a steeper slope (Fig 5-6, -6.3 μm/mm) than for human eyes (Fig 4-8, -3.0 μm/mm). This difference in slopes is a direct reflection on the differences in equivalent power, and axial lengths of emmetropic eyes in the two species.

The influence of scan path on RNFL measures was investigated using interpolated elliptical scans 300-600 μm from the rim margin. As anticipated, there was linear decrease in RNFL thickness with increasing distance from the ONH. However, measures of the RNFL area remained constant. In general, these findings were in agreement with corresponding histological data. Specifically, while the RNFL thickness decreases with increasing distance from the ONH rim margin,[157] the change in thickness is not explained by axonal loss to RGCs within the region.[119] When elliptical scans were calculated using each individual's transverse scaling from schematic eye calculations, the RNFL thickness measures for each elliptical scan distance were not significantly related to axial length. In general, scan paths that were 550 μm from the rim margin resulted in global thickness measures that were similar to those acquired using standard circular scan methods (Fig 5-8).

SD OCT Morphological Measures in Experimental Glaucoma

RNFL measures from 550 μm elliptical scans were investigated in six rhesus monkeys with experimental glaucoma. The repeatability, based on the control eyes (4.0 μm) was used to determine progression, while the 95% confidence interval of the normative data was used for disease detection. RNFL loss was investigated as a function of both the cumulative/integrated IOP and duration from the first laser treatment. In general, although there was a significant relationship with IOP, the rate of change for each animal was different (Fig 6-7G). These results are in agreement with previous reports where the relationship between visual function and intraocular pressure was not significant.[326]

The percent vascular contribution to the RNFL increased with disease progression. However, the major retinal vascular content within the RNFL decreased

linearly with area measures. Although elevated intraocular pressure can lead to vascular obstruction, the patency of the retinal vasculature of the six animals was normal, as determined with fluorescein angiography. Hence, the changes in vascular contribution most likely represent a combination of loss in neuronal tissue and a reduction in the vessel caliber associated with disease progression, which corresponds to observations in human patients.[48, 77-79]

In contrast to RNFL measures, ONH morphology, and in particular the neural rim volume was significantly related to IOP. For the six monkeys, a small change in IOP resulted in a significant decrease in rim volume. However, other ONH parameters, such as cup depth did not show a similar trend. These results illustrate the differences in ONH morphology between subjects (Fig 6-5). Specifically, physiologically deep cups may show less changes in cup depth compared to animals with shallow baseline cupping. And although animals have differences in ONH shape and cup depth, the axonal content is relatively similar. Hence, it is not surprising that baseline neural rim volume measures had the smallest variance of all ONH parameters (Table 6-1). These findings and association of ONH morphological measures with IOP are in agreement with previous reports using this experimental glaucoma model.[114,366]

Although both RNFL measures and ONH rim volume represent axonal content, the two measures were not linearly related. As illustrated by the exponential rise to maximum relationship, a significant decrease in rim volume precedes changes in RNFL measures. This finding is also supported by the earlier time points at which progression was noted for rim volume compared to RNFL measures (Tables 6-3&4). In general, these longitudinal data provide supporting evidence for the biomechanical paradigm of glaucoma.[113]

The longitudinal study also provides support for macular analysis in glaucoma assessment. Although none of the animals in the study showed changes beyond the normative data, the macula volume decreased at a steady rate over time, showing progression only at later stages in the disease. In addition, changes in total macular volume were linearly related to changes in the corresponding sector of the peripapillary RNFL area (Fig 6-13).

FUTURE DIRECTIONS

Measures of RNFL area should correspond well with the ganglion cell content within the eye. However, *in vivo* measures include non-neuronal tissue. Hence, to use RNFL area as a surrogate for RGC content, it is essential that a relationship between optic nerve axonal counts be established at various stages of disease. These data will indirectly provide information on changes in the non-neuronal tissue within the RNFL associated with glaucomatous disease progression. Subsequently, measures of axonal content from RNFL measures will aid in investigations of structure-functional relationships. For RNFL to be used as a structural endpoint in disease diagnosis or progression, it is essential for these measures to accurately predict visual function.

As illustrated in the last experiment, the morphological structures of the eye change at varying rates with elevated IOP. Although RNFL measures have the largest dynamic range, the ONH rim volume was the first to change. Similarly, although the macula volume did not fall below the normative data, each animal showed progression. From these observations, it is likely that assessment of all these measures may provide useful insight into disease state. For example, changes in ONH parameters may be useful in assessing glaucoma suspects, and their conversion to glaucoma. Similarly, investigations of macula volume may provide useful diagnostic information for changes

in advanced disease, where visual field defects have encroached within the central 20 degrees. However, results from the present study suggest that an isolation of the RGC/IPL layers will improve the diagnostic capability of macular measurements in glaucoma. Although a majority of this work will be done in the rhesus monkey, it is also important that the finding be translated to patients with glaucoma.

CONCLUSION

An *in vivo* morphological assessment of the posterior segment can provide valuable information on the health of the eye. However, analysis is dependent on the properties of the imaging device and the algorithms used for quantification. For structural measures to be used as endpoints in detection of disease or disease progression, measures need to be repeatable and have good correspondence with retinal anatomy. The series of studies presented in this dissertation illustrate the importance of scaling and segmentation in the accurate analysis of the RNFL as imaged with SD OCT. The future directions are aimed at developing a structure functional relationship that will aid in validating the use of objective structural measures in assessing visual function in glaucomatous optic neuropathy.

REFERENCES

1. Herrel A, Podos J, Vanhooydonck B, Hendry AP. Force-velocity trade-off in Darwin's finch jaw function: a biomechanical basis for ecological speciation? *Funct Ecol.* Feb 2009;23(1):119-125.

2. Herrel A, Podos J, Huber SK, Hendry AP. Bite performance and morphology in a population of Darwin's finches: implications for the evolution of beak shape. *Funct Ecol.* Feb 2005;19(1):43-48.

3. Podos J. Correlated evolution of morphology and vocal signal structure in Darwin's finches. *Nature.* Jan 11 2001;409(6817):185-188.

4. Pannese E. The black reaction. *Brain research bulletin.* 1996;41(6):343-349.

5. Raviola E, Mazzarello P. The diffuse nervous network of Camillo Golgi: facts and fiction. *Brain research reviews.* Jan 7 2011;66(1-2):75-82.

6. Cajal SR. ¿Neuronismo o reticularismo? Las pruebas objetivas de la unidad anatómica de las células nerviosas. *Arch. Neurobiol.* 1933;13:1-144.

7. Piccolino M. Cajal and the retina: a 100-year retrospective. *Trends in neurosciences.* Dec 1988;11(12):521-525.

8. Harwerth RS. Charles F. Prentice Award Lecture 2006: a neuron doctrine for glaucoma. *Optom Vis Sci.* Jun 2008;85(6):436-444.

9. Wald G. The chemistry of rod vision. *Science.* Mar 16 1951;113(2933):287-291.

10. Provencio I, Rodriguez IR, Jiang G, Hayes WP, Moreira EF, Rollag MD. A novel human opsin in the inner retina. *J Neurosci.* Jan 15 2000;20(2):600-605.

11. Hattar S, Liao HW, Takao M, Berson DM, Yau KW. Melanopsin-containing retinal ganglion cells: architecture, projections, and intrinsic photosensitivity. *Science.* Feb 8 2002;295(5557):1065-1070.

12. Hecht S, Shlaer S, Pirenne MH. Energy, Quanta, and Vision. *The Journal of general physiology.* Jul 20 1942;25(6):819-840.

13. Hecht S, Shlaer S, Pirenne MH. Energy at the Threshold of Vision. *Science.* Jun 20 1941;93(2425):585-587.

14. Baylor DA, Lamb TD, Yau KW. Responses of retinal rods to single photons. *J Physiol.* Mar 1979;288:613-634.

15. Baylor DA, Lamb TD, Yau KW. The membrane current of single rod outer segments. *J Physiol.* Mar 1979;288:589-611.

16. Lamb TD, Baylor DA, Yau KW. The membrane current of single rod outer segments. *Vision Res.* 1979;19(4):385.

17. Rieke F, Baylor DA. Origin of reproducibility in the responses of retinal rods to single photons. *Biophysical journal.* Oct 1998;75(4):1836-1857.

18. Hecht S, Haig C, Chase AM. The Influence of Light Adaptation on Subsequent Dark Adaptation of the Eye. *The Journal of general physiology.* Jul 20 1937;20(6):831-850.

19. Hampson EC, Vaney DI, Weiler R. Dopaminergic modulation of gap junction permeability between amacrine cells in mammalian retina. *J Neurosci.* Dec 1992;12(12):4911-4922.

20. Tamura T, Nakatani K, Yau KW. Calcium feedback and sensitivity regulation in primate rods. *The Journal of general physiology.* Jul 1991;98(1):95-130.

21. Dunn FA, Lankheet MJ, Rieke F. Light adaptation in cone vision involves switching between receptor and post-receptor sites. *Nature.* Oct 4 2007;449(7162):603-606.

22. Harwerth RS, Carter-Dawson L, Shen F, Smith EL, 3rd, Crawford ML. Ganglion cell losses underlying visual field defects from experimental glaucoma. *Invest Ophthalmol Vis Sci.* Sep 1999;40(10):2242-2250.

23. Allingham RR, Damji KF, Shields MB. *Shields textbook of glaucoma.* 6th ed. Philadelphia: Wolters Kluwer Health/Lippincott Williams & Wilkins; 2011.

24. Anderson DR, Anderson DR. *Perimetry with and without automation.* 2nd ed. St. Louis: Mosby; 1987.

25. Johnson CA. Standardizing the measurement of visual fields for clinical research: Guidelines from the Eye Care Technology Forum. *Ophthalmology.* Jan 1996;103(1):186-189.

26. Harrington DO. The Bjerrum Scotoma. *Am J Ophthalmol.* Apr 1965;59:646-656.

27. Drance SM. The glaucomatous visual field. *Br J Ophthalmol.* Mar 1972;56(3):186-200.

28. Kitazawa Y, Yamamoto T. Glaucomatous visual field defects: their characteristics and how to detect them. *Clinical neuroscience.* 1997;4(5):279-283.

29. Quigley HA, Miller NR, George T. Clinical evaluation of nerve fiber layer atrophy as an indicator of glaucomatous optic nerve damage. *Arch Ophthalmol.* Sep 1980;98(9):1564-1571.

30. Sommer A, Miller NR, Pollack I, Maumenee AE, George T. The nerve fiber layer in the diagnosis of glaucoma. *Arch Ophthalmol.* Dec 1977;95(12):2149-2156.

31. Frisen L. Photography of the Retinal Nerve-Fiber Layer - an Optimized Procedure. *Brit J Ophthalmol.* 1980;64(9):641-650.

32. Heijl A, Lindgren G, Olsson J. Normal variability of static perimetric threshold values across the central visual field. *Arch Ophthalmol.* Nov 1987;105(11):1544-1549.

33. Keltner JL, Johnson CA, Quigg JM, Cello KE, Kass MA, Gordon MO. Confirmation of visual field abnormalities in the Ocular Hypertension Treatment Study. Ocular Hypertension Treatment Study Group. *Arch Ophthalmol.* Sep 2000;118(9):1187-1194.

34. Johnson CA, Keltner JL, Cello KE, et al. Baseline visual field characteristics in the ocular hypertension treatment study. *Ophthalmology.* Mar 2002;109(3):432-437.

35. Henson DB, Chaudry S, Artes PH, Faragher EB, Ansons A. Response variability in the visual field: comparison of optic neuritis, glaucoma, ocular hypertension, and normal eyes. *Invest Ophthalmol Vis Sci.* Feb 2000;41(2):417-421.

36. Reus NJ, Lemij HG, Garway-Heath DF, et al. Clinical assessment of stereoscopic optic disc photographs for glaucoma: the European Optic Disc Assessment Trial. *Ophthalmology.* Apr 2010;117(4):717-723.

37. Teitelbaum BA, Haefs R, Connor D. Interobserver variability in the estimation of the cup/disk ratio among observers of differing educational background. *Optometry.* Nov 2001;72(11):729-732.

38. Fechtner RD, Lama P. Advances in optic nerve head analysis in glaucoma. *Seminars in ophthalmology.* Sep 1999;14(3):180-188.

39. Giangiacomo A, Garway-Heath D, Caprioli J. Diagnosing glaucoma progression: current practice and promising technologies. *Curr Opin Ophthalmol.* Apr 2006;17(2):153-162.

40. Kim J, Dally LG, Ederer F, et al. The Advanced Glaucoma Intervention Study (AGIS): 14. Distinguishing progression of glaucoma from visual field fluctuations. *Ophthalmology.* Nov 2004;111(11):2109-2116.

41. Kerrigan-Baumrind LA, Quigley HA, Pease ME, Kerrigan DF, Mitchell RS. Number of ganglion cells in glaucoma eyes compared with threshold visual field tests in the same persons. *Invest Ophthalmol Vis Sci.* Mar 2000;41(3):741-748.

42. Quigley HA, Dunkelberger GR, Green WR. Retinal ganglion cell atrophy correlated with automated perimetry in human eyes with glaucoma. *Am J Ophthalmol.* May 15 1989;107(5):453-464.

43. Garway-Heath DF, Caprioli J, Fitzke FW, Hitchings RA. Scaling the hill of vision: the physiological relationship between light sensitivity and ganglion cell numbers. *Invest Ophthalmol Vis Sci.* Jun 2000;41(7):1774-1782.

44. Garway-Heath DF, Poinoosawmy D, Fitzke FW, Hitchings RA. Mapping the visual field to the optic disc in normal tension glaucoma eyes. *Ophthalmology.* Oct 2000;107(10):1809-1815.

45. Ferreras A, Pablo LE, Garway-Heath DF, Fogagnolo P, Garcia-Feijoo J. Mapping standard automated perimetry to the peripapillary retinal nerve fiber layer in glaucoma. *Invest Ophthalmol Vis Sci.* Jul 2008;49(7):3018-3025.

46. Harwerth RS, Crawford ML, Frishman LJ, Viswanathan S, Smith EL, 3rd, Carter-Dawson L. Visual field defects and neural losses from experimental glaucoma. *Progress in retinal and eye research.* Jan 2002;21(1):91-125.

47. Hood DC, Anderson SC, Wall M, Kardon RH. Structure versus function in glaucoma: an application of a linear model. *Invest Ophthalmol Vis Sci.* Aug 2007;48(8):3662-3668.

48. Hood DC, Anderson SC, Wall M, Raza AS, Kardon RH. A test of a linear model of glaucomatous structure-function loss reveals sources of variability in retinal nerve fiber and visual field measurements. *Invest Ophthalmol Vis Sci.* Sep 2009;50(9):4254-4266.

49. Swanson WH, Felius J, Pan F. Perimetric defects and ganglion cell damage: interpreting linear relations using a two-stage neural model. *Invest Ophthalmol Vis Sci.* Feb 2004;45(2):466-472.

50. Harwerth RS, Wheat JL, Fredette MJ, Anderson DR. Linking structure and function in glaucoma. *Progress in retinal and eye research.* Jul 2010;29(4):249-271.

51. Wride N, Habib M, Morris K, Campbell S, Fraser S. Clinical evaluation of a rapid, pupil-based assessment of retinal damage associated with glaucoma. *Clin Ophthalmol.* 2009;3:123-128.

52. Chen Y, Wyatt HJ, Swanson WH, Dul MW. Rapid pupil-based assessment of glaucomatous damage. *Optom Vis Sci.* Jun 2008;85(6):471-481.

53. Ventura LM, Porciatti V. Pattern electroretinogram in glaucoma. *Curr Opin Ophthalmol.* Apr 2006;17(2):196-202.

54. Luo X, Patel NB, Harwerth RS, Frishman LJ. Loss of the low-frequency component of the global-flash multifocal electroretinogram in primate eyes with experimental glaucoma. *Invest Ophthalmol Vis Sci.* May 2011;52(6):3792-3804.

55. Viswanathan S, Frishman LJ, Robson JG, Harwerth RS, Smith EL, 3rd. The photopic negative response of the macaque electroretinogram: reduction by experimental glaucoma. *Invest Ophthalmol Vis Sci.* May 1999;40(6):1124-1136.

56. Viswanathan S, Frishman LJ, Robson JG, Walters JW. The photopic negative response of the flash electroretinogram in primary open angle glaucoma. *Invest Ophthalmol Vis Sci.* Feb 2001;42(2):514-522.

57. Frishman LJ, Shen FF, Du L, et al. The scotopic electroretinogram of macaque after retinal ganglion cell loss from experimental glaucoma. *Invest Ophthalmol Vis Sci.* Jan 1996;37(1):125-141.

58. Nakamura M, Ishikawa K, Nagai T, Negi A. Receiver-operating characteristic analysis of multifocal VEPs to diagnose and quantify glaucomatous functional damage. *Documenta ophthalmologica. Advances in ophthalmology.* Oct 2011;123(2):93-108.

59. Arvind H, Klistorner A, Grigg J, Graham SL. Low-luminance contrast stimulation is optimal for early detection of glaucoma using multifocal visual evoked potentials. *Invest Ophthalmol Vis Sci.* May 2011;52(6):3744-3750.

60. Horn FK, Bergua A, Junemann A, Korth M. Visual evoked potentials under luminance contrast and color contrast stimulation in glaucoma diagnosis. *J Glaucoma.* Dec 2000;9(6):428-437.

61. Leite MT, Rao HL, Weinreb RN, et al. Agreement among spectral-domain optical coherence tomography instruments for assessing retinal nerve fiber layer thickness. *Am J Ophthalmol.* Jan 2011;151(1):85-92.

62. Tan BB, Natividad M, Chua KC, Yip LW. Comparison of Retinal Nerve Fiber Layer Measurement Between 2 Spectral Domain OCT Instruments. *J Glaucoma.* Jun 1 2011.

63. Patel NB, Wheat JL, Rodriguez A, Tran V, Harwerth RS. Agreement between Retinal Nerve Fiber Layer Measures from Spectralis and Cirrus Spectral Domain OCT. *Optom Vis Sci.* May 2012;89(5):652-666.

64. Keeler CR. The ophthalmoscope in the -lifetime of Hermann von Helmholtz. *Arch Ophthalmol.* Feb 2002;120(2):194-201.

65. Helmholtz Hv, Shastid TH. *The description of an ophthalmoscope : being an English translation of von Helmholtz's "Beschreibung eines Augenspiegels" (Berlin, 1851).* Chicago: Cleveland Press; 1916.

66. Quigley HA. Open-angle glaucoma. *N Engl J Med.* Apr 15 1993;328(15):1097-1106.

67. Gloster J, Parry DG. Use of Photographs for Measuring Cupping in Optic Disk. *Brit J Ophthalmol.* 1974;58(10):850-862.

68. Abramoff MD, Alward WL, Greenlee EC, et al. Automated segmentation of the optic disc from stereo color photographs using physiologically plausible features. *Invest Ophthalmol Vis Sci.* Apr 2007;48(4):1665-1673.

69. Jampel HD, Friedman D, Quigley H, et al. Agreement among glaucoma specialists in assessing progressive disc changes from photographs in open-angle glaucoma patients. *Am J Ophthalmol.* Jan 2009;147(1):39-44.

70. Webb RH, Hughes GW, Delori FC. Confocal scanning laser ophthalmoscope. *Applied optics.* Apr 15 1987;26(8):1492-1499.

71. Cioffi GA, Robin AL, Eastman RD, Perell HF, Sarfarazi FA, Kelman SE. Confocal laser scanning ophthalmoscope. Reproducibility of optic nerve head topographic measurements with the confocal laser scanning ophthalmoscope. *Ophthalmology.* Jan 1993;100(1):57-62.

72. Akar Y, Orhan M, Irkec M. Reproducibility of the measurements of the optic nerve head topographic variables with a confocal scanning laser ophthalmoscope. *Japanese journal of ophthalmology.* Mar-Apr 2003;47(2):173-177.

73. Burk RO, Vihanninjoki K, Bartke T, et al. Development of the standard reference plane for the Heidelberg retina tomograph. *Graefes Arch Clin Exp Ophthalmol.* May 2000;238(5):375-384.

74. Breusegem C, Fieuws S, Stalmans I, Zeyen T. Variability of the standard reference height and its influence on the stereometric parameters of the heidelberg retina tomograph 3. *Invest Ophthalmol Vis Sci.* Nov 2008;49(11):4881-4885.

75. Asaoka R, Strouthidis NG, Kappou V, Gardiner SK, Garway-Heath DF. HRT-3 Moorfields reference plane: effect on rim area repeatability and identification of progression. *Br J Ophthalmol.* Nov 2009;93(11):1510-1513.

76. Weinreb RN, Dreher AW, Coleman A, Quigley H, Shaw B, Reiter K. Histopathologic validation of Fourier-ellipsometry measurements of retinal nerve fiber layer thickness. *Arch Ophthalmol.* Apr 1990;108(4):557-560.

77. Knighton RW, Huang XR, Greenfield DS. Analytical model of scanning laser polarimetry for retinal nerve fiber layer assessment. *Invest Ophthalmol Vis Sci.* Feb 2002;43(2):383-392.

78. Dreher AWPOB, San Diego, CA, 92192), Reiter, Klaus (Ploeck II, W-6900 Heidelberg, DE), Inventor. Retinal eye disease diagnostic system. 1994.

79. Mai TA, Reus NJ, Lemij HG. Retinal nerve fiber layer measurement repeatability in scanning laser polarimetry with enhanced corneal compensation. *J Glaucoma.* Jun-Jul 2008;17(4):269-274.

80. Medeiros FA, Bowd C, Zangwill LM, Patel C, Weinreb RN. Detection of glaucoma using scanning laser polarimetry with enhanced corneal compensation. *Invest Ophthalmol Vis Sci.* Jul 2007;48(7):3146-3153.

81. Mai TA, Reus NJ, Lemij HG. Diagnostic accuracy of scanning laser polarimetry with enhanced versus variable corneal compensation. *Ophthalmology.* Nov 2007;114(11):1988-1993.

82. Fujimoto JG, De Silvestri S, Ippen EP, Puliafito CA, Margolis R, Oseroff A. Femtosecond optical ranging in biological systems. *Opt Lett.* Mar 1 1986;11(3):150.

83. Takada K, Yokohama I, Chida K, Noda J. New measurement system for fault location in optical waveguide devices based on an interferometric technique. *Applied optics.* May 1 1987;26(9):1603-1606.

84. Youngquist RC, Carr S, Davies DE. Optical coherence-domain reflectometry: a new optical evaluation technique. *Opt Lett.* Mar 1 1987;12(3):158-160.

85. Fercher AF, Mengedoht K, Werner W. Eye-length measurement by interferometry with partially coherent light. *Opt Lett.* Mar 1 1988;13(3):186-188.

86. Huang D, Swanson EA, Lin CP, et al. Optical coherence tomography. *Science.* Nov 22 1991;254(5035):1178-1181.

87. Hee MR. *Optical Coherence Tomography of the Eye*. Cambridge, MA: Dept. of Electrical Engineering and Computer Science, Massachusetts Institute of Technology; 1997.

88. Hong S, Kim CY, Lee WS, Seong GJ. Reproducibility of peripapillary retinal nerve fiber layer thickness with spectral domain cirrus high-definition optical coherence tomography in normal eyes. *Japanese journal of ophthalmology.* Jan 2010;54(1):43-47.

89. Seibold LK, Mandava N, Kahook MY. Comparison of retinal nerve fiber layer thickness in normal eyes using time-domain and spectral-domain optical coherence tomography. *Am J Ophthalmol.* Dec 2010;150(6):807-814.

90. Pierre-Kahn V, Tadayoni R, Haouchine B, Massin P, Gaudric A. Comparison of optical coherence tomography models OCT1 and Stratus OCT for macular retinal thickness measurement. *Br J Ophthalmol.* Dec 2005;89(12):1581-1585.

91. Kiernan DF, Hariprasad SM, Chin EK, Kiernan CL, Rago J, Mieler WF. Prospective comparison of cirrus and stratus optical coherence tomography for quantifying retinal thickness. *Am J Ophthalmol.* Feb 2009;147(2):267-275.

92. Forooghian F, Cukras C, Meyerle CB, Chew EY, Wong WT. Evaluation of time domain and spectral domain optical coherence tomography in the measurement of diabetic macular edema. *Invest Ophthalmol Vis Sci.* Oct 2008;49(10):4290-4296.

93. Huang Y, Cideciyan AV, Papastergiou GI, et al. Relation of optical coherence tomography to microanatomy in normal and rd chickens. *Invest Ophthalmol Vis Sci.* Nov 1998;39(12):2405-2416.

94. Abbott CJ, McBrien NA, Grunert U, Pianta MJ. Relationship of the optical coherence tomography signal to underlying retinal histology in the tree shrew (Tupaia belangeri). *Invest Ophthalmol Vis Sci.* Jan 2009;50(1):414-423.

95. Anger EM, Unterhuber A, Hermann B, et al. Ultrahigh resolution optical coherence tomography of the monkey fovea. Identification of retinal sublayers by correlation with semithin histology sections. *Exp Eye Res.* Jun 2004;78(6):1117-1125.

96. Gloesmann M, Hermann B, Schubert C, Sattmann H, Ahnelt PK, Drexler W. Histologic correlation of pig retina radial stratification with ultrahigh-resolution optical coherence tomography. *Invest Ophthalmol Vis Sci.* Apr 2003;44(4):1696-1703.

97. Strouthidis NG, Grimm J, Williams GA, Cull GA, Wilson DJ, Burgoyne CF. A comparison of optic nerve head morphology viewed by spectral domain optical coherence tomography and by serial histology. *Invest Ophthalmol Vis Sci.* Mar 2010;51(3):1464-1474.

98. Strouthidis NG, Yang H, Fortune B, Downs JC, Burgoyne CF. Detection of optic nerve head neural canal opening within histomorphometric and spectral domain optical coherence tomography data sets. *Invest Ophthalmol Vis Sci.* Jan 2009;50(1):214-223.

99. Srinivasan VJ, Wojtkowski M, Witkin AJ, et al. High-definition and 3-dimensional imaging of macular pathologies with high-speed ultrahigh-resolution optical coherence tomography. *Ophthalmology.* Nov 2006;113(11):2054-2065.

100. Alam S, Zawadzki RJ, Choi S, et al. Clinical application of rapid serial fourier-domain optical coherence tomography for macular imaging. *Ophthalmology.* Aug 2006;113(8):1425-1431.

101. Zawadzki RJ, Jones SM, Olivier SS, et al. Adaptive-optics optical coherence tomography for high-resolution and high-speed 3D retinal in vivo imaging. *Opt Express.* Oct 17 2005;13(21):8532-8546.

102. Minckler DS, Bunt AH, Johanson GW. Orthograde and retrograde axoplasmic transport during acute ocular hypertension in the monkey. *Invest Ophthalmol Vis Sci.* May 1977;16(5):426-441.

103. Quigley HA, Green WR. The histology of human glaucoma cupping and optic nerve damage: clinicopathologic correlation in 21 eyes. *Ophthalmology.* Oct 1979;86(10):1803-1830.

104. Olmedo M, Cadarso-Suarez C, Gomez-Ulla F, Val C, Fernandez I. Reproducibility of optic nerve head measurements obtained by optical coherence tomography. *European journal of ophthalmology.* Jul-Aug 2005;15(4):486-492.

105. Savini G, Carbonelli M, Parisi V, Barboni P. Repeatability of optic nerve head parameters measured by spectral-domain OCT in healthy eyes. *Ophthalmic surgery, lasers & imaging : the official journal of the International Society for Imaging in the Eye.* May-Jun 2011;42(3):209-215.

106. Gonzalez-Garcia AO, Vizzeri G, Bowd C, Medeiros FA, Zangwill LM, Weinreb RN. Reproducibility of RTVue retinal nerve fiber layer thickness and optic disc measurements and agreement with Stratus optical coherence tomography measurements. *Am J Ophthalmol.* Jun 2009;147(6):1067-1074.

107. Sihota R, Sony P, Gupta V, Dada T, Singh R. Comparing glaucomatous optic neuropathy in primary open angle and chronic primary angle closure glaucoma eyes by optical coherence tomography. *Ophthalmic Physiol Opt.* Sep 2005;25(5):408-415.

108. Mwanza JC, Oakley JD, Budenz DL, Anderson DR, Cirrus Optical Coherence Tomography Normative Database Study G. Ability of cirrus HD-OCT optic nerve head parameters to discriminate normal from glaucomatous eyes. *Ophthalmology.* Feb 2011;118(2):241-248.

109. Fujiwara T, Imamura Y, Margolis R, Slakter JS, Spaide RF. Enhanced depth imaging optical coherence tomography of the choroid in highly myopic eyes. *Am J Ophthalmol.* Sep 2009;148(3):445-450.

110. Imamura Y, Iida T, Maruko I, Zweifel SA, Spaide RF. Enhanced depth imaging optical coherence tomography of the sclera in dome-shaped macula. *Am J Ophthalmol.* Feb 2011;151(2):297-302.

111. Spaide RF, Koizumi H, Pozzoni MC. Enhanced depth imaging spectral-domain optical coherence tomography. *Am J Ophthalmol.* Oct 2008;146(4):496-500.

112. Girard MJ, Strouthidis NG, Ethier CR, Mari JM. Shadow removal and contrast enhancement in optical coherence tomography images of the human optic nerve head. *Invest Ophthalmol Vis Sci.* Sep 2011;52(10):7738-7748.

113. Burgoyne CF. A biomechanical paradigm for axonal insult within the optic nerve head in aging and glaucoma. *Exp Eye Res.* Aug 2011;93(2):120-132.

114. Strouthidis NG, Fortune B, Yang H, Sigal IA, Burgoyne CF. Longitudinal change detected by spectral domain optical coherence tomography in the optic nerve head and peripapillary retina in experimental glaucoma. *Invest Ophthalmol Vis Sci.* Mar 2011;52(3):1206-1219.

115. Strouthidis NG, Fortune B, Yang H, Sigal IA, Burgoyne CF. Effect of acute intraocular pressure elevation on the monkey optic nerve head as detected by spectral domain optical coherence tomography. *Invest Ophthalmol Vis Sci.* 2011;52(13):9431-9437.

116. Quigley HA, Hohman RM, Addicks EM, Massof RW, Green WR. Morphologic changes in the lamina cribrosa correlated with neural loss in open-angle glaucoma. *Am J Ophthalmol.* May 1983;95(5):673-691.

117. Kiumehr S, Park SC, Dorairaj S, et al. In Vivo Evaluation of Focal Lamina Cribrosa Defects in Glaucoma. *Arch Ophthalmol.* Jan 9 2012.

118. Park SC, Kiumehr S, Teng CC, Tello C, Liebmann JM, Ritch R. Horizontal Central Ridge of the Lamina Cribrosa and Regional Differences in Laminar Insertion in Normal Subjects. *Invest Ophthalmol Vis Sci.* Jan 20 2012.

119. Curcio CA, Allen KA. Topography of ganglion cells in human retina. *J Comp Neurol.* Oct 1 1990;300(1):5-25.

120. Tan O, Li G, Lu AT, Varma R, Huang D, Advanced Imaging for Glaucoma Study G. Mapping of macular substructures with optical coherence tomography for glaucoma diagnosis. *Ophthalmology.* Jun 2008;115(6):949-956.

121. Zeimer R, Asrani S, Zou S, Quigley H, Jampel H. Quantitative detection of glaucomatous damage at the posterior pole by retinal thickness mapping. A pilot study. *Ophthalmology.* Feb 1998;105(2):224-231.

122. Lederer DE, Schuman JS, Hertzmark E, et al. Analysis of macular volume in normal and glaucomatous eyes using optical coherence tomography. *Am J Ophthalmol.* Jun 2003;135(6):838-843.

123. Hess DB, Asrani SG, Bhide MG, Enyedi LB, Stinnett SS, Freedman SF. Macular and retinal nerve fiber layer analysis of normal and glaucomatous eyes in children using optical coherence tomography. *Am J Ophthalmol.* Mar 2005;139(3):509-517.

124. Raza AS, Cho J, de Moraes CG, et al. Retinal ganglion cell layer thickness and local visual field sensitivity in glaucoma. *Arch Ophthalmol.* Dec 2011;129(12):1529-1536.

125. Leung CK, Chan WM, Yung WH, et al. Comparison of macular and peripapillary measurements for the detection of glaucoma: an optical coherence tomography study. *Ophthalmology.* Mar 2005;112(3):391-400.

126. Wollstein G, Ishikawa H, Wang J, Beaton SA, Schuman JS. Comparison of three optical coherence tomography scanning areas for detection of glaucomatous damage. *Am J Ophthalmol.* Jan 2005;139(1):39-43.

127. Hood DC, Raza AS, de Moraes CG, et al. Initial arcuate defects within the central 10 degrees in glaucoma. *Invest Ophthalmol Vis Sci.* Feb 2011;52(2):940-946.

128. Vajaranant TS, Anderson RJ, Zelkha R, et al. The relationship between macular cell layer thickness and visual function in different stages of glaucoma. *Eye.* May 2011;25(5):612-618.

129. Cordeiro DV, Lima VC, Castro DP, et al. Influence of optic disc size on the diagnostic performance of macular ganglion cell complex and peripapillary retinal nerve fiber layer analyses in glaucoma. *Clin Ophthalmol.* 2011;5:1333-1337.

130. Seong M, Sung KR, Choi EH, et al. Macular and peripapillary retinal nerve fiber layer measurements by spectral domain optical coherence tomography in normal-tension glaucoma. *Invest Ophthalmol Vis Sci.* Mar 2010;51(3):1446-1452.

131. Schuman JS, Hee MR, Puliafito CA, et al. Quantification of nerve fiber layer thickness in normal and glaucomatous eyes using optical coherence tomography. *Arch Ophthalmol.* May 1995;113(5):586-596.

132. Blumenthal EZ, Williams JM, Weinreb RN, Girkin CA, Berry CC, Zangwill LM. Reproducibility of nerve fiber layer thickness measurements by use of optical coherence tomography. *Ophthalmology.* Dec 2000;107(12):2278-2282.

133. Carpineto P, Ciancaglini M, Zuppardi E, Falconio G, Doronzo E, Mastropasqua L. Reliability of nerve fiber layer thickness measurements using optical coherence tomography in normal and glaucomatous eyes. *Ophthalmology.* Jan 2003;110(1):190-195.

134. Budenz DL, Anderson DR, Varma R, et al. Determinants of normal retinal nerve fiber layer thickness measured by Stratus OCT. *Ophthalmology.* Jun 2007;114(6):1046-1052.

135. Budenz DL, Fredette MJ, Feuer WJ, Anderson DR. Reproducibility of peripapillary retinal nerve fiber thickness measurements with stratus OCT in glaucomatous eyes. *Ophthalmology.* Apr 2008;115(4):661-666.

136. Harwerth RS, Wheat JL, Rangaswamy NV. Age-related losses of retinal ganglion cells and axons. *Invest Ophthalmol Vis Sci.* Oct 2008;49(10):4437-4443.

137. Harwerth RS, Wheat JL. Modeling the effects of aging on retinal ganglion cell density and nerve fiber layer thickness. *Graefes Arch Clin Exp Ophthalmol.* Feb 2008;246(2):305-314.

138. Wheat JL, Rangaswamy NV, Harwerth RS. Correlating RNFL thickness by OCT with perimetric sensitivity in glaucoma patients. *J Glaucoma.* Feb 2012;21(2):95-101.

139. Sung KR, Wollstein G, Schuman JS, et al. Scan quality effect on glaucoma discrimination by glaucoma imaging devices. *Br J Ophthalmol.* Dec 2009;93(12):1580-1584.

140. Vizzeri G, Bowd C, Medeiros FA, Weinreb RN, Zangwill LM. Effect of signal strength and improper alignment on the variability of stratus optical coherence tomography retinal nerve fiber layer thickness measurements. *Am J Ophthalmol.* Aug 2009;148(2):249-255.

141. Gabriele ML, Ishikawa H, Wollstein G, et al. Optical coherence tomography scan circle location and mean retinal nerve fiber layer measurement variability. *Invest Ophthalmol Vis Sci.* Jun 2008;49(6):2315-2321.

142. Vizzeri G, Bowd C, Medeiros FA, Weinreb RN, Zangwill LM. Effect of improper scan alignment on retinal nerve fiber layer thickness measurements using Stratus optical coherence tomograph. *J Glaucoma.* Aug 2008;17(5):341-349.

143. Kim JS, Ishikawa H, Gabriele ML, et al. Retinal nerve fiber layer thickness measurement comparability between time domain optical coherence tomography (OCT) and spectral domain OCT. *Invest Ophthalmol Vis Sci.* Feb 2010;51(2):896-902.

144. Hwang YH, Lee JY, Kim YY. The effect of head tilt on the measurements of retinal nerve fibre layer and macular thickness by spectral-domain optical coherence tomography. *Br J Ophthalmol.* Nov 2011;95(11):1547-1551.

145. Langenegger SJ, Funk J, Toteberg-Harms M. Reproducibility of retinal nerve fiber layer thickness measurements using the eye tracker and the retest function of Spectralis SD-OCT in glaucomatous and healthy control eyes. *Invest Ophthalmol Vis Sci.* May 2011;52(6):3338-3344.

146. Medeiros FA, Zangwill LM, Alencar LM, et al. Detection of glaucoma progression with stratus OCT retinal nerve fiber layer, optic nerve head, and macular thickness measurements. *Invest Ophthalmol Vis Sci.* Dec 2009;50(12):5741-5748.

147. Grewal DS, Sehi M, Paauw JD, Greenfield DS. Detection of Progressive Retinal Nerve Fiber Layer ThicknessLoss With Optical Coherence Tomography Using4 Criteria for Functional Progression. *J Glaucoma.* Jun 8 2011.

148. Medeiros FA, Leite MT, Zangwill LM, Weinreb RN. Combining structural and functional measurements to improve detection of glaucoma progression using Bayesian hierarchical models. *Invest Ophthalmol Vis Sci.* Jul 2011;52(8):5794-5803.

149. Chung JK, Yoo YC. Correct calculation circle location of optical coherence tomography in measuring retinal nerve fiber layer thickness in eyes with myopic tilted discs. *Invest Ophthalmol Vis Sci.* 2011;52(11):7894-7900.

150. Strouthidis NG, Yang H, Reynaud JF, et al. Comparison of clinical and spectral domain optical coherence tomography optic disc margin anatomy. *Invest Ophthalmol Vis Sci.* Oct 2009;50(10):4709-4718.

151. Savini G, Barboni P, Parisi V, Carbonelli M. The influence of axial length on retinal nerve fibre layer thickness and optic-disc size measurements by spectral-domain OCT. *Br J Ophthalmol.* Jan 2012;96(1):57-61.

152. Samarawickrama C, Wang XY, Huynh SC, Burlutsky G, Stapleton F, Mitchell P. Effects of refraction and axial length on childhood optic disk parameters measured by optical coherence tomography. *Am J Ophthalmol.* Sep 2007;144(3):459-461.

153. Leung CK, Mohamed S, Leung KS, et al. Retinal nerve fiber layer measurements in myopia: An optical coherence tomography study. *Invest Ophthalmol Vis Sci.* Dec 2006;47(12):5171-5176.

154. Kang SH, Hong SW, Im SK, Lee SH, Ahn MD. Effect of myopia on the thickness of the retinal nerve fiber layer measured by Cirrus HD optical coherence tomography. *Invest Ophthalmol Vis Sci.* Aug 2010;51(8):4075-4083.

155. Huynh SC, Wang XY, Rochtchina E, Mitchell P. Peripapillary retinal nerve fiber layer thickness in a population of 6-year-old children: findings by optical coherence tomography. *Ophthalmology.* Sep 2006;113(9):1583-1592.

156. Savini G, Zanini M, Carelli V, Sadun AA, Ross-Cisneros FN, Barboni P. Correlation between retinal nerve fibre layer thickness and optic nerve head size: an optical coherence tomography study. *Br J Ophthalmol.* Apr 2005;89(4):489-492.

157. Varma R, Skaf M, Barron E. Retinal nerve fiber layer thickness in normal human eyes. *Ophthalmology.* Dec 1996;103(12):2114-2119.

158. Savini G, Barboni P, Carbonelli M, Zanini M. The effect of scan diameter on retinal nerve fiber layer thickness measurement using stratus optic coherence tomography. *Arch Ophthalmol.* Jul 2007;125(7):901-905.

159. Seider MI, Lee RY, Wang D, Pekmezci M, Porco TC, Lin SC. Optic disk size variability between African, Asian, white, Hispanic, and Filipino Americans using Heidelberg retinal tomography. *J Glaucoma.* Oct-Nov 2009;18(8):595-600.

160. Sample PA, Girkin CA, Zangwill LM, et al. The African Descent and Glaucoma Evaluation Study (ADAGES): design and baseline data. *Arch Ophthalmol.* Sep 2009;127(9):1136-1145.

161. Girkin CA, Sample PA, Liebmann JM, et al. African Descent and Glaucoma Evaluation Study (ADAGES): II. Ancestry differences in optic disc, retinal nerve fiber layer, and macular structure in healthy subjects. *Arch Ophthalmol.* May 2010;128(5):541-550.

162. Quigley HA, Coleman AL, Dorman-Pease ME. Larger optic nerve heads have more nerve fibers in normal monkey eyes. *Arch Ophthalmol.* Oct 1991;109(10):1441-1443.

163. Qiao-Grider Y, Hung LF, Kee CS, Ramamirtham R, Smith EL, 3rd. Normal ocular development in young rhesus monkeys (Macaca mulatta). *Vision Res.* May 2007;47(11):1424-1444.

164. Harwerth RS, Vilupuru AS, Rangaswamy NV, Smith EL, 3rd. The relationship between nerve fiber layer and perimetry measurements. *Invest Ophthalmol Vis Sci.* Feb 2007;48(2):763-773.

165. Yang H, Downs JC, Sigal IA, Roberts MD, Thompson H, Burgoyne CF. Deformation of the normal monkey optic nerve head connective tissue after acute

IOP elevation within 3-D histomorphometric reconstructions. *Invest Ophthalmol Vis Sci.* Dec 2009;50(12):5785-5799.

166. Cull G, Cioffi GA, Dong J, Homer L, Wang L. Estimating normal optic nerve axon numbers in non-human primate eyes. *J Glaucoma.* Aug 2003;12(4):301-306.

167. Hood DC, Fortune B, Arthur SN, et al. Blood vessel contributions to retinal nerve fiber layer thickness profiles measured with optical coherence tomography. *J Glaucoma.* Oct-Nov 2008;17(7):519-528.

168. Ogden TE. Nerve fiber layer of the primate retina: thickness and glial content. *Vision Res.* 1983;23(6):581-587.

169. Mitchell P, Leung H, Wang JJ, et al. Retinal vessel diameter and open-angle glaucoma: the Blue Mountains Eye Study. *Ophthalmology.* Feb 2005;112(2):245-250.

170. Amerasinghe N, Aung T, Cheung N, et al. Evidence of retinal vascular narrowing in glaucomatous eyes in an Asian population. *Invest Ophthalmol Vis Sci.* Dec 2008;49(12):5397-5402.

171. Ikram MK, de Voogd S, Wolfs RC, et al. Retinal vessel diameters and incident open-angle glaucoma and optic disc changes: the Rotterdam study. *Invest Ophthalmol Vis Sci.* Apr 2005;46(4):1182-1187.

172. Jonas JB, Martus P, Horn FK, Junemann A, Korth M, Budde WM. Predictive factors of the optic nerve head for development or progression of glaucomatous visual field loss. *Invest Ophthalmol Vis Sci.* Aug 2004;45(8):2613-2618.

173. Sanchez-Cano A, Baraibar B, Pablo LE, Honrubia FM. Magnification characteristics of the Optical Coherence Tomograph STRATUS OCT 3000. *Ophthalmic Physiol Opt.* Jan 2008;28(1):21-28.

174. Bennett AG, Rudnicka AR, Edgar DF. Improvements on Littmann's method of determining the size of retinal features by fundus photography. *Graefes Arch Clin Exp Ophthalmol.* Jun 1994;232(6):361-367.

175. Garway-Heath DF, Rudnicka AR, Lowe T, Foster PJ, Fitzke FW, Hitchings RA. Measurement of optic disc size: equivalence of methods to correct for ocular magnification. *Br J Ophthalmol.* Jun 1998;82(6):643-649.

176. Littmann H. [Determination of the real size of an object on the fundus of the living eye]. *Klin Monbl Augenheilkd.* Apr 1982;180(4):286-289.

177. Leung CK, Cheng AC, Chong KK, et al. Optic disc measurements in myopia with optical coherence tomography and confocal scanning laser ophthalmoscopy. *Invest Ophthalmol Vis Sci.* Jul 2007;48(7):3178-3183.

178. Lapuerta P, Schein SJ. A four-surface schematic eye of macaque monkey obtained by an optical method. *Vision Res.* Aug 1995;35(16):2245-2254.

179. Bennett AG, Rabbetts RB. The Schematic Eye. In: Bennett AG, Rabbetts RB, eds. *Clinical Visual Optics*. London: Butterworths; 1989:249-274.

180. Liampa Z, Kynigopoulos M, Pallas G, Gerding H. Comparison of two partial coherence interferometry devices for ocular biometry. *Klin Monbl Augenheilkd.* Apr 2010;227(4):285-288.

181. Cruysberg LP, Doors M, Verbakel F, Berendschot TT, De Brabander J, Nuijts RM. Evaluation of the Lenstar LS 900 non-contact biometer. *Br J Ophthalmol.* Jan 2010;94(1):106-110.

182. Lam AK, Chan R, Pang PC. The repeatability and accuracy of axial length and anterior chamber depth measurements from the IOLMaster. *Ophthalmic Physiol Opt.* Nov 2001;21(6):477-483.

183. Santodomingo-Rubido J, Mallen EA, Gilmartin B, Wolffsohn JS. A new non-contact optical device for ocular biometry. *Br J Ophthalmol.* Apr 2002;86(4):458-462.

184. Atchison DA, Markwell EL, Kasthurirangan S, Pope JM, Smith G, Swann PG. Age-related changes in optical and biometric characteristics of emmetropic eyes. *Journal of vision.* 2008;8(4):1-20.

185. Bengtsson B, Andersson S, Heijl A. Performance of time-domain and spectral-domain Optical Coherence Tomography for glaucoma screening. *Acta ophthalmologica.* Oct 14 2010.

186. Giani A, Cigada M, Choudhry N, et al. Reproducibility of retinal thickness measurements on normal and pathologic eyes by different optical coherence tomography instruments. *Am J Ophthalmol.* Dec 2010;150(6):815-824.

187. Vizzeri G, Weinreb RN, Gonzalez-Garcia AO, et al. Agreement between spectral-domain and time-domain OCT for measuring RNFL thickness. *Br J Ophthalmol.* Jun 2009;93(6):775-781.

188. Leung CK, Cheung CY, Weinreb RN, et al. Retinal nerve fiber layer imaging with spectral-domain optical coherence tomography: a variability and diagnostic performance study. *Ophthalmology.* Jul 2009;116(7):1257-1263.

189. Mayer MA, Hornegger J, Mardin CY, Tornow RP. Retinal Nerve Fiber Layer Segmentation on FD-OCT Scans of Normal Subjects and Glaucoma Patients. *Biomedical optics express.* 2010;1(5):1358-1383.

190. Koozekanani D, Boyer K, Roberts C. Retinal thickness measurements from optical coherence tomography using a Markov boundary model. *IEEE transactions on medical imaging.* Sep 2001;20(9):900-916.

191. Springer AD, Hendrickson AE. Development of the primate area of high acuity. 2. Quantitative morphological changes associated with retinal and pars plana growth. *Vis Neurosci.* Sep-Oct 2004;21(5):775-790.

192. Boothe RG, Dobson V, Teller DY. Postnatal development of vision in human and nonhuman primates. *Annual review of neuroscience.* 1985;8:495-545.

193. Movshon JA, Kiorpes L, Hawken MJ, Cavanaugh JR. Functional maturation of the macaque's lateral geniculate nucleus. *J Neurosci.* Mar 9 2005;25(10):2712-2722.

194. Ordy JM, Samorajski T, Collins RL, Nagy AR. Postnatal Development of Vision in a Subhuman Primate (Macaca Mulatta); a Multidisciplinary Study. *Arch Ophthalmol.* May 1965;73:674-686.

195. Teller DY. First glances: the vision of infants. the Friedenwald lecture. *Invest Ophthalmol Vis Sci.* Oct 1997;38(11):2183-2203.

196. Norcia AM, Tyler CW, Hamer RD. Development of contrast sensitivity in the human infant. *Vision Res.* 1990;30(10):1475-1486.

197. Kiorpes L, Movshon JA. Peripheral and central factors limiting the development of contrast sensitivity in macaque monkeys. *Vision Res.* Jan 1998;38(1):61-70.

198. Boothe RG, Kiorpes L, Williams RA, Teller DY. Operant measurements of contrast sensitivity in infant macaque monkeys during normal development. *Vision Res.* 1988;28(3):387-396.

199. Mayer DL, Dobson V. Visual acuity development in infants and young children, as assessed by operant preferential looking. *Vision Res.* 1982;22(9):1141-1151.

200. Ellemberg D, Lewis TL, Liu CH, Maurer D. Development of spatial and temporal vision during childhood. *Vision Res.* Jul 1999;39(14):2325-2333.

201. Kiorpes L. Development of vernier acuity and grating acuity in normally reared monkeys. *Vis Neurosci.* Sep-Oct 1992;9(3-4):243-251.

202. Kiorpes L, Kiper DC. Development of contrast sensitivity across the visual field in macaque monkeys (Macaca nemestrina). *Vision Res.* Jan 1996;36(2):239-247.

203. Simons K, National Research Council (U.S.). Committee on Vision. *Early visual development : normal and abnormal.* New York: Oxford University Press; 1993.

204. Werner JS, Chalupa LM. *The visual neurosciences.* Cambridge, Mass.: MIT Press; 2004.

205. Jacobs DS, Blakemore C. Factors limiting the postnatal development of visual acuity in the monkey. *Vision Res.* 1988;28(8):947-958.

206. Williams RA, Booth RG. Development of optical quality in the infant monkey (Macaca nemestrina) eye. *Invest Ophthalmol Vis Sci.* Nov 1981;21(5):728-736.

207. Ramamirtham R, Kee CS, Hung LF, Qiao-Grider Y, Roorda A, Smith EL, 3rd. Monochromatic ocular wave aberrations in young monkeys. *Vision Res.* Oct 2006;46(21):3616-3633.

208. Ramamirtham R, Kee CS, Hung LF, et al. Wave aberrations in rhesus monkeys with vision-induced ametropias. *Vision Res.* Sep 2007;47(21):2751-2766.

209. Hendrickson A, Kupfer C. The histogenesis of the fovea in the macaque monkey. *Invest Ophthalmol Vis Sci.* Sep 1976;15(9):746-756.

210. Packer O, Hendrickson AE, Curcio CA. Development redistribution of photoreceptors across the Macaca nemestrina (pigtail macaque) retina. *J Comp Neurol.* Aug 22 1990;298(4):472-493.

211. Springer AD, Hendrickson AE. Development of the primate area of high acuity. 1. Use of finite element analysis models to identify mechanical variables affecting pit formation. *Vis Neurosci.* Jan-Feb 2004;21(1):53-62.

212. Provis JM, Diaz CM, Dreher B. Ontogeny of the primate fovea: a central issue in retinal development. *Progress in neurobiology.* Apr 1998;54(5):549-580.

213. Hendrickson A. A morphological comparison of foveal development in man and monkey. *Eye.* 1992;6 (Pt 2):136-144.

214. Yuodelis C, Hendrickson A. A qualitative and quantitative analysis of the human fovea during development. *Vision Res.* 1986;26(6):847-855.

215. Hendrickson A. Morphological Development of the Primate Retina. In: Simons K, ed. *Early Visual Development, Normal and Abnormal*. 1 ed. New York: Oxford University Press; 1993:287-295.

216. La Vail MM, Rapaport DH, Rakic P. Cytogenesis in the monkey retina. *J Comp Neurol.* Jul 1 1991;309(1):86-114.

217. Hendrickson AE, Provis JM. Comparison of development of the primate fovea centralis with peripheral retina. In: Sernagor E, Eglen S, Harris B, Wong R, eds. *Retinal Development*. New York: Cambridge University Press; 2006:126-149.

218. Banks MS, Bennett PJ. Optical and photoreceptor immaturities limit the spatial and chromatic vision of human neonates. *Journal of the Optical Society of America. A, Optics and image science.* Dec 1988;5(12):2059-2079.

219. Wilson HR. Development of spatiotemporal mechanisms in infant vision. *Vision Res.* 1988;28(5):611-628.

220. Kiorpes L, Tang C, Hawken MJ, Movshon JA. Ideal observer analysis of the development of spatial contrast sensitivity in macaque monkeys. *Journal of vision.* 2003;3(10):630-641.

221. Springer AD, Hendrickson AE. Development of the primate area of high acuity, 3: temporal relationships between pit formation, retinal elongation and cone packing. *Vis Neurosci.* Mar-Apr 2005;22(2):171-185.

222. Curcio CA, Sloan KR, Kalina RE, Hendrickson AE. Human photoreceptor topography. *J Comp Neurol.* Feb 22 1990;292(4):497-523.

223. Curcio CA, Sloan KR, Jr., Packer O, Hendrickson AE, Kalina RE. Distribution of cones in human and monkey retina: individual variability and radial asymmetry. *Science.* May 1 1987;236(4801):579-582.

224. Patel NB, Luo X, Wheat JL, Harwerth RS. Retinal nerve fiber layer assessment: area versus thickness measurements from elliptical scans centered on the optic nerve. *Invest Ophthalmol Vis Sci.* Apr 2011;52(5):2477-2489.

225. Holden AL, Fitzke FW. Image size in the fundus: structural evidence for wide-field retinal magnification factor. *Br J Ophthalmol.* Mar 1988;72(3):228-230.

226. Bengtsson B, Krakau CE. Correction of optic disc measurements on fundus photographs. *Graefes Arch Clin Exp Ophthalmol.* 1992;230(1):24-28.

227. Hung LF, Crawford ML, Smith EL. Spectacle lenses alter eye growth and the refractive status of young monkeys. *Nature medicine.* Aug 1995;1(8):761-765.

228. Smith EL, 3rd, Hung LF. The role of optical defocus in regulating refractive development in infant monkeys. *Vision Res.* Apr 1999;39(8):1415-1435.

229. Smith EL, 3rd, Hung LF, Huang J. Relative peripheral hyperopic defocus alters central refractive development in infant monkeys. *Vision Res.* Sep 2009;49(19):2386-2392.

230. Smith EL, 3rd, Huang J, Hung LF, Blasdel TL, Humbird TL, Bockhorst KH. Hemiretinal form deprivation: evidence for local control of eye growth and refractive development in infant monkeys. *Invest Ophthalmol Vis Sci.* Nov 2009;50(11):5057-5069.

231. Huang J, Hung LF, Ramamirtham R, et al. Effects of form deprivation on peripheral refractions and ocular shape in infant rhesus monkeys (Macaca mulatta). *Invest Ophthalmol Vis Sci.* Sep 2009;50(9):4033-4044.

232. Zuclich JA, Lund DJ, Stuck BE. Wavelength dependence of ocular damage thresholds in the near-ir to far-ir transition region: proposed revisions to MPES. *Health Phys.* Jan 2007;92(1):15-23.

233. Delori FC, Webb RH, Sliney DH, American National Standards I. Maximum permissible exposures for ocular safety (ANSI 2000), with emphasis on ophthalmic devices. *J Opt Soc Am A Opt Image Sci Vis.* May 2007;24(5):1250-1265.

234. Hung LF, Ramamirtham R, Huang J, Qiao-Grider Y, Smith EL, 3rd. Peripheral refraction in normal infant rhesus monkeys. *Invest Ophthalmol Vis Sci.* Sep 2008;49(9):3747-3757.

235. Kee CS, Hung LF, Qiao Y, Habib A, Smith EL, 3rd. Prevalence of astigmatism in infant monkeys. *Vision Res.* May 2002;42(11):1349-1359.

236. Qiao-Grider Y, Hung LF, Kee CS, Ramamirtham R, Smith EL, 3rd. A comparison of refractive development between two subspecies of infant rhesus monkeys (Macaca mulatta). *Vision Res.* Jun 2007;47(12):1668-1681.

237. Wakitani Y, Sasoh M, Sugimoto M, Ito Y, Ido M, Uji Y. Macular Thickness Measurements in Healthy Subjects with Different Axial Lengths Using Optical Coherence Tomography. *Retina, The Journal of Retinal and Vitreous Diseases.* 2003;23(2):177-182.

238. Stewart CV, Tsai CL, Roysam B. The dual-bootstrap iterative closest point algorithm with application to retinal image registration. *IEEE transactions on medical imaging.* Nov 2003;22(11):1379-1394.

239. Canny J. A computational approach to edge detection. *IEEE Trans Pattern Anal Mach Intell.* Jun 1986;8(6):679-698.

240. Podoleanu A, Charalambous I, Plesea L, Dogariu A, Rosen R. Correction of distortions in optical coherence tomography imaging of the eye. *Phys Med Biol.* Apr 7 2004;49(7):1277-1294.

241. Drexler W, Fujimoto JG. State-of-the-art retinal optical coherence tomography. *Progress in retinal and eye research.* Jan 2008;27(1):45-88.

242. Springer AD. New role for the primate fovea: a retinal excavation determines photoreceptor deployment and shape. *Vis Neurosci.* Jul-Aug 1999;16(4):629-636.

243. Rapaport DH, Rakic P, LaVail MM. Spatiotemporal gradients of cell genesis in the primate retina. *Perspectives on developmental neurobiology.* 1996;3(3):147-159.

244. Kirby MA, Steineke TC. Morphogenesis of retinal ganglion cells: a model of dendritic, mosaic, and foveal development. *Perspectives on developmental neurobiology.* 1996;3(3):177-194.

245. Kiorpes L, Movshon JA. Differential development of two visual functions in primates. *Proc Natl Acad Sci U S A.* Nov 1989;86(22):8998-9001.

246. Brown AM, Dobson V, Maier J. Visual-Acuity of Human Infants at Scotopic, Mesopic and Photopic Luminances. *Vision Research.* 1987;27(10):1845-1858.

247. Rolls ET, Cowey A. Topography of the retina and striate cortex and its relationship to visual acuity in rhesus monkeys and squirrel monkeys. *Exp Brain Res.* 1970;10(3):298-310.

248. Perry VH, Cowey A. The ganglion cell and cone distributions in the monkey's retina: implications for central magnification factors. *Vision Res.* 1985;25(12):1795-1810.

249. Curcio CA, Hendrickson, A.E. Chapter 5 Organization and development of the primate photoreceptor mosaic. *Progress in Retinal Research.* 1991 1991;10:89-120.

250. Packer O, Hendrickson AE, Curcio CA. Photoreceptor topography of the retina in the adult pigtail macaque (Macaca nemestrina). *J Comp Neurol.* Oct 1 1989;288(1):165-183.

251. Lujan BJ, Roorda A, Knighton RW, Carroll J. Revealing Henle's fiber layer using spectral domain optical coherence tomography. *Invest Ophthalmol Vis Sci.* Mar 2011;52(3):1486-1492.

252. Abercrombie M. Estimation of nuclear population from microtome sections. *Anat Rec.* Feb 1946;94:239-247.

253. Blakemore C, Vital-Durand F. Organization and post-natal development of the monkey's lateral geniculate nucleus. *J Physiol.* Nov 1986;380:453-491.

254. Blakemore C, Molnar Z. Factors involved in the establishment of specific interconnections between thalamus and cerebral cortex. *Cold Spring Harb Symp Quant Biol.* 1990;55:491-504.

255. Fernandez EJ, Hermann B, Povazay B, et al. Ultrahigh resolution optical coherence tomography and pancorrection for cellular imaging of the living human retina. *Opt Express.* Jul 21 2008;16(15):11083-11094.

256. Grunert U, Greferath U, Boycott BB, Wassle H. Parasol (P alpha) ganglion-cells of the primate fovea: immunocytochemical staining with antibodies against GABAA-receptors. *Vision Res.* Jan 1993;33(1):1-14.

257. Fukuda Y, Sawai H, Watanabe M, Wakakuwa K, Morigiwa K. Nasotemporal overlap of crossed and uncrossed retinal ganglion cell projections in the Japanese monkey (Macaca fuscata). *J Neurosci.* Jul 1989;9(7):2353-2373.

258. Leventhal AG, Thompson KG, Liu D. Retinal ganglion cells within the foveola of New World (Saimiri sciureus) and Old World (Macaca fascicularis) monkeys. *J Comp Neurol.* Dec 8 1993;338(2):242-254.

259. Drasdo N, Millican CL, Katholi CR, Curcio CA. The length of Henle fibers in the human retina and a model of ganglion receptive field density in the visual field. *Vision Res.* Oct 2007;47(22):2901-2911.

260. Hoyt WF. Fundoscopy of the retinal nerve fiber layer in neurosurgical practice. *Neurologia medico-chirurgica.* 1973;13:3-20.

261. Chen TC, Cense B, Pierce MC, et al. Spectral domain optical coherence tomography: ultra-high speed, ultra-high resolution ophthalmic imaging. *Arch Ophthalmol.* Dec 2005;123(12):1715-1720.

262. Nassif N, Cense B, Park BH, et al. In vivo human retinal imaging by ultrahigh-speed spectral domain optical coherence tomography. *Opt Lett.* Mar 1 2004;29(5):480-482.

263. Fujimoto JG. Optical coherence tomography for ultrahigh resolution in vivo imaging. *Nature biotechnology.* Nov 2003;21(11):1361-1367.

264. de Boer JF, Cense B, Park BH, Pierce MC, Tearney GJ, Bouma BE. Improved signal-to-noise ratio in spectral-domain compared with time-domain optical coherence tomography. *Opt Lett.* Nov 1 2003;28(21):2067-2069.

265. Schuman JS, Pedut-Kloizman T, Hertzmark E, et al. Reproducibility of nerve fiber layer thickness measurements using optical coherence tomography. *Ophthalmology.* Nov 1996;103(11):1889-1898.

266. Mwanza JC, Chang RT, Budenz DL, et al. Reproducibility of peripapillary retinal nerve fiber layer thickness and optic nerve head parameters measured with cirrus HD-OCT in glaucomatous eyes. *Invest Ophthalmol Vis Sci.* Nov 2010;51(11):5724-5730.

267. Wang XY, Huynh SC, Burlutsky G, Ip J, Stapleton F, Mitchell P. Reproducibility of and effect of magnification on optical coherence tomography measurements in children. *Am J Ophthalmol.* Mar 2007;143(3):484-488.

268. Savini G, Zanini M, Barboni P. Influence of pupil size and cataract on retinal nerve fiber layer thickness measurements by Stratus OCT. *J Glaucoma.* Aug 2006;15(4):336-340.

269. Feuer WJ, Budenz DL, Anderson DR, et al. Topographic differences in the age-related changes in the retinal nerve fiber layer of normal eyes measured by Stratus optical coherence tomography. *J Glaucoma.* Mar 2011;20(3):133-138.

270. Salchow DJ, Oleynikov YS, Chiang MF, et al. Retinal nerve fiber layer thickness in normal children measured with optical coherence tomography. *Ophthalmology.* May 2006;113(5):786-791.

271. Harman A, Abrahams B, Moore S, Hoskins R. Neuronal density in the human retinal ganglion cell layer from 16-77 years. *Anat Rec.* Oct 1 2000;260(2):124-131.

272. Balazsi AG, Rootman J, Drance SM, Schulzer M, Douglas GR. The effect of age on the nerve fiber population of the human optic nerve. *Am J Ophthalmol.* Jun 1984;97(6):760-766.

273. Repka MX, Quigley HA. The effect of age on normal human optic nerve fiber number and diameter. *Ophthalmology.* Jan 1989;96(1):26-32.

274. Skaf M, Bernardes AB, Cardillo JA, et al. Retinal nerve fibre layer thickness profile in normal eyes using third-generation optical coherence tomography. *Eye.* Apr 2006;20(4):431-439.

275. Bayraktar S, Bayraktar Z, Yilmaz OF. Influence of scan radius correction for ocular magnification and relationship between scan radius with retinal nerve fiber

layer thickness measured by optical coherence tomography. *J Glaucoma.* Jun 2001;10(3):163-169.

276. Salchow DJ, Hwang AM, Li FY, Dziura J. Effect of contact lens power on optical coherence tomography of the retinal nerve fiber layer. *Invest Ophthalmol Vis Sci.* Mar 2011;52(3):1650-1654.

277. Lee J, Kim NR, Kim H, et al. Negative refraction power causes underestimation of peripapillary retinal nerve fibre layer thickness in spectral-domain optical coherence tomography. *Br J Ophthalmol.* Sep 2011;95(9):1284-1289.

278. Sardar DK, Swanland GY, Yow RM, Thomas RJ, Tsin AT. Optical properties of ocular tissues in the near infrared region. *Lasers in medical science.* Mar 2007;22(1):46-52.

279. Bland JM, Altman DG. Measurement error. *BMJ.* Sep 21 1996;313(7059):744.

280. Vitale S, Sperduto RD, Ferris FL, 3rd. Increased prevalence of myopia in the United States between 1971-1972 and 1999-2004. *Arch Ophthalmol.* Dec 2009;127(12):1632-1639.

281. Nanavaty MA, Daya SM. Refractive lens exchange versus phakic intraocular lenses. *Curr Opin Ophthalmol.* Jan 2012;23(1):54-61.

282. Maldonado MJ, Nieto JC, Pinero DP. Advances in technologies for laser-assisted in situ keratomileusis (LASIK) surgery. *Expert Rev Med Devices.* Mar 2008;5(2):209-229.

283. Sutton GL, Kim P. Laser in situ keratomileusis in 2010 - a review. *Clin Experiment Ophthalmol.* Mar 2010;38(2):192-210.

284. Lichtinger A, Rootman DS. Intraocular lenses for presbyopia correction: past, present, and future. *Curr Opin Ophthalmol.* Jan 2012;23(1):40-46.

285. Hirsch MJ, Weymouth FW. Prevalence of refractive anomalies. In: Grosvenor T, Flom MC, eds. *Refractive Anomalies: Research and Clinical Applications*. 3 ed. Boston: Butterworth-Heinemann; 1991:15-38.

286. Sorsby A, Benjamin B, Sheridan M, Stone J, Leary GA. Refraction and its components during the growth of the eye from the age of three. *Memo Med Res Counc.* 1961;301(Special):1-67.

287. Atchison DA. Age-related paraxial schematic emmetropic eyes. *Ophthalmic Physiol Opt.* Jan 2009;29(1):58-64.

288. Sung KR, Kim DY, Park SB, Kook MS. Comparison of retinal nerve fiber layer thickness measured by Cirrus HD and Stratus optical coherence tomography. *Ophthalmology.* Jul 2009;116(7):1264-1270.

289. Knight OJ, Chang RT, Feuer WJ, Budenz DL. Comparison of retinal nerve fiber layer measurements using time domain and spectral domain optical coherent tomography. *Ophthalmology.* Jul 2009;116(7):1271-1277.

290. Nassif N, Cense B, Park B, et al. In vivo high-resolution video-rate spectral-domain optical coherence tomography of the human retina and optic nerve. *Opt Express.* Feb 9 2004;12(3):367-376.

291. Sakamoto A, Hangai M, Yoshimura N. Spectral-domain optical coherence tomography with multiple B-scan averaging for enhanced imaging of retinal diseases. *Ophthalmology.* Jun 2008;115(6):1071-1078.

292. Costello F, Coupland S, Hodge W, et al. Quantifying axonal loss after optic neuritis with optical coherence tomography. *Ann Neurol.* Jun 2006;59(6):963-969.

293. Sergott RC. Optical coherence tomography: measuring in-vivo axonal survival and neuroprotection in multiple sclerosis and optic neuritis. *Curr Opin Ophthalmol.* Dec 2005;16(6):346-350.

294. Ratchford JN, Quigg ME, Conger A, et al. Optical coherence tomography helps differentiate neuromyelitis optica and MS optic neuropathies. *Neurology.* Jul 28 2009;73(4):302-308.

295. Horn FK, Mardin CY, Laemmer R, et al. Correlation between local glaucomatous visual field defects and loss of nerve fiber layer thickness measured with polarimetry and spectral domain OCT. *Invest Ophthalmol Vis Sci.* May 2009;50(5):1971-1977.

296. Townsend KA, Wollstein G, Schuman JS. Imaging of the retinal nerve fibre layer for glaucoma. *Br J Ophthalmol.* Feb 2009;93(2):139-143.

297. Tan BB, Natividad M, Chua KC, Yip LW. Comparison of Retinal Nerve Fiber Layer Measurement Between 2 Spectral Domain OCT Instruments. *J Glaucoma.* Jun 1.

298. Kim JS, Ishikawa H, Sung KR, et al. Retinal nerve fibre layer thickness measurement reproducibility improved with spectral domain optical coherence tomography. *Br J Ophthalmol.* Aug 2009;93(8):1057-1063.

299. Bendschneider D, Tornow RP, Horn FK, et al. Retinal nerve fiber layer thickness in normals measured by spectral domain OCT. *J Glaucoma.* Sep 2010;19(7):475-482.

300. Da Pozzo S, Iacono P, Marchesan R, Minutola D, Ravalico G. The effect of ageing on retinal nerve fibre layer thickness: an evaluation by scanning laser polarimetry with variable corneal compensation. *Acta ophthalmologica Scandinavica.* Jun 2006;84(3):375-379.

301. Savini G, Barboni P, Parisi V, Carbonelli M. The influence of axial length on retinal nerve fibre layer thickness and optic-disc size measurements by spectral-domain OCT. *Br J Ophthalmol.* Feb 24.

302. Jonas JB, Schmidt AM, Muller-Bergh JA, Schlotzer-Schrehardt UM, Naumann GO. Human optic nerve fiber count and optic disc size. *Invest Ophthalmol Vis Sci.* May 1992;33(6):2012-2018.

303. Chang M, Yoo C, Kim SW, Kim YY. Retinal vessel diameter, retinal nerve fiber layer thickness, and intraocular pressure in korean patients with normal-tension glaucoma. *Am J Ophthalmol.* Jan 2011;151(1):100-105.

304. Atchison DA, Smith G. Chromatic dispersions of the ocular media of human eyes. *J Opt Soc Am A Opt Image Sci Vis.* Jan 2005;22(1):29-37.

305. Van Rijn LJ, Van der Steen J, Collewijn H. Instability of ocular torsion during fixation: cyclovergence is more stable than cycloversion. *Vision Res.* Apr 1994;34(8):1077-1087.

306. Van Rijn LJ, Van der Steen J, Collewijn H. Eye torsion elicited by oscillating gratings: effects of orientation, wavelength and stationary contours. *Vision Res.* Feb 1994;34(4):533-540.

307. Altman DG, Bland JM. Measurement in Medicine - the Analysis of Method Comparison Studies. *Statistician.* 1983;32(3):307-317.

308. Bland JM, Altman DG. Statistical methods for assessing agreement between two methods of clinical measurement. *Lancet.* Feb 8 1986;1(8476):307-310.

309. Mwanza JC, Bhorade AM, Sekhon N, et al. Effect of cataract and its removal on signal strength and peripapillary retinal nerve fiber layer optical coherence tomography measurements. *J Glaucoma.* Jan 2011;20(1):37-43.

310. McGraw KO, Wong SP. Forming inferences about some intraclass correlations coefficients (vol 1, pg 30, 1996). *Psychol Methods.* Dec 1996;1(4):390-390.

311. Cheung CY, Leung CK, Lin D, Pang CP, Lam DS. Relationship between retinal nerve fiber layer measurement and signal strength in optical coherence tomography. *Ophthalmology.* Aug 2008;115(8):1347-1351.

312. Lee J, Koh D, Ong CN. Statistical evaluation of agreement between two methods for measuring a quantitative variable. *Computers in biology and medicine.* 1989;19(1):61-70.

313. Mylonas G, Ahlers C, Malamos P, et al. Comparison of retinal thickness measurements and segmentation performance of four different spectral and time domain OCT devices in neovascular age-related macular degeneration. *Br J Ophthalmol.* Nov 2009;93(11):1453-1460.

314. Leung CK, Cheung CY, Weinreb RN, et al. Comparison of macular thickness measurements between time domain and spectral domain optical coherence tomography. *Invest Ophthalmol Vis Sci.* Nov 2008;49(11):4893-4897.

315. Knighton RW, Qian C. An optical model of the human retinal nerve fiber layer: implications of directional reflectance for variability of clinical measurements. *J Glaucoma.* Feb 2000;9(1):56-62.

316. Scoles D, Gray DC, Hunter JJ, et al. In-vivo imaging of retinal nerve fiber layer vasculature: imaging histology comparison. *BMC ophthalmology.* 2009;9:1-9.

317. Ogden TE. Nerve fiber layer of the macaque retina: retinotopic organization. *Invest Ophthalmol Vis Sci.* Jan 1983;24(1):85-98.

318. Tan JC, Poinoosawmy D, Fitzke FW, Hitchings RA. Magnification changes in scanning laser tomography. *J Glaucoma.* Apr 2004;13(2):137-141.

319. Resnikoff S, Pascolini D, Etya'ale D, et al. Global data on visual impairment in the year 2002. *Bulletin of the World Health Organization.* Nov 2004;82(11):844-851.

320. Quigley HA. Neuronal death in glaucoma. *Progress in retinal and eye research.* Jan 1999;18(1):39-57.

321. Weinreb RN, Khaw PT. Primary open-angle glaucoma. *Lancet.* May 22 2004;363(9422):1711-1720.

322. Wojtkowski M, Srinivasan V, Ko T, Fujimoto J, Kowalczyk A, Duker J. Ultrahigh-resolution, high-speed, Fourier domain optical coherence tomography and methods for dispersion compensation. *Opt Express.* May 31 2004;12(11):2404-2422.

323. Sander B, Larsen M, Thrane L, Hougaard JL, Jorgensen TM. Enhanced optical coherence tomography imaging by multiple scan averaging. *Br J Ophthalmol.* Feb 2005;89(2):207-212.

324. Gaasterland D, Kupfer C. Experimental glaucoma in the rhesus monkey. *Investigative ophthalmology.* Jun 1974;13(6):455-457.

325. Quigley HA, Hohman RM. Laser energy levels for trabecular meshwork damage in the primate eye. *Invest Ophthalmol Vis Sci.* Sep 1983;24(9):1305-1307.

326. Harwerth RS, Smith EL, 3rd, DeSantis L. Experimental glaucoma: perimetric field defects and intraocular pressure. *J Glaucoma.* Dec 1997;6(6):390-401.

327. Harwerth RS. Primate Glaucoma Models. In: Pang IH, Clark AF, eds. *Animal Models for Retinal Disease*. 1 ed. New York: Humana Press; 2010.

328. Harwerth RS, Smith EL, 3rd, DeSantis L. Behavioral perimetry in monkeys. *Invest Ophthalmol Vis Sci.* Jan 1993;34(1):31-40.

329. Downs JC, Yang H, Girkin C, et al. Three-dimensional histomorphometry of the normal and early glaucomatous monkey optic nerve head: neural canal and subarachnoid space architecture. *Invest Ophthalmol Vis Sci.* Jul 2007;48(7):3195-3208.

330. Sasaoka M, Nakamura K, Shimazawa M, Ito Y, Araie M, Hara H. Changes in visual fields and lateral geniculate nucleus in monkey laser-induced high intraocular pressure model. *Exp Eye Res.* May 2008;86(5):770-782.

331. Fortune B, Yang H, Strouthidis NG, et al. The effect of acute intraocular pressure elevation on peripapillary retinal thickness, retinal nerve fiber layer thickness, and retardance. *Invest Ophthalmol Vis Sci.* Oct 2009;50(10):4719-4726.

332. Sanfilippo PG, Cardini A, Hewitt AW, Crowston JG, Mackey DA. Optic disc morphology--rethinking shape. *Progress in retinal and eye research.* Jul 2009;28(4):227-248.

333. Mikelberg FS, Drance SM, Schulzer M, Yidegiligne HM, Weis MM. The normal human optic nerve. Axon count and axon diameter distribution. *Ophthalmology.* Sep 1989;96(9):1325-1328.

334. Mikelberg FS, Yidegiligne HM, White VA, Schulzer M. Relation between optic nerve axon number and axon diameter to scleral canal area. *Ophthalmology.* Jan 1991;98(1):60-63.

335. Panda-Jonas S, Jonas JB, Jakobczyk M, Schneider U. Retinal photoreceptor count, retinal surface area, and optic disc size in normal human eyes. *Ophthalmology.* Mar 1994;101(3):519-523.

336. Ogden TE. Nerve fiber layer of the primate retina: morphometric analysis. *Invest Ophthalmol Vis Sci.* Jan 1984;25(1):19-29.

337. Sanchez RM, Dunkelberger GR, Quigley HA. The number and diameter distribution of axons in the monkey optic nerve. *Invest Ophthalmol Vis Sci.* Sep 1986;27(9):1342-1350.

338. Ramanujan S. Modular Equations and Approximations to p. *Pure and Applied Mathematics Quarterly.* 1913-1914;45:350-372.

339. Baleanu D, Tornow RP, Horn FK, et al. Retinal Nerve Fiber Layer Thickness in Normals Measured by Spectral Domain OCT. *J Glaucoma.* Dec 30 2009.

340. Hougaard JL, Ostenfeld C, Heijl A, Bengtsson B. Modelling the normal retinal nerve fibre layer thickness as measured by Stratus optical coherence tomography. *Graefes Arch Clin Exp Ophthalmol.* Dec 2006;244(12):1607-1614.

341. Huang J, Liu X, Wu Z, et al. Macular and retinal nerve fiber layer thickness measurements in normal eyes with the Stratus OCT, the Cirrus HD-OCT, and the Topcon 3D OCT-1000. *J Glaucoma.* Feb 2011;20(2):118-125.

342. Savini G, Carbonelli M, Barboni P. Retinal nerve fiber layer thickness measurement by Fourier-domain optical coherence tomography: a comparison between cirrus-HD OCT and RTVue in healthy eyes. *J Glaucoma.* Aug 2010;19(6):369-372.

343. Jonas JB, Fernandez MC, Naumann GO. Parapapillary atrophy and retinal vessel diameter in nonglaucomatous optic nerve damage. *Invest Ophthalmol Vis Sci.* Oct 1991;32(11):2942-2947.

344. Rader J, Feuer WJ, Anderson DR. Peripapillary vasoconstriction in the glaucomas and the anterior ischemic optic neuropathies. *Am J Ophthalmol.* Jan 15 1994;117(1):72-80.

345. Fortune B, Cull GA, Burgoyne CF. Relative course of retinal nerve fiber layer birefringence and thickness and retinal function changes after optic nerve transection. *Invest Ophthalmol Vis Sci.* Oct 2008;49(10):4444-4452.

346. Lam TT, Kwong JM, Tso MO. Early glial responses after acute elevated intraocular pressure in rats. *Invest Ophthalmol Vis Sci.* Feb 2003;44(2):638-645.

347. Nickells RW. From ocular hypertension to ganglion cell death: a theoretical sequence of events leading to glaucoma. *Canadian journal of ophthalmology. Journal canadien d'ophtalmologie.* Apr 2007;42(2):278-287.

348. Tezel G, Fourth APORICWG. The role of glia, mitochondria, and the immune system in glaucoma. *Invest Ophthalmol Vis Sci.* Mar 2009;50(3):1001-1012.

349. Morrison JC, Cork LC, Dunkelberger GR, Brown A, Quigley HA. Aging changes of the rhesus monkey optic nerve. *Invest Ophthalmol Vis Sci.* Aug 1990;31(8):1623-1627.

350. Nangia V, Matin A, Bhojwani K, Kulkarni M, Yadav M, Jonas JB. Optic disc size in a population-based study in central India: the Central India Eye and Medical Study (CIEMS). *Acta ophthalmologica.* Feb 2008;86(1):103-104.

351. Wang Y, Xu L, Zhang L, Yang H, Ma Y, Jonas JB. Optic disc size in a population based study in northern China: the Beijing Eye Study. *Br J Ophthalmol.* Mar 2006;90(3):353-356.

352. Xu L, Li Y, Wang S, Wang Y, Wang Y, Jonas JB. Characteristics of highly myopic eyes: the Beijing Eye Study. *Ophthalmology.* Jan 2007;114(1):121-126.

353. Rajan MS, Keilhorn I, Bell JA. Partial coherence laser interferometry vs conventional ultrasound biometry in intraocular lens power calculations. *Eye.* Sep 2002;16(5):552-556.

354. Holzer MP, Mamusa M, Auffarth GU. Accuracy of a new partial coherence interferometry analyser for biometric measurements. *Br J Ophthalmol.* Jun 2009;93(6):807-810.

355. The Advanced Glaucoma Intervention Study (AGIS): 7. The relationship between control of intraocular pressure and visual field deterioration.The AGIS Investigators. *Am J Ophthalmol.* Oct 2000;130(4):429-440.

356. Gordon MO, Beiser JA, Brandt JD, et al. The Ocular Hypertension Treatment Study: baseline factors that predict the onset of primary open-angle glaucoma. *Arch Ophthalmol.* Jun 2002;120(6):714-720.

357. Anderson DR. Collaborative normal tension glaucoma study. *Curr Opin Ophthalmol.* Apr 2003;14(2):86-90.

358. Weinreb RN, Shakiba S, Sample PA, et al. Association between quantitative nerve fiber layer measurement and visual field loss in glaucoma. *Am J Ophthalmol.* Dec 1995;120(6):732-738.

359. Harwerth RS, Carter-Dawson L, Smith EL, 3rd, Barnes G, Holt WF, Crawford ML. Neural losses correlated with visual losses in clinical perimetry. *Invest Ophthalmol Vis Sci.* Sep 2004;45(9):3152-3160.

360. Harwerth RS, Carter-Dawson L, Smith EL, 3rd, Crawford ML. Scaling the structure--function relationship for clinical perimetry. *Acta ophthalmologica Scandinavica.* Aug 2005;83(4):448-455.

361. Gramer E, Gerlach R, Krieglstein GK, Leydhecker W. [Topography of early glaucomatous visual field defects in computerized perimetry]. *Klin Monbl Augenheilkd.* Jun 1982;180(6):515-523.

362. Burgoyne CF, Downs JC, Bellezza AJ, Suh JK, Hart RT. The optic nerve head as a biomechanical structure: a new paradigm for understanding the role of IOP-related stress and strain in the pathophysiology of glaucomatous optic nerve head damage. *Progress in retinal and eye research.* Jan 2005;24(1):39-73.

363. Jonas JB, Gusek GC, Guggenmoos-Holzmann I, Naumann GO. Variability of the real dimensions of normal human optic discs. *Graefes Arch Clin Exp Ophthalmol.* 1988;226(4):332-336.

364. Rasmussen CA, Kaufman PL. Primate glaucoma models. *J Glaucoma.* Aug 2005;14(4):311-314.

365. Burke JA, Potter DE. The ocular effects of xylazine in rabbits, cats, and monkeys. *Journal of ocular pharmacology.* Winter 1986;2(1):9-21.

366. Yang H, Thompson H, Roberts MD, Sigal IA, Downs JC, Burgoyne CF. Deformation of the early glaucomatous monkey optic nerve head connective

tissue after acute IOP elevation in 3-D histomorphometric reconstructions. *Invest Ophthalmol Vis Sci.* Jan 2011;52(1):345-363.

367. Jonas JB, Gusek GC, Naumann GO. Optic disc, cup and neuroretinal rim size, configuration and correlations in normal eyes. *Invest Ophthalmol Vis Sci.* Jul 1988;29(7):1151-1158.

368. Caprioli J, Miller JM. Optic disc rim area is related to disc size in normal subjects. *Arch Ophthalmol.* Dec 1987;105(12):1683-1685.

369. Coleman AL, Quigley HA, Vitale S, Dunkelberger G. Displacement of the optic nerve head by acute changes in intraocular pressure in monkey eyes. *Ophthalmology.* Jan 1991;98(1):35-40.

370. Friedman DS, Wolfs RCW, O'Colmain B, et al. Prevalence of open-angle glaucoma among adults in the United States. *Arch Ophthalmol-Chic.* Apr 2004;122(4):532-538.

371. Leske MC. The epidemiology of open-angle glaucoma: a review. *American journal of epidemiology.* Aug 1983;118(2):166-191.

372. Sommer A, Tielsch JM, Katz J, et al. Relationship between intraocular pressure and primary open angle glaucoma among white and black Americans. The Baltimore Eye Survey. *Arch Ophthalmol.* Aug 1991;109(8):1090-1095.

373. Tielsch JM. The epidemiology and control of open angle glaucoma: a population-based perspective. *Annual review of public health.* 1996;17:121-136.

374. Gutteridge IF. Normal tension glaucoma: diagnostic features and comparisons with primary open angle glaucoma. *Clinical & experimental optometry : journal of the Australian Optometrical Association.* May-Jun 2000;83(3):161-172.

375. Quigley HA, Broman AT. The number of people with glaucoma worldwide in 2010 and 2020. *Br J Ophthalmol.* Mar 2006;90(3):262-267.

376. Williams DR. Aliasing in human foveal vision. *Vision Res.* 1985;25(2):195-205.

377. Wakitani Y, Sasoh M, Sugimoto M, Ito Y, Ido M, Uji Y. Macular thickness measurements in healthy subjects with different axial lengths using optical coherence tomography. *Retina.* Apr 2003;23(2):177-182.

378. Savini G, Carbonelli M, Barboni P. Spectral-domain optical coherence tomography for the diagnosis and follow-up of glaucoma. *Curr Opin Ophthalmol.* Mar 2011;22(2):115-123.

379. Toteberg-Harms M, Sturm V, Knecht PB, Funk J, Menke MN. Repeatability of nerve fiber layer thickness measurements in patients with glaucoma and without glaucoma using spectral-domain and time-domain OCT. *Graefes Arch Clin Exp Ophthalmol.* Feb 2012;250(2):279-287.

380. Carpineto P, Nubile M, Agnifili L, et al. Reproducibility and Repeatability of Cirrus HD-OCT Peripapillary Retinal Nerve Fibre Layer Thickness Measurements in Young Normal Subjects. *Ophthalmologica. Journal international d'ophtalmologie. International journal of ophthalmology. Zeitschrift fur Augenheilkunde.* Jan 19 2012;227(3):139-145.